TOWARDS THE CULTIVATION OF 'UNCULTIVABLE' MICROBES: THE DESIGN AND DEVELOPMENT OF A MICROBIAL DOMESTICATION POD CONTAINING MICROENCAPSULATED MARINE SEDIMENT BACTERIA

A Thesis

Submitted to the Graduate Faculty

in Partial Fulfillment of the Requirements

for the Degree of Master of Science

in Sustainable Design Engineering

Faculty of Sustainable Design Engineering

University of Prince Edward Island

Tartela Alkayyali

Charlottetown, Prince Edward Island

August 2019

ABSTRACT

The emergence of antibiotic resistance calls for discovering and researching microbial-origin natural products for antibiotic activity. Since nearly 99% of microbes are 'uncultivable' in standard laboratory conditions, developing cultivation methods for these microbes is of high importance to natural product discovery. This thesis explored the potential for growing 'uncultivable' microbes through the design of a microbial domestication pod (MD Pod). The MD Pod is a 3D printed device containing a cylindrical cavity in which the microbes are placed. Microbes are prevented from migrating across the MD Pod through two enclosing polycarbonate (PCTE) membranes. The PCTE membranes also allow for the diffusion of nutrients, chemicals, and wastes across the MD Pod, supplying the microbes with substances needed for their growth and survival. The MD Pod is different from other similar devices by providing a single cavity for the growth of diverse microbial samples at once, enabling better cell-to-cell communication and, therefore, better chances of growth through achieving quorum sensing.

This thesis also explored the effect of encapsulating microbial cells in agarose microbeads through the use of a 3D printed, 1000 µm cross-flow microfluidic device, in which the shear stress of a mineral oil phase (containing 4% v/v surfactant), caused droplet formation of an agarose/cell mixture. Single-cell encapsulation is targeted to provide each microbe with a separate microbead to grow, and the microbeads are expected to provide the growing microbes with nutrients. Several MD Pod *in-situ* incubation tests were implemented using marine sediment bacteria collected from North River and Brackley Beach, Prince Edward Island. Most of the tests showed

contamination of the used MD Pod devices (confirmed using polymerase chain reaction-denaturing gradient gel electrophoresis (PCR-DGGE) analysis). However, devices showing no contamination led to observing that encapsulated microbes formed single colonies after *in-situ* incubation, which is expected to make downstream microbial isolation easier.

Three known marine sediment bacteria, *M. polaris* (Gram-negative), *P. aquimaris* (Gram-negative), and *B. licheniformis* (Gram-positive), were used as representative bacteria to examine the effect of encapsulation on their growth. It was observed that these species do not form colonies on agar plates from their encapsulated samples when their microbeads were suspended in 50% Instant Ocean®, but *B. licheniformis* grew into individual colonies when its microbeads were suspended in 10% Marine Broth. Moreover, better cell survival and viability were observed for the three representative species when their respective microbeads were suspended in 10% Marine Broth. This suggested that growth on plates from encapsulated samples might not be suitable for all types of bacteria and that their suspending solution must contain a dilute amount of nutrients (in addition to salts) for their continued growth. It was also found that higher temperatures (40ºC and 45ºC) decreased the survival of the three species, suggesting that exposure to the encapsulation temperature (45ºC) might limit the types of bacteria that could be cultivated after encapsulation.

This thesis also explored the design of a system that provided separation of the mineral oil (used in the encapsulation) from an aqueous phase. Two systems were designed and tested, with a cartridge filter-inspired separation column showing approximately 97% - 99% separation. The system was further tested for microbead

transfer from the oil phase to the aqueous phase. Through imaging, microbeads were observed in the collected aqueous phase, indicating that this system could be coupled with the microbead generation system to achieve higher throughput.

Last but not the least, an alternative microfluidic chip fabrication method was proposed and developed. A scaffold (of the desired microfluidic channels) was 3D printed using acrylonitrile butadiene styrene (ABS), then it was dissoluted in acetone at controlled conditions. The resulting scaffold was then placed in liquid polydimethylsiloxane (PDMS) and cured. A microfluidic chip was obtained by dissolving the internal scaffold using acetone. A T-junction microfluidic chip was produced using this method and was tested for droplet generation, suggesting that such a chip could be used for encapsulating the marine sediment bacteria. Finally, the ability of this method to fabricate microfluidic chips with different geometries was confirmed by fabricating a bifurcation channel and a drug testing microfluidic chip.

PREFACE

The present thesis is an outcome of a multi-disciplinary research collaboration between the Faculty of Sustainable Design Engineering and the Departments of Chemistry and Biomedical Sciences at the University of Prince Edward Island (UPEI). Funding was provided by the Natural Sciences and Engineering Council of Canada (NSERC), Mitacs, UPEI scholarships, and Nautilus BioSciences Canada.

Multiple people contributed to the present work. Details of all contributions are as follows:

- Chapter 1:
  - Sections 1.3.1.1, 1.3.1.2, and 1.3.1.3 were drafted with Emily Pope.
  - Monica Cella reviewed the text of sections 1.3.2, 1.3.3, and 1.3.5.
- Chapter 2:
  - The second paragraph in section 2.1, the caption of Figure 2.2, and the text in sections 2.2.3.1, 2.2.3.2, 2.2.4.1, 2.2.4.2, 2.3.4.1.1, 2.3.4.2.1, and 2.3.5 were drafted and/or co-written with Emily Pope.
  - The laboratory work in this chapter included the work of two Masters students: Tartela Alkayyali and Emily Pope. Tartela's contributions were all the designs, developments, and tests presented in this chapter. Emily's contributions were: microbial culturing and testing (*E. coli*, MSB, *M. polaris*, *P. aquimaris*, and *B. licheniformis*), cell encapsulation, MSB and marine species cell survival and viability tests, MD Pod *in-situ* incubations and cell migration tests, and PCR and DGGE application.
  - Dr. Walid Mazyan contributed to the design of the F-MD Pod.
  - Bradley Haltli suggested the removal of the loading port from the F-MD Pod design and suggested the presented unloading procedure.
  - Sydney Wheatley helped in cell viability imaging and analysis of *M. polaris*, *P. aquimaris*, and *B. licheniformis.*
- Chapter 3:
  - Dr. Walid Mazyan contributed to conducting some of the tests presented in Table 3.1.
  - Dr. Walid Mazyan contributed to the design and testing of the cartridge filter-inspired oil removal system.

- Chapter 4:
  - Chuck Terrio and Anthony Van Beek helped in building the shaker setup (Setup D).
  - Anthony Van Beek 3D printed all scaffold prototypes.
  - Dr. Doug Dahn supplied the bright filed microscope used for imaging the channel dimensions before and after dissolution.
  - Dr. Christian Lacroix helped in SEM imaging the scaffolds at different stages of dissolution.
  - Dr. Russell Kerr provided access to Cytation™ 5 for microbead imaging and analysis.
  - Monica Cella reviewed the text of this chapter.
- Appendix:
  - Bradley Haltli contributed to testing the dyes presented in Table F.1.
  - The protocols presented in Appendices D and E were co-written with Emily Pope.

Publications and conference posters and presentations:

- The text, figures, and tables presented in sections 1.3.2 and 1.3.3 were published as a review paper in *Analytica Chimica Acta* as per the following citation:
  - T. Alkayyali, T. Cameron, J. Tweel, B. Haltli, R. Kerr, and A. Ahmadi, "Microfluidic and Cross-Linking Methods for Microencapsulation of Living Cells and Bacteria- A Review," *Analytica Chimica Acta*, vol. 1053C, pp. 1-21, 2019

  with Tartela Alkayyali being the first author and main contributor to the writing of this work. The work can be accessed through: https://www.sciencedirect.com/science/article/pii/S0003267019300236?via%3Dihub
- The data and results related to the cell survival and viability of *M. polaris*, *P. aquimaris*, and *B. licheniformis*, the results of the effect of temperature on these species (sections 2.3.4.1.3 and 2.3.4.2.3), as well as the material biocompatibility study (section 2.3.5) will be submitted as a research article to *Lab on a Chip*, 2019.
- The work presented in Chapter 2 resulted in the following conference proceedings:
  - T. Alkayyali, E. Pope, B. Haltli, R. Kerr, and A. Ahmadi, "Cultivation of 'Uncultivable' Marine Sediment Bacteria Using a Microbial Domestication Pod (MD Pod)", accepted in the International Conference on Miniaturized Systems for Chemistry and Life Sciences (μTAS) 2019, Oct 27-31, Basel, Switzerland. Conference proceeding and poster presentation.
  - T. Alkayyali, B. Haltli, R. Kerr, and A. Ahmadi, "A Microbial Domestication Pod for the Discovery of Natural Products," μTAS 2018, Nov 11-15, Kaohsiung, Taiwan. Conference proceeding and poster presentation.
  - T. Alkayyali, T. Cameron, J. Tweel, B. Haltli, R. Kerr, and A. Ahmadi, "A Growth Chamber for the Discovery of New Natural Products Using Bacteria

Encapsulation in Agarose Microbeads," CSME2018 International Congress, May 27-30, Toronto, Canada. Conference proceeding and oral presentation.

- T. Alkayyali, "A Growth Chamber for the Discovery of Natural Products Using Bacteria Microencapsulation," the 2018 UPEI Annual Graduate Studies and Research Conference, May 16-18, Charlottetown, Canada. Oral presentation.
- T. Alkayyali, "A Growth Chamber for the Discovery of Natural Products Using Bacteria Microencapsulation," the UPEI FSDE Expo, Apr 18, 2019 and Apr 20, 2018. Poster presentations.
- T. Alkayyali, "A Growth Chamber for the Discovery of Natural Products Using Bacteria Microencapsulation," the UPEI FSDE Graduate Research Seminar Series, Sep 19 and Mar 28, 2018. Oral presentations.

- The work presented in Chapter 3 resulted in the following conference proceeding:
  - T. Alkayyali and A. Ahmadi, "Microfluidic Oil/Water Separation Using a Hydrophobic-Oleophilic Stainless Steel Membrane," CSME-CFDSC Congress 2019, Jun 2-5, London, Canada. Conference proceeding and oral presentation.
- The data and results related to the cell survival and viability of *P. aquimaris* before and after oil removal using the cartridge filter-inspired oil removal system (shown in sections 3.2.2 and 3.3.2) as well as a comparison of the viability obtained using traditional microbead washing over cell strainers will be submitted as a letter to *RSC Advances*, 2019.
- The text presented in sections 1.3.5 and 5.2 (paragraphs 4 and 5) and the text and figures presented in Chapter 4 will submitted as a research article as per the following:
  - T. Alkayyali and A. Ahmadi, "Fabrication of Microfluidic Chips Using Controlled Dissolution of 3D Printed Scaffolds," *Journal of Materials Processing Technology*, 2019.

ACKNOWLEDGEMENTS

This two year journey, undoubtedly, would not have been possible without the blessings of Allah, Who guided my path towards completing this project. I am forever grateful to You for opening my mind to think, develop, and contribute to advancing science. I am also grateful to You for granting me this learning opportunity, my place of living, health and well-being, source of income, and all the nice people I met.

My parents, Dr. Andi Hijazi and Eng. Munther Alkayyali, are the reason behind my passion for continuing my education. Seeing my mom make time to gain a PhD encouraged me to not stop at my Bachelor's degree, and my father always encouraged me and my sisters to be independent and seek knowledge. I hope I will always be the apple of your eyes. Thank you for investing in me and for always praying for me. Many thanks to Dr. Amani Al-Othman for showing me that women can be great scientists.

Dr. Walid Mazyan, the flower of my heart, is the one person who supported me through all the hardships I faced throughout my Master's degree with no questions asked. I cannot thank you enough for always listening to me, helping me in the lab, and suggesting ideas for improving my work ethics and deliverables. Thank you for believing in me in my darkest hours, for wanting me to continue my education further, and for being patient throughout my thesis-writing days. You are the perfect husband.

I also thank you my supervisors, Dr. Ali Ahmadi and Dr. Russell Kerr, for always providing your valuable insight towards delivering the best results. Thank you for making this learning opportunity possible and for showing me that multi-disciplinary projects are fun and unique. I would not have gained a wealth of engineering and microbiology skills without working in both of your labs and using your diverse, specialized equipment.

Of course, Bradley Haltli, is not to be forgotten. He is the brain behind confirming every idea I proposed for the merge between engineering and microbiology. Thank you for providing me with your professional support and for training me to perform lab cell work from level zero. I will not forget that.

Emily Pope is the most amazing lab partner anyone could have. From the moment she joined the lab, she was there to help me carry out the tasks needed to complete the project. She woke up at 4:00AM to accompany me to check on the MD Pods in a river, worked with me for over 12 hours straight, on numerous occasions, just to complete one run, and continued to help me to the day of my thesis defense. I cannot thank you enough for being very supportive. I could not have asked for a better friend AND lab partner.

The superstars behind the scenes are Chuck Terrio, Anthony Van Beek, and Andrew Townshend. Thank you for always fixing my setups, 3D printing countless prototypes, and machining tens of models. None of what I did would have been possible without your help. I really loved working with you and I will miss our chats!

I would also like to thank Sydney Wheatley for spending hours squinting at live and dead bacteria (sorry!), and for offering support when I really needed it. Thank you Hadeel, Amal, Cereena, Razan, Emad, Shadi, Haifa, Fatima, Tiffany, Haley, Rodolfo, Enoo, Ankita, Matthew, Nick, Noelle, Hope, Stacey, Zach, Vernon, Logan, Leon, and Anna for being the very supportive and kind friends anyone could ask for.

Last but not the least, thanks to NSERC (Discovery Grant), Mitacs (Accelerate), and UPEI for funding this valuable research and enabling me to expand my education.

DEDICATION

To mom, dad, and Walid

TABLE OF CONTENTS

LIST OF FIGURES

LIST OF TABLES

ABBREVIATIONS

3T3	3-day transfer, inoculum 3×10^5 cells
2D	Two-dimensional
3D	Three-dimensional
A	Adenine
ABS	Acrylonitrile butadiene styrene
C	Cytosine
CAD	Computer-aided design
$-CF_3$	Trifluoromethyl functional groups
CTAB	Cetyltrimethylammonium bromide
DAPI	4′,6-diamidino-2-phenylindole dihydrochloride
DGGE	Denaturing gradient gel electrophoresis
DI water	Deionized water
dMA	Dilute Marine Agar
DMAO	A green, cell-permeable fluorescent dye, for which the abbreviation, chemical name, and structure are proprietary of PromoCell, Germany
DNA	Deoxyribonucleic acid
DOS	Dioctyl sulfosuccinate
DRIE	Deep reactive ion etching
eISR	Enhanced internal scaffold removal
ERS	*E. coli* re-suspended solution
EthD-III	Ethidium homodimer III
EWS	*E. coli* working solution
F	Forward
FDA	Food and Drug Administration
FDM	Fused-deposition modeling
F-MD Pod	Final MD Pod
FSS	Filter-sterilized seawater
G	Guanine
GFP	Green Fluorescence Protein

GO	Graphene oxide
HA	Hyaluronic acid
HFE7500	Hydrofluoroether
iChip	Isolation chip
ID	Internal diameter
IPA	Isopropyl alcohol
ISR	Internal scaffold removal
k	The actual number of cells encapsulated
LB	Lysogeny broth
LCST	Lower critical solution temperature
LED	Light emitting diodes
MD Pod	Microbial domestication pod
MED	Monolithic elastomer device
M-MD Pod	Metallic MD Pod
mPEG-PDLLA	A semi-permeable membrane composed of poly(ethylene glycol)-b-poly(D,L-lactic acid)
MRS	MSB re-suspended solution
MSB	Marine sediment bacteria
MTS	Methyltrichlorosilane
MWS	MSB working solution
NaCl	Sodium chloride
NIH/3T3 cells	Mouse fibroblast-like cell line
OD	Outer diameter
$OD_{600\ nm}$	Optical density
-OH	Hydroxyl group
OTS	Octadecyltrichlorosilane
p	Frequency of encapsulating a certain number of cells in a droplet
PBS	Phosphate-buffered saline
PCP	Porous coordination polymer
PCR	Polymerase chain reaction
PCTE	Polycarbonate track etch
PDMS	Polydimethylsiloxane

PE	Prince Edward Island
PEG	Poly(ethylene glycol)
PEG-DA	Poly(ethylene glycol) diacrylate
PEG-NB	Polyethylene glycol norbornene
PEI	Poly(ethyleneimine)
PEO	Poly(ethylene oxide)
PES	Polyethersulfone
PGPR	Polyglycerol polyricinoleate
pH	A scale of acidity and basicity
PID	Proportional–integral–derivative
PLLA	Poly(L-lactic acid)
PMMA	Polymethyl methacrylate
PNIPAAm	Poly(N-isopropyl acrylamide) homo-polymer
PVA	Poly-vinyl alcohol
R	Reverse
R2A	Reasoner's 2A agar
RNA	Ribonucleic acid
rRNA	Ribosomal RNA
SDS	Sodium dodecyl sulfate
SEM	Scanning electron microscopy
SiO_2	Silicon dioxide
SLA	Stereolithography
S-MD Pod	Small MD Pod
SSS	Stainless steel shavings
T	Thymine
TAE	Tris-acetate-EDTA
U	Uracil
UCST	Upper critical solution temperature
USA	United States of America
UV	Ultra violet
λ	The average number of cells per droplet volume

Units

bps	Base pairs
cfu	Colony-forming units
Hz	Hertz
ppt	Parts-per-trillion, 10^{-12}
RFU	Relative fluorescence units
RPM	Rotations per minute
V	Volts
v/v	Volume per volume
w/v	Weight per volume
Ɵ	Contact angle

CHAPTER 1 : GENERAL INTRODUCTION AND LITERATURE REVIEW

1.1 Overview

Currently, plenty of pathogens have developed resistance toward available antibiotics [1,2]. Resistance has been noticed since the beginning of the antibiotic era, and it usually appears shortly after antibiotic application, or after many years [1]. The economic and health risks associated with resistant pathogens are very high [3]; over $2.2 billion are spent each year in the United States of America (USA) civilian non-institutionalized adult population [4] and over 23,000 annual deaths in the USA are linked to antibiotic-resistant bacteria [5]. Such risks necessitate the discovery of new natural products that lead to the creation of clinically valuable antibiotics [6]. Usually, antibiotics are developed from chemicals produced by microorganisms [7]. In specific, natural products, also referred to as secondary metabolites, are chemicals produced by microorganisms and which are not required for growth and reproduction and frequently exhibit biological activity, including antimicrobial activities. Natural products are used in a variety of biological applications, including human and veterinary medicine and agriculture [8]. It is not surprising that scientists have focused on marine natural product discovery [9–12] after heavily exploring terrestrial habitats. In fact, more than 30,000 novel marine natural products have been discovered to date, with a lot of potential from secondary metabolites produced by marine invertebrates [13] which might be used as pharmaceutical drugs [14]. It is believed that many symbiotic microorganisms are the true source of secondary metabolites, such as actinobacteria [11], which are increasingly targeted in marine natural products discovery programs.

Although culturing microorganisms isolated from marine environments might seem straightforward, only about 1% of microbial species from such environments can be

cultured under standard laboratory conditions and using conventional media [15]. This phenomenon is referred to as 'The Great Plate Count Anomaly' [16], which states that approximately 99% of bacteria are 'uncultivable' [17] and highlights the untapped resources of biological and chemical diversity [15]. There are several reasons that cause this phenomenon: culturing in a laboratory might destroy the interactions occurring between organisms in their natural environment, affect cell-to-cell communication [18], inhibit the growth of slow-growing bacteria by fast-growing ones [19], alter ideal substrate combinations, concentrations [20], and conditions (pH, nutrients, osmosis, pressure, and temperature) [21,22], decrease culture growth rate by viral infections, poison bacteria through the use of relatively high concentration substrates required for growth, and neglect the first round of culture that might not be detectable using cell density detection methods [22,23]. Therefore, a different method of culturing should be implemented to grow 'uncultivable' bacteria, leading the way for marine natural product discovery.

1.2 Objectives and Hypotheses

This thesis focused on designing a device that enables *in-situ* incubation of marine sediment bacteria (MSB) with the aim of culturing 'uncultivable' bacteria and, ultimately, identifying new marine natural products. This device, herein named microbial domestication pod (MD Pod), was three-dimensionally (3D) printed using a commercial 3D printer. The MD Pod is a growth chamber exhibiting a cylindrical cavity in which the bacteria to be cultured are suspended. The chamber is enclosed by two membranes which prevent cell migration across the chamber but allow chemical and nutrient diffusion. 3D printing was chosen as the method of fabricating the MD Pod because it allows for rapid prototyping and design troubleshooting while offering low logistical costs and higher product quality [24]. The MD Pod is hypothesized to offer an advantage over other similar *in-situ* incubation growth chambers [25–28] in the way that different bacterial species are incubated together in one shared space inside the MD Pod's cylindrical cavity, leading to increased cell-to-cell communication [29] and quorum sensing [30]. Therefore, combining *in-situ* incubation technology with co-culturing is foreseen to increase microbial cultivability [31] of bacteria that have, to date, resisted attempts to domesticate.

Another focus of this thesis was to develop a system for encapsulating MSB in hydrogel microbeads. Single-cell encapsulation is hypothesized to protect 'uncultivable' bacteria from fast-growers [32,33] and aid at single species isolation after successful microbe domestication. Moreover, in this thesis, MSB were 'dislodged' from sediment particles to accurately measure cell concentration to be used in the encapsulation process and to enable convenient downstream microbial isolation after incubation. 'Dislodging'

MSB might cause them to lose necessary nutrients and/or supporting surfaces on which they used to live [34], which could decrease chances of their cultivability. Therefore, it is hypothesized that encapsulating MSB in a hydrogel might supply them with some of the nutrients necessary for their survival and might provide them with a substratum during incubation. Therefore, encapsulating MSB offers an additional advantage of the MD Pod over other growth chambers.

To encapsulate MSB, a 3D printed cross-flow microfluidic chip was used to generate microbeads from a hydrogel premixed with the 'dislodged' MSB. Microfluidics was chosen since it offers high-throughput, monodisperse droplet generation compared to other methods [35]. Additionally, the microfluidic chip was fabricated using 3D printing as opposed to the traditional method of soft lithography (in which polydimethylsiloxane (PDMS) is typically used as the building elastomer) [36]. Although 3D printing microfluidic chips still lacks in terms of lowest channel sizes printable, speed, and resin biocompatibility [37], it was used here due to its ability to produce chips at a significantly lower cost and shorter production time, while enabling easy and relatively fast prototype development [38]. In this thesis, stereolithography (SLA) was used as the 3D printing technology because it has the highest printing resolution compared to other technologies [37]. As for cross-flow microfluidic devices, droplet generation is obtained through the difference in interfacial tension of two immiscible phases [39] and the shear stress imposed on the hydrogel by a continuous phase [40]. Therefore, in this thesis, mineral oil was used as the continuous phase, given its common use in cell encapsulation applications [41–43]. In-depth information about these technologies, materials, and methods are presented in the following sections. Detailed materials, methods, results, and

discussion related to the utilization of the microfluidic chip and the MD Pod are presented in Chapter 2.

Although oil is typically used as the continuous phase to produce aqueous droplets in microfluidics [44], oil is undesired and should be removed or washed away [45,46]. Moreover, oils usually cause PDMS microfluidic devices to swell [44], could result in aggregation of the produced microbeads [47], and might have downstream effects on cell viability [48] in cell encapsulation applications, which was undesirable in the realm of this thesis. Therefore, Chapter 3 presents the design and preliminary testing of an oil-water separation system which transferred the produced hydrogel microbeads from the aqueous phase to the continuous phase and provided separation of both phases. This system could later be integrated with the cross-flow microfluidic device used to encapsulate MSB to provide a method of decreasing residual oil compared to traditional microbead washing over cell strainers. It is hypothesized that with less residual oil present in the final microbead solution and with 'on-chip' oil removal [48], a higher cell viability will be obtained.

Lastly, as previously mentioned, the use of 3D printing to fabricate microfluidic chips provides a one-step, inexpensive, fast, and customizable microfluidic device fabrication approach [38,49,50]. Nonetheless, this method is still limited in terms of minimum channel size printable [49,50], optical transparency [51,52], and residue resins and/or support structures [38,50,51], and the biocompatibility of 3D printing materials is debatable [49,52,53]. Moreover, although soft lithography is successful in fabricating intricate micro-devices, it entails several limitations. For example, the cured PDMS must be completely bonded to a substrate to ensure leak-proof channels [54,55], and inlet and

outlet holes should be punched in the PDMS elastomer, which might destroy the chip [55,56], often leading to restarting the fabrication process. Soft lithography is also time consuming [52], labor intensive [37], difficult to commercialize [38], and often requires access to a clean room and micro-patterning equipment [50,57]. Therefore, optimization of this method, or development of other methods, is needed. Chapter 4 illustrates the development of a method named enhanced internal scaffold removal (eISR), which combined the application of 3D printing and soft lithography techniques. eISR is hypothesized to provide an alternative, and relatively fast and user-friendly, microfluidic chip fabrication method using readily available and cheap equipment. Chips produced through eISR could potentially be used for MSB encapsulation.

1.3 Literature Review

1.3.1 Methods of culturing 'uncultivable' bacteria

1.3.1.1 Single-cell isolation

Single-cell isolation is one method used for culturing 'uncultivable' bacteria, and it has been shown that dilution-to-extinction enables the recovery of novel strains [19]. This method utilizes bacterial solutions that are diluted using a specific dilution series. Each dilution is then cultured on growth media and incubated to determine the dilution at which growth is observed. To further optimize the recovery rate obtained through single-cell isolation, micromanipulation, flow cytometry, and microfluidic on-chip cultivation are methods that could be used to culture thousands of individual cells [26,58,67,59–66]. Although single-cell isolation is popular and often successful, it limits the growth of many bacteria due to the lack of cell-to-cell communication. When cells communicate, they exchange signal molecules, like auto-inducers and peptides, which govern cell behavior [30,68,69]. When such molecules reach a threshold concentration because of population growth, bacterial gene expression begins to alter. This effect changes the physiology and morphology of cells and enables bacteria to regulate their behavior in specific social conditions that affect their growth [29,35].

1.3.1.2 Co-culture

Co-culture is another cultivation method that promotes the identification of growth factors responsible for microbial communities cultivation [70]. In co-culture, colonies, usually two or three species, are grown close to each other, which promotes their growth through signal factors exchange [58] and makes the conditions more

favorable for bacterial growth [18,71]. Through this method, several 'uncultivable' marine bacteria were grown in the presence of helper bacterial strains [21] or were used to obtain natural products [72–75]. Also, many cells were conveniently co-cultured using microfluidics [76–78]. Microfluidic co-culture systems offer the ability to co-culture hundreds, if not thousands, of microbial pairs at a time. However, careful and precise inoculation of different and complex combinations of microbial pairs and cultivation conditions should be practiced [79]. In general, co-culture is limited by the countless possible combinations of different species and growth media necessary for cultivation. It is also challenged by uneven growth rates of the co-cultured colonies, different abiotic incubation conditions, and different nutrient requirements [79]. Some might argue that implementing *in-situ* cultivation is another form of microbial co-culture [19], which laid the groundwork for the introduction of diffusion growth chambers.

1.3.1.3 Diffusion growth chambers

Diffusion growth chambers often have hollow structures, fitted with filter membranes housing microorganisms, and are placed in natural environments for *in-situ* sample incubation [22,80]. The membranes allow for the exchange of nutrients and chemical signals between housed microorganisms and the environment while preventing neighboring microorganisms from entering the growth chamber [22,80]. The use of diffusion growth chambers enabled the cultivation of microorganisms with unknown, or difficult to mimic, incubation requirements and has shown improved cultivation efficiency and microorganism diversity [80,81]. After growth, the newly domesticated colonies could be sub-cultured in a laboratory and inspected for their properties [81].

Due to its promising outcomes, the use of diffusion growth chambers has been implemented by many researchers. For example, Doty *et al.* cultivated approximately 40% of soil bacteria using a soil growth chamber (Figure 1.1(a)), with ten isolates having an identity score of <98% compared to known species using 16S rRNA sequencing [27], suggesting that this cultivation method could result in the cultivation of new, unidentified species. Kaeberlein *et. al* mixed microorganisms obtained from marine sediment with agar made with seawater and placed this medium between two membranes, creating a diffusion chamber (Figure 1.1(b)) [82]. The diffusion chamber was then incubated on top of a marine sediment sample kept in a marine aquarium. This method resulted in a 300-fold increase in the number of micro colonies grown using the diffusion chamber as opposed to growth on standard petri dishes. However, no growth was observed upon transfer of a single species micro colony to a new petri dish, likely due to the lack of chemical signals from other species which indicate the existence of a familiar growth environment [82]. This indicates the advantage of *in-situ* cultivation which ensures the existence of necessary environmental growth factors [81]. A similar diffusion chamber was employed by Ferrari *et. al* (Figure 1.1(c)) [26], with some success reported for new bacterial species belonging to the family *Oxalobacteraeceae* after secondary transfer of individual micro colonies to new petri dishes [32]. A similar approach was also carried out by Bollmann *et. al* (Figure 1.1(d)), in which diffusion growth chambers, containing a cell-agar suspension, were incubated on top of a marine sediment sample for 4 weeks, then the chamber-grown materials were inoculated in 3 subsequent chamber generations. The repeated incubation has resulted in the increased isolation of different species,

specifically from the rarely cultivated groups of *Verrucomicrobia* and *Acidobacteria* [83].

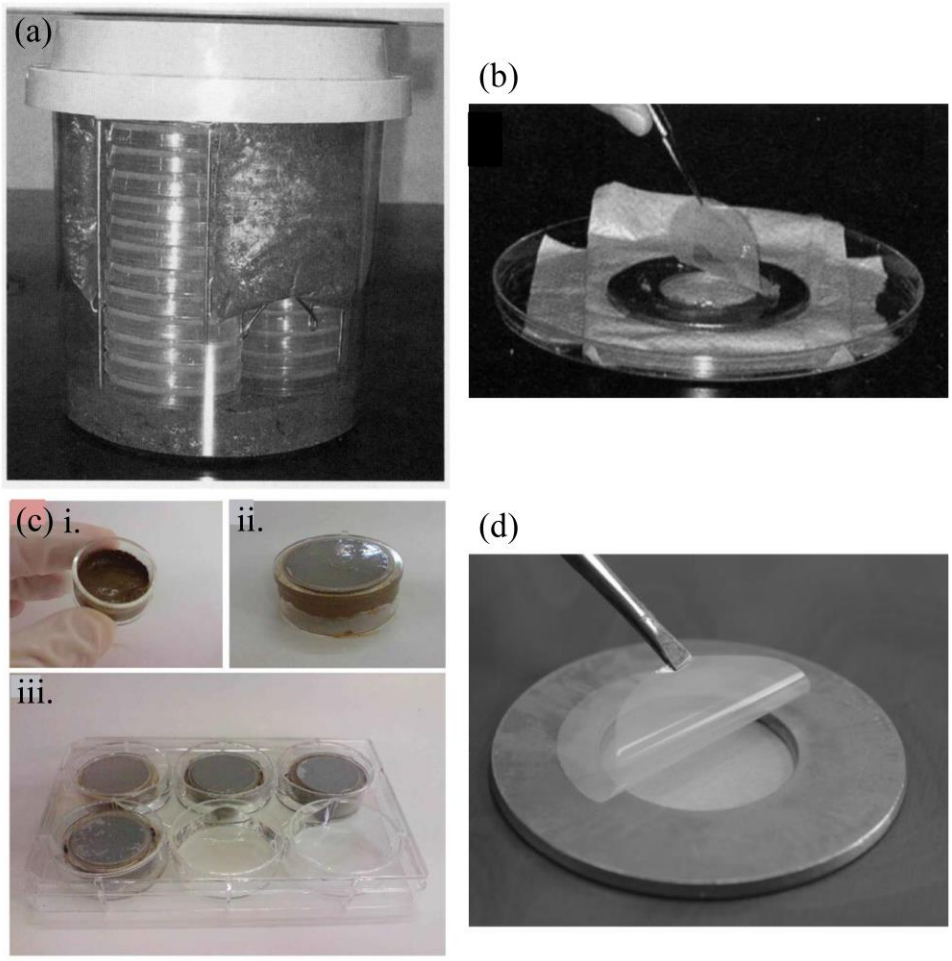

Figure 1.1: Diffusion growth chambers used to cultivate microorganisms. (a) A soil incubation chamber in which petri dishes, streaked with dilute soil samples, are stacked. The chamber is filled with 5 cm of soil and the internals are surrounded by perforated soil bags [27]. (b) A diffusion growth chamber composed of a washer sandwiched between two polycarbonate membranes. The sample is mixed with agar and placed inside the washer. The sample is incubated by placing the chamber over the surface of marine sediment. Republished with permission of American Association for the Advancement of Science, from Ref. [82]; permission conveyed through Copyright Clearance Center, Inc. (c) i. A tissue culture inset is used as the diffusion chamber, in which a soil substrate is placed. ii. Microorganisms are inoculated on a polycarbonate membrane, which is placed on an inverted inset. The contact between the membrane and the soil allows for the diffusion of nutrients. iii. The prepared insets are placed in a 6-well plate, humidified with sterile water, sealed with Parafilm, and incubated for the desired duration. Reprinted by permission from Copyright Clearance Center, Inc.: Springer Nature, Nature Protocols, Ref. [26], © 2008. (d) A diffusion chamber similar to that shown in (b). Reprinted from Ref. [83], https://creativecommons.org/licenses/by/4.0/.

More recent and successful diffusion growth chambers are the isolation chip, or iChip, and the I-tip. The iChip is a device with 384 miniature diffusion chambers, each containing approximately a single environmental cell (Figure 1.2(a)). The iChip provides high-throughput cultivation by combining microbe growth and isolation in a single step [84]. The iChip led to increased colony counts and a greater diversity of cultured microbes compared to traditional culturing methods [84]. Additionally, the iChip was utilized by Jung *et al.* to grow isolates obtained from lake sediment in Greenland by incubating them in sediment for one month. It was found that cultivated isolates exhibited temperature-related adaptations compared to the same isolates grown in a standard laboratory [85]. The iChip also enabled the discovery of a new antibiotic, teixobactin, by cultivating cells isolated from a soil sample in Maine, USA [86]. Jung *et al.* also used the I-tip for cultivation of microbes in endemic sponges from Lake Baikal, Russia. The I-tip is made from a micropipette tip filled with agar and glass microbeads (Figure 1.2(b)). This method led to the growth of 34 species from 5 different phyla, while standard laboratory cultivation of the same isolates led to the growth of 16 species from 3 different phyla [28]. Although these methods are successful in microbe cultivation, the iChip still lacks in terms of easy assembly, disassembly, and microbe retrieval (currently performed through single 'poking' of the 384 holes using sterile paper clips). The iChip also still lacks cell-to-cell communication due to the placement of single cells in individual holes. As for the I-tip, it requires difficult aseptic assembly and the chosen medium and glass beads could be selective to certain bacteria, which might decrease microbial recovery and limit cell-to-cell communication.

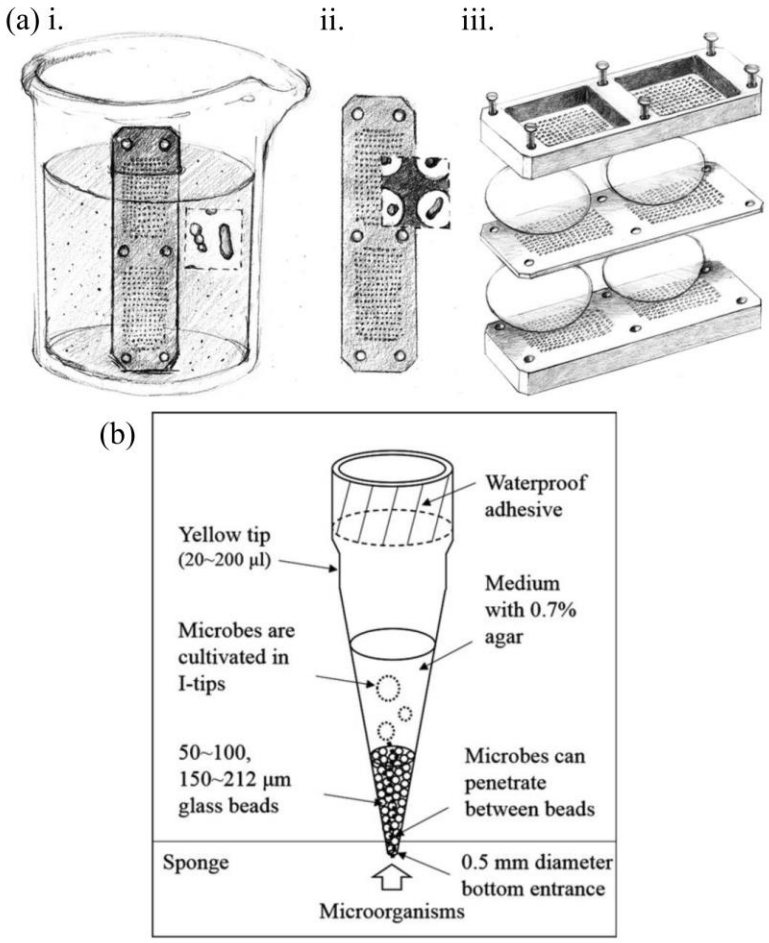

Figure 1.2: More recent *in-situ* cultivation diffusion growth chambers. (a) i. The miniature holes in the iChip are loaded with cells by dipping the iChip in a gel suspension containing environmental cells. ii. The dip is estimated to capture a single cell in each hole. iii. The iChip is assembled by being sandwiched between polycarbonate membranes. Seal is provided by pressure of six screws existing on upper and bottom plates. Reprinted from Ref. [84], https://creativecommons.org/licenses/by/4.0/. (b) The I-tip is composed of a 20-200 µL pipette tip filled with glass microbeads and a growth medium. The device is sealed from the top using a waterproof adhesive and is open from the bottom to allow for diffusion of microorganisms, nutrients, and other molecules from the natural environment into the medium. Reprinted from Ref. [28], by permission of Oxford University Press.

An improvement to current *in-situ* growth chambers is the encapsulation of cells in individual gel micro droplets and their suspension in a single growth chamber. Cell encapsulation could enable the diffusion of compounds between natural habitats and the encapsulated cells [23]. At the same time, each encapsulated cell is enclosed in a porous medium and separated from neighboring cells, which results in a low concentration of

cells, similar to natural bacterial clusters [29]. The encapsulation also acts as a form of dilution-to-extinction, which could eliminate potential competition between bacteria and could result in the cultivation of pure cultures [18] if upstream single-cell encapsulation is achieved. Hence, cell encapsulation could contribute to increasing the cultivation efficiency of many 'uncultivable' microbial taxa [80]. Zengler *et. al* encapsulated environmental bacteria, taken from marine sediment and terrestrial soil samples, using emulsification in agarose gel micro droplets and placed them in a growth column through which a low nutrient flux was supplied (Figure 1.3). This method resulted in the growth and isolation of many bacterial species and 'uncultivable' phylotypes [87,88]. Similarly, Shiqi *et al.* [89] encapsulated microorganisms in agarose microbeads and placed them in a column similar to that employed by Zengler *et al.* [87]. Shiqi *et al.* concluded that cultivation in hydrogel microbeads results in higher frequencies of novel bacterial taxa when compared to standard plating [89]. More cell encapsulation approaches used to cultivate slow-growing organisms are outlined by Zhang *et al.* [19].

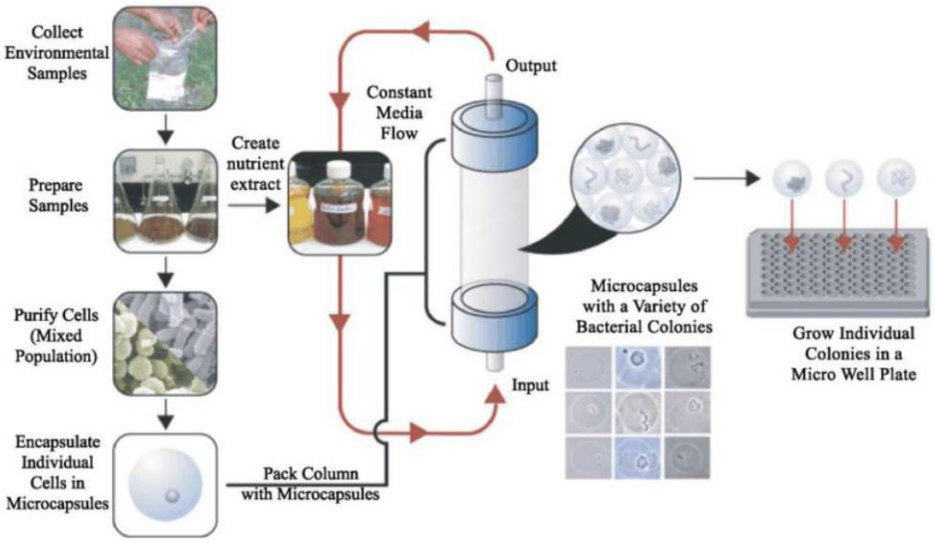

Figure 1.3: A high-throughput microbial growth column in which microorganisms (encapsulated in microbeads through emulsification) are suspended and a continuous flow of media is supplied [88]. Reprinted by permission from Copyright Clearance Center Inc.: Springer Nature, Nature Reviews Microbiology, Ref. [90], © 2004.

1.3.1.4 Conclusion

Based on the presented information thus far, the combination of single-cell isolation and co-culture techniques could highly improve *in-situ* cultivation of 'uncultivable' microbes. Lodhi *et al.* suggest that combining the features of diffusion chambers and the iChip to create a device that enables co-culture among incubated microbes could increase cell-to-cell communication and, therefore, enable increased novel antibiotic production [31]. Alain and Querellou further support the expected success of microbial cultivation through creating an *in-situ* cultivation device that promotes cell-to-cell communication [22].

Therefore, this thesis aimed at increasing the microbial recovery rate obtained by traditional plating methods, and ultimately, other *in-situ* cultivation methods, through the combination of single-cell isolation and co-culture strategies. Single-cell isolation was achieved by encapsulating microbes in agarose microbeads using microfluidics, and co-culture was achieved by suspending the microbeads in a liquid medium inside a device that is incubated *in-situ*. To the author's best knowledge, no literature has been published to date reporting the use of microfluidic cell encapsulation for natural product discovery using an *in-situ* cultivation device. Microfluidics was selected herein as the method of microbead generation due to its high-throughput production ability, size reproducibility, and the use of low reagent amounts compared to other methods [40]. Additionally, microfluidics enables minimizing the size of agar plates to micro-hydrogel particles that allow fast nutrient diffusion [91], which, in turn, aids in the cultivation of 'uncultivable' bacteria [92]. Moreover, microfluidics enables the integration of active elements, such as coolers and heaters [93], which could be added to the encapsulation

setup to control the temperature of agarose and prevent its gelation prior to encapsulation. The combination of microfluidics and microbial manipulation could provide a platform for isolating and/or identifying ‘uncultivable’ microbes [94] through the ability to control chemical and physical cell-encapsulation and cultivation conditions at the microscale [95].

1.3.2 Hydrogel cross-linking methods

The microencapsulation of cells in three dimensional (3D) environments is a promising technology for *in-situ* cell culturing [96]. 3D polymer microstructures allow for inward diffusion of oxygen, nutrients, and growth factors, and outward diffusion of wastes [97]. In particular, hydrogels allow for embedding cells in an aqueous environment that is soft, biocompatible, and stress-protective [97,98]. Numerous methods and materials are being tested for cell encapsulation in microbeads. Some of the methods include microfluidics, emulsification, extrusion, lithography, and bioprinting [99–101]. Common hydrogel materials are carbohydrates (such as alginate, agarose, carrageenan, chitosan, gellan gum, and hyaluronic acid (HA)) and proteins (such as collagen, gelatin, fibrin, elastin, and silk fibroin) [100]. Each of these methods and materials has been the subject of experimental designs for the encapsulation of a variety of cells [102]. Certain combinations of methods and materials affect the efficiency of cell encapsulation. Efficiency is characterized by cell viability, cell function, microbead size uniformity, and microbead shape. Moreover, the gelation process of the droplets is an important factor in increasing the encapsulation efficiency. Herein, the term ‘droplet’ refers to the hydrogel being in liquid form, while the term ‘microbead’ refers to the hydrogel after gelation.

As cell-encapsulating droplets form in a microfluidic device, they exit the drop formation region in the sol phase, which means that the polymer used for encapsulation is still able to flow. The transition from the sol phase to a gel phase is critical for maintaining cell viability. A cross-linking agent, also known as a polymerizing agent, is responsible for the sol-gel transition. The environmental conditions of the transition should have a minimum effect on cell viability and expose the cells to minimum stress

[100]. The density of cross-links formed among polymer chains affects microbead structural integrity [103]. Therefore, the nature and intensity of the cross-linking agent as well as its application method to the cell-encapsulating microbeads are important factors in the gelation process [100]. Cross-linking methods can be thermally, ionically, or photo-induced. Illustrations of these cross-linking methods are shown in Figure 1.4 and discussed in the following sections. Characteristics of those methods when used in cell encapsulation are summarized in Table 1.1, providing a map for researchers for the selection of a hydrogel material and a cross-linking method suitable with the application at hand.

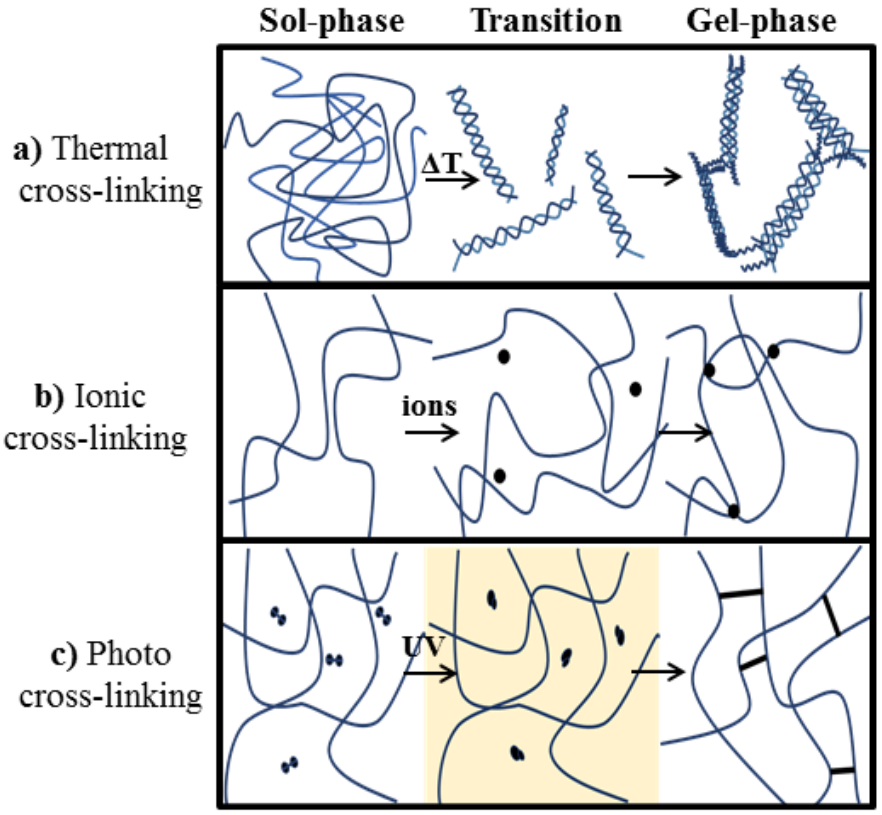

Figure 1.4: Diagrams of three cross-linking processes. (a) Thermal cross-linking: polymer chains form helical structures as the sol-gel transition temperature is reached. (b) Ionic cross-linking: polymer chains of a certain charge are joined through binding to ions of the opposite charge. (c) Photo cross-linking: as ultra violet (UV) light is applied, photo-initiators form free radicals (rods) that cross-link the polymer chains [100].

Table 1.1: Characteristics of thermal, ionic, and photo cross-linking methods in cell encapsulation applications.

Cross-Linking Method	Sol-Gel Transition Properties and Advantages	Characteristics of Common Materials	Possible Blends	Cell Encapsulation Applications	Cell Viability
Thermal	• Transition temperature should be close to cell physiologic temperature [96,100]. • Fast gelation in aqueous environments [97]. • Simple gelation without using ions or gel stabilization [111].	• Agarose: mechanically weaker than alginate and carrageenan [111] with cell capture ability [66]. Higher rigidity is expected upon longer gelation time [112]. • Collagen: low or undetectable cytotoxicity [113] and poor mechanical strength [114]. • Carrageenan: viral inhibition ability [115]; can be used in drug release [116] and tissue engineering	• Collagen/agarose : increased cell viability and attachment [108]. • Gelatin/agarose: increased cell division [109]. • Agarose/methoxy groups: gelling temperature lowered to 30ºC [97]. • Agarose/PLGA: smooth surface and slow release of protein drugs [110]. • Chitosan /agarose: stable in acidic aqueous environments and higher elastic modulus than	• Encapsulation of *E. coli* MK01 cells in agarose and liberating them through enzymatic digestion for enrichment rate determination [106]. • Encapsulation of *E. coli* MG1655, *P. aeruginosa* PAO1, *B. subtilis* BB1, and *E. coli* FB76 in agarose for cell stiffness measurement [107]. • Encapsulation of *B. subtilis* in water-oil-water mPEG-PDLLA	• 80% for *E. coli* DH5a strain 1598 in agarose microbeads [104]. • >99% for 12 representative slow and fast-growing Gram-positive and Gram-negative bacteria encapsulated in ultra-low gelling temperature agarose [33]. • 79.1 ± 3.2% for mouse fibroblast-like NIH/3T3 cells encapsulated in collagen [105]. • >90% for rat adipose-derived stem cells

Table 1.1 *(continued)*

Cross-Linking Method	Sol-Gel Transition Properties and Advantages	Characteristics of Common Materials	Possible Blends	Cell Encapsulation Applications	Cell Viability
Thermal (continued)	• Transition temperature should be close to cell physiologic temperature [96,100]. • Fast gelation in aqueous environments [97]. • Simple gelation without using ions or gel stabilization [111].	applications [120]. • Chitosan: uniform morphology andlow shrinkage ratio [121], with concentration affecting microbead size [45]. • PNIPAAm: stable in physiologic media and noncytotoxic with good permeability [113], but could swell [99] or even collapse [122] at high temperatures.	agarose microbeads [119]. • Collagen/ alginate: production of anisotropic hemispheres for cell culture applications [105].	for toxicity reduction of selenium contamination [118].	and human hepatocellular carcinoma HepG2 cells in gelatin containing phenolic hydroxyl groups [117].

Table 1.1 (*continued*)

Cross-Linking Method	Sol-Gel Transition Properties and Advantages	Characteristics of Common Materials	Possible Blends	Cell Encapsulation Applications	Cell Viability
Ionic	• Gelation using $CaCl_2$ is rapid and poorly controlled due to its high solubility in aqueous environments [128]. • Temperature affects the degree of gelation and the hydrogel mechanical properties [128]. • Low long-term stability due to release of divalent ions to surrounding aqueous media [128].	• Alginate: gels at mild conditions and has low toxicity [103]; mechanical strength can be increased by increasing molecular weight, G-block length [128], or alginate content [129]. • Chitosan: not mechanically stable [130]; porous [131,132]; swelling ratio increases with more acidic cross-linking solutions [133]; degradation increases with more acidic	• Alginate/agarose: improved morphology, storage modulus, and loss modulus with higher agarose content [124]. • Alginate/starch: stable and enable sufficient diffusion of nutrients and metabolites [127]. • Alginate/chitosan: more drug entrapment, slower release, and higher stability with multilayer chitosan coating	• Encapsulation of UFV-AREG1 bacteriophage in alginate microbeads for sanitizer development [126]. • Encapsulation of *P. putida* K2440, *Synechocystis sp.* PCC 6803, and *Chlamydomonas reinhardtii* CC-4532 in alginate microbeads immobilized on microarrays for microscopic inspection of cells and colony picking [125]. • Encapsulation of	• Improved with lower cross-linker concentration [123]. • >90% for Sertoli cells in alginate/agarose microbeads [124]. • High cell viability for *P. putida* cells in alginate microbeads [125]. • 84% for antibody-secreting hybridoma cells (9E10) and 86% for mouse breast cancer cells (M6C) in alginate microbeads [46].

Table 1.1 *(continued)*

Cross-Linking Method	Sol-Gel Transition Properties and Advantages	Characteristics of Common Materials	Possible Blends	Cell Encapsulation Applications	Cell Viability
Ionic (continued)	• Could eliminate the need for an oil phase using external gelation [142,143].	surrounding solution [139]. • κ-carrageenan: enhances cell viability, entrapment, and proliferation; noncytotoxic [140]; storage modulus increases more with monovalent ions compared to divalent ions [141].	[135]; higher cell survival [136,137]. • Alginate/HA: more alginate causes lower swelling in a saline solution. The hydrogel is porous, noncytotoxic, and a good cell adhesive [138]. • Alginate/PEG acrylate: mechanically stable hydrogels at physiological conditions, good biocompatibility, and no toxicity. Porosity could be controlled using	*Salmonella enterica* ATCC19585 bacteriophage in pH-responsive alginate for delivery and release in the gastrointestinal tract [134].	

Table 1.1 (*continued*)

Cross-Linking Method	Sol-Gel Transition Properties and Advantages	Characteristics of Common Materials	Possible Blends	Cell Encapsulation Applications	Cell Viability
Ionic (continued)			PEG acrylate content [143]. • Alginate/PEG-DA: swelling ratio < alginate and > PEG-DA, porous, and biocompatible [144]. • Alginate/PEI: better mechanical stability [145], less calcium, and slower diffusion than alginate[146]. • Alginate/ι-carrageenan: stable in aqueous media; higher viability with more carrageenan [147].		

Table 1.1 (*continued*)

Cross-Linking Method	Sol-Gel Transition Properties and Advantages	Characteristics of Common Materials	Possible Blends	Cell Encapsulation Applications	Cell Viability
Photo	• Cell viability decreases with a longer exposure time to UV light, but is not noticeably affected by higher UV intensity [158]. • Different microbead shapes can be obtained using different photomasks and stop-flow lithography [151,159]. • Could be used to produce multi-layered hydrogels [160].	• PEG-DA: mechanically stable in aqueous solutions [148], hydrophilic, biocompatible, and porous [156]. • PEG-NB: more cytocompatible and sustains cell survival and viability for longer periods than PEG-DA [149]. • Chitosan: nontoxic *in-vitro* [157].	• Chitosan/PEG: higher protein binding capacity and smaller mesh size with higher chitosan content [153]. • Collagen/glycosaminoglycan: supports cell proliferation and biosynthetic activity and has good compressive stiffness [154]. • Collagen/PEG-NB: porous structure, high swelling ratio, and stiff matrices [155]. • Collagen/gelatin:	• Encapsulation of autoinducer sensing reporter *E. coli* TOP10 in alginate microbeads reinforced in an alginate−methacrylate layer to prevent cell leaching. The microbeads could be used for *P. aeruginosa* detection [152]. • Encapsulation of tobacco mosaic virus in PEG-DA to enable exploitation of nano functional materials in stable and readily	• 90% for 3T3 fibroblast cells in collagen-gelatin microbeads [114]. • 90% for porcine mesenchymal stem cells in PEG-DA microbeads [148]. • >90% for human lung adenocarcinoma epithelial cells A549s in PEG-NB microbeads [149]. • Decreases with higher monomer concentration [150,151].

Table 1.1 *(continued)*

Cross-Linking Method	Sol-Gel Transition Properties and Advantages	Characteristics of Common Materials	Possible Blends	Cell Encapsulation Applications	Cell Viability
Photo (continued)	• Generation of phot-responsive Janus droplets [165] and core-shell droplets [166].		lower swelling ratio with lower gelatin content [114]. • Gelatin/methac-rylate or methacrylamide: mechanical properties, porosity, and swelling ratio are affected by cross-linking density [162,163]. Higher droplet diameters achieved by increasing the gelatin methacrylate concentration [164]. • Alginate/methac-rylate:	useable 3D formats [161].	

Table 1.1 *(continued)*

Cross-Linking Method	Sol-Gel Transition Properties and Advantages	Characteristics of Common Materials	Possible Blends	Cell Encapsulation Applications	Cell Viability
Photo (continued)			low swelling ratio, high stability, and good permeability [152]. • HA/methacrylate: higher mechanical integrity, viscosity, and cytotoxicity with higher HA content [167].		

1.3.2.1 Thermal cross-linking

The concept of thermal cross-linking is simple: a polymer forms a gel as a certain sol-gel transition temperature is reached. Thus, such polymers are called thermoresponsive polymers. A sol-gel transition temperature close to the physiological conditions of the encapsulated cells is recommended for maintaining cell viability [100]. Also, polymers that form hydrogels should not be toxic to the encapsulated cells [103]. The main advantages of thermoresponsive polymers are the fast gelation in an aqueous environment and the production of microbeads of adequate mechanical strength [97].

Some polymers form a gel when cooled, while others form a gel when heated [168]. Polymers that harden when cooled have an upper critical solution temperature (UCST), above which the polymer is miscible with water. When the polymer temperature is decreased below the UCST, it becomes hydrophobic and immiscible, hence forming a gel [100]. On the other hand, polymers that harden when heated have a lower critical solution temperature (LCST), below which they are miscible with water [100]. They form a gel when the LCST is exceeded. Thermoresponsive polymers have ionic or secondary forces, which means gelation can be reversed simply by changing the temperature [100].

Thermoresponsive polymers can be natural or synthetic. One example of a natural thermoresponsive polymer is agarose, a polysaccharide derived from red algae [100]. Agarose produces a hydrogel at concentrations as low as 0.2% when the transition temperature of 37ºC is reached by cooling [97,100,169]. A gel is formed as the random-coil conformations of liquid agarose form aggregated double helices [100] as illustrated in Figure 1.4(a). The transition temperature can be lowered to 30ºC upon blending with methoxy substitutions [97] or to 18 – 26ºC by using a low-gelling

temperature agarose [112]. Agarose is known for its stability, durability, cell compatibility, and ease of preparation [98], although it has lower mechanical strength than other materials, such as alginate and carrageenan [97]. Cell viability inside agarose microbeads can be increased if the concentration of agarose is increased [97]. However, viability can be compromised at very high concentrations. This is due to the formation of tightly packed helices, which decrease pore size and affect mass transport properties inside microbeads [100]. Mixing agarose with certain polymers results in increased mechanical strength, decreased sol-gel transition temperature, and/or enhanced agarose stability, durability, and cell compatibility. For instance, it has been shown that agarose-gelatin mixtures enhance cell division [97], a characteristic important for cell culture applications. Other possible blends are outlined in Table 1.1.

Other examples of natural thermoresponsive polymers are collagen, gelatin, carrageenan, and chitosan. Collagen is ubiquitous in biomedical applications due to its natural abundance as a protein in mammalian tissues [100,103]. It has three polypeptide strains that form a three-stranded rope. The strands can self-aggregate and form fibers. The mechanical properties of these fibers can be enhanced by thermal cross-linking through heating [103] or blue light irradiation [170]. A protein derivative of animal-origin collagen is gelatin, which can be used in the microencapsulation of probiotic microorganims as it forms a gel when cooled below 35ºC [100,171,172]. Gelatin microbeads can liquefy if heated up to the cell physiological temperature [100]. Stabilizing gelatin microbeads is recommended by using a chemical, such as glutaraldehyde or salts of chrome [100,172]. As for thermoresponsive polysaccharides, carrageenan is derived from marine macro-algae [172]. Only kappa and iota carrageenan

types can form hydrogels, since the lambda carrageenan type has more sulfate groups that hinder the formation of double helical structures [100,172]. Kappa carrageenan can entrap cells and keep them viable when it solidifies. However, the produced microbeads are brittle and unable to withstand stresses [171,172]. On the contrary, iota carrageenan produces microbeads that are soft and easily deformed [100]. Finally, chitosan is a hydrophilic, linear polysaccharide that is suitable for *in-vivo* use and is extracted from chitin [100,103]. Its derivatives and blends can be thermally cross-linked [103] and form a gel at physiological temperatures [100]. It is nontoxic but can be chemotaxic to neutrophils [103].

Although natural thermoresponsive polymers have been long studied in cell microencapsulation, synthetic polymers are increasingly receiving attention. They have several advantages, but they need further advancement in terms of biocompatibility [97]. Usually, the pore size of synthetic materials, such as poly(ethylene glycol) diacrylate (PEG-DA), is too small to allow for mass transport in microbeads [168]. An example of a synthetic thermoresponsive polymer is poly(N-isopropyl acrylamide) homo-polymer (PNIPAAm), which can form a tri-block copolymer with poly(ethylene glycol) (PEG) and harden at 30ºC [97]. This polymer has good physiological stability and mechanical strength and is not cytotoxic *in-vitro* [97]. Other examples include block copolymers of poly(ethylene oxide) (PEO) with poly(L-lactic acid) (PLLA), and PEG with PLLA, which have been used in tissue engineering and drug delivery applications [103,173,174]. Elastin-like polypeptides are also thermoresponsive polymers that polymerize upon heating. Their sol-gel transition temperature is influenced by their molecular weight and concentration [100].

1.3.2.2 Ionic cross-linking

Ionic cross-linking is a rapid process [152] that happens when a polyelectrolyte spontaneously forms an ionotropic gel upon contact with a divalent ion, also known as the ionic cross-linking agent [97,98]. The morphology of the resulting gel depends directly on the nature of the cross-linking agent as well as the polyelectrolyte molecular weight, architecture, density, and charge [97]. It is also important to consider the design and geometry of fluidic channels that introduce the cross-linking agent to the microfluidic device. After droplets are formed, the cross-linking agent diffuses into the droplets and solidifies them [98]. There are several materials that can be ionically cross-linked and used in cell encapsulation. However, alginate is the most widely used material [97].

Alginate is a natural, linear copolymer isolated from brown algae [175], seaweed, or bacteria [103]. It is a hydrophilic polysaccharide that is commonly used in food industries, pharmaceutical industries [175,176], drug delivery, stem cell research, and tissue engineering [177]. It solidifies ionically upon contact with divalent ions to produce 3D matrices around cells [46]. Alginate microbeads enable diffusion of nutrients and wastes to and from cells, respectively [46,127]. This polymer has many advantages that make it one of the most commonly used hydrogels in cell microencapsulation [97,98,100,152,172,176]. It is non-toxic, biocompatible, biodegradable, easy to polymerize, and commercially available [46,101]. Also, it forms a gel at conditions that are suitable for providing long term cell viability [103,171,176].

Alginate chains are composed of β-D-mannuronic acid (M) and α-L-guluronic acid (G) which contain a sodium ion, arranged in a block-wise pattern [100,171,172,175,176]. A sodium-alginate solution is prepared by dissolving alginate

powder in an aqueous sodium chloride (NaCl) solution [175,177]. Gelation happens by cross-linking pairs of G blocks [175] to form an egg-box structure joined by ionic bridges when a divalent ion, such as Ca^{2+}, Ba^{2+}, or Sr^{2+}, reacts with alginate, substitutes Na^{+} ions, and binds to free carboxyl groups of the G block [97,101,103,152,176–178]. The degree of cross-linking affects the mechanical strength and pore size of the microbeads, which can be manipulated by adjusting the ratio of M and G blocks and the chain's molecular weight [97,100,103,172,176]. A solution containing a divalent ion is considered the cross-linking agent for alginate. The choice of the divalent ion depends on the type of gelation desired [177]. The microbead mechanical strength decreases with more swelling and increases when the divalent ion has a greater affinity to alginate [103]. The affinity of different divalent ions to alginate decreases as follows: Cd^{2+} >Ba^{2+} >Sr^{2+} >Ca^{2+} >Ni^{2+} >Cu^{2+} >Mn^{2+} [176]. Mechanical stability can be enhanced by using Ba^{2+} ions, which also contribute to decreased swelling [176]. Goh *et al.* suggest that some trivalent ions, such as La^{3+},Pr^{3+}, and Nd^{3+}, show affinity to both the M and G blocks of alginate [179], but a subsequent study revealed that the cross-linking of alginate was more efficient using divalent ions than any type of trivalent ions [180]. Moreover, the concentration of the cross-linking agent affects the size and shape of the produced microbeads [178]. A higher cross-linking agent concentration decreases the diffusion of nutrients and wastes across the alginate matrix [100].

Alginate droplets can polymerize internally or externally, based on the source of divalent ions. In internal gelation, the dispersed phase, containing a solution of alginate, cells, and $CaCO_3$, is pinched-off by the continuous phase containing acidic oil that enhances the release of Ca^{2+} ions (Figure 1.5(a)) [46,98,101,168]. The use of $CaCO_3$ and

the exposure to a low pH oil affect the viability of cells, since direct contact of cells with acidic media reduces viability before microbeads are formed [46]. Cellular damage can be decreased by the use of separate microfluidic streams of the alginate-cell solution and $CaCO_3$ [46]. Internal gelation promotes the production of monodisperse, homogeneous microbeads with controllable size and acceptable cell viability [46,101]. Higher viability can be achieved by increasing the $CaCO_3$ concentration, since CO_3^{2-} ions act as a buffer to the acetic acid and increase the pH [101]. Internal polymerization also allows for high-throughput microbead processing [98]. In contrast, the external gelation method employs a stream of alginate-cell droplets that come in contact with an aqueous solution of divalent ions in the form of a bath or is co-flowed with a $CaCl_2$ solution (Figure 1.5(b)) [46,98,127,142,175,176] or a $BaCl_2$ solution (Figure 1.5(c)) [126,181]. If the flow rate of the alginate towards the cross-linking solution is low, tail-shaped gel microbeads will form (Figure 1.6(b and c)) [126,181]. Adjusting the flow rate of the dispersed phase and using alginate-agarose blends can produce better microbead morphologies with smoother surfaces [181]. A smooth microbead surface enables less fibrotic overgrowth and less foreign body reactions for *in-vivo* applications [142]. External gelation can produce heterogeneous, non-spherical core-shell microbeads if rapid polymerization occurs (Figure 1.6(a)). However, it can produce microbeads with high cell viability after encapsulation [181,182].

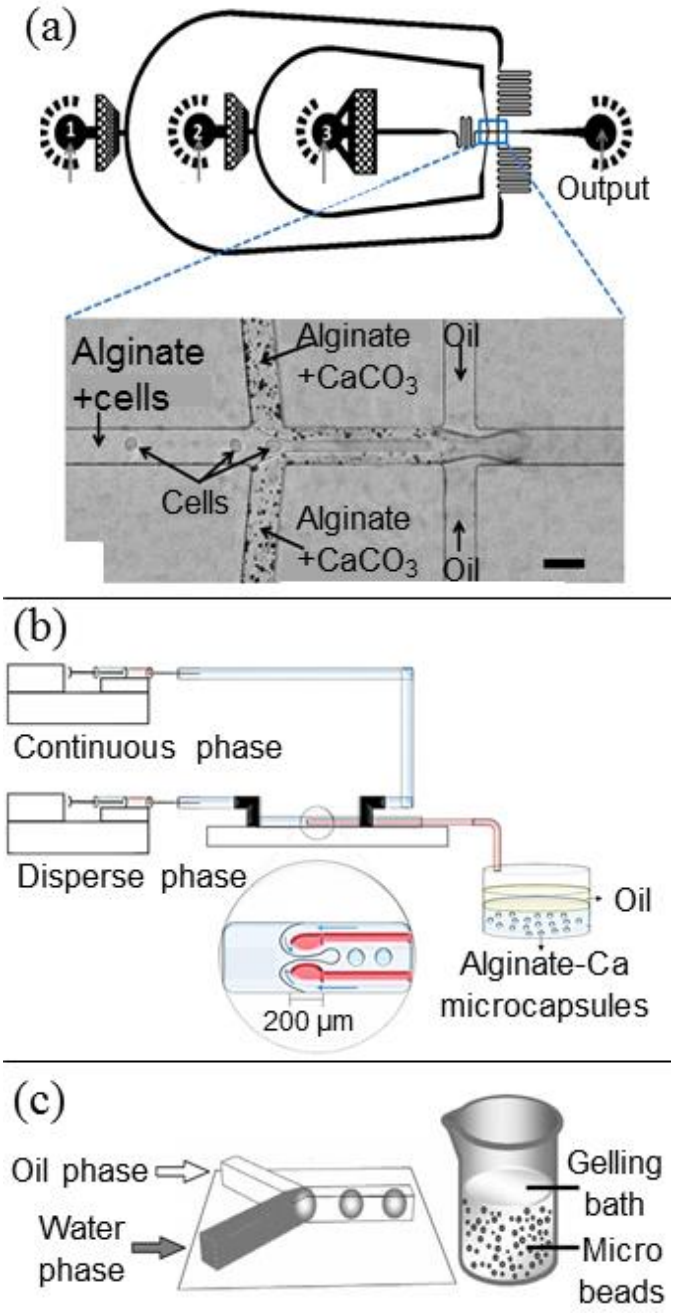

Figure 1.5: Internal and external gelation of alginate. (a) A schematic representation and a bright field image of a flow-focusing device with three inlets and two consecutive junctions used for internal gelation of alginate. 1 refers to the oil phase, 2 refers to alginate and $CaCO_3$, and 3 refers to alginate and cells. Scale bar is 50 µm. Reprinted by permission from Copyright Clearance Center: Springer, Microfluidics and Nanofluidics, Ref. [46], © 2014. External gelation of alginate using baths of (b) Ca^{2+} ions and (c) Ba^{2+} ions. (b) is reprinted from Ref. [126], ©2017, with permission from Elsevier. (c) is reprinted from Ref. [124], © 2009, with permission from Acta Materialia Inc.

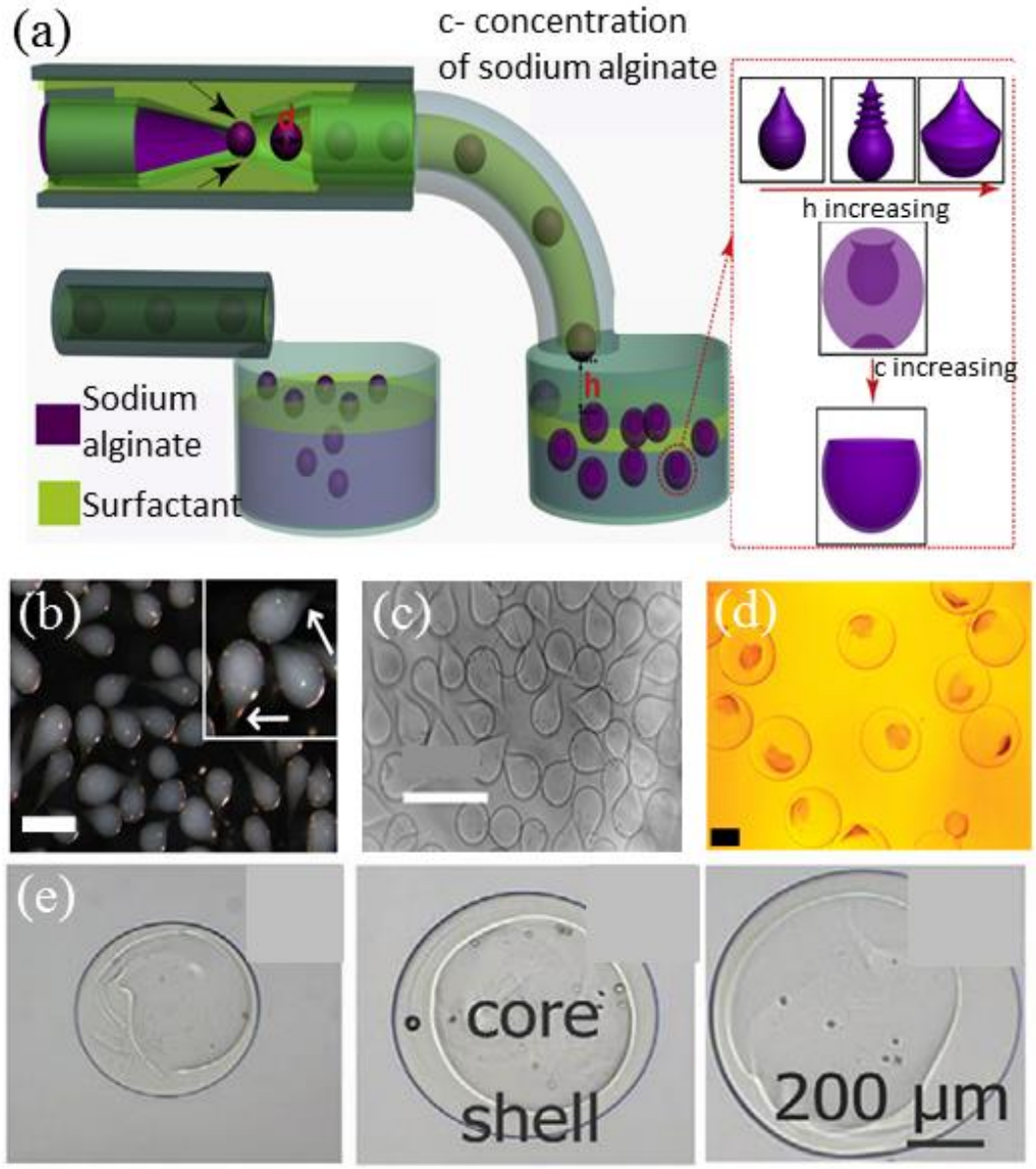

Figure 1.6: Tail-shaped and core-shell alginate microbeads. (a) Microbeads exhibiting different shapes according to variations of counter-flow nozzle diameter, ‘d’, elevation from cross-linking bath, ‘h’, and concentration of sodium alginate, ‘c’. Reprinted from Ref. [183], © 2014, with permission from Elsevier. (b and c) Tail-shaped alginate microbeads formed by external gelation. Scale bar is 400 µm in (b) and 500 µm in (c). (b) is reprinted from Ref. [124], © 2009, with permission from Acta Materialia Inc. (c) is reprinted from Ref. [126], © 2017, with permission from Elsevier. (d) Microbeads with a core-shell structure. The core is made up of PC12 cells in a culture medium and the shell is made from alginate. Scale bar is 200 µm. Reprinted from Ref. [178], https://creativecommons.org/licenses/by/3.0/. (e) A micrograph showing core-shell microbeads with controllable outer diameter and shell thickness. Reprinted from Ref. [184], https://creativecommons.org/licenses/by/3.0/.

As with any other material, alginate has some disadvantages. One disadvantage is the lack of sufficient adherence of mammalian cells to the alginate matrix when they are directly mixed [178]. Moreover, cells can protrude from the microbeads, which decreases their immune response and viability [178]. Such issues can be avoided by using a core-shell structure, which entails the encapsulation of a microbead in a second hydrogel (Figure 1.6(d and e)) [178]. Other disadvantages include the breakage of ionic cross-links by cationic scavengers or chelators, which leads to microbead instability, reduced mechanical strength, and uncontrollable permeability [97,152]. To overcome ionic breakage, covalent or photo cross-linking methods are recommended [152]. Other solutions can be mixing alginate with other materials such as starch, poly(ethyleneimine) (PEI), or PEG [97], using additives, or coating the microbeads [171]. In general, coating hydrogel microbeads improves their permeability and stability, controls cell release, and ensures biocompatibility [97].

There are other materials that can be ionically cross-linked to encapsulate living cells. Chitosan can be polymerized by the use of anions and polyanions as cross-linking agents [171]. It can be combined with alginate and produce microbeads that show no fibrous growth because of chitosan's inhibitory properties [97]. Chitosan can also be used to coat alginate microbeads and promote cell viability [172]. Moreover, HA can be covalently cross-linked using hydrazide derivatives [103]. It is commonly used in encapsulating cells that have extracellular matrices rich in HA, such as chondrocytes [100]. Iota and kappa carrageenan can also be ionically cross-linked [100]. In general, blends of polysaccharides show better bead mechanical stability than individual

polysaccharides [97]. Table 1.1 provides more details of possible blends of ionically-cross-linked materials.

1.3.2.3 Photo cross-linking

Photo cross-linking is the process of forming a gel through exposing a monomer or pre-polymer material to light, usually UV light, in the presence of a photo-initiator [98,99,101]. The UV light activates the photo-initiator and causes free radicals to form through a photosensitive chemical reaction [98–100]. These free radicals polymerize and cause covalent bonds to cross-link monomer chains, which solidify the polymer [98,99]. The type of the photo-initiator determines the wavelength to be used and the rate of cross-linking achieved [100].

Photo cross-linking is achieved through photolithography, which is based on photo-patterning of a hydrogel using a photomask to define different shapes and sizes of microstructures (Figure 1.7) [99,100,159,168]. In a batch photolithography process, droplets can be collected and photo cross-linked in a bulk solution outside of the microfluidic device [149]. The pattern of the photomask determines the parts of the gel that are cross-linked; liquid hydrogel that is not cross-linked can be removed later [99]. Photolithography enables the creation of thin layers of hydrogel, which creates multi-layer and precise structures [99,100]. Microbeads produced by photolithography tend to have high mechanical strength and support high cell viability and proliferation [100]. However, long droplet collection times can lead to decreased cell viability [149].

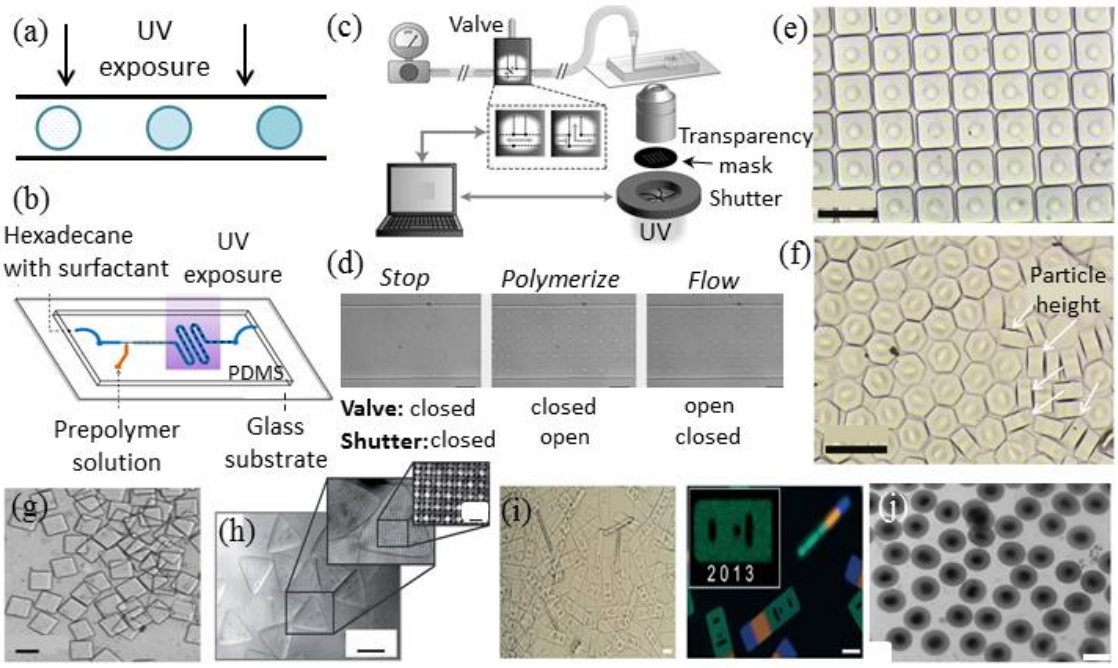

Figure 1.7: Photo-crosslinking and different shapes of microbeads produced through photo polymerization. (a) Schematic of continuous-flow photo cross-linking. Adapted from Ref. [44]. (b) Continuous-flow photo cross-linking in a serpentine channel. Reprinted by permission from Copyright Clearance Center: Springer, Microfluidics and Nanofluidics, Ref. [148], © 2015. (c) A computer-controlled stop-flow lithography setup using a pressure source and a 3-way solenoid valve. A photomask is used to define the shape of the produced microbeads. (d) Micrographs of a stop-flow photo cross-linking process, with the open position indicating a specified input pressure and the closed position indicating atmospheric pressure through manipulation of the 3-way solenoid valve shown in (c). Scale bars are 50 μm. Reproduced from Ref. [185] with permission from The Royal Society of Chemistry. (e – g) Photo cross-linked microbeads with different geometries. (e) and (f) are reprinted from Ref. [186], https://creativecommons.org/licenses/by/3.0/. Scale bars are 500 μm. (g) is reproduced from Ref. [151] with permission from The Royal Society of Chemistry. Scale bar is 100 μm. (h) Triangular microbeads formed by photo cross-linking with inset showing a scanning electron microscopy (SEM) micrograph of grid-like structures on the microbeads surface formed by the used photo mask. Scale bar is 50 μm and inset scale bar is 5 μm. Reprinted from Ref. [158], https://creativecommons.org/licenses/by/3.0/. (i) Multifunctional barcoded microbeads formed by three phase laminar flows and cross-linked through a mask with an array of barcode particle shapes. The image on the right shows three distinct compartments with “2013” code. Scale bars are 70 μm. Reproduced from Ref. [159] with permission from The Royal Society of Chemistry. (j) Core-shell microbeads formed using photo cross-linking. Scale bar is 200 μm. Reprinted by permission from Copyright Clearance Center: Springer, Chinese Journal of Polymer Science, Ref. [166], © 2016.

Photolithography can also be a continuous process. Specifically, flow lithography happens when photo cross-linking is performed *in-situ* (i.e. particles solidify while they are in the microfluidic device) [98,148]. Several designs can be implemented to prevent exposure of specific reagents in the microfluidic device to UV light. For example, light can be irradiated through a specific transparent window or through long spiral and serpentine channels that allow a certain period of exposure to complete the polymerization [98,148,149]. Usually, continuous-flow lithography is used to polymerize particles of different shapes and it enables high-throughput production of microbeads (Figure 1.7(a and b)) [97,98]. The main design parameter in such a setup is ensuring sufficient exposure of droplets to UV light [98] while maintaining a reasonable flow rate. Although this method seems practical, 'smeared' microbeads can form when photo cross-linking happens as the droplets flow inside capillaries [99,168]. Therefore, a compromise should be reached between particle shape and high-throughput production [168]. A solution to the 'smeared' microbead shape is the use of stop-flow lithography (Figure 1.7(c and d)) [150,151,185,186]. This method has low throughput but ensures control over microbead size, shape, and collection efficiency [149]. The throughput is a function of UV exposure time and polymerization kinetics [149]. Regular-shaped microbeads are formed when the flow is stopped, UV light is applied, droplets are cross-linked, and flow is reinstated, all happening during the period of exposure [99,168]. Stop-flow lithography allows for high resolution and high-throughput microbead production, and has been used to encapsulate cells with acceptable cell viability [150,168].

In general, photo cross-linking enables the high-throughput production of monodisperse, spherical microbeads [44] with high porosity [168]. It can also be used to produce microbeads with different shapes that cannot be easily made using other methods (Figure 1.7(e – i)) [98] as well as multifunctional Janus droplets [122,161] and core-shell microbeads (Figure 1.7(j)) [166]. Photo cross-linking creates irreversible covalent bonds that increase microbead stability [100,152]. In fact, the degree of cross-linking affects the size and rigidity of the microbeads [148]. Denser cross-linking leads to reduced swelling [152] and can produce microbeads that are highly stable after long term encapsulation [148]. Also, microbead porosity can be controlled by changing the concentrations of the hydrogel and the photo-initiator [182]. It should be noted that a high monomer or pre-polymer concentration can lead to decreased cell viability and increased cell coalescence [150]. This is the result of having more free radicals formed upon irradiation, which causes a higher degree of cross-linking and decreases the diffusion of nutrients and wastes to and from cells, respectively [150]. Free radicals could be damaging to cells, but careful selection of the photo-initiator and light wavelength can make the process more biocompatible [99]. As might be expected, irradiation using UV light can cause cell damage or death, and hence reduced viability [158]. This necessitates the use of photo cross-linking under mild conditions, such as short exposure times [101]. Also, some photo-initiators are toxic [97]. Examples of photo-initiators are Eosin Y [97], 2-hydroxy-1-[4-(hydroxyethoxy) phenyl]-2-methyl- 1-propanone [150], lithium acylphosphinate salt [149], and 2-hydroxy-2-methylpropiophenone [161]. Strategies used to increase cell viability in photo cross-linking processes include decreasing the

photo-initiator concentration, decreasing UV exposure time, and increasing the light wavelength [152].

Polymers that can be used in photo cross-linking usually have to be chemically modified by adding functional groups, like acrylates [100]. PEG-based gels are commonly used in photo cross-linking due to their cytocompatibility with cells, synthetic versatility, and the ability to control their hydrogel network properties [149]. PEG-DA can be photo cross-linked to create microbeads with permeable membranes that act as immune barriers [97]. It can also be used to encapsulate cells with confirmed functionality [161] as well as to encapsulate drugs [148]. Changing the molecular weight and concentration of a monomer can be used to manipulate the degradation rate of PEG-DA microbeads [148]. Cells that are photo-encapsulated in PEG-based gels can remain viable well after incubation (e.g. up to 8 days in PEG-NB) [99,106,149]. However, they face oxygen and nutrient diffusion limitations, which restrict microbead size and decrease cell viability at the microbead center [103]. Although PEG-DA has been widely used as the hydrogel material in photo cross-linking, one study suggests that PEG-NB is more cytocompatible [149]. Also, poly(ethylene oxide) (PEO) is a synthetic, hydrophilic polymer approved by the Food and Drug Administration (FDA) for biomedical applications [103]. Both PEG and PEO-based gels can be photo cross-linked by modifying the ends of the polymer chains with acrylates or methacrylates in the presence of a photo-initiator and exposing them to UV light [97,99,103]. PEO microbeads exhibit stiff matrices with high shear and compression moduli [103].

Some natural polymers can be used in photo cross-linking. For example, methacrylate groups can be added to gelatin chains to produce gelatin–methacrylamide,

which can be photo-crosslinked [99,100]. Similarly, treating HA with methacrylic anhydride to produce methacrylated HA enables cell encapsulation [99,100]. Collagen can be photo cross-linked using UV light [97,103]. Also, some adhesive medical gels are made from chitosan and its derivatives, which can be photo cross-linked and are nontoxic *in-vitro* [103]. Finally, bacteria encapsulated in photo cross-linked alginate methacrylate can remain viable and active with minimum leaching after incubation [152].

1.3.2.4 Conclusion

Once droplets are produced in a microfluidic device, they are polymerized to form microbeads. The method of polymerization and the type of polymers used affect cell viability. Thermal cross-linking enables fast polymerization and produces microbeads of adequate mechanical strength. The sol-gel transition temperature should closely match the optimal cultivation temperature of the cells. Ionic cross-linking rapidly forms a gel upon contact with a divalent ion solution. Specifically, internal gelation produces monodisperse and homogenous microbeads that support high cell viability, while external gelation can often produce heterogeneous and non-spherical, core-shell microbeads with high cell viability. Mechanical stability of ionically cross-linked microbeads can be enhanced by using combinations of polymers. In photo cross-linking polymerization, droplets containing a photo-initiator solidify upon UV irradiation. Photo cross-linked microbeads show high mechanical strength and stability, with high cell viability over long term incubation. Therefore, in this thesis, thermal cross-linking was chosen to be used as the hydrogel polymerization method due to the least amount of equipment needed to achieve gelation, compared to setups needed to achieve ionic or photo cross-linking.

Moreover, agarose was chosen as the hydrogel due to its stability, durability, cell compatibility, and ease of preparation [98].

1.3.3 Microfluidic droplet generation devices

Although multiple methods exist for droplet generation for cell encapsulation, they have limitations in terms of repeatability, ease of creation, variable size distribution, and non-uniform morphology [101,187]. On the other hand, microfluidics is gaining popularity due to its high-throughput and droplet size reproducibility (diameters of tens to hundreds of microns) [46,98,101,124,161,168,169,188]. This method enables multiple laboratory operations to be performed using small amounts of reagents in a short time; this is the basis of 'lab-on-a-chip' applications [44,98,101,189,190]. Through microfluidics, microbead size and morphology can be precisely tuned [99,148,161,187]. The small size of microbeads is important in ensuring sufficient oxygen and nutrient diffusion, increasing cell viability, and reducing immune response [46]. For cell culture applications, microfluidics present a platform that isolates microbeads from cross-contamination caused by bacteria and small molecules in the atmosphere; it can easily encapsulate cells using dust-free, sterile, and disposable devices [101]. The most commonly used devices are T-junction, flow-focusing, and co-flow, which are illustrated in Figure 1.8 and thoroughly explained in the following sections. Characteristics of these devices when used in cell encapsulation are summarized in Table 1.2. Cross-flow [96,149,168,169,189,191] and counter-flow devices [192,193] have similar working principles as T-junction and flow-focusing devices as well as co-flow devices, respectively [194,195]. Therefore, they are not directly addressed in this thesis.

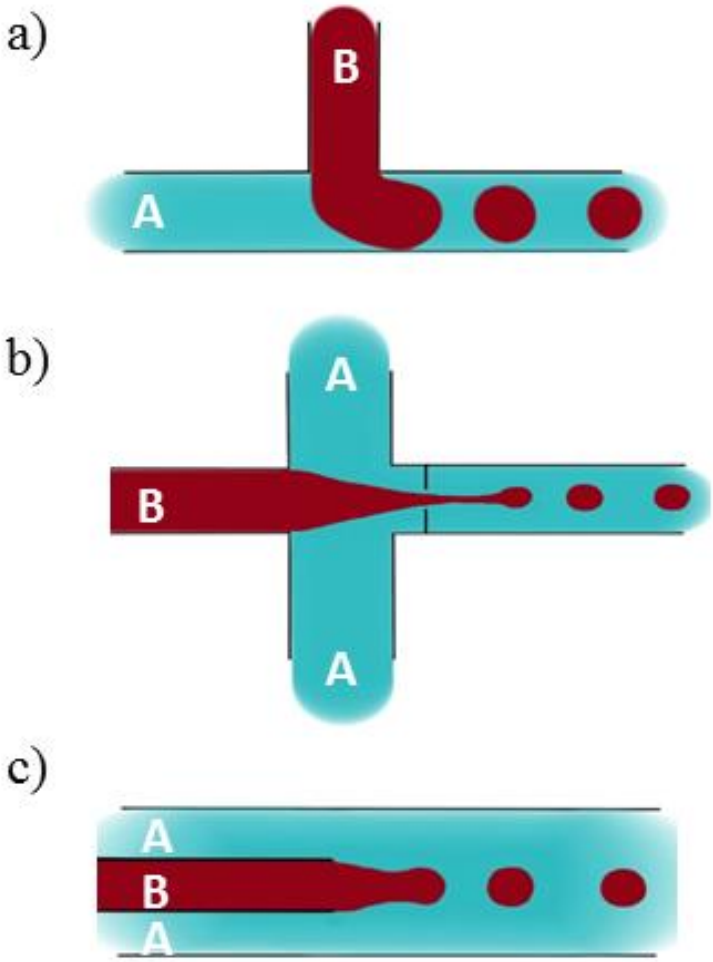

Figure 1.8: Geometric illustrations of three microfluidic devices: (a) T-junction, (b) flow-focusing, and (c) co-flow. ‘A’ represents the continuous phase and ‘B’ represents the dispersed phase.

Table 1.2: Characteristics of T-junction, flow-focusing, and co-flow devices used for cell encapsulation.

Microfluidic Device	Fabrication Materials	Geometry	Droplet Size Distribution	Droplet Generation Frequency	Multiple Device Settings	Types of Cells Encapsulated	Cell Viability	Other Characteristics
T-junction	• PDMS [43,112,148]. • PMMA [194]. • Cyclo olefin copolymer, polystyrene, and polypropylene [62]. • 3D printing resins [57].	• V and Y-junctions with different confluence angles [78,195,200,201]. • Double junctions (cross-flow) [39,43]. • K-junction [202]. • Constricted neck	• Uniform [44,168,169]. • 94 -150 μm [123]. • 16.7 - 85.7 μm [148].	• Tens to several hundred hertz to avoid high shear stress [101].	• Series [43,44]. • Parallel [197,198]. • Factory-on-chip [199].	• R1 and YC5-YFP-NEO murine embryonic stem cells [112]. • ATCC HB8065 hepatocellular carcinoma cells [43]. • Jurkat, Clone E6-1 (acute human leukemia T cell) [123].	• 79.6 ± 2.5% and 80.0 ± 1.6% for murine embryonic stem cells [112]. • 74.3% for Jurkat, Clone E6-1 [123].	• Addition of active elements [55,187,196].

Table 1.2 *(continued)*

Microfluidic Device	Fabrication Materials	Geometry	Droplet Size Distribution	Droplet Generation Frequency	Multiple Device Settings	Types of Cells Encapsulated	Cell Viability	Other Characteristics
Flow-focusing	• PDMS [96,161,203]. • Polyurethane elastomer [213]. • Glass capillaries [214]. • 3D printing materials [215,216].	[212].	• 30–170 µm [156]. • 40–100 µm [43]. • 76 µm with a coefficient of variation of 6.26% [203]. • 198 µm with a coefficient of variation of 2.5% in a circular setting [207]. • Narrow size	• 1200 Hz [119]. • In the range of 1000 Hz [44]. • >500 Hz [96]. • Up to 250 Hz [211].	• Parallel [208,209]. • Circular [207,210].	• *E. coli* BL21(DE3) [156]. • *E. coli* K12 (ATCC 700926) and nontoxigenic *E. coli* O157 (ATCC 700728) [207]. • *E. coli* MG1655 [96]. • Human lung adenocarcinoma epithelial cells (A549s)	• >90% for human lung adenocarcinoma epithelial cells (A549s) [149]. • >90% for *E. coli* K12 cells [206].	• Addition of active elements for uniform droplet generation [203] and sorting/merging [204]. • Janus droplet generation [99,205]. • Double emulsion droplet generation [99,125]. • Relatively more complex geometry than other devices [44].

Table 1.2 *(continued)*

Microfluidic Device	Fabrication Materials	Geometry	Droplet Size Distribution	Droplet Generation Frequency	Multiple Device Settings	Types of Cells Encapsulated	Cell Viability	Other Characteristics
Co-flow	• Glass capillaries [214,217,219,227,228]. • Glass capillary and PDMS [229]. • PDMS [230]. • 3D printing resins [57,220]. • Needles and borosilicate capillaries [231].	• Counter-flow [219]. • Double coaxial devices [226].	distribution [43,203,213] • Highly monodisperse if in dripping regime [219,224]. • Polydispersity in dripping regime is 1.5–2.5% [225]. • <100 μm [224]. • 168± 13 μm droplets [117].	• 100 to 5000 Hz [219]. • > 5000 Hz [224].	• Parallel [222,223].	[149]. • *aSccharomyces cerevisiae* yeast cells [217]. • Mouse L929 fibroblast cells [117].	• 87% for *Saccha-romyces cerevisiae* yeast cells [217]. • >90% for mouse L929 fibroblast cells [117].	• Double emulsion droplet generation [214,217–219]. • Core-shell droplet generation [178,220]. • Hollow-core droplet generation [221].

In flow-focusing and co-flow microfluidic devices, droplet generation is the result of the shear stress of a continuous phase on a dispersed phase, while in T-junction devices, droplet generation is caused by the pressure of a continuous phase on a dispersed phase. Both phases are usually immiscible liquids: the dispersed phase is hydrophilic, biocompatible, and can be a stream of cells suspended in a polymer [99]; the continuous phase can be a nontoxic oil or an aqueous solution of lower viscosity than the dispersed phase [99]. As the continuous phase meets the dispersed phase, shear stress and pressure cause the dispersed phase to pinch-off and form droplets [43,44,233,234,99,112,148,168,194,203,213,232]. The continuous phase serves as the carrier for the dispersed phase and it should contain a surfactant to lower the surface tension of hydrogels, reduce the wettability at channel walls, and act as a stabilizer for the produced emulsion [98,194,235].

Many factors must be considered when hydrogel microbeads are formed using a microfluidic device. To obtain uniformly-sized microbeads, careful consideration must be given to the flow rate of each phase [43,44,168,213,232], viscosity of each phase [44,98,101,148,168,169,213], the concentrations of the hydrogel and the surfactant [44,98,189,190,194], channel dimensions and geometry [44,96,98,101,148,161,168,190,213], wetting nature of the channels [44], and the driving force (pressure or volumetric-driven flow) [44,169,236].

1.3.3.1 Commonly used surfactants in cell encapsulation applications

Surfactants used specifically in cell microencapsulation applications include: Span® 80 [41,43,63,77,96,164,188,214,237], poly-vinyl alcohol (PVA) [238], sodium dioctyl sulfosuccinate (DOS) [239], Tween 80 [240], CR310 and PO500 [191], Pico-Surf

[149], Pico-Surf 1 [114,241,242], 008- FluoroSurfactant [68,106,212], triblock copolymer [114,243], EA [204,244], polyglycerol polyricinoleate (PGPR) [134,193], PFPE-PEG block copolymer [78], Abil-EM90 [156], decanoate [245], PEG-Krytox [246], and fluorinated surfactant [46]. The concentration of several surfactants, such as Tween 20, TX 100, sodium dodecyl sulfate (SDS), and cetyltrimethylammonium bromide (CTAB), was correlated to dynamic interfacial tension in microfluidic systems [227,247]. Adjusting the surfactant concentration causes changes in interfacial tension and droplet formation regimes [194,214] and diameters [188]. Some studies suggest that surfactant use might be detrimental to cell viability [171,248], affect downstream microbiology [41], and/or interfere or inhibit biochemical reactions [249]. Other studies report that the use of some surfactants is biocompatible [162,241] or does not affect cell viability [63]. Holtze *et al.* developed biocompatible non-ionic fluorosurfactants to be used in biological assays [250]. Avoiding the use of surfactants is beneficial in some applications as these chemicals can negatively affect cell viability and can complicate the microbead retrieval from the continuous phase due to the formation of highly stable emulsions.

1.3.3.2 T-junction devices

The use of T-junctions is common in microfluidic cell encapsulation [213], mainly due to the ease of droplet generation and uniform microbead size distribution [44,168,169]. The basic geometry employs a dispersed phase that is injected perpendicularly into a continuous phase [44,98,190,194]. The dispersed phase almost blocks the flow in the horizontal channel. One alteration to the T-junction geometry is the head-on approach (Figure 1.9(a)), where both phases collide with each other and leave

through a perpendicular stem [44,232]. Other alterations involve the addition of active elements (Figure 1.9(b – d)), such as heaters for the inlets, coolers for the outlet, inflatable gas chambers, mechanical or pneumatic dispensing microvalves (Figure 1.9(e - h)) [44], and/or biosensors [251]. Sometimes, a more simple alteration is the use of double T-junctions in series [43] for mixing purposes.

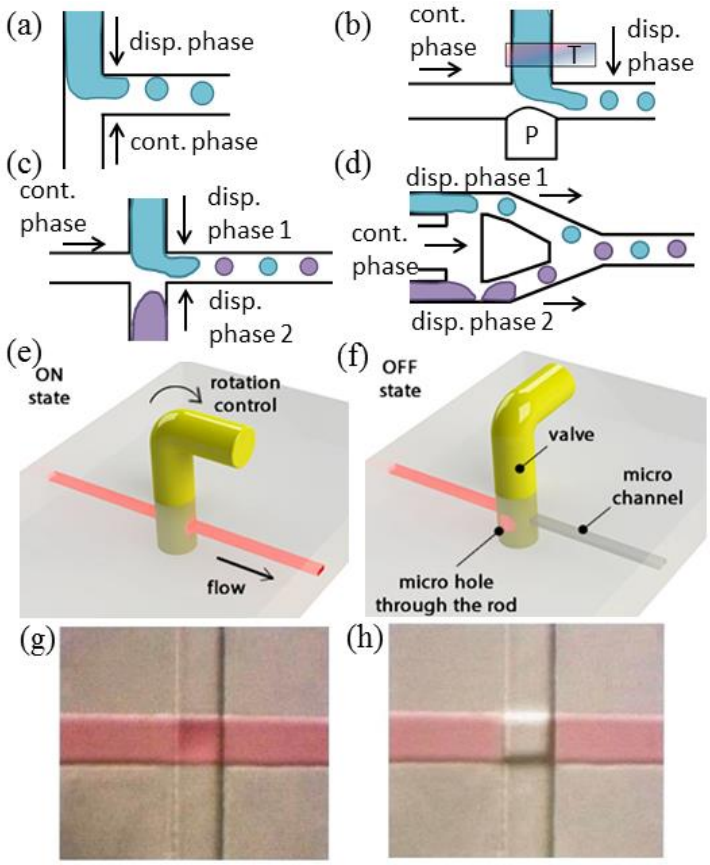

Figure 1.9: Possible alterations to T-junction devices. (a) Head-on approach where dispersed and continuous phases collide perpendicularly. Active elements added to Tjunction devices: (b) a temperature controller, 'T', added to the dispersed phase inlet to variate its temperature, and channel geometry could be controlled using a gas pressure source, 'P'; (c and d) configurations of double T-junctions in series used to generate two alternating types of droplets. Adapted from Ref. [44]. (e and f) A twisting plug microvalve in ON and OFF positions. It is fabricated by boring a hole through a cylindrical rod and inserted into a punched hole in the microchannel. Reprinted from Ref. [55], © 2017, with permission from Elsevier. (g and h) A pneumatic gas-actuated microvalve in open and closed positions. Flow is controlled by changing the pressure in a gas channel separated from the flow channel by a thin PDMS film. Reprinted from Ref. [196], https://creativecommons.org/licenses/by/3.0/.

T-junction devices can be fabricated in different ways according to the application and nature of cells to be encapsulated. Some T-junctions are made in PDMS and mounted on a glass substrate [43,112,148]. PDMS is commonly used because it is hydrophobic, which assists in forming water-based droplets in the continuous phase [43]. Other T-junction devices are made in polymethyl methacrylate (PMMA) [194] and various other materials [62]. The choice of fabrication material is directed by the continuous phase components' compatibility, the strength of the material, and the ability to withstand swelling [169]. A wide variety of cells and materials can be encapsulated using T-junctions. For example, a cancer drug was encapsulated in PEG-DA [148], embryonic stem cells were encapsulated in agarose [112], and hepatocellular carcinoma cells were encapsulated in alginate [43].

Microbead size distribution can be controlled by adjusting the flow rates of the continuous and dispersed phases [148,161]. The size distribution is more affected by the flow rate of the continuous phase [112,148,194,252]. Smaller microbeads are formed at higher flow rates of the continuous phase due to the higher shear stress exerted on the dispersed phase [112]. Usually, a larger channel diameter is designated for the continuous phase than that for the dispersed phase [43,112,148,194,252], as this affects the magnitude of shear stress imposed on the dispersed phase. As for viscosity, a higher value for the continuous phase results in smaller microbead size, also due to higher shear stress [169]. The effect of T-junction channel geometry is shown in Figure 1.10(a and b).

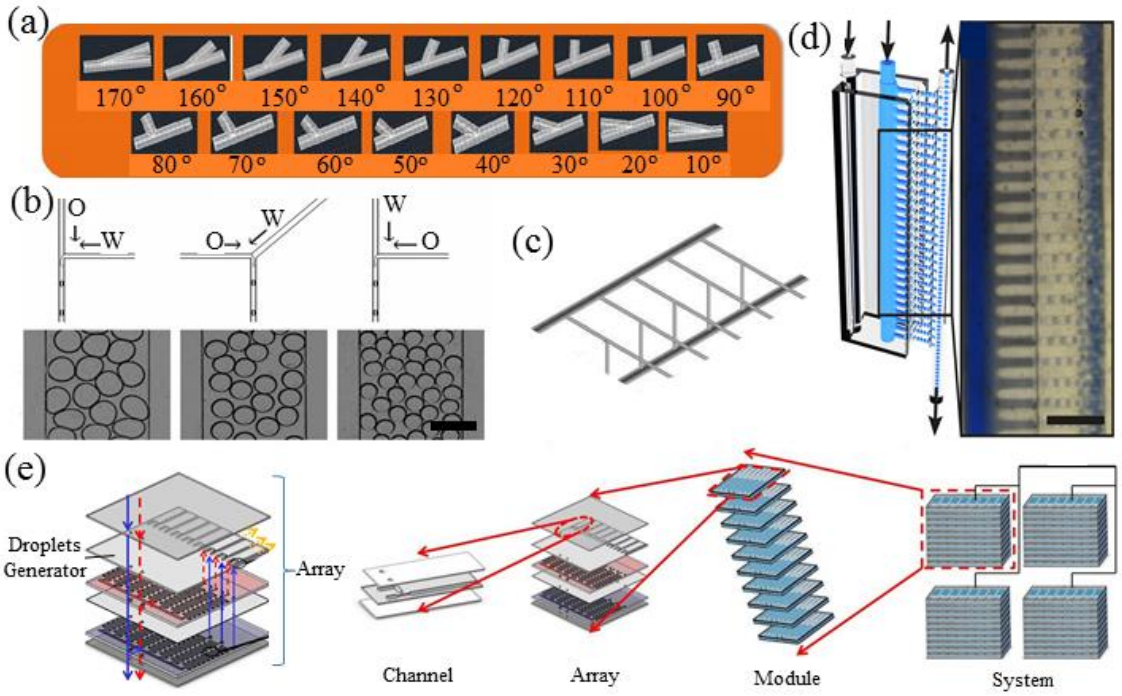

Figure 1.10: Confluence angles and parallel settings of T-junction devices. (a) Different geometries of the confluence angle of T-junction microfluidic devices. Reprinted from Ref. [200], © 2016, with permission from Elsevier. (b) The effect of 0°, 45°, and 90° confluence angles of oil (O, continuous) and water (W, dispersed) phases on droplet diameters with constant channel dimensions of 15 µm x 15 µm and a flow rate ratio of 1:1. Scale bar is 100 µm. Reprinted figure with permission from Ref. [195], © 2009 by the American Physical Society. (c) Six T-junction devices arranged in parallel. Reprinted by permission of Taylor & Francis Ltd (http://www.tandfonline.com) from Ref. [197]. (d) 28 T-junction devices arranged in parallel with inlets for the continuous and dispersed phases and two outlets for the generated droplets. Scale bar is 5 µm. Reprinted with permission from Ref. [198], © 2015 American Chemical Society. (e) Parallel T-junction devices arranged in an 80 mm x 80 mm array and stacked to form modules. Modules can be integrated to create a large-scale device known as factory-on-chip. Dashed red arrows refer to dispersed phase, solid blue arrows refer to continuous phase, and dotted yellow arrows refer to produced emulsions. Reprinted from Ref. [199], © 2017, with permission from Elsevier.

Generally, cell viability is greatly affected by the surfactant and type of continuous phase material being used [99]. Also, the duration of culturing affects the amount of nutrients available inside the microbeads, which stresses the need for a quick transfer of the encapsulated cells into a suitable culturing medium [99]. Some experiments reported high cell viability for embryonic stem cells encapsulated in agarose

microbeads using a T-junction [112]. Other mammalian cells showed high viability and enzyme activity when cultured for a week in PEG-DA microbeads [99].

Moreover, high-throughput monodisperse cell microencapsulation can be achieved through the use of T-junctions [148]. In specific, producing a larger number of droplets is possible through the use of several T-junctions in parallel (Figure 1.10(c – e)) [44,101]. However, this arrangement can produce microbeads with poor size uniformity due to multimodal processes [168]. In fact, having multiple inflow streams lead to nonlinear fluid dynamics that could result in uniform, multimodal, or chaotic droplet formation [169]. Monodisperse droplet formation in a parallelized droplet generation device is highly affected by the pressure inside the device [198] and the number and organization of microfluidic channels [199]. Specifically, pressure variations at different intersections inside such devices should be minimized to generate monodisperse droplets [198].

The frequency of droplet generation in T-junction devices is limited to several hundred hertz to avoid high shear stress on the encapsulated cells [101] and a short droplet breakoff time [44]. Also, low frequencies are not favorable because they lead to unstable droplet generation by the low shear force exerted on the dispersed phase [44]. Therefore, the frequency must be tuned to a value where stable droplet generation is sustained with minimal effect on the viability of the encapsulated cells. Moreover, the number of encapsulated cells can reach several hundred thousand per hour [101] when the device is properly tuned and system geometry is carefully chosen [44]. Some companies have developed commercial microfluidic droplet makers/encapsulators (such as Droplet Pack by Elveflow and Droplet Generation by Dolomite Microfluidics)

[253,254] and organ-on-chip platforms (such as Organ-on-Chip Platform by Fluigent and Microfluidic Organ-on-Chip Pack by Elveflow) [255,256] (Please note that there is no conflict of interest with these companies). However, such systems could be expensive and do not allow easy integration of foreign active elements if needed. Information about microfluidic cell sorting commercialization is discussed by Shields *et al.* [257].

1.3.3.3 Flow-focusing devices

Encapsulating cells in polymer microbeads is perhaps most commonly performed using flow-focusing devices [44,99,213]. In a flow-focusing device, a laminar flow dispersed phase moves through a nozzle, or orifice, to flow within a continuous phase [44,99,233]. Shear stress is caused by a reduction in the size of the dispersed phase channel at the orifice, at which hydrodynamic flow-focusing occurs [44]. It is important to use a surfactant in the continuous phase to decrease surface tension and prevent coalescence [149,232]. However, some studies suggest that the use of a surfactant can be eliminated [182,258] if the shear force at the tip of the orifice can be sufficient to cause droplet pinch-off [169].

One use of a flow-focusing device is the creation of Janus droplets (Figure 1.11(a and b)) [98,99,168,169]. These droplets are heterogeneous and composed of two miscible solutions [98,99,161] with matching viscosities [98]. Janus droplets can be used for co-culture [99], biosensing, electric and magnetic manipulation, and therapeutic and diagnostic applications [122]. Other uses of flow-focusing devices involve the creation of double emulsions where droplets are enclosed in other droplets (Figure 1.11(c and d)) [99], which can be applied to control cell release and proliferation [99,233]. Cell release can also be decreased by shortening the incubation time of

microencapsulated cells [96]. Some examples of cells encapsulated through the use of a flow-focusing device include: human lung adenocarcinoma epithelial cells encapsulated in polyethylene glycol norbornene (PEG-NB) [149], bacterial cells encapsulated in agarose microparticles [96], and functionalized viral nanotemplates encapsulated in PEG-DA [161].

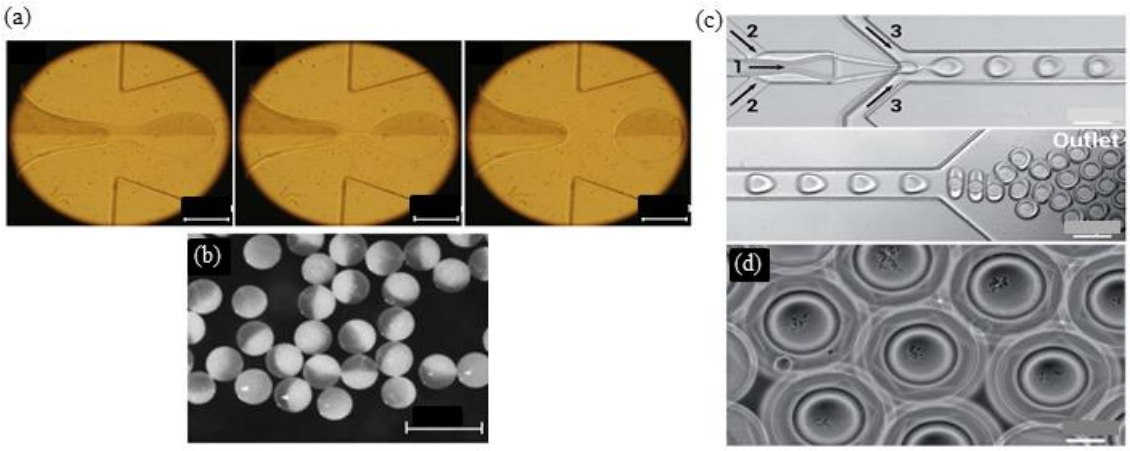

Figure 1.11: Janus and double emulsion droplet produced using flow-focusing devices. (a) A Janus droplet generated using a flow-focusing microfluidic device. (b) PLGA Janus droplets. Scale bars are 200 μm. Reprinted from Ref. [205], © 2017, with permission from Elsevier. (c) Double emulsion droplets production using a flow-focusing microfluidic device; 1 refers to 0.15% w/v alginate loaded with *Pseudomonas putida* bacteria, 2 refers to hydrofluoroether (HFE7500) with 1% w/v of fluorinated surfactant, and 3 refers to 10% w/v PVA and 100 g L^{-1} sucrose. Scale bars are 100 μm. (d) Double emulsion droplets containing *P. putida*. Scale bar is 25 μm. Reproduced from Ref. [125] with permission from The Royal Society of Chemistry.

The fabrication material of flow-focusing devices is highly dependent on cell compatibility. They can be fabricated in PDMS poured onto an SU-8 micropatterned silicon wafer, also known as soft lithography [96,149,161,203,233]. PDMS structures are commonly used for cell culture as they allow for the diffusion of oxygen, nutrients, and wastes [233]. Additionally, flow-focusing devices can be fabricated in polyurethane elastomer using soft lithography [213]. Other fabrication methods use glass capillaries from chromatography components that are commercially available, easy to assemble, and

easy to clean [214]. The demand for a convenient fabrication method of flow-focusing devices is higher than that of T-junctions due to the former's more complex geometry [44]. Recently, 3D printing technology has been used for the development of microfluidic devices (Figure 1.12) [37,38,49,50,52,259–261].

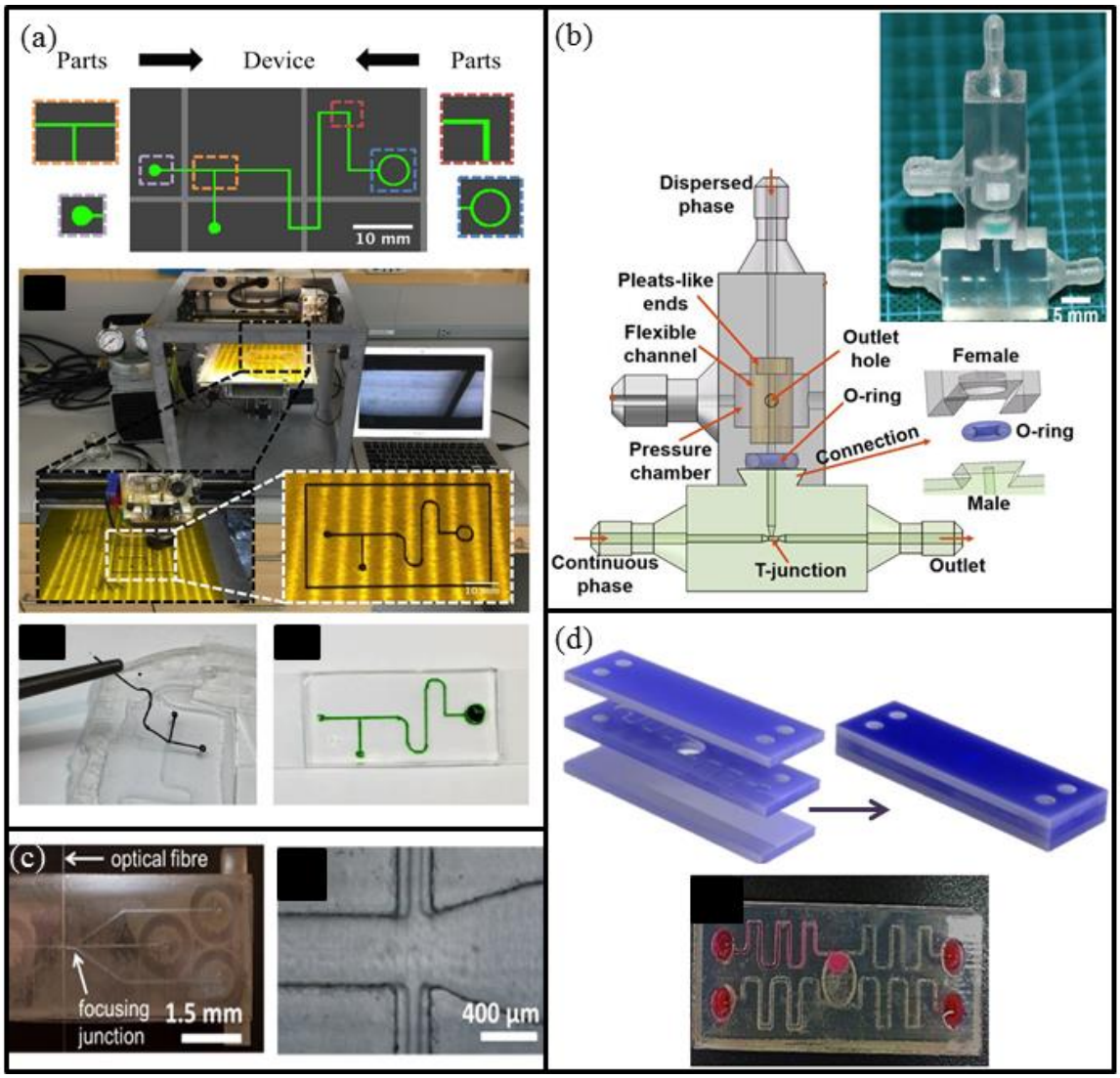

Figure 1.12: The use of 3D printing in the fabrication of microfluidic devices. (a) Common parameterized microfluidic features were combined together to create a T-junction microfluidic device. The device was printed from ABS and PDMS was poured over it, degassed, and cured. The ABS was then removed using forceps, inlets and outlets were punched, the PDMS device was plasma treated and bonded to a glass slide, and the channels were filled with food coloring. Reprinted from Ref. [262], https://creativecommons.org/licenses/by/4.0/. (b) A 3D printed T-junction device with multiple components that could be assembled based on application. The figure shows the use of a pressure component for droplet generation. Reprinted from Ref. [57], https://creativecommons.org/licenses/by/4.0/. (c) A 3D printed hydrodynamic flow-focusing device with an integrated optical fiber for particle analysis. Reprinted from Ref. [263], © 2017, with permission from Elsevier. (d) A 3D printed rotational flow microfluidic device composed of 3 layers and 500 µm channels. Reprinted by permission from Copyright Clearance Center: Springer, Microfluidics and Nanofluidics, Ref. [51], © 2016.

It has been shown that increasing the flow rate ratio of the continuous phase to the dispersed phase causes a decrease in droplet size [96,161,169,213]. However, if a threshold of flow rates is reached, a jet of the dispersed phase will form instead of droplets [43], which decreases the efficiency of microencapsulation. Also, increasing the viscosity of the dispersed phase leads to the generation of larger droplets and a narrow size distribution due to a longer pinch-off time [213]. Moreover, better control of droplet size is directly related to orifice diameter [44].

A flow-focusing device enables the encapsulation of a single cell in each microbead [44,96,99] and achieves a narrow size distribution [43,169,203,213]. These advantages enable precise cell encapsulation for high-throughput cell screening [149]. Through flow-focusing devices, cell viability in microbeads can be high after microencapsulation [149]. Maximum cell viability inside microbeads is a function of the hydrogel material, size of each microbead, and number of cells in each microbead [96].

Another advantage of flow-focusing devices is the feasibility of high-throughput droplet production. Droplet generation frequency can reach several thousand hertz [44,96]. Production frequency can be further increased if flow-focusing devices are arranged in parallel or circular settings (Figure 1.13) [44,168]. Moreover, the addition of active elements to a flow-focusing device can increase monodispersity and droplet generation [203] by manipulating the viscosity, flow rate, and/or surfactant concentration of the flowing phases [44,169]. In general, the production of small-sized droplets at high frequencies is achieved by proper adjustment of flow rates and selection of the orifice diameter.

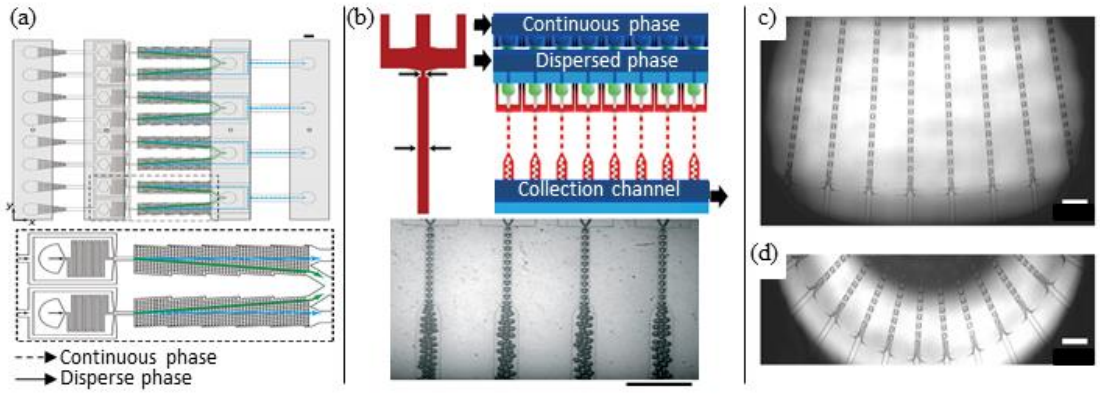

Figure 1.13: Parallel flow-focusing device settings. (a) Eight parallel flow-focusing microfluidic devices with 100 µm channels made from PDMS. Scale bar is 1 mm. Reprinted from Ref. [208], © 2018, with permission from Elsevier. (b) Eight parallel flow-focusing microfluidic devices made using a 3D monolithic elastomer device (MED) and an optical micrograph of droplet generation. Scale bar is 500 µm. Reproduced from Ref. [209] with permission from The Royal Society of Chemistry. Circular settings of (c) 128 and (d) 64 cross-flow junctions for large-scale droplet generation. The devices were fabricated using deep reactive ion etching (DRIE) technique on a synthetic silica glass substrate with 100 µm channels. Scale bars are 500 µm. Reproduced from Ref. [210] with permission from The Royal Society of Chemistry.

1.3.3.4 Co-flow devices

The third commonly used microfluidic device employs the concept of co-flow. Simply, the dispersed phase flows parallel to the continuous phase [168,169]. Unlike flow focusing devices which are based on the pinch-off at the nozzle, droplets form in co-flow devices when the shear stress applied by the continuous phase on the dispersed phase exceeds the interfacial tension of the phases [44,98,99,219]. If droplet break-up happens near the tip of the nozzle, the breakup is called dripping (Figure 1.14(a) i.) [169]; dripping generates microbeads that are highly monodisperse [219]. On the other hand, if droplet break-up happens from an extended thread downstream of the nozzle, the breakup is called jetting (Figure 1.14(a) ii. and iii.) [169]; jetting can be highly unstable and irregular at high Reynold numbers [44]. Microbead sizes formed through jetting are related to the channel dimensions and the ratio of flow rates [44]. The transition from

dripping to jetting happens after a critical velocity of the continuous phase is exceeded [169]. Usually, when two immiscible phases co-flow, a distinctive curved interface forms between them before break-up [168]. This curvature is affected by the interfacial tension of the two phases and by the liquid-solid surface tension between the continuous phase and the device interiors [168]. Although surfactants are commonly used to create stable emulsions [236], the use of a surfactant could be eliminated in a co-flow device [235]. The laminar flow of the two phases in a co-flow device can be used to generate microbeads with amphiphilic properties [98,99,168]. In addition, co-flow devices can be used to generate double emulsion microbeads [168,214,219,252] or multi-component droplets that could be used for co-encapsulation and micro-reactions with precise control of the number of inner droplets [264].

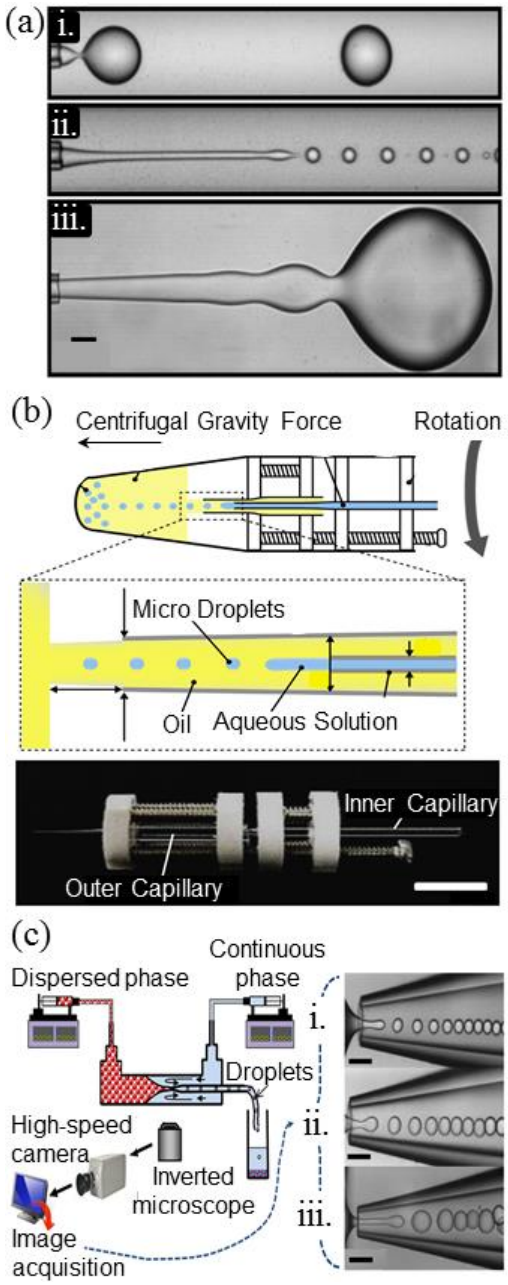

Figure 1.14: Droplet formation using co-flow devices. (a) Co-flow microfluidic devices in the i. dripping regime, ii. narrowing jetting regime, and iii. widening jetting regime. Scale bar is 50 μm. Reprinted figure with permission from Ref. [265], © 2007 by the American Physical Society. (b) A centrifuge-based axisymmetric co-flow microfluidic device made from inner and outer glass capillaries held together by a polyacetal plastic holder and has a sampling micro tube for collecting the droplets. Scale bar is 1 cm. Reprinted from Ref. [217], © 2014, with permission from The Society for Biotechnology. (c) A counter-flow microfluidic device made from a round inner glass capillary in a square glass capillary attached over a glass slide. The setup enables monitoring of droplet generation with i. and ii. showing monodispersed droplets in the dripping regime and iii. showing polydispersed droplets in the jetting regime. Scale bars are 250 μm. Adapted with permission from Ref. [192], © 2015 American Chemical Society.

Co-flow devices are typically fabricated from commercial glass capillaries in which a circular capillary is placed concentrically in a square or circular outer flow tube (Figure 1.14(b and c)) [169,214,217,219,252,266] and less frequently from PDMS [168]. Devices made from glass capillaries exhibit excellent chemical resistance when organic solvents are used, such as tetrahydrofuran and chloroform, which greatly swell PDMS [267]. Some examples of microencapsulation applications using co-flow devices include: encapsulation of mammalian cells in alginate [46], encapsulation of yeast cells [217], and encapsulation of lysozyme protein in polycaprolactone [268].

In contrast to flow-focusing devices, co-flow devices produce large microbead diameters, typically a few hundred microns [214], but could produce <50 μm droplets depending on the inner nozzle diameter [217]. Generally, co-flow results in highly monodisperse microbeads [169]. Furthermore, increasing the dispersed phase concentration leads to larger microbead diameters [178,268]. This is the result of higher viscosity and tension forces, which lead to a longer droplet pinch-off time [178]. Smaller microbeads can be formed by decreasing the interfacial tension between the phases [213], or increasing the velocity of the continuous phase [169]. On the other hand, increasing the dispersed phase flow rate leads to larger droplet formation [169].

Some studies suggest that the use of a co-flow device is preferred in cell encapsulation [44]. Generally, high cell viability can be achieved after microencapsulation using co-flow methodologies [217]. The encapsulation efficiency is directly related to the concentration of polymer in the dispersed phase and the flow rates of the phases [268]. Specifically, the concentration of the polymer affects microbead porosity and surface morphology, which affect cell proliferation and release [268].

1.3.3.5 Conclusion

Microencapsulation in 3D structures provides cells with a medium through which physiological factors can be maintained. Cells are widely encapsulated using microfluidic devices as they enable microbead shape and size control, high-throughput production, and elimination of cross-contamination. In a microfluidic device, multiple factors contribute to the production of uniformly-sized microbeads. These factors include phase flow rates, viscosity, surface tension, material type and concentration, and device geometry and dimensions. Common traits are observed among microfluidic devices, and examples include: a dispersed phase is pinched-off by the shear stress exerted by a continuous phase; higher continuous phase flow rates and viscosity cause smaller microbeads to form; and high-throughput microbead production can be achieved by setting up several devices or channels in parallel. Regardless of these similarities, each of the discussed microfluidic devices has unique advantages and disadvantages. T-junction devices allow for high-throughput production of a large number of encapsulated cells if the frequency and geometry are carefully tuned. Flow-focusing devices enable single cell encapsulation in each droplet at high production frequencies and narrow size distributions, despite having the most complex geometry of the three devices discussed. As for co-flow devices, they exhibit simple fabrication and generate highly monodisperse microbeads, although the size of produced microbeads can be often larger than those of T-junction and flow-focusing devices.

Based on the discussed information, this thesis implemented the use of a cross-flow microfluidic device to encapsulate MSB. Cross-flow devices have similar working principles as T-junction and flow-focusing devices, except that a cross-flow

device does not have an orifice, eliminating the complex geometry fabrication step commonly faced in the fabrication of flow-focusing devices. This was especially important in the device selection process, given the available microfabrication equipment. Through SLA 3D printing, a microfluidic device can be easily manufactured, with minimum reported channel dimensions of 265 μm ± 15 μm [57]. Therefore, such a cross-flow device is able to produce somewhat monodisperse microbeads at a frequency of several thousand hertz and with good cell viability. Finally, Span® 80 was used as the surfactant to lower the surface tension of agarose due to the former's common application in microfluidics.

1.3.4 Oil removal approaches

1.3.4.1 Microbead transfer across a laminar interface

Microbeads produced through microfluidic devices are usually desired to be in an aqueous phase for downstream applications [269]. Therefore, a method of transferring microbeads from the oil phase to an aqueous phase is needed. Microbeads are typically washed with aqueous media over cell strainers to remove the used oil phase [77,104,158]. However, on-chip microbead washing is preferred since it shows higher cell viability [48] and decreases manual steps, which, in turn, decreases the potential for sample contamination.

Wong *et al.* introduced a method of transferring aqueous droplets across a laminar interface through treating the internal surfaces of the main channel of a bifurcation device (or a device having two connected Y-junctions [270]) with opposite surface properties, i.e. one side is hydrophobic and the other is hydrophilic (Figure 1.15(a)) [271]. A hydrophobic surface has a contact angle, Θ, of $90° < \Theta < 150°$, and a hydrophilic surface has a Θ of $10° < \Theta < 90°$ [272]. After careful manipulation of the ratio between the aqueous and oil flow rates, no oil (or traces of oil [273]) is observed in the collected microbeads suspension [271], and the microbeads transferred spontaneously from the oil phase to the aqueous phase by use of a decreased gradient of interfacial tensions [270]. However, this method requires accurate flow rate manipulation, which if not achieved, results in the oil leaking into the microbead collection channel [271]. Moreover, treatment of the internal channel with two different surface properties as well as the fabrication of a narrower oil exit channel (Figure 1.15(b)) can be difficult [272].

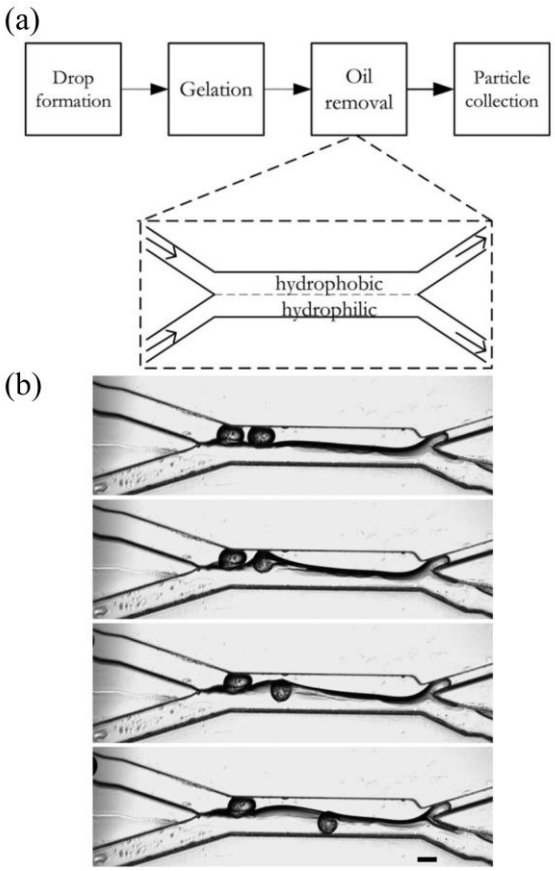

Figure 1.15: Microbead transfer across a laminar interface in a bifurcation device. (a) Schematic of the steps involved in microbead generation and collection in an aqueous phase, with an illustrated bifurcation device showing two surface properties, hydrophobic and hydrophilic, which enhance the transfer of microbeads from the oil phase to the aqueous phase. (b) 10 ms timeframes showing a hydrogel microbead transfer from an oil phase (top) to an aqueous phase (bottom) at set flow rates. The oil phase has a narrower exit channel (top right). Scale bar is 100 μm. (a) and (b) are Reproduced from Ref. [271] with permission from The Royal Society of Chemistry.

1.3.4.2 On-chip fluid depletion and microfiltration

Other methods of obtaining hydrogel microbeads in an aqueous phase involve washing away the oil phase on-chip. Avoiding single-channel surface treatment with two opposite properties, Deng *et al.* successfully fabricated a microfluidic device composed of a droplet generation zone, a serpentine section for droplet gelation, and a microbead 'extraction' region to wash off the oil phase [48]. In the extraction region, a series of wide channels infused water (or an aqueous medium) onto a perpendicular main channel

containing the microbeads-in-oil mixture (Figure 1.16(a)), creating a laminar-like oil/water interface. Simultaneously, narrow channels, positioned perpendicularly on the bottom side of the main channel and narrow enough to prevent microbeads from exiting, provide an exit for the washed away oil. Using this device, no oil was obtained in the collected microbeads suspension, and higher cell viability (approximately 80%) was obtained compared to traditional microbead washing and centrifugation (approximately 50%) [48]. It is worthy to mention that providing no oil removal resulted in poor cell viability (less than 10%) [48]. Similar results are obtained by Hong *et al.* through washing microbeads from oil using culture media introduced to an extraction chamber (Figure 1.16(b)), where microbeads are collected after formation and gelation [274]. Additionally, Angelescu and Siess used a series of microfluidic capillaries, or a 'comb,' branched out from a main channel to separate oil and water phases. However, <10% of the collected fluid contained oil due to the oil being trapped in the main channel as the water flowed out [275].

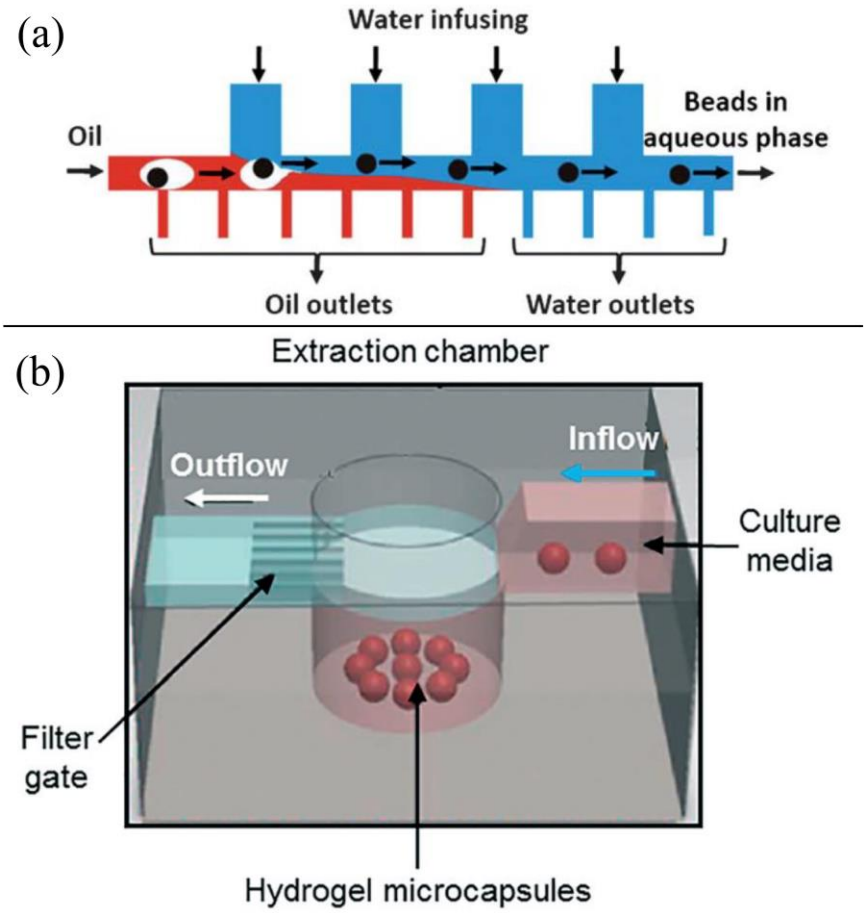

Figure 1.16: On-chip oil depletion methods. (a) An illustration showing a main channel carrying microbeads (black circles) in oil, with water infusing from the top, creating a laminar-like interface through which microbeads transfer to the aqueous phase. Through multiple water-infusing channels, the oil is depleted and exits from the narrow bottom channels. Reproduced from Ref. [48] with permission from The Royal Society of Chemistry. (b) An extraction chamber in which microbeads are collected, the oil flow rate is suspended, and a stream of culture media is introduced to wash the microbeads from oil. A filter gate is shown which acts to remove the washing/washed fluids and to prevent microbeads from exiting the chamber during washing. Microbeads are later collected from the chamber using a pipette [274]. Reproduced from Ref. [47] with permission from The Royal Society of Chemistry.

Similar approaches utilize the force of a buffer phase, which could be an aqueous medium, to hydrodynamically focus microbeads and cross-filter them across ‘posts,’ or micro-filters (Figure 1.17(a)) [240,276]. Other approaches involve sandwiching a PDMS membrane between two channels, resulting in a multi-layered device (Figure 1.17(b))

used for particle separation [277,278]. Overall, these methods are successful in microfiltration applications.

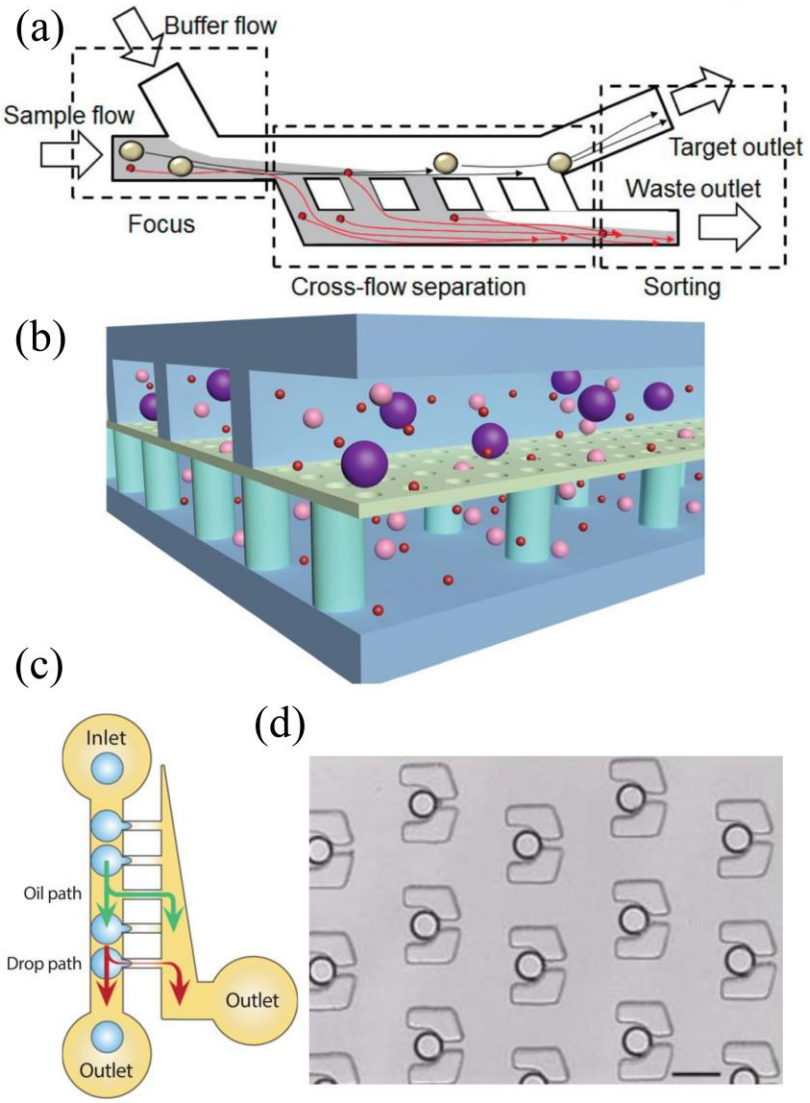

Figure 1.17: Microfiltration devices and on-chip fluid depletion methods. (a) A device with 'posts' that act as filters to sort droplets according to size. The use of a buffer fluid in this device enhances particle sorting. Reprinted from Ref. [276], with the permission of AIP Publishing. (b) A multi-layered PDMS device with the top layer consisting of channels introducing the medium to be processed, a sandwiched PDMS membrane through which filtration occurs, and a bottom layer which collects the filtered fluids (the bottom layer has PDMS pillars to support the sandwiched membrane). Reprinted by permission from Copyright Clearance Center Inc.: Springer Nature, Microfluids and Nanofluids, Ref. [277], © 2018. (c) An oil extractor in which oil is depleted from the main channel through thin drainage channels that connect to the 'Outlet' (right) using applied negative pressure, without allowing droplets to pass through the drainage channels. Reprinted from Ref. [279], with the permission of AIP Publishing. (d) Microbeads (circles) 'parked' using geometrical networks of posts. Once a microbead is trapped between two posts, other microbeads pass outside the 'parking,' leading to trapping a single microbead at a time. Scale bar is 75 μm. Reproduced from Ref. [280] with permission from The Royal Society of Chemistry.

Other researchers created devices that extract oil [279] or a phase from a diphasic fluid [281] through the use of narrow side channels (Figure 1.17(c)) or sudden channel expansions [282], respectively. These methods resulted in concentrating the desired particles in the incoming fluid, without completely depleting the fluid. An approach that could be used to wash the microbeads from the oil phase is to 'park' the microbeads [280]. This could be achieved through trapping the microbeads (using geometrical networks of posts set at specific locations in the device, or 'parking spots' (see Figure 1.17(d))), suspending the oil phase flow rate, infusing water, then reversing the flow to re-obtain the microbeads [283].

1.3.4.3 Membrane separation

Oil/water mixture separation could be achieved using sorbent surfaces. Such surfaces started developing in response to the increasing frequency of oil spills occurring in open water bodies [284]. For example, Li *et. al* developed a superhydrophobic and superoleophilic fabric that could be used as a membrane to separate oil from water (Figure 1.18(a)), with a separation efficiency >94.6% [285]. A superhydrophobic surface has a Θ of >150°, and a superoleoophilic surface has a Θ of <10° [272]. Similarly, Wang *et al*. treated filter paper with octadecyltrichlorosilane (OTS) and methyltrichlorosilane (MTS) to render a superhydrophobic surface that is able to separate oil from water with 99.4% separation efficiency [286]. More examples achieved similar results through modifying the surface properties of a sponge using a porous coordination polymer (PCP) treated with trifluoromethyl functional groups ($-CF_3$) and graphene oxide (GO) (from which oil is continuously pumped out, Figure 1.18(b)) [287], graphene [288–291], and

silicon dioxide (SiO_2) [292]. Many other sorbents were also developed for oil/water mixture separation [293–299].

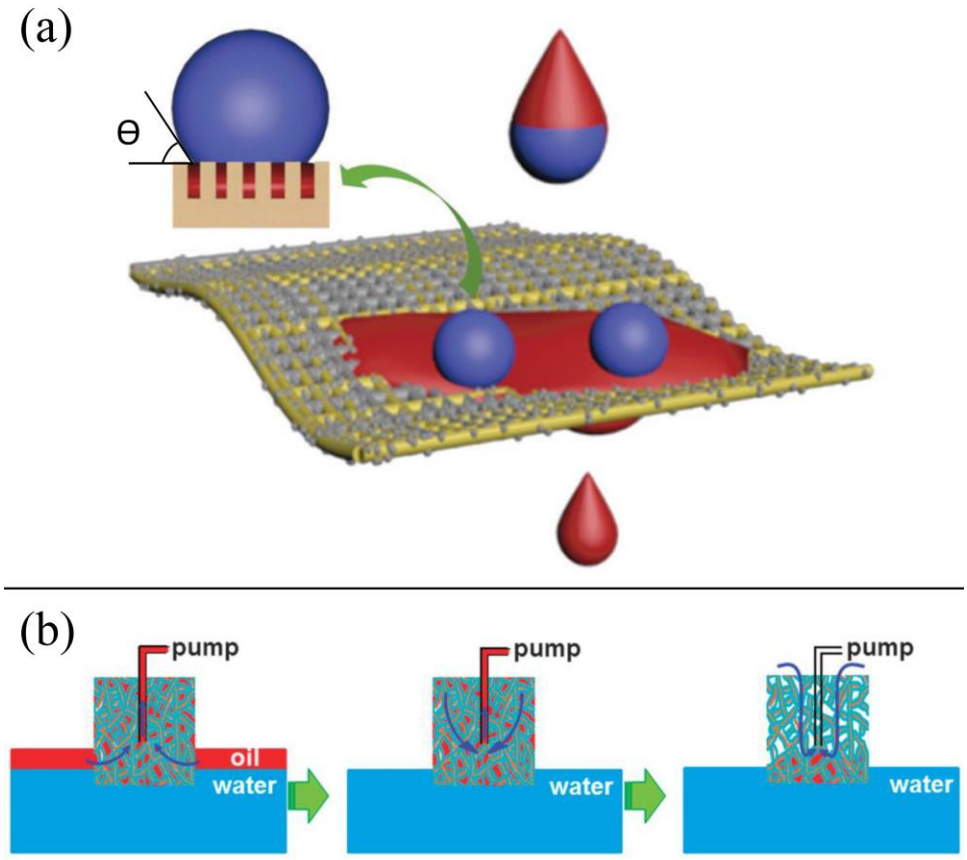

Figure 1.18: Sorbents used to separate oil/water mixtures. (a) A superhydrophobic and superoleophilic fabric used to separate oil (red) from water (purple). Water does not permeate through the fabric and has a contact angle, Θ, of 159 ± 1°, while oil has a contact angle of 0°. Reproduced from Ref. [285] with permission from the PCCP Owner Societies. (b) An illustration showing a commercial macro-porous sponge treated with $–CF_3$ and GO to render a hydrophobic and oleophilic surface that is capable of absorbing oil (red) from an oil/water mixture. A pump is shown to continuously remove oil from the sponge. Reprinted from Ref. [287], https://creativecommons.org/licenses/by/4.0/.

In terms of using such sorbents in microfluidic devices, Angelescu and Siess used a hydrophobic membrane to separate oil from water [275]. The membrane is adhesively connected to a PDMS chamber containing a gas, water, and oil mixture, with the chamber exhibiting a network of open micro-channels placed on the membrane. Although no water was observed with the exiting oil, there is no data reporting the amount of oil

remaining with the water phase, which is important in oil/water separation approaches used with cell encapsulation applications.

1.3.4.4 Conclusion

Most of the discussed methods show a high separation efficiency of oil/water mixtures. However, methods involving microbead transfer across a laminar interface require careful flow rate manipulation [275], as minute changes in the flow rates will allow oil to exit with the collected microbeads suspension and/or prevent microbead transfer from the oil phase to the aqueous phase. Moreover, creating a laminar interface is greatly enhanced by treating the main channel with opposite surface properties, which could be difficult to achieve.

As for on-chip fluid depletion methods, complex soft lithography fabrication steps are needed to create such devices having narrow channels, posts, and multi-layered membranes, not to mention the difficulty of sealing the microfluidic chips after fabrication [272]. Although these methods show that a fluid could be depleted using a buffer fluid, they are not tested for microbead transfer from an oil phase to an aqueous phase nor using immiscible fluids.

Finally, the use of sorbents, treated to have specific surface chemistry properties, is well demonstrated to separate oil/water mixtures with high separation efficiency. However, they, too, are not tested for microbead transfer from an oil phase to an aqueous phase. The treatment of sorbents to have hydrophobic and oleophilic properties could be complex, but commercial ‘oil absorbents’ are readily available. Therefore, a simple, sterile, continuous flow device was developed in this thesis. Complex fabrication steps were bypassed using 3D printing, and oil/water separation was attempted using a

hydrophobic-oleophilic treated membrane or a commercially-available oil absorbent material. There is no current literature reporting the use of these elements for microbead transfer from the oil phase to an aqueous phase after microfluidic droplet generation, suggesting the novelty of this approach.

1.3.5 Microfluidic device fabrication methods

1.3.5.1 Soft lithography

The most commonly-used fabrication method of microfluidic devices is soft lithography. In soft lithography, a liquid elastomer, typically polydimethylsiloxane (PDMS), is casted on a micro-patterned mold, cured, removed, and placed on a substrate to seal the micro-channels [36]. Although soft lithography is successful in fabricating intricate micro-devices, it entails several limitations. For example, the cured elastomer mold must be completely bonded to the substrate to ensure leak-proof channels [54,55]. Moreover, punching holes in the elastomer for inlets and outlets might destroy the chip [55,56], often leading to restarting the fabrication process. This method is also time consuming [52], labor intensive [37], difficult to commercialize [38], and often requires access to a clean room and micro-patterning equipment [50,57]. Therefore, optimization of this method, or development of other methods, is needed.

1.3.5.2 3D printing

Recently, the introduction of 3D printing technology has increased the potential for alternative fabrication methods of microfluidic systems. Many microfluidic chips are fabricated using commercial 3D printers (refer to Figure 1.12). SLA, fused-deposition modeling (FDM), and inkjet printing are the most common 3D printing technologies and are well-illustrated by Au *et al.* (see Figure 1.19) [37]. These 3D printing technologies are extensively used to fabricate microfluidic devices for droplet generation [57,216], cell encapsulation [215], electrophoresis [300], and particle focusing applications [263]. Macdonald *et al.* assessed these 3D printing technologies for suitability in microfluidic

applications, in terms of printer performance and laminar flow characteristics [301]. 3D printing is also being used in soft lithography to create molds for PDMS casting [53,261,262,302]. In general, 3D printing offers a one-step, inexpensive, fast, and customizable method of microfluidic device fabrication [38,49,50], and offers the possibility for large scale commercialization [52]. Nonetheless, this method is still limited in terms of minimum channel size printable [49,50], optical transparency [51,52], and residue resins and/or support structures [38,50,51]. Also, the biocompatibility of 3D printing materials is debatable [49,52,53].

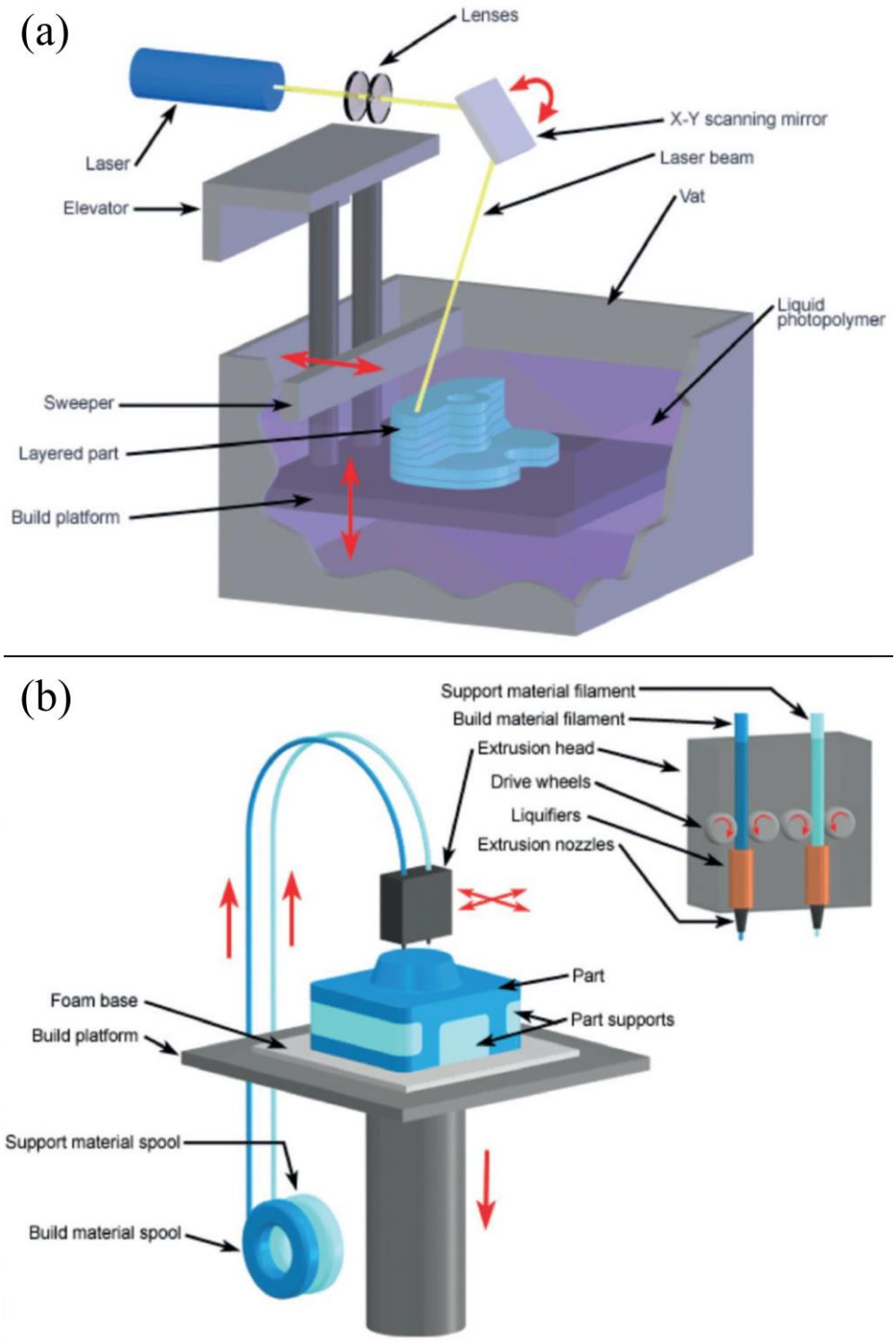

Figure 1.19: Illustrations of three of the most common 3D printing technologies: (a) SLA, (b) FDM (also called thermoplastic extrusion), and (c) photopolymer inkjet printing. Reprinted from Ref. [37], with permission from John Wiley and Sons (images courtesy of CustomPartNet.com).

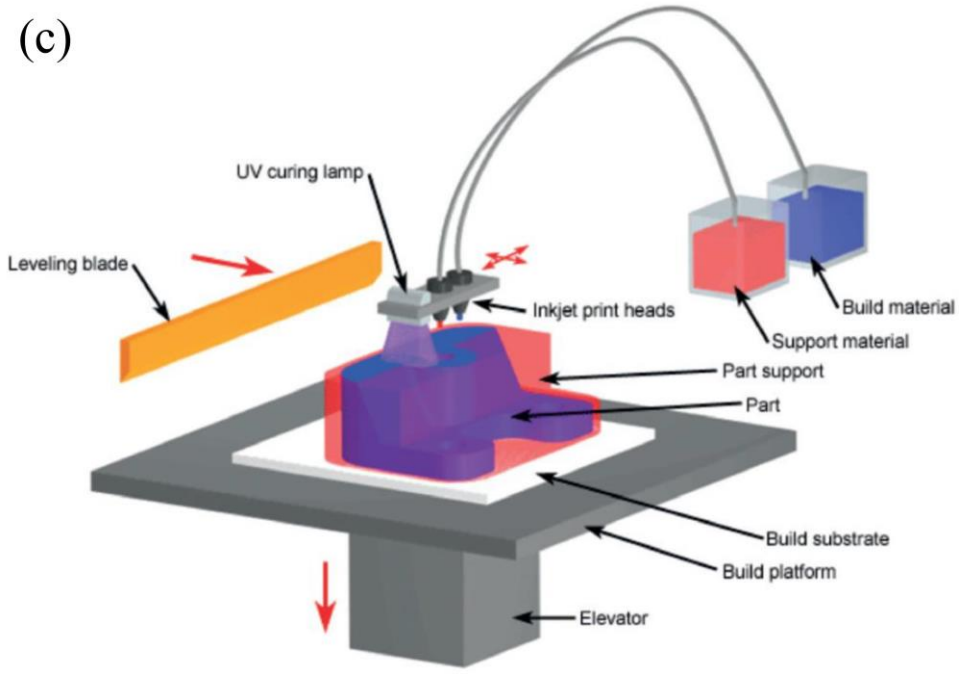

Figure 1.19 *(continued).*

1.3.5.3 Internal scaffold removal

The use of 3D printing has inspired introducing new approaches for microfluidic chip fabrication, such as removing internal scaffolds, i.e., internal scaffold removal (ISR) [303]. In ISR, channels of the desired shape are 3D printed using a solvent-soluble material and placed in liquid PDMS. The PDMS is cured and the scaffold is dissolved using the appropriate solvent, leaving hollow channels in the PDMS structure. Water soluble sugars, PVA, and the thermoplastic acrylonitrile butadiene styrene (ABS) were used as the 3D printing materials for microfluidic channels using the ISR method [303–306]. Kang *et al.* used several materials and studied the effects of six solvents on the final PDMS structure, with acetone and methanol having the least effect on PDMS swelling and cracking [307].

1.3.5.4 Conclusion

ISR proves to be a reliable method for creating hollow structures inside PDMS without the need for sealing the channels. This method also decreases the amount of laborious work involved in microfluidic chip fabrication using soft lithography. However, current literature does not present fabrication of channels that could be used for droplet generation, which is a major application of microfluidics. Moreover, the sizes of the obtained channels are limited by the diameter of the nozzle head used in 3D printing. Therefore, adding a step to the ISR process in which channel dimensions are reduced before PDMS casting could enable the use of this method for fabrication of smaller microfluidic channels.

It is known that ABS is soluble in acetone. Multiple studies have investigated the effect of acetone vapor smoothing [308,309] and acetone bath soaking [310] on the surface properties of ABS parts. However, to the best of the author's knowledge, there is no literature involving the study of ABS dissolution in acetone to obtain smaller channels for use with ISR. Hence, in this thesis, a controlled ABS scaffold dissolution step in acetone was investigated before placement in PDMS to fabricate microfluidic chips, resulting in a method called eISR herein.

CHAPTER 2 : MICROFLUIDIC ENCAPSULATION OF MARINE SEDIMENT BACTERIA (MSB) TOWARDS NATURAL PRODUCT DISCOVERY THROUGH AN *IN-SITU* MD POD

2.1 Introduction

In this thesis, an *in-situ* growth chamber, the MD Pod (Figure 2.1), combined the features of single-cell isolation and co-culture and was used to promote the growth of 'uncultivable' MSB, which could lead to the discovery of new marine natural products. The MD Pod was made from a thermoplastic polymer using FDM 3D printing since the MD Pods do not require high printing resolution. The MD Pod was enclosed by two polycarbonate track etch (PCTE) membranes to prevent cell migration while allowing for nutrient, chemical, and waste diffusion.

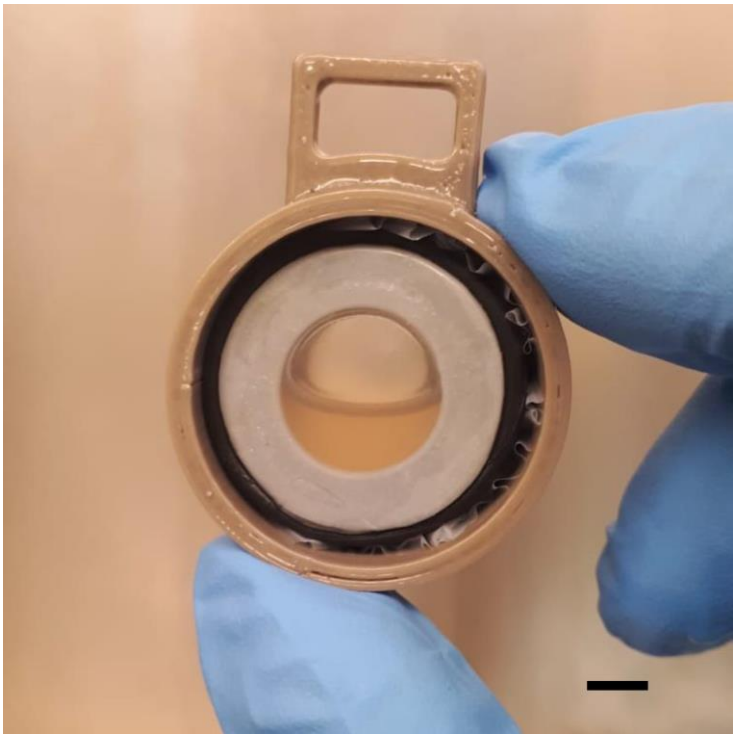

Figure 2.1: An assembled MD Pod placed in a casing and loaded with an MSB sample. Scale bar is 4 mm.

The process used in this work, shown in Figure 2.2, began by 'dislodging' bacteria from marine sediment through a series of shaking steps. A cross-flow microfluidic chip was used to encapsulate bacteria in agarose microbeads using the shear

stress of a mineral oil continuous phase. The diameter of the microbeads was chosen to be 100 μm to have enough space for the encapsulated cells to divide and form micro-colonies inside the microbeads [311]. The microbeads were washed several times to remove mineral oil then loaded into the MD Pod, which was placed in sediment for *in-situ* incubation. After a certain incubation duration, the MD Pod was retrieved and the microbeads were dispensed on dilute Marine Agar (dMA) and inspected periodically for the growth of microbial colonies. This method allows bacteria to maintain an exchange of chemical signals with surrounding cells and with the environment to promote cell growth [22,29,31], while the microbeads offer a space for individual cells to grow separately from the surrounding microorganisms [34] existing in the MD Pod.

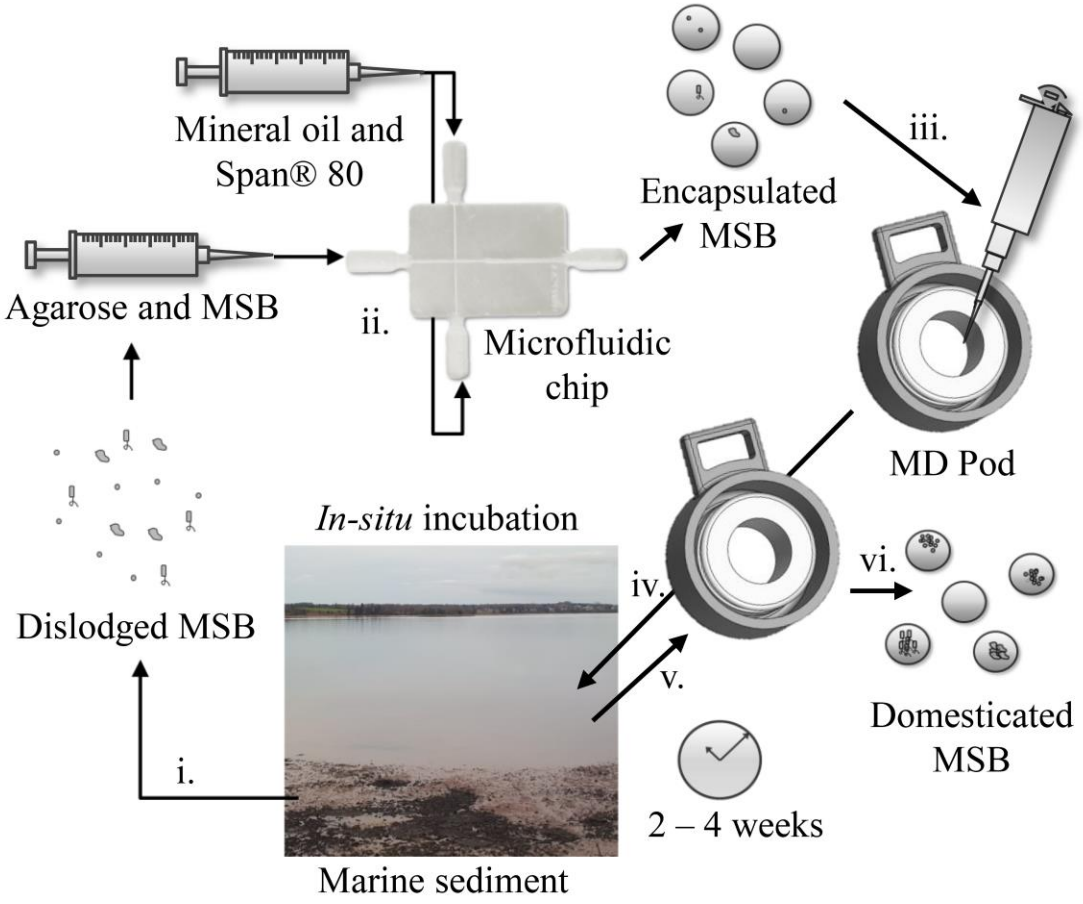

Figure 2.2: Process schematic of microfluidic encapsulation of marine sediment bacteria (MSB) and *in-situ* incubation using an MD Pod. The process used is: (i) aseptic collection and dislodging of MSB; (ii) encapsulation of MSB in agarose microbeads using a cross-flow microfluidic chip; (iii) loading of encapsulated cells into the MD Pod using a micropipette; (iv) insertion of the MD Pod into the native marine environment for *in-situ* incubation; (v) retrieval of the MD Pod; and (vi) unloading of domesticated cells from the MD Pod.

2.2 Materials and Methods

2.2.1 Microfluidic chip fabrication

A comb-like structure was designed using SolidWorks CAD software (2016-2017 and 2017-2018 versions, Dassault Systèmes, France) to have straight and square flow-through channels with increasing dimensions from 100 μm to 1400 μm in 100 μm increments (Figure 2.3). The comb-like structure was 3D printed using a Form 2 SLA printer (Clear resin, Formlabs, USA) and was used to assess the lowest channel size printable using this printer. The channels were repeatedly flushed with 99% isopropyl alcohol (IPA) for opening.

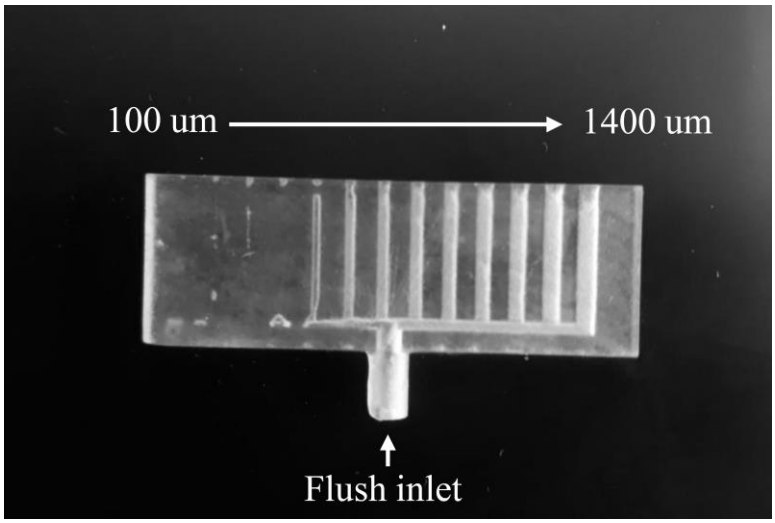

Figure 2.3: A comb-like structure used to assess the printability of internal channels using Form 2 SLA 3D printer. Square flow-through channels of increasing dimensions (100 μm to 1400 μm) were designed and 3D printed.

After identification of the successfully printable channel dimensions using the comb-like structure, microfluidic chips have been fabricated with different channel dimensions and are shown in Appendix A. A microfluidic chip with square dimensions of 1000 μm was used in this thesis. It consisted of cross-flow channels with in-line inlets and outlets (Figure 2.4) and was made from a methacrylate photopolymer (Clear resin,

Formlabs, USA). The chip was oriented at 70º on the building platform, with the outlet channel facing the platform and using automatically-generated supports, and using 25 µm printing resolution. After printing, the chip was immediately washed with 99% IPA for 1 min. Residue resin was removed by inserting a 400 µm nozzle cleaner rod inside the channels and removing the liquid resin using syringe suction. After all residue resin was removed, the chip was soaked in a bath of 99% IPA for 20 mins, with agitation in the bath for 1 min after each 10 mins.

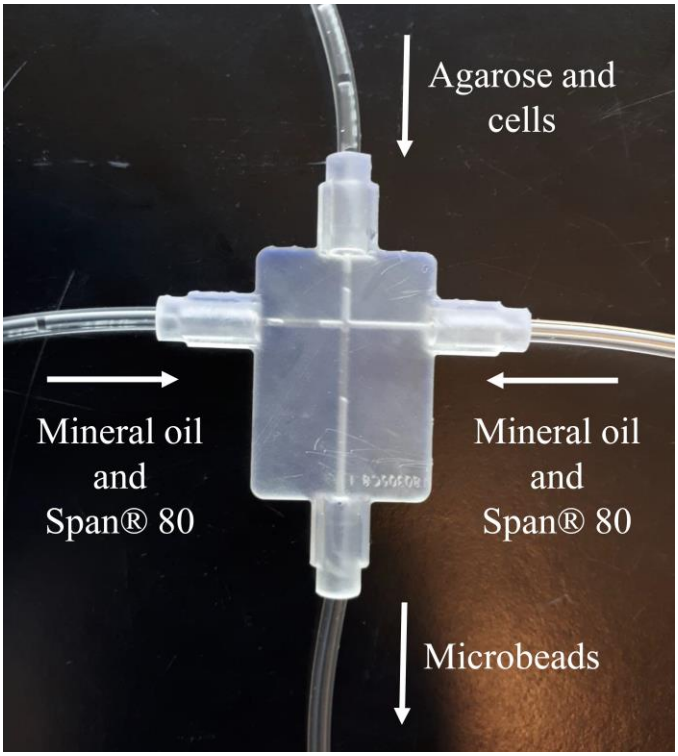

Figure 2.4: A cross-flow microfluidic chip with 1000 µm square channels and in-line inlets and outlets. The chip was 3D printed using Clear resin, Form 2.

2.2.2 MD Pod fabrication

2.2.2.1 Device fabrication

The MD Pod aimed to provide a space to suspend the microbeads after bacterial encapsulation and house the microbeads during *in-situ* incubation in sediment. To prevent the escape of the microbeads and the infiltration of bacteria from the external environment, the cavity of the MD Pod was enclosed by two 30 nm pore size, 47 mm diameter, and 3 – 24 μm nominal thickness PCTE membranes (SterliTech, USA). The pores of the PCTE membranes allow for nutrient and chemical exchange between the cells and the environment, and prevent cell migration [84] in or out of the MD Pod. This type of membrane material was used since it was used successfully in other similar applications [25]. Other materials could be used as long as they are biocompatible and provide a pore size that prevents cell migration and allows the necessary diffusion.

After multiple prototypes exhibiting different features and made from different materials (Figure B.1), the final MD Pod (F-MD Pod) was designed using CAD software (Figure 2.5(a)) and 3D printed using Cool Grey 1.75 mm ABS thermoplastic filament and a 400 μm nozzle head (Zortrax M200, Poland). Each MD Pod could hold a maximum volume of 2.68 mL. A smaller MD Pod (Figure 2.5(b)), herein named Small MD Pod (S-MD Pod), was also designed and printed to investigate the potential for this shape of the MD Pod to be miniaturized. The S-MD Pod could hold a maximum volume of 1.64 mL. After printing, the top and bottom sides were smoothed by rubbing on sand paper. Afterwards, the whole MD Pod body was smoothed by dipping in a bath of 100% acetone (Sigma Aldrich, USA) for 1 s and left to dry on a flat surface at room temperature. Moreover, a protective casing (Figure 2.5(c and d)) was designed, printed,

and smoothed according to the same procedure. This casing was used to provide protection for the MD Pod during insertion and retrieval from sediment, since the PCTE membranes are extremely fragile and can easily be damaged. The casing also provided a tag holder to label different samples inside the MD Pods.

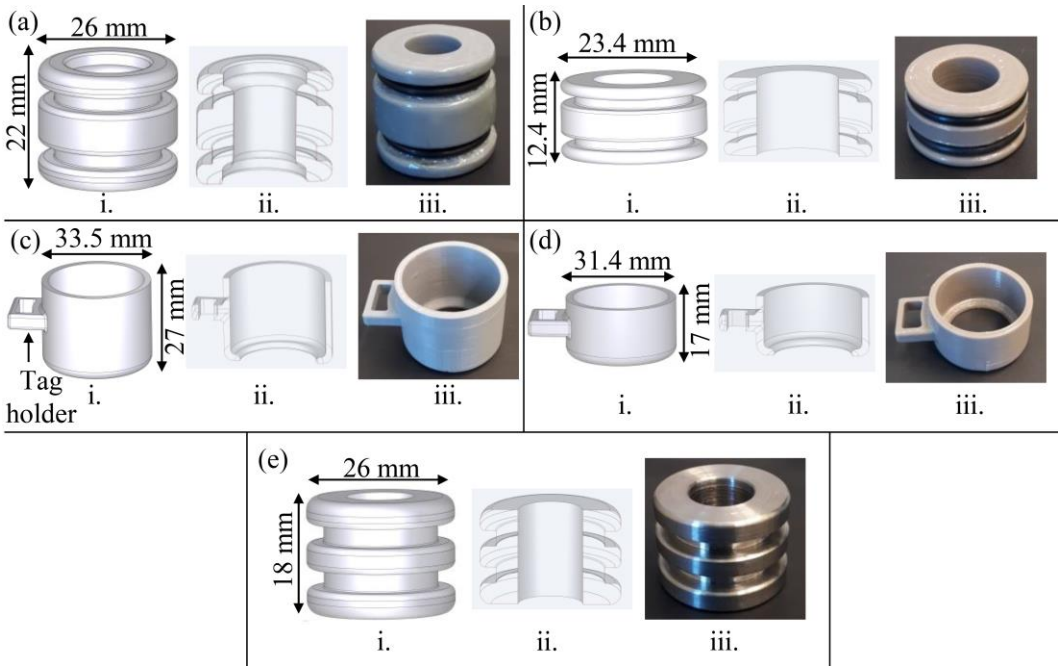

Figure 2.5: MD Pods and casings used for *in-situ* incubation. Illustrations show (a) the F-MD Pod, (b) the S-MD Pod, (c) a casing for F-MD Pod and M-MD Pod, (d) a casing for S-MD Pod (with an indicated tag holder), and (e) the M-MD Pod, with i. representing the CAD design and outer dimensions of each part, ii. representing a longitudinal cross-section of each part, and iii. representing the 3D printed (a – d) or machined (e) parts.

Additionally, to investigate the effect of different materials on microbial growth, 304 stainless steel (McMaster-Carr, USA) was machined and smoothed using a lathe to create a Metallic MD Pod (M-MD Pod, Figure 2.5(e)) of the same circular outer dimensions as that shown in Figure 2.5(a) and a maximum volume of 2.03 mL. An ABS casing was used for the M-MD Pods.

2.2.2.2 MD Pod sterilization

To sterilize the MD Pods before use, all MD Pods, casings, rubber bands, and O-rings were soaked in 20% bleach (prepared from 5.25% NaOCl bleach) for 20 mins. Two O-rings (McMaster-Carr, USA) were then placed in each of the two grooves in the MD Pod body. The MD Pods were soaked again in 20% bleach for 20 mins, washed in a bath of sterile deionized (DI) water, soaked in 70% IPA for 10 mins, and washed in another bath of DI water. PCTE membranes and tweezers were autoclaved at 121ºC and 30 mins in sterilization autoclave pouches. PCTE membranes were handled using gloves and tweezers, since skin oils damage the membrane. To maintain sterility, autoclaved tweezers were used to transfer PCTE membranes. M-MD Pods were sterilized by autoclaving. After this process, the MD Pods were ready for assembly and sample loading. Details about the three types of MD Pods are summarized in Table 2.1.

Table 2.1: Summary of MD Pod properties used for *in-situ* incubation.

MD Pod Type	Building Material	Sterilization Method	Type of O-rings Used	Maximum Internal Volume
F-MD Pod	ABS	20% bleach followed by 70% IPA	2 × 17 mm ID/ 21 mm OD under membrane, 2 × 17 mm ID/ 21 mm OD over membrane, and 2 × 20 mm ID/ 26 mm OD over membrane	2.68 mL
S-MD Pod	ABS	20% bleach followed by 70% IPA	2 × 17 mm ID/ 21 mm OD under membrane and 4 × 17 mm ID/ 21 mm OD over membrane	1.64 mL
M-MD Pod	304 stainless steel	Autoclave	2 × 17 mm ID/ 21 mm OD under membrane, 2 × 17 mm ID/ 21 mm OD over membrane, and 2 × 20 mm ID/ 26 mm OD over membrane	2.03 mL

2.2.2.3 MD Pod assembly

To assemble the MD Pods, sterile petri dishes were used to provide a sterile working surface. The components of the MD Pod are shown in Figure 2.6. An O-ring dispenser (Figure 2.7) was designed and printed using ABS (Zotrax, Poland) and was smoothed according to the discussed process to aid in stretching the O-rings over the S-MD Pods without tearing the PCTE membranes. The O-ring dispenser was also sterilized according to the previously described procedure. The detailed MD Pod assembly process is illustrated in Figure 2.8. Briefly, the MD Pod was aseptically transferred to a petri dish. A PCTE membrane was placed on top of the MD Pod, and an O-ring was placed on the O-ring dispenser. The top cap of the O-ring dispenser was gently pushed over the MD Pod to snap the O-ring directly in the top groove, sealing the device. Another O-ring was placed using the same procedure to provide additional seal. The MD Pod was then aseptically flipped, loaded with the sample, and the same steps were performed for closing the device using a membrane and two more O-rings. In total, each MD Pod has six O-rings to ensure seal. Finally, the MD Pod was placed in a casing, and held in place using a rubber band. The assembly time of each MD Pod was 5 mins on average.

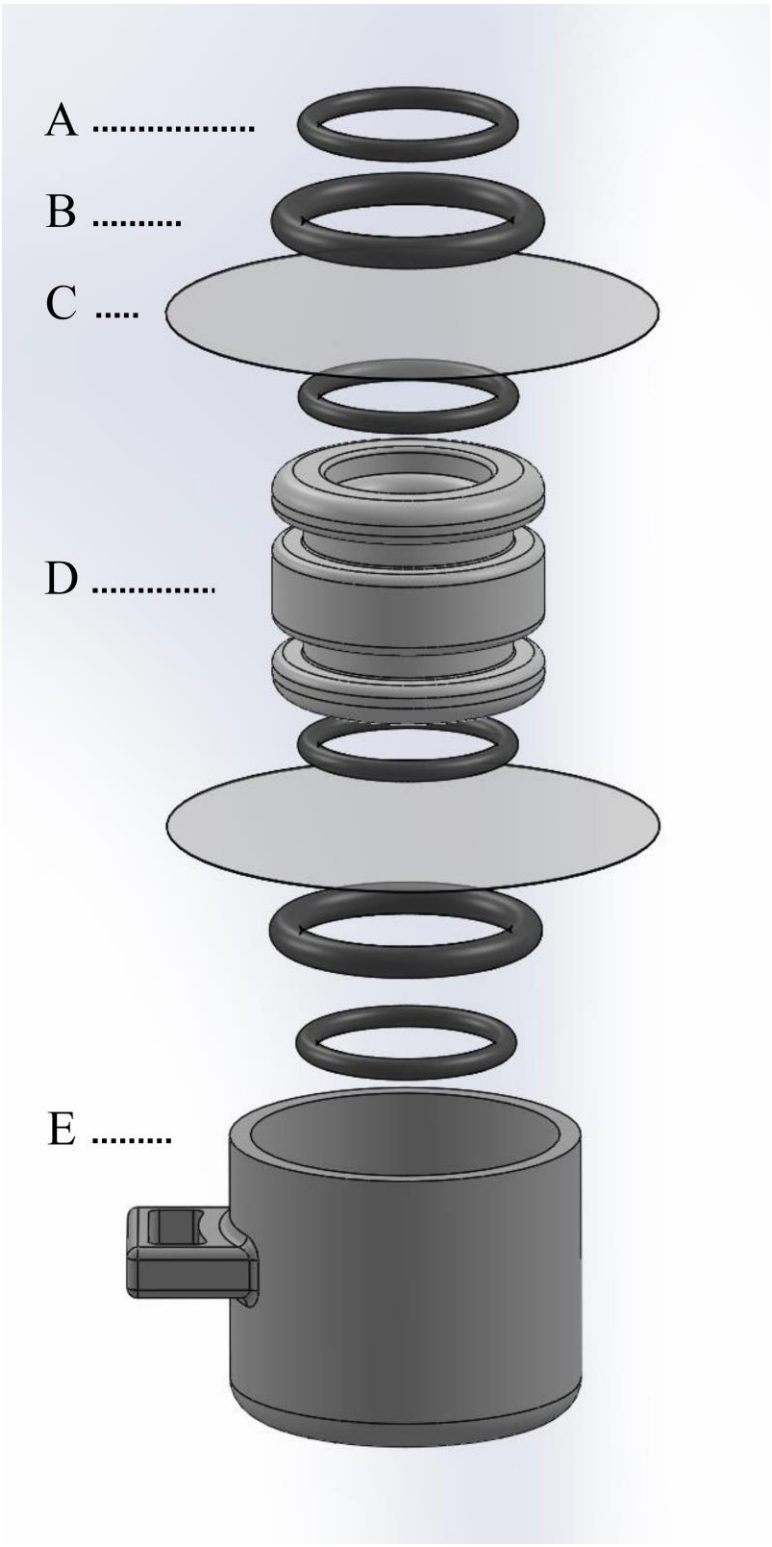

Figure 2.6: Exploded assembly of the F-MD Pod. ‘A’ represents four 17 mm ID/ 21 mm OD O-rings, ‘B’ represents two 20 mm ID/ 26 mm OD O-rings, ‘C’ represents two PCTE membranes, ‘D’ represents the body of the F-MD Pod, and ‘E’ represents the protective casing.

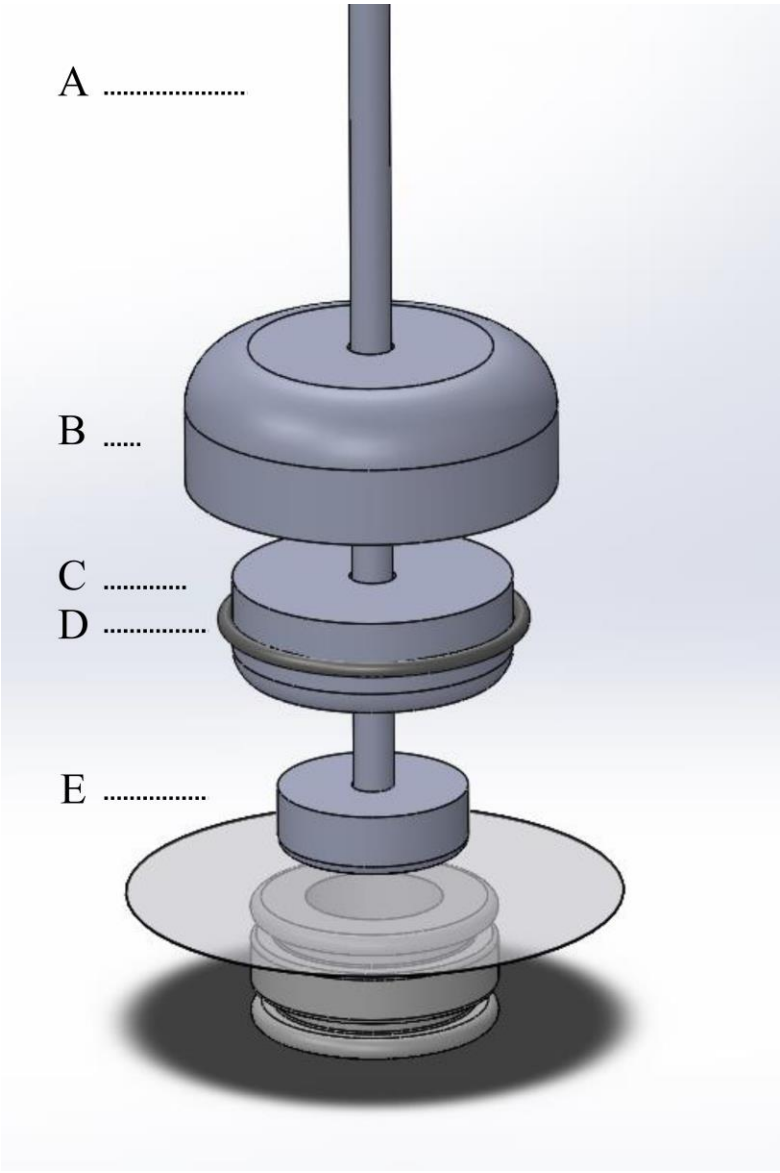

Figure 2.7: Assembly of the O-ring dispenser. ‘A’ is a stem used to hold the O-ring dispenser parts together. ‘B’ is a top cap that enables dispensing the O-ring. ‘C’ is a holder for the O-ring (‘D’). ‘B’ and ‘C’ move along the stem. ‘E’ is a piece that holds down the membrane over the S-MD Pod as the O-ring is being dispensed.

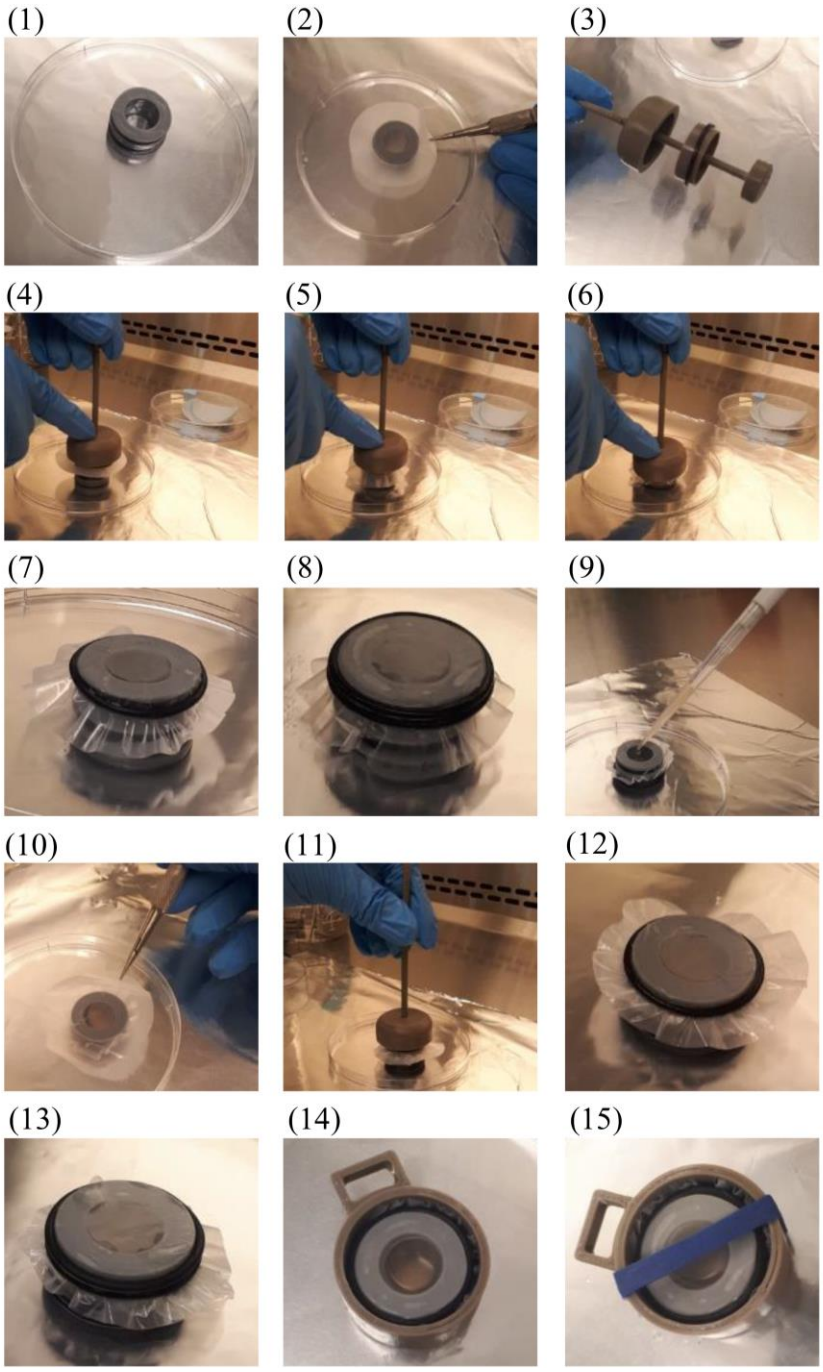

Figure 2.8: Graphic manual for the assembly and loading of S-MD Pods. (1) Transfer the S-MD Pod aseptically to a petri dish. (2) Place a PCTE membrane on top of the MD Pod, and (3) place an O-ring on the O-ring dispenser. (4 – 6) Gently push the top cap of the O-ring dispenser over the MD Pod to snap the O-ring directly in the top groove, sealing the device. (7) One O-ring is now installed using the O-ring dispenser. (8) Repeat steps (3 – 6) to install a second O-ring. (9) Flip the MD Pod and load it with the sample. (10) Place a PCTE membrane on the MD Pod, and (11 – 13) use the O-ring dispenser to install two O-rings. The MD Pod is now closed. (14) Place the assembled MD Pod in a casing, and (15) hold it in place using a rubber band.

2.2.3 Bacteria preparation

2.2.3.1 *Escherichia coli*

For proof of concept purposes, *Escherichia coli* K12 ER2925 (New England Biolabs, Ipswich, USA) was streaked on lysogeny broth (LB) agar plates (Miller, Sigma Aldrich, USA) and incubated at 37ºC overnight. *E. coli* was then inoculated in 5 mL of LB broth in an open shaker for 1 day at 200 RPM. For encapsulation, optical density ($OD_{600\ nm}$) was measured using NanoDrop® ND-1000 Spectrophotometer (ThermoFisher, USA) with a path length of 1 mm. An $OD_{600\ nm}$ of approximately 0.2 was used (corresponding to approximately 3.34×10^7 cells/mL). Then, 250 µL of the inoculum was added to 5 mL of LB broth and centrifuged at 4500 × *g* for 5 mins to pellet the cells. This pellet corresponded to approximately 8.35×10^6 cells, which should result in an approximately 36% single-cell encapsulation rate according to the Poisson distribution, which is demonstrated as:

$$p(k,\lambda) = \frac{\lambda^k e^{-\lambda}}{k!}, \quad (1)$$

in which p is the frequency of encapsulating a certain number of cells in a droplet, k is the actual number of cells encapsulated, and λ is the average number of cells per droplet volume [89,312]. The droplet diameter used was 100 µm.

2.2.3.2 Environmental marine sediment bacteria

MSB were dislodged from marine sediment samples collected from intertidal zones in North River, Prince Edward Island (PE) (46.24º N, -63.15º W (Location 1)) and Brackley Beach, PE (46.43º N, -63.19º W (Location 2), and 46.43º N, -63.12º W (Location 3)) (Figure 2.9). Marine sediment (approximately 10 mL) was aseptically

collected in Falcon tubes. For Location 1, samples were stored at -24ºC until use. For Location 2, samples were stored at -24ºC until use and a plastic box was filled with sediment and seawater from the study site and kept undisturbed at 4ºC with an air bubbler to serve as a simulated natural environment. The height of sediment in the box was 10 cm and the water level above the sediment was 5.5 cm. For Location 3, sediment was collected in a box and transferred to an aquarium equipped with an air bubbler, two gravel aerators (used to aerate the sediment), a filter, a heater, and a thermometer. The height of sediment in the aquarium was 11 cm and the water level above the sediment was 11 cm. The temperature, salinity, and pH of the seawater were recorded weekly using a thermometer, a salinity probe, and a pH probe, respectively, and DI water was added weekly to compensate for evaporation. For Location 3, approximately 10 mL samples were collected aseptically from the aquarium on the day of encapsulation. Seawater was collected from the three locations and filter-sterilized using a 0.45 µm filter followed by a 0.2 µm filter (Sigma Aldrich, USA). Filter-sterilized seawater (FSS) was stored at 4ºC (for Locations 1 and 2) and at room temperature (for Location 3) until use.

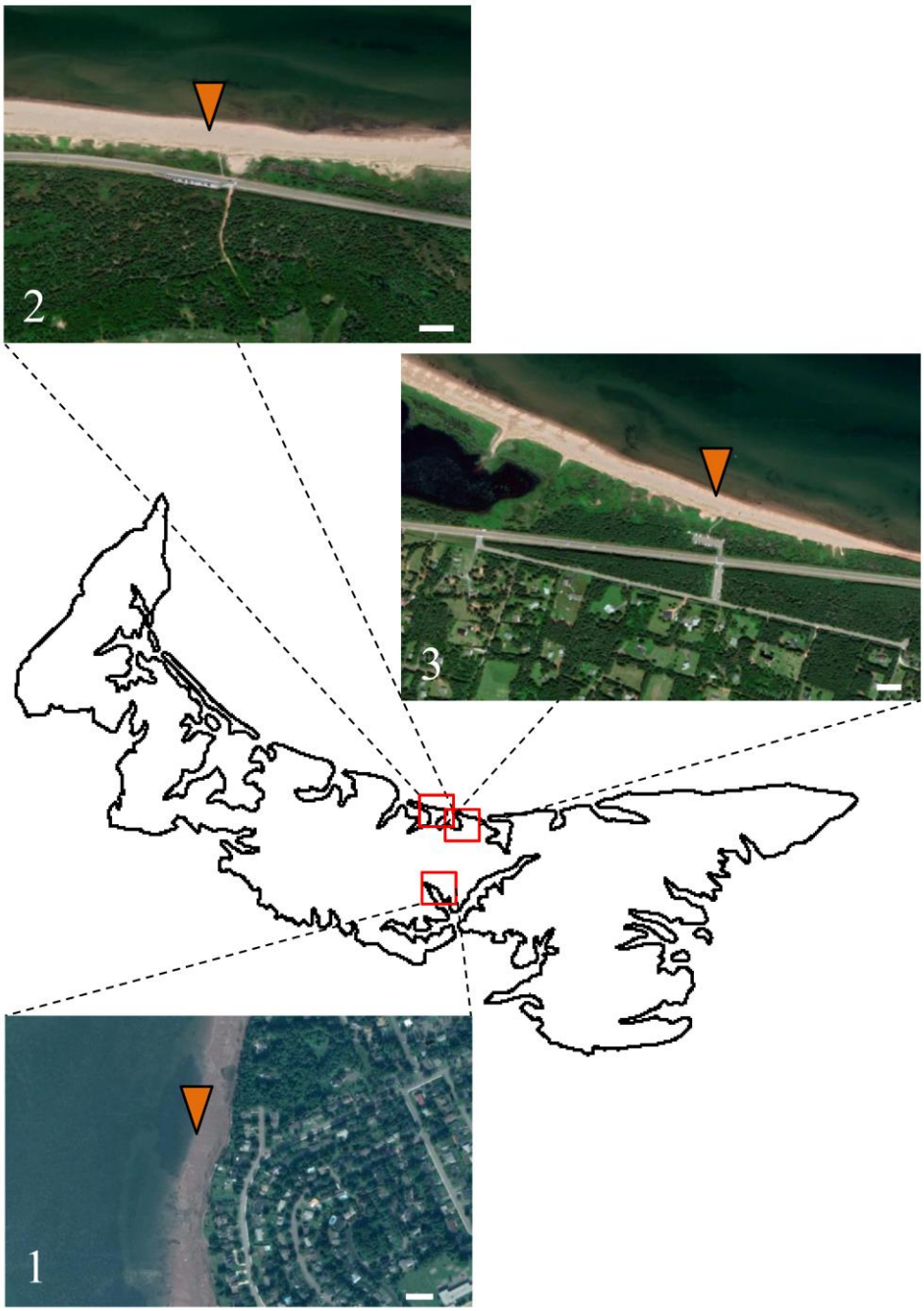

Figure 2.9: A map of PE with insets showing the three locations where samples were taken from. Inset scale bar is 50 m. Map data ©2019 Google.

To reduce the amount of seawater bacteria from the marine sediment samples, excess seawater in the samples was decanted, and 15 – 20 mL of FSS was used to wash the marine sediment. The samples were gently inverted 10 times and the washing seawater was decanted after sediment was allowed to settle. To dislodge MSB from

sediment particles, 10 mL of FSS was added to 10 mL of the washed marine sediment. The samples were vortexed for 3 mins, placed horizontally on a shaker at 400 RPM and 4ºC for 1 hr, and vortexed for additional 30 s. The supernatant was transferred to a new Falcon tube. For Locations 1 and 2, additional centrifugation at 500 × *g* for 7 mins was performed to ensure removal of large sediment particles. Since more than 84% of soil bacteria adheres to particles [34], fine sediment particles were not further removed from the supernatant, and were not removed at all for Location 3 (7-minute centrifugation was not performed). The optical density of the supernatant was measured; an $OD_{600\ nm}$ of >0.025 should be used, since lower values do not enable formation of a pellet. Therefore, a certain volume was taken from each sample based on an $OD_{600\ nm}$ that corresponds to approximately 6.68×10^6 cells/mL (based on corresponding an OD of 1 to 1×10^8 *E. coli* cells/mL). MSB suspensions were centrifuged at 6,000 × *g* for 10 mins (for Locations 1 and 2) and at 4,500 × *g* for 5 mins (for Location 3) to obtain a pellet. A summary of the parameters used for each location is presented in Table 2.2.

Table 2.2: Summary of sample collection locations, storage, and MSB pellet formation parameters.

Location	Sampling Location Coordinates	10 mL Sediment Sample Storage	FSS Storage	MSB Pellet Formation
1	46.24º N, -63.15º W	-24ºC until use	4ºC until use	Centrifugation at 500 × *g* for 7 mins followed by centrifugation at 6,000 × *g* for 10 mins
2	46.43º N, -63.19º W	-24ºC until use	4ºC until use	Centrifugation at 500 × *g* for 7 mins followed by centrifugation at 6,000 × *g* for 10 mins
3	46.43º N, -63.12º W	Collected directly from aquarium maintained at approximately 23ºC	Room temperature until use	Centrifugation at 4,500 × *g* for 5 mins

2.2.3.3 Known PE marine sediment species

To further validate the encapsulation process parameters, three known PE marine sediment species were selected from the Kerr Lab culture collection (Canada): two Gram-negative (*Marimonas polaris* and *Psychrobacter aquimaris*) and one Gram-positive (*Bacillus licheniformis*) bacteria. All species were isolated from PE marine sediments. All strains were grown on Marine Agar (BD Difco™, Fischer Scientific, USA) at room temperature for further studies. Gram-positive and Gram-negative bacteria were selected to benchmark the behavior of taxonomically diverse bacteria [313] against the processes used in this thesis.

M. polaris, *P. aquimaris*, and *B. licheniformis* were cultured in 5 mL of Marine Broth (BD Difco™, Fischer Scientific, USA) at room temperature and 200 RPM

overnight. Pellets of the three strains, corresponding to approximately 8.35×10^6 cells, were formed according to the same procedure used previously with *E. coli* and MSB.

2.2.4 Bacteria encapsulation

2.2.4.1 *Escherichia coli*

For *E. coli*, 4 mL of 1% w/v agarose (Sigma Aldrich, USA) were vortexed with the pelleted *E. coli* for 10 s and used as the dispersed phase. Mineral oil (Sigma Aldrich, USA) with 4% v/v Span® 80 nonionic surfactant (Sigma Aldrich, USA) was used as the continuous phase [96]. Two syringe pumps (Chemyx Fusion 100, USA) were used to drive the flow in the microfluidic chip (Figure 2.10). The dispersed phase was set at 5 mL/hr and the continuous phase was set at 110 mL/hr. A split junction (shown in Figure 2.10) was designed and 3D printed using Clear resin to split the continuous phase flow coming into two sides of the microfluidic chip (as previously shown in Figure 2.4), with 2 mm square channels. An aluminum heat block was built for the dispersed phase to keep its temperature at 45ºC to prevent agarose from gelling before encapsulation. The block was machined to have the same features as the agarose syringe, needle tip, tubing, and the microfluidic chip to prevent agarose gelation and maintain a stable flow. Heat was supplied through two 1 inch 50 W cartridge heaters and temperature was monitored and controlled using a thermocouple and a proportional–integral–derivative (PID) controller, respectively (all items were purchased from Omega Engineering, Canada). A pump extension was built from an aluminum rod to enable pushing the agarose syringe while being placed in the heat block. Downstream, the microbeads outlet tube was cooled using a Peltier cooler system (Amazon, Canada), with an average surface temperature of 16ºC.

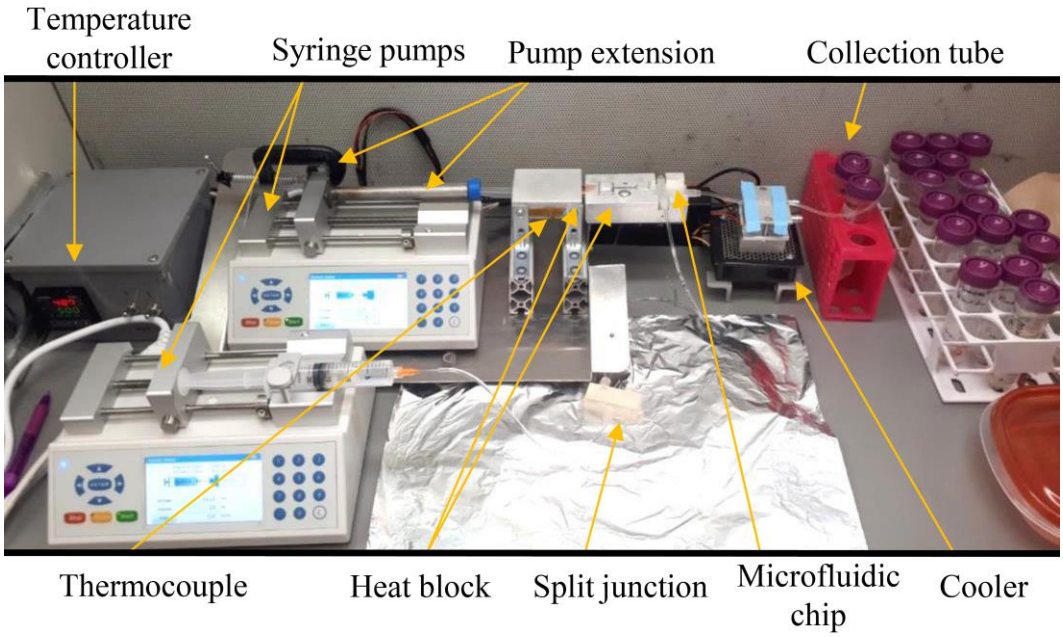

Figure 2.10: The setup used to encapsulate *E. coli* and MSB. The continuous and dispersed phase flow rates into the microfluidic chip were controlled using syringe pumps. The continuous phase was split into two using a split junction. Agarose was heated using a heat block, with the heat supplied from two cartridge heaters (not shown; fitted inside the heat block), and temperature was controlled and measured by a PID temperature controller and thermocouple, respectively. The agarose syringe was pushed using a pump extension. Microbeads were cooled down using a Peltier cooler and were collected in a tube.

After microbeads were formed and collected in a Falcon tube, microbeads were poured over a 60 µm cell strainer (pluriSelect Life Science, Germany) and washed with 10 mL of LB broth to remove mineral oil. Microbeads collected in the strainer were washed onto a 100 µm cell strainer with 10 mL of LB broth to obtain a solution of microbeads having a diameter between 60 µm and 100 µm. This solution is herein named the *E. coli* working solution (EWS). Blank agarose microbeads were prepared using the same steps as encapsulated *E. coli* microbeads, and an *E. coli* pellet was re-suspended in 4 mL of LB broth, herein named *E. coli* re-suspended solution (ERS), to serve as controls in characterization tests. Encapsulation and microbead washing were performed

aseptically in a laminar flow hood to prevent contamination. A detailed protocol for bacteria preparation and encapsulation is presented in section A.4.

For encapsulation rate evaluation, 100 µL samples of the EWS solution (each containing approximately 100 to 200 microbeads) were suspended in a 96-well plate and inspected using bright field imaging and a 20x objective (Cytation™ 5 Imaging Multi-Mode Reader, BioTek, USA).

2.2.4.2 Environmental marine sediment bacteria

For MSB, the pelleted cells were vortexed with 4 mL of agarose for 10 s. Encapsulation was performed as described above, except that the microbead washing was performed using FSS. The 10 mL solution containing microbeads with encapsulated MSB is herein named the MSB working solution (MWS). On average, the encapsulation of MSB took 25 mins, and the microbeads were washed in approximately 35 mins. Blank agarose microbeads were also prepared using the same steps outlined above to serve as a control during *in-situ* incubation and characterization tests. All solutions containing microbeads were handled using wide-mouth pipette tips to prevent clogging of pipette tips and to ensure that microbeads were not damaged during transfer. Moreover, another MSB pellet was re-suspended in 4 mL of FSS by vortexing for 10 s. Herein, this solution is referred to as MSB re-suspended solution (MRS), which resulted in the same cell density (approximately 2×10^3 cells/mL) as that of MWS when serially diluted using a ten-fold series to a 10^{-3} solution using FSS. This solution was used to compare the effect of encapsulation on MSB in characterization tests performed in this thesis.

2.2.4.3 Known PE marine sediment species

Cell pellets of *M. polaris*, *P. aquimaris*, and *B. licheniformis* were encapsulated to characterize the effect of the encapsulation process on marine bacteria. The three strains were encapsulated by vortexing their respective pellets in 4 mL of agarose, each of which was used in the previously outlined encapsulation process. However, the formed microbeads were washed with 10 mL of Instant Ocean® (Instant Ocean, USA), which was prepared in sterile DI water then further diluted to a 50% solution using sterile DI water. Pellets of each strain were re-suspended in 4 mL of 50% Instant Ocean®, which was then diluted using a ten-fold series to a 10^{-3} solution using 50% Instant Ocean®. Both sets of solutions were stored in test tubes (25 mm × 150 mm) with plastic caps that allow gas exchange at room temperature until further processing. Another set of encapsulated and re-suspended samples of the three species was prepared using 10% Marine Broth (BD Difco™, Fischer Scientific, USA). The encapsulated and re-suspended bacterial samples were stored at room temperature on a rocker for the required duration of testing.

2.2.5 Cell survival and viability assessment

2.2.5.1 PrestoBlue®

To determine if cells survive the encapsulation process, 10 µL of 40 µg/mL PrestoBlue® (ThermoFisher, USA) cell viability reagent in 1× phosphate-buffered saline (PBS) (Sigma Aldrich, USA) was added to the wells of 96-well multi-well plates (0.37 mL, Falcon® 96-well Clear Microplate, Corning Inc., USA) containing 90 µL of sample prepared on each reading day. PrestoBlue® contains resazurin, a non-toxic [314] and non-fluorescent dye, which is reduced to resorufin, a bright fluorescent dye, by the metabolic activities of living cells [91,142]. Samples include: EWS compared to blank microbeads in LB broth, ERS compared to LB broth, MWS compared to blank microbeads in FSS, and MRS compared to FSS, all of which were left undisturbed on the bench at room temperature for the analysis duration. Data from blank samples was subtracted from the data of their respective samples containing cells. After addition of PrestoBlue® to microbial samples in multi-well plates, samples were incubated for 1 hr at room temperature. Fluorescence readings were measured using a SpectraMax M5^{e} spectrophotometer (Molecular Devices, USA) using excitation/emission wavelengths of 560/590 nm. Higher fluorescence intensities were correlated to more viable cells [142,148]. The encapsulation process and cell survival determination using PrestoBlue® were performed four times with *E. coli* to ensure the repeatability of the encapsulation process.

2.2.5.2 Live/Dead bacterial staining

A Live/Dead bacterial staining kit (PromoCell, Germany) was used to assess cell viability of encapsulated cells. Live and dead cells were stained with DMAO, a green,

cell-permeable fluorescent dye detected using a green fluorescence protein (GFP) filter cube (465 nm light emitting diodes (LED)). Ethidium homodimer III (EthD-III), a red fluorescent dye detected using a Texas Red filter cube (590 nm LED), only stains dead bacteria having damaged cell membranes. The dye mixture was prepared according to the manufacturer's method by mixing one volume of DMAO, two volumes of EthD-III, and 8 volumes of 0.85% NaCl. For each 100 µL of bacterial sample, 1 µL of the dye mixture was added, and 15 mins were allowed for sample incubation at room temperature. This prepared a 100x dye. A 1x dye was prepared by diluting 1 µL of the 100x dye in 100 µL of 0.85% NaCl. Some samples were fluorescently-imaged using Cytation™ 5 Imaging Multi-Mode Reader, while others were imaged using Revolve 4 microscope (Echo Inc., USA) in the upright position. Viability was calculated as the percentage of live cells (i.e. (live cell count/total cell count) x 100%) based on three images taken for each sample.

2.2.5.3 DAPI

MSB cells were stained using 4′,6-diamidino-2-phenylindole dihydrochloride (DAPI) (Sigma Aldrich, USA) [84,147], a blue fluorescent dye that is cell-permeable and stains nucleic deoxyribonucleic acid (DNA) [315]. The dye was prepared by adding 2 mL of sterile DI water to 10 mg of DAPI powder to make a 5 mg/mL stock solution. An intermediate solution was prepared by adding 2 µL of the stock solution to 100 µL of sterile DI water, resulting in a concentration of 0.1 mg/mL. The stain solution was prepared by adding 1 µL of the intermediate solution to 1 mL of sterile DI water, resulting in a 0.1 µg/mL solution. Stained cells were observed using Cytation™ 5 equipped with a DAPI filter cube (365 nm LED).

2.2.6 Material biocompatibility

To test the biocompatibility of the plastic polymers and stainless steel used to construct the MD Pods and microfluidic chip, approximately 2 mm^3 pieces of the polymers and approximately 5 mm long stainless steel shavings (SSS) were autoclaved. The plastic polymers were Clear cured resin (Formlabs, USA), denoted as Polymer A (used to fabricate the microfluidic chip and the split junction), Dental LT cured resin (Formlabs, USA), denoted as Polymer B (used to fabricate prototypes of the MD Pod as illustrated in Appendix B), and ABS filament (Zortrax, Poland), denoted as Polymer C (used to fabricate the F and S-MD Pods). Stainless steel was used to fabricate the M-MD Pods.

For biocompatibility assessment using PrestoBlue®, two pieces of each material were aseptically added to each 1 mL of sample in a tube, and five tubes were prepared for readings taken over five days to maintain the concentration of material:sample constant (one tube was used per day; see Figure 2.11). All tubes were left undisturbed on the bench at room temperature. Samples used were ERS, MRS, LB broth, and FSS. On each reading day, four 90 µL samples were taken from each sample tube and placed in a 96-well plate and 10 µL of PrestoBlue® was added to all wells. Fluorescence readings were taken using the same method used for cell survival measurement.

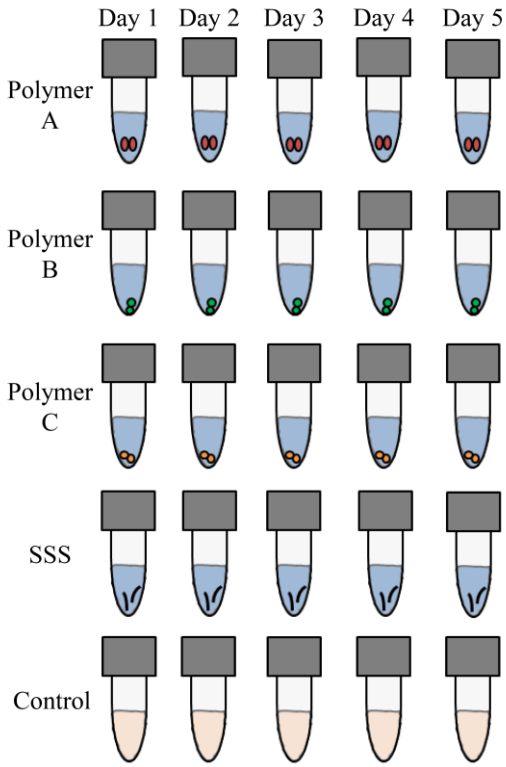

Figure 2.11: An illustration of the sample preparation for material biocompatibility assessment. Tubes were prepared to observe the effect of three plastic polymers (Clear resin (Polymer A), Dental LT resin (Polymer B), and ABS (Polymer C)) and SSS on the cell survival of *E. coli* and MBS using PrestoBlue® over five days.

Additionally, the biocompatibility of four plastic polymers was correlated to *E. coli* cell viability using the Live/Dead assay. Four polymers were tested: Clear (Polymer A), Dental LT (Polymer B), cured Tough resin (Formalbs, USA) (Polymer C), and ABS (Polymer D). One piece (approximately 2 mm^3) of each autoclaved photopolymer was added to each micro-well containing 100 µL of the EWS solution, with LB broth as the control. 1 µL of the DMAO/EthD-III dye mixture was added. The same samples in the wells were observed over 5 days in the presence of these polymers.

2.2.7 Cell migration across the MD Pod

To ensure that samples loaded in the MD Pod did not get contaminated by microbes existing in the environment surrounding the MD Pod, the MD Pod was tested for cell migration across the PCTE membranes. Each MD Pod type was tested for cell migration and was aseptically loaded with approximately 50% of its internal volume with FSS (F-MD Pods were loaded with 1.5 mL, S-MD Pods were loaded with 750 μL, and M-MD Pods were loaded with 1 mL). Two other membrane materials, polyethersulfone (PES) (47 mm diameter and 0.03 μm pore size) and nylon (47 mm diameter and 0.1 μm pore size) (SterliTech, USA), were also inspected for cell migration under the same conditions as PCTE. After loading, the MD Pods were transported from the laminar flow hood to the incubation environment using petri dishes. The MD Pods were buried under approximately 5 cm of marine sediment and incubated for three days unless otherwise stated. Incubation was performed either in the sediment box or in the aquarium (see Table 2.3), according to the samples to be incubated in the MD Pods after verification of no cell migration.

Table 2.3: Cell migration test parameters.

Test #	MD Pods Used	Membranes Used	Incubation Conditions	Additional Information
1	1 × F-MD Pod 2 × S-MD Pod	Non-autoclaved PCTE	Sediment box at 4ºC	MD Pods were closed by needle tips (see Figure B.1(l))
2	2 × F-MD Pod 2 × S-MD Pod	Non-autoclaved PCTE	Sediment box at 4ºC	
3	5 × S-MD Pod	Autoclaved PCTE	Sediment box at room temperature	Sediment box had a lot of growth
4	4 × S-MD Pod 1 × M-MD Pod	Autoclaved PES	Sediment box at room temperature	Sediment box had a lot of growth
5	3 × S-MD Pod 1 × M-MD Pod	Autoclaved nylon	Sediment box at room temperature	Sediment box had a lot of growth
6	5 × M-MD Pod	Autoclaved PCTE	Aquarium at 23ºC	MD Pods were assembled over O-rings to prevent membrane tears
7	5 × S-MD Pod	Autoclaved PCTE	Aquarium at 23ºC	
8	6 × S-MD Pod	3 MD Pods with autoclaved PCTE and 3 MD Pods with 70% IPA-sterilized PCTE (10 mins contact time)	Aquarium at 23ºC	The O-ring dispenser was used for assembling all MD Pods.
9	1 × S-MD Pod 1 × F-MD Pod	Autoclaved PCTE	On the bench	• Filled with sterile DI water. • Incubated for 2 days.
10	1 × S-MD Pod 1 × F-MD Pod	Autoclaved PCTE	Aquarium at 23ºC	• Filled with sterile DI water. • Incubated for 2 days.

Following incubation, the MD Pods were gently unburied and placed on sterile petri dishes. The rubber band and the casing were carefully removed, then the MD Pod was gently washed in a sterile DI water beaker. The MD Pod was transferred again to a new petri dish. The top first O-ring was carefully removed, and the second O-ring and the membrane were carefully rolled from one side to the other, making sure that no parts

touch the MD Pod body. The MD Pod contents were aseptically removed and placed in 15 mL Falcon tubes. For each MD Pod, 100 µL samples were plated onto three dMA plates using cell spreaders. Additionally, 100 µL FSS samples (and sterile DI water for Tests # 9 and 10) were plated onto three dMA plates to serve as the control. Observed growth on the MD Pod content plates was compared to growth on the control plates to ensure no cell migration occurred across the MD Pods. This procedure was applied for unloading all MD Pods used in this thesis. A detailed protocol for MD Pod loading, unloading, and other related information is presented in Appendix E.

2.2.8 MD Pod in-situ incubation

MD Pod *in-situ* incubation was performed using samples of the MWS and MRS solutions, with blank microbeads and FSS acting as controls, respectively. Each MD Pod was loaded with approximately 50% liquid as previously described and was tagged according to the solution it contained. After that, each MD Pod was gently buried under approximately 5 cm of sediment in an incubation environment (Figure 2.12) and incubated for a certain period of time (Table 2.4).

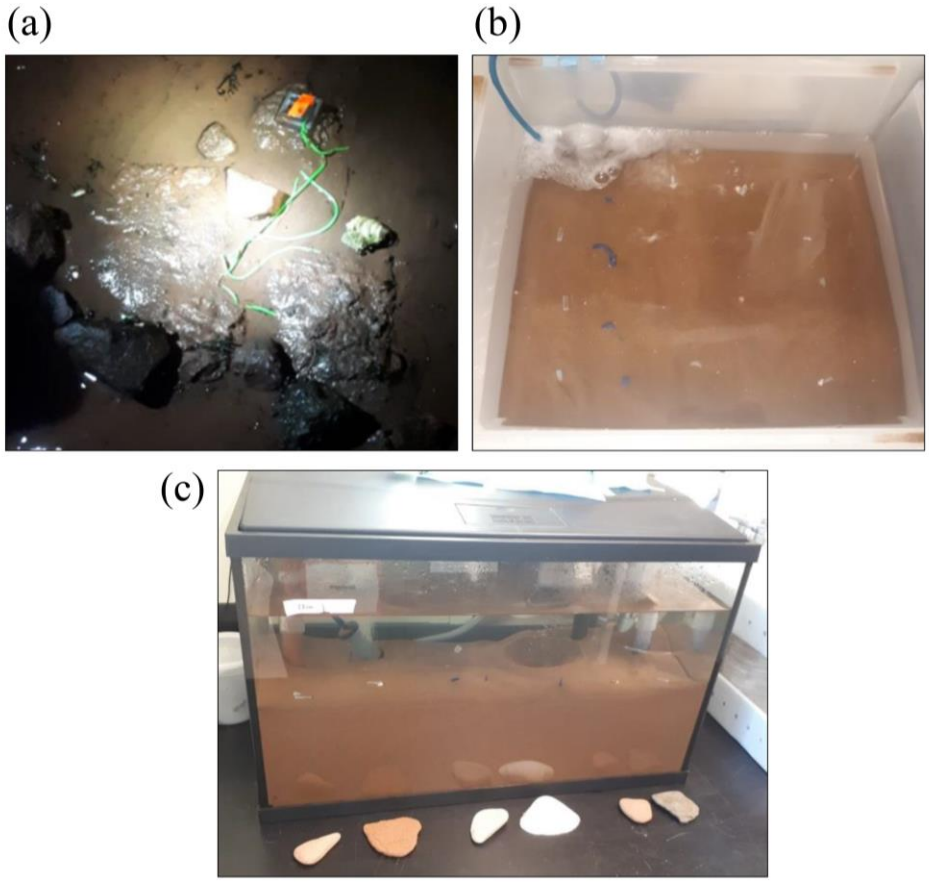

Figure 2.12: Incubation setups used for MD Pod *in-situ* incubation. (a) MD Pods were incubated in the intertidal zone at Location 1. The MD Pods were buried under sediment and tied together to a dive weight to prevent their dislocation during incubation. (b) The sediment box containing sediment collected from Location 2. A bubbler is shown in the top left corner to aerate the seawater in the box. Several MD Pod tags are shown at the sediment surface. (c) The aquarium containing sediment collected from Location 3. It was equipped with an air bubbler, two sediment aerators, a filter, a heater, and a thermometer. Several MD Pod tags are shown at the sediment surface.

Table 2.4: MD Pod *in-situ* incubation runs and parameters.

Run #	MSB Sampling Location	Incubation Environment	Incubation Duration	Samples Incubated	Viability Assays	Plated Dilutions	Plate Incubation Conditions	Additional Information
1	Location 1	Location 1 (Nov 6 – 24, 2018)	19 days	• MWS: 3 × F-MD Pod and 2 × S-MD Pod. • MRS: 3 × F-MD Pod and 2 × S-MD Pod. • Blank beads: 2 × F-MD Pod and 1 × S-MD Pod. • FSS: 2 × F-MD Pod and 1 × S-MD Pod.	L/D[a]	• MWS: 10^0 – 10^{-2} • MRS: 10^0 – 10^{-4} • Blank beads: 10^0 • FSS: 10^0	Room temperature	• All MD Pods were closed by needle tips (see Figure A.2.1(l)). • MD Pods were sealed using 4 O-rings.

Table 2.4 *(continued)*

Run #	MSB Sampling Location	Incubation Environment	Incubation Duration	Samples Incubated	Viability Assays	Plated Dilutions	Plate Incubation Conditions	Additional Information
2	Location 2	Sediment box at 4ºC	21 days	• MWS: 3 × F-MD Pod and 3 × S-MD Pod. • MRS: 3 × F-MD Pod and 3 × S-MD Pod. • Blank beads: 2 × F-MD Pod and 2 × S-MD Pod. • FSS: 2 × F-MD Pod and 2 × S-MD Pod.	• PB[b] • L/D	• MWS: 10^{0} – 10^{-2} • MRS: 10^{-1} – 10^{-3} • Blank beads: 10^{0} • FSS: 10^{0}	Room temperature	• PB: well plate was incuba-ted at 30ºC through-out the reading duration.

Table 2.4 *(continued)*

Run #	MSB Sampling Location	Incubation Environment	Incubation Duration	Samples Incubated	Viability Assays	Plated Dilutions	Plate Incubation Conditions	Additional Information
3	Location 2	Sediment box at 4ºC	16 days	• MWS: 4 × M-M D Pod. • MRS: 4 × M-M D Pod. • Blank beads: 3 × M-M D Pod. • FSS: 3 × M-M D Pod.	• PB • L/D	• MWS: 10^{0} • MRS: 10^{-1} – 10^{-3} • Blank beads: 10^{0} • FSS: 10^{0}	Room temperature and 4ºC	• Sediment box shaken twice a day, 20× each. • Autoclaved membranes • More sediment included with MSB. • PB plates and culture plates incubated at room temperature and at 4ºC. • L/D: using EthD-III and DAPI.

Table 2.4 *(continued)*

Run #	MSB Sampling Location	Incubation Environment	Incubation Duration	Samples Incubated	Viability Assays	Plated Dilutions	Plate Incubation Conditions	Additional Information
4	Location 3	Aquarium maintained at 23ºC	10 days	• MWS: 6 × S-MD Pod. • MRS: 6 × S-MD Pod. • Blank beads: 4 × S-MD Pod. • FSS: 4 × S-MD Pod.	-	• MWS: 10^{0} – 10^{-1} • MRS: 10^{-2} – 10^{-3} • Blank beads: 10^{0} • FSS: 10^{0}	Room temperature	• O-ring dispenser was used to assemble all the MD Pods. • Autocla-ved membra-nes.

Table 2.4 *(continued)*

Run #	MSB Sampling Location	Incubation Environment	Incubation Duration	Samples Incubated	Viability Assays	Plated Dilutions	Plate Incubation Conditions	Additional Information
5	Location 3	Aquarium maintained at 23ºC	10 days	• MWS: 3 × F-MD Pod. • MRS: 3 × F-MD Pod. • Blank beads: 2 × F-MD Pod and 1 × S-MD Pod. • FSS: 2 × F-MD Pod and 1 × S-MD Pod.	-	• MWS: 10^0 – 10^{-1} • MRS: 10^{-2} – 10^{-3} • Blank beads: 10^0 • FSS: 10^0	Room temperature	• Autoclaved membranes. • O-ring dispenser not used for the S-MD Pods.

[a]L/D: Live/Dead.
[b]PB: PrestoBlue®.

After incubation, MWS and MRS solutions obtained from each MD Pod were serially diluted from 10^0 to 10^{-4}. Then, triplicate 100 µL of certain dilutions from each MD Pod (see Table 2.4) were plated onto three dMA plates and incubated at room temperature for three weeks. All remaining solutions obtained from the incubated MD Pods were directly frozen at -24ºC. To determine the preliminary success of the MD Pod *in-situ* incubation, growth of microbes obtained from the incubated MD Pod solutions was compared to growth obtained through traditional plating through observation of colony counts. Traditional plating was performed by spreading triplicate 100 µL samples of MWS and MRS on dMA plates, with plates of blank microbeads and FSS acting as controls, before MD Pod *in-situ* incubation. Additionally, cell viability assessment was performed using PrestoBlue® and Live/Dead assays according to the procedures explained previously. Finally, to determine if microbial growth was enhanced by changing the temperature of plate incubation, duplicate plates obtained from Run # 3 (traditional plating samples and samples obtained from after incubation) as well as duplicate samples of well plates assayed using PrestoBlue® were incubated at room temperature and at 4ºC.

2.2.9 Cell diversity analysis

2.2.9.1 Background information

To analyze the diversity of microbial species existing in the MSB samples before and after *in-situ* incubation, DGGE was used. DGGE is an approach that has been extensively used for the determination of genetic diversity in complex microbial populations [316–320].

In DGGE, equal-length DNA fragments are separated in a gel based on their different base pair (bp) sequences [321]. Bp is a unit demonstrating the hydrogen bonds connecting two nitrogenous bases, such as thymine (T) to adenine (A) and guanine (G) to cytosine (C) [322], resulting in the helical structure of DNA [323]. In ribonucleic acid (RNA), uracil (U) takes the place of T [324]. A sequence is the order of bps in DNA and RNA, resulting in the different genes and alleles (variations of a gene) of organisms. Moreover, DNA is composed of two polynucleotide strands (Figure 2.13(a)), with each nucleotide composed of a sugar molecule (either deoxyribose in DNA or ribose in RNA), a phosphate group, and a nitrogenous base (Figure 2.13(b)) [324]. Each strand has a side called the 5’-end, in which a phosphate is attached to the 5'-carbon atom of the nucleotide, and another side called the 3’-end, in which a hydroxyl group (-OH) is attached to the 3'-carbon atom of the nucleotide. The two strands in DNA are antiparallel, meaning that the 5’-end of one strand is paired with the 3’-end of the second strand and vice versa (Figure 2.13(a)) [322].

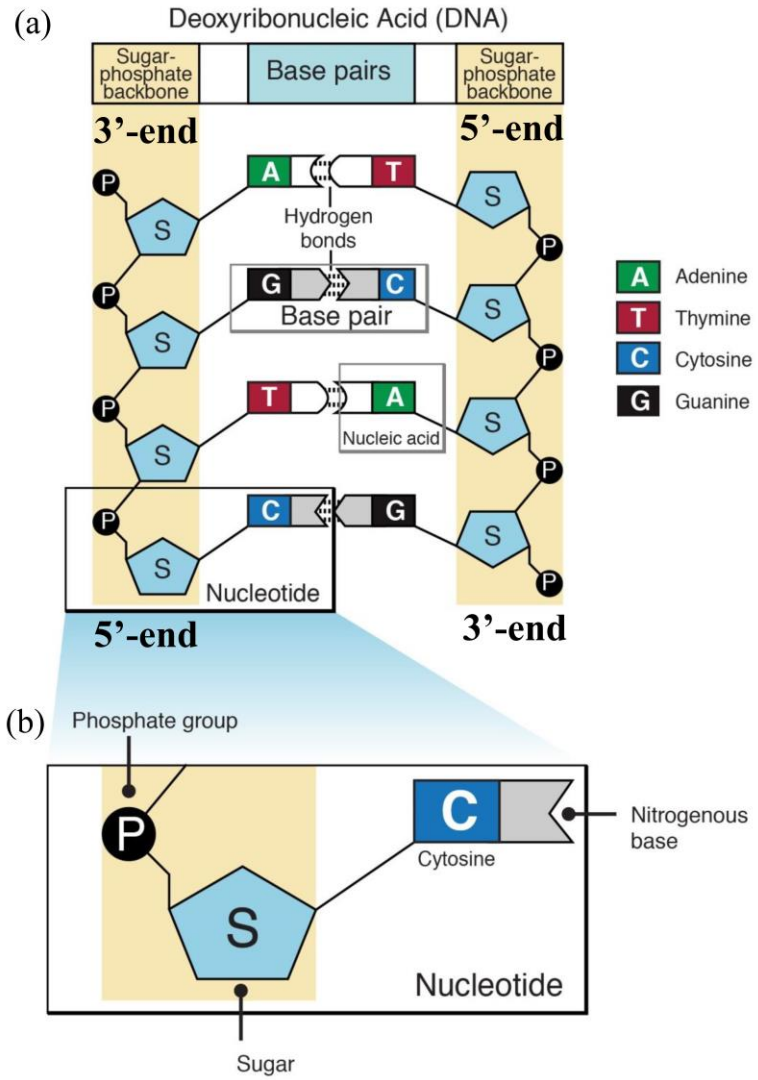

Figure 2.13: The strands composing DNA. (a) Each strand is composed of nucleotide units (b), made up of a phosphate group, a sugar, and a nitrogenous base. Nitrogenous bases are held together through hydrogen bonds, composing base pairs. A 3'-end is paired with a 5'-end and vice versa. Images are courtesy of National Human Genome Research Institute, https://www.genome.gov/.

DGGE employs a gel with an increasing gradient of chemical denaturants, typically urea and formamide [325]. By electrophoresis, double-stranded DNA passes through the gradient. Based on the GC content and the sequence of each DNA molecule, the DNA will denature at a particular denaturant concentration in the gradient gel [325]. DNA containing a higher GC content will migrate further down the gel. Moreover, upon application of heat, which is part of DGGE, double-stranded DNA begins to 'melt,' or

form single-stranded DNA [326]. Single-stranded DNA migrates slowly in the DGGE gel compared to double-stranded DNA, due to the former's interactions with the gel through unbonded nucleotides [325]. Therefore, as double-stranded DNA begins to denature and form a branched structure, it retards in the gel, creating bands that could be visualized after electrophoresis (Figure 2.14). If electrophoresis is continued, the denaturing DNA will continue to branch out, resulting in single strands of DNA that do not form clear bands in the gel. Hence, DNA should be 'clamped' prior to performing DGGE, and GC-rich 'clamps' are usually used because they remain base-paired during denaturation [325]. A GC-clamp is placed adjacent to the highest DNA melting region, resulting in denaturation only towards the GC-clamp. Therefore, no multiple melting directions would occur, which might cause smears or multiple bands in the gel [325], and nearly 100% of the sequence variations existing in a microbial population is detected [321].

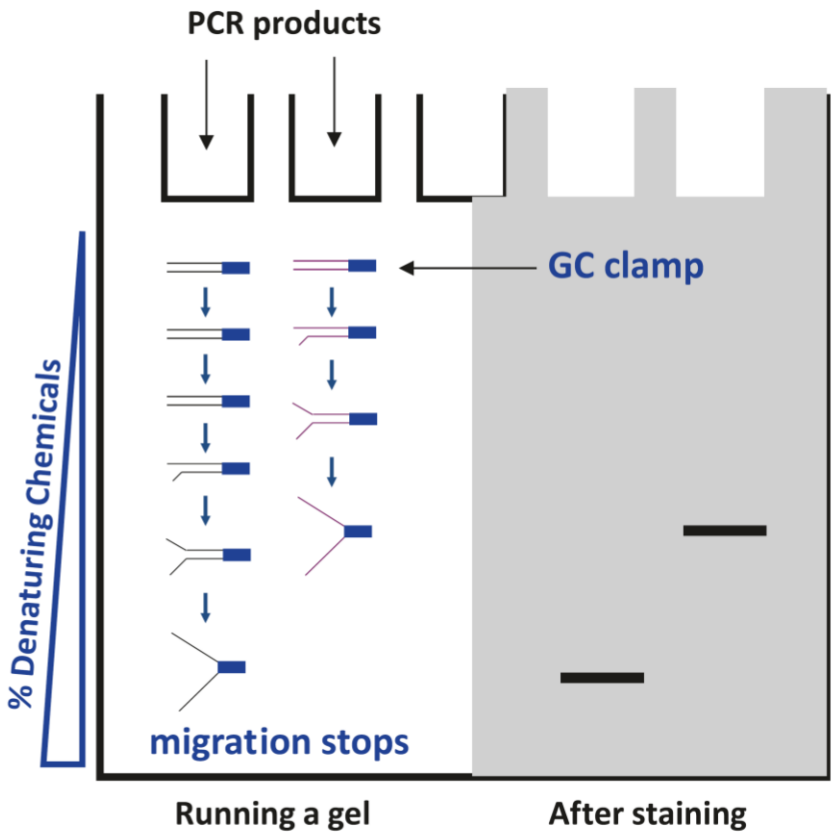

Figure 2.14: A DGGE gel showing DNA denaturing when running the gel. A GC-clamp aids in stopping DNA migration across the gel, containing an increasing gradient of denaturant chemicals, as denaturation is complete. Bands are observed after staining the gel at the locations where DNA migration stopped. Reprinted by permission from Copyright Clearance Center Inc.: Springer Nature, Ref. [327], © 2017.

Before performing DGGE, the DNA of environmental samples, also called template DNA, was amplified using PCR. PCR is a technique that enables the direct amplification and generation of a considerable amount of specific DNA fragments, or amplicons [328,329]. DGGE commonly uses equal-length amplicons of the 16s ribosomal RNA (rRNA) gene [325]. The 16s rRNA gene is widely used for deducing phylogentic relationships among prokaryotes [330] due to its ease of isolation, existence in all self-replicating systems [331], and minute evolutionary changes [330].

In PCR, a specific DNA region is amplified, in this thesis, the 16s rRNA gene. A PCR can amplify even a single DNA molecule [332], making this method compatible

with diversity analysis of microbial communities that include few cells of certain species. The PCR process starts by DNA denaturation, by which the DNA strands separate through application of heat with a temperature above the melting point of the target DNA (Figure 2.15) [333]. The second step is called annealing, in which short DNA fragments with a pre-defined sequence, called primers, bind to target DNA and specify the DNA region to be amplified [333]. This occurs upon reduction of heat, and the primers only bind to complementary sequence regions in the DNA strand, i. e. A to G and C to T [333]. Therefore, 'forward' and 'reverse' primers are used [327]. Finally, the primers are extended to match the DNA strand sequence through the activity of a DNA polymerase. This polymerase allows nucleotides (A, T, G, and C, previously added to the reaction mix) to bind and form the PCR product upon temperature increase [333]. These steps are repeated in cycles, with each cycle doubling the amount of DNA molecules.

DNA amplification is greatly affected by the choice of primer sequences. Usually, primers that are 20 – 24 nucleotides-long are selective enough for specific DNA fragments [332]. A higher annealing temperature and longer primers can also contribute to a more selective amplification [332]. Universal primers are commonly used to target specific genes, and in DGGE, one of the primers must have a GC-clamp attached to the 5'-end [327] to stop DNA denaturation in the gel. A GC-clamp is typically 35 – 40 nucleotides-long [325]. The GC-clamp is added to the target DNA in a process called nested PCR. In this process, a set of two primers amplifies the DNA template, and a second set of primers reduces and equalizes the length of the DNA fragments produced by the first PCR, amplifies them, and adds the GC-clamp, creating a more target-sensitive product than that produced by a single PCR [334] due to the shorter fragments produced.

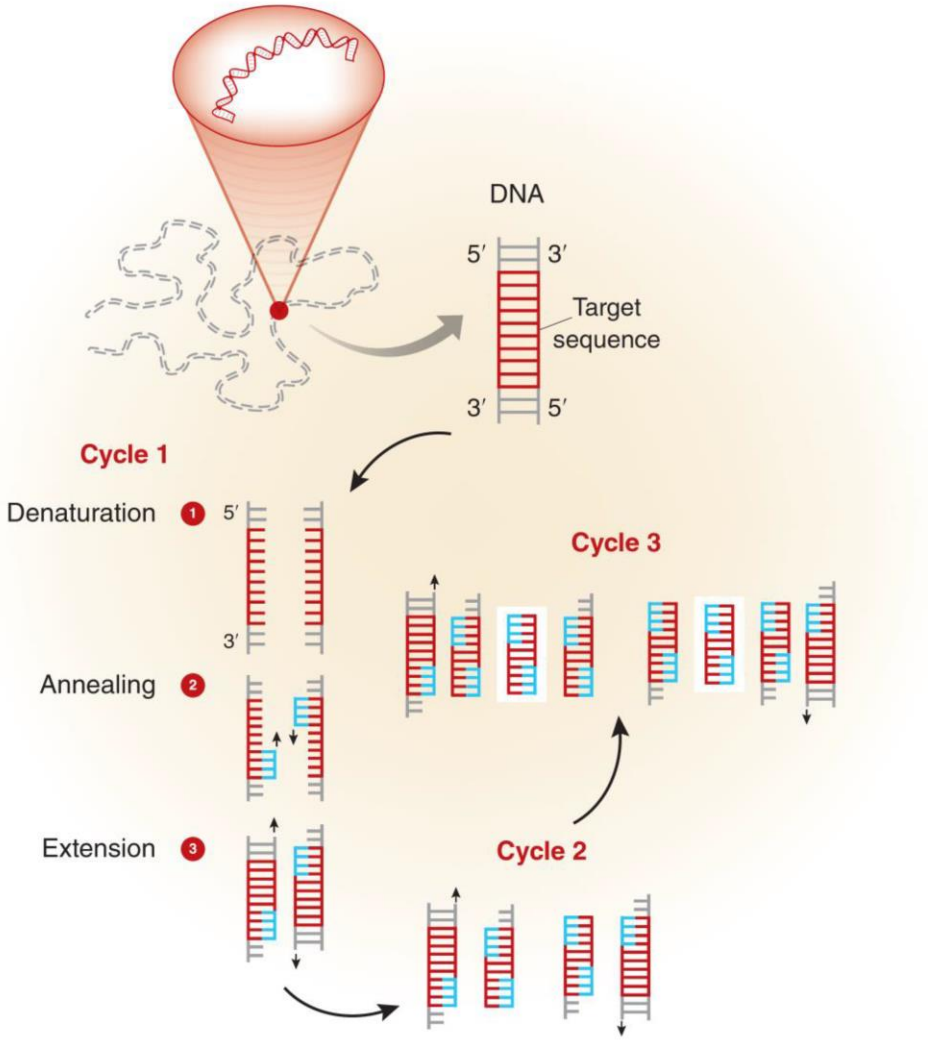

Figure 2.15: Schematic of the polymerase chain reaction (PCR) principle. A target sequence in the DNA molecule (red) is denatured through application of heat. In the annealing step, forward and reverse primers (blue) bind to specific complimentary regions of the denatured DNA strands. The primers DNA fragments are then extended through the action of a polymerase that allows nucleotides to bind to the DNA strands upon application of heat. Repetition of these steps, represented as cycles, results in generating numerous, identical DNA fragments. Reprinted from Ref. [333], © 2013, with permission from Elsevier.

2.2.9.2 PCR parameters

To perform PCR, DNA was extracted from 100 µL of sample according to the manufacturer's protocol (DNeasy Ultraclean Microbial Kit, Qiagen, Germany) [335]. The DNA template was then amplified using primer sets that were chosen based on literature

citing their use for DGGE analysis of MSB communities. Primer Set A [336] was composed of 27F (5'-AGAGTTTGATCMTGGCTCAG-3') and 1525R (5'-AAGGAGGTGATCCAGCC-3') [337] followed by a nested PCR using 27F-GC (5'-CGCCCGCCGCGCGCGGCGGGCGGGGCGGGGGCACGGGGGGAGAGTTTGATCMTGGCTCAG-3') [338] and 534R (5'-ATTACCGCGGCTGCTGG-3') [320], in which F denotes 'forward' and R denotes 'reverse.' Primer Set B was composed of 27F and 1492R (5'-GGTTACCTTGTTACGACTT-3') [339,340] followed by a nested PCR using 357F-GC (5'-CGCCCGCCGCGCGCGGCGGGCGGGGCGGGGGCACGGGGGGCCTACGGGAGGCAGCAG-3') and 907R (5'-CCGTCAATTCCTTTGAGTTT-3') [341]. Primer Set C was composed of 1070F (5'-ATGGCTGTCGTCAGCT-3') and GC-clamped 1392R (5'-CGCCCGCCGCGCCCCGCGCCCGGCCCGCCGCCCCCGCCCCACGGGCGGTGTGTAC-3') [320]. All primers were purchased from Eurofins Genomics (Canada). Nested PCRs were performed using a 10^{-2} dilution of the initial PCR amplification product, diluted in DI water.

Each PCR reaction mixture was prepared by adding 8.25 μL of DI water, 12.5 μL of EconoTaq® PLUS GREEN 2X Master Mix (Lucigen, USA) containing Mg^{2+} ions, and 1.5 μL of each 10 μM F and R primer, resulting in a 23.75 μL mixture. A master mix is usually prepared to accommodate the total number of reactions to be performed (to have equal amounts of reagents used in each reaction) [328]. 1.25 μL of DNA template was added to each 23.75 μL of master mix. The reaction mixture components were added in the outlined order while over ice, and the final mixture was voretexed. The reaction mixture was then placed in a thermal cycler (Mastercycler™ Nexus Thermal Cycler,

Eppendorf™, Germany) set at the conditions outlined in Table 2.5. PCR amplification was assessed by analyzing 3 μL of each reaction on a 1% agarose gel which was run at 115 V for 45 mins. The GeneRuler Ladder Mix (Fisher Scientific, USA) (3 μL of 0.5 μg/μL) was used as a molecular weight marker on each gel [341]. DNA was visualized by ethidium bromide (OmniPur®, EMD Millipore, USA) (0.5 μg/mL). Imaging of gels was performed using a BioSpectrum® AC Imaging System (UVP, USA) using a 570 – 640 nm ethidium bromide filter and transillumination at 365 nm. Images were captured using VisionWorks™ LS Image Acquisition and Analysis Software (UVP, USA).

Table 2.5: Thermal cycler conditions used for PCR using three primer sets.

	Primer Set A			**Primer Set B**			**Primer Set C**		
Initial PCR	*27F and 1525R*			*27F and 1492R*			*1070F and GC-1392R*		
	Time	Temperature (ºC)	Number of Cycles	Time	Temperature (ºC)	Number of Cycles	Time	Temperature (ºC)	Number of Cycles
Denaturation	3 min	95	1	2 min	95	1	5 min	94	1
Annealing	45 s	95	30	30 s	94	30	30 s	94	27
	1 min	54		30 s	52		1 min	65 – 55[c]	
	1.5 min	72		1.5 min	72		3 min	72	
Final Extension	10 min	72	1	5 min	72	1	5 min	72	1
Nested PCR (using a 10^{-2} dilution of the initial PCR product)	*27F-GC and 534R*			*357F-GC and 907R*			-		
	Time	Temperature (ºC)	Number of Cycles	Time	Temperature (ºC)	Number of Cycles			
Denaturation	5 min	95	1	5 min	95	1			
Annealing	1 min	95	10 then	1 min	95	20 then			
	1 min	66[a]		40 s	66[b]				
	2 min	72		40 s	72				
	1 min	95	20	1 min	95	15			
	1.5 min	56		40 s	56				
	2 min	72		40 s	72				
Final Extension	7 min	72	1	30 min	72	1			
Final PCR Amplicon Length	507 bps			550 bps			322 bps		

[a]Decreased by 1ºC per cycle.
[b]Decreased by 0.5ºC per cycle.
[c]Decreased by 0.5ºC every cycle for 20 cycles; last 7 cycles were at 55ºC.

2.2.9.3 DGGE experimental setup

To prepare the gel used for DGGE, low (0%) and high (100%) denaturant solutions were prepared. For a 100 mL 0% solution, 2 mL of 50x tris-acetate-EDTA (TAE) buffer, 27 mL of 30% acrylamide/N, N′methylenebisacrylamide solution (37.5:1 acrylamide:N, N′methylenebisacrylamide) (Sigma Aldrich, USA), and 71 mL of DI water were mixed. For a 100 mL 100% solution, 42 g of urea (VWR, USA) was dissolved in 40 mL of formamide (Sigma Aldrich, USA) in a volumetric flask over a hotplate. 2 mL of 50x TAE buffer and 27 mL of 30% acrylamide/N, N′methylenebisacrylamide were added. The volumetric flask was filled up to the 100 mL mark using DI water. The 0% and 100% solutions were stored in the dark at 4ºC. The 100% solution could crystallize upon storage. Therefore, it was heated up in a warm bath before use.

A 6% acrylamide gel (in which the gradient is the denaturant) was used to perform DGGE, since this gradient provides separation of 300 – 1000 bps [342]; the amplicons produced through PCR lie in this range. To make the 6% gradient gel, 30% and 70% solutions were prepared from the 0% and 100% solutions. To prepare 25 mL of the 30% solution, 17.5 mL of 0% and 7.5 mL of 100% were mixed. To prepare 25 mL of the 70% solution, 5 mL of 0% and 20 mL of 100% were mixed. DGGE was performed using Bio-Rad DCode^{TM} Universal Mutation Detection System (Bio-Rad Laboratories, USA), which was operated according to the manufacturer's recommendations [342]. 5 µL of each of N,N,N',N'-tetramethylethylenediamine (TEMED) (VWR, USA) and 10% ammonium persulfate (APS, prepared as 0.1 g in 1 mL DI water) (VWR, USA) were added to every 1 mL of denaturant solution used to make the DGGE gel. Once added, TEMED and APS cause the acrylamide/N, N′methylenebisacrylamide solutions to

polymerize in approximately 7 – 10 mins. Therefore, they were added directly before casting each solution. Moreover, APS has to be prepared fresh and should be used within a week if stored at 4ºC. To cast the gel, 1 mL of the 0% solution was loaded first into the core and was allowed to polymerize for 10 mins. Next, the 30% and 70% solutions (to which TEMED and APS were just added) were loaded separately in 25 mL syringes and injected into the core using the manufacturer's gradient wheel (Figure 2.16). The gel was allowed to polymerize for 45 mins. Lastly, a comb was inserted between the glass plates in the core to produce wells in which samples could be placed later. To stack up the gel, 4 mL of the 0% solution was loaded evenly to the sides of the comb using a pipette tip. The gel was then left to polymerize for 1 – 2 hrs.

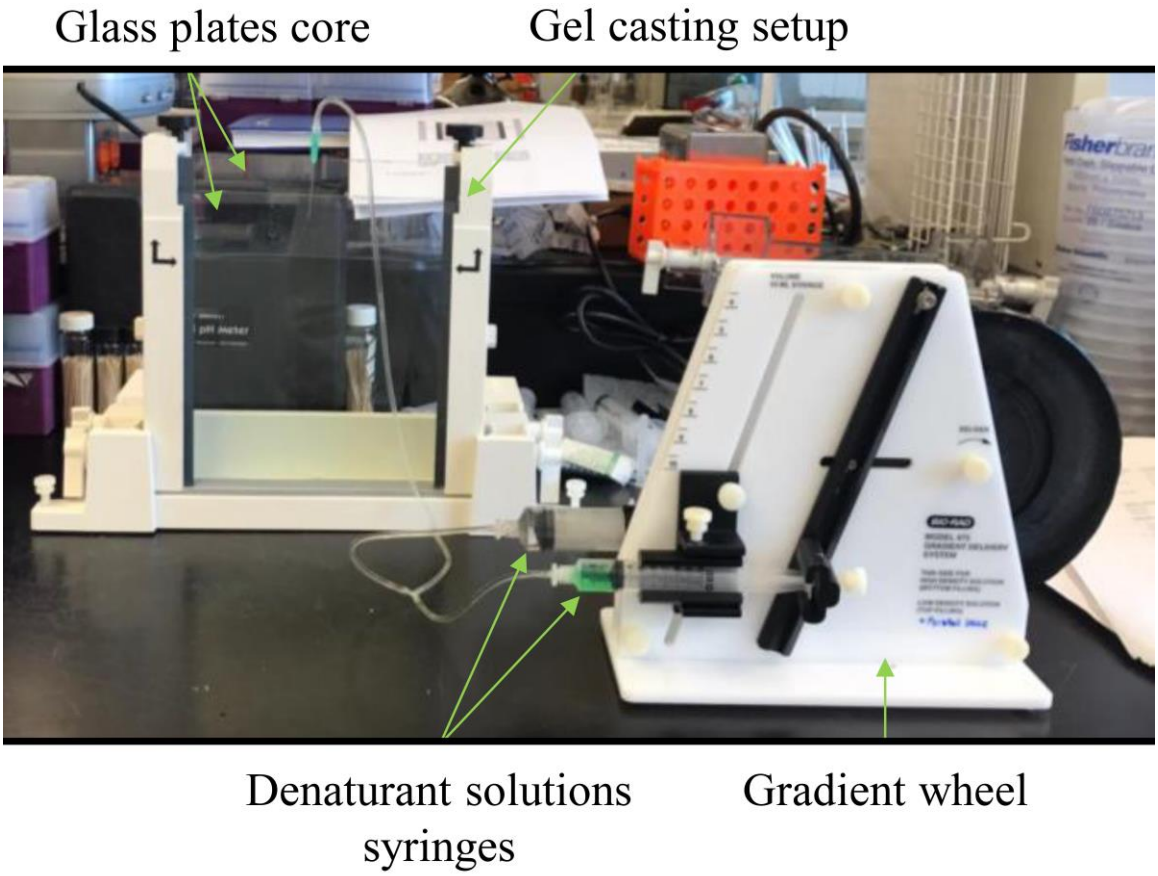

Figure 2.16: The DGGE gel casting setup. The glass plate core and the gradient wheel are highlighted. Denaturant solution syringes are filled with green-dyed water for ease of visualization.

Simultaneously, the electrophoresis tank was filled with approximately 7 L of 1x TAE buffer and was preheated to 65ºC. After complete polymerization, the core was carefully transferred to the tank, and approximately 0.5 L of 1x TAE buffer was added to cover the gel. The comb was carefully removed from the core, and the produced wells were gently flushed with 1x TAE buffer using a needle to remove non-polymerized denaturant solutions. The gel was pre-run at 55ºC for 60 mins. The buffer level should always be above the gel core when running. Afterwards, the temperature was adjusted to 60ºC and the setup was allowed to stabilize for 10 – 15 mins. To run the DGGE

(Figure 2.17), each well was loaded with 10 µL of the PCR product, and the system was run at the conditions outlined in Table 2.6.

Table 2.6: The DGGE apparatus running conditions according to the primer sets used when performing PCR.

	Primer Set A	Primer Set B	Primer Set C
Voltage (V)	60	100	70
Time (hrs)	24	18	16
Temperature (°C)	60	60	60
Reference	[336]	[341]	[320]

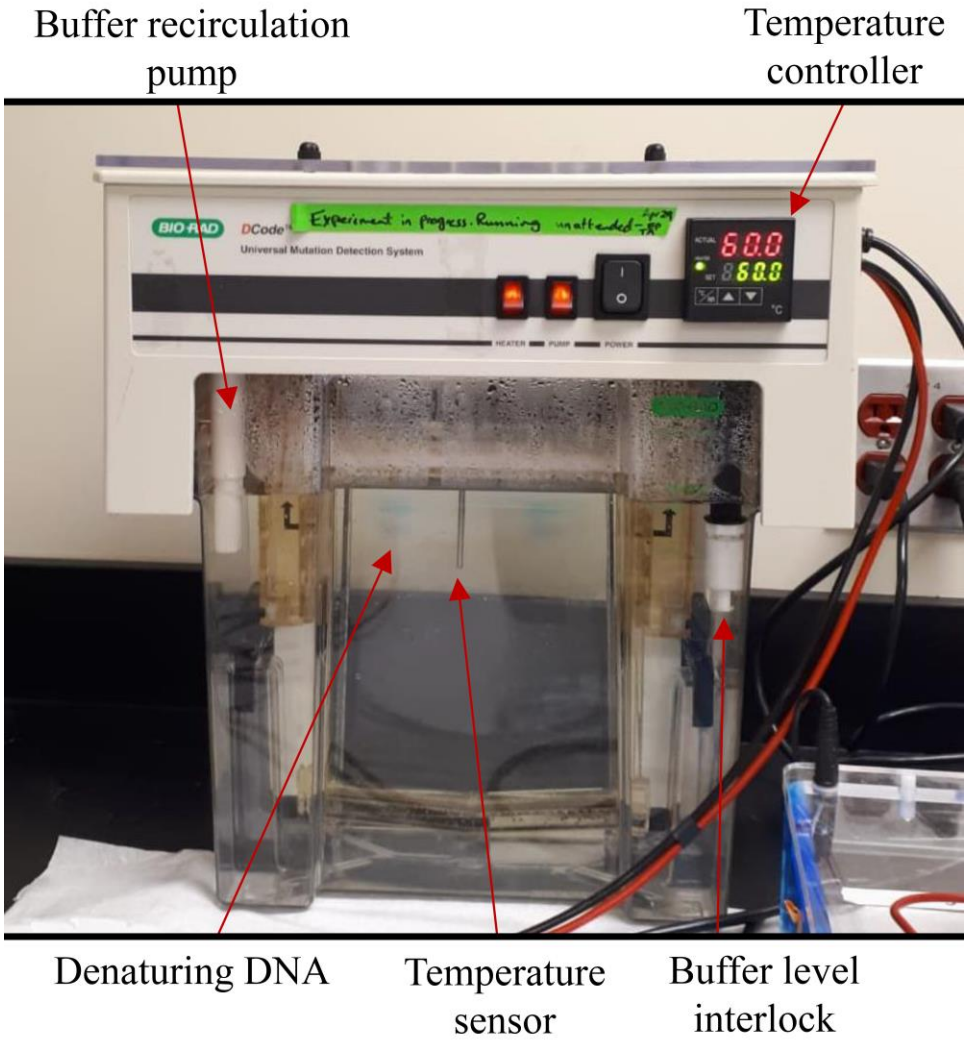

Figure 2.17: A running DGGE setup. A temperature controller, a temperature sensor, a buffer level interlock, and a buffer recirculation pump are outlined. The setup is equipped with a ceramic heater (not shown; placed at the back of the buffer level interlock). Denaturing DNA is visually observed after 2 hrs of electrophoresis.

After completion of the electrophoresis, the core was removed from the tank and the top glass plate was removed with extreme caution (the gel was very thin and could be easily torn). The gel (while on the bottom glass plate) was immersed in a bath of 1:2000 dye:buffer (1 mg/mL ethidium bromide:1x TAE buffer) for 30 mins. The gel was then de-stained through immersion into a 1x TAE buffer bath for 30 mins. The gel was visualized using the UV illumination instrument and parameters outlined previously. DGGE bands were analyzed using an automated band matching software (BioNumerics 6.6, Applied Maths, USA).

2.3 Results and Discussion

2.3.1 Microfluidic chip fabrication

Through flushing the channels of the comb-like structure (Figure 2.3), it has been found that the smallest printable square channel dimension is ≥600 μm (seen as the first open channel from the left in Figure 2.3) using the Form 2 3D printer. Therefore, the microfluidic chip was fabricated using conservative 1000 μm square channels. Although the smallest produced channel dimensions (600 μm) differ from those obtained in previous literature (e.g. 265 μm ± 15 μm [57]), the intended application in this thesis did not necessitate the use of truly microfluidic channels.

Additionally, the final microfluidic chip exhibited inline inlets and outlets because these resulted in easier opening and residue resin removal after 3D printing. The inlets and outlets also exhibited reinforced walls to minimize breakage (refer to Figure A.2) through the action of connecting and disconnecting tubing and repeated use.

2.3.2 MD Pod fabrication

The F-MD Pod design was a result of numerous prototypes (see appendix B). Each of these prototypes was tested for sealing through gently pushing against the top and bottom membranes when the MD Pod was loaded with water. All designs exhibiting leaks were redesigned and optimized. Additionally, the MD Pods internal cavity was made as wide as possible to increase the contact surface area between the samples and the incubation environment. The final MD Pod designs are shown in Figures 2.1 and B.1(e). Although the latter design was smaller and did not leak water, it suffered from a laborious assembly procedure, which became more strenuous as the assembly was required to be sterile, i.e. all parts had to be dipped in 70% IPA for at least 10 mins before assembly, and extreme caution must be taken when assembling, in terms of using sterile tweezers, gloves, and a working surface. The average assembly time for this design was approximately 30 mins, which is considerably long when requiring multiple MD Pods. Moreover, this design implemented the use of 11 pairs of screws and nuts to provide seal, which resulted in high stress over the plastic body parts and eventually cracked the majority of the assembled MD Pods. Few of the MD Pods sustained the stress and remained in good shape while suspended in LB broth for over 1 year. Nonetheless, due to the difficulty of aseptically assembling this design and the durability problems encountered (i.e. cracking), the F-MD Pod design was used for the remainder of this thesis.

The F-MD Pod shape did not use any screws and nuts to provide seal, eliminating the mechanical issue faced with the other MD Pod design. Instead, seal in the F-MD Pod was achieved using multiple O-rings placed above and below the PCTE membranes

(refer to Figure 2.6). Additionally, aseptic assembly of this design required a shy 5 mins, decreasing the laborious work involved with assembling the other MD Pod design, and was comparable to the assembly time of other growth chambers [84]. An advantage over other growth chambers, however, was the ease of disassembly and sample collection from the F-MD Pod cavity. A pipette was used to collect the incubated liquids, which were easily loaded in tubes and stored for further use. A downside of the F-MD Pod was the relatively large overall size. Therefore, the S-MD Pod was fabricated, and smaller sizes could still be obtained. The M-MD Pod was also fabricated to expedite the sterilization process through autoclaving instead of using bleach.

Moreover, stretching the O-rings over the MD Pods while the membrane is placed could be burdensome and would likely tear the membranes during placement. Therefore, the O-ring dispenser (Figure 2.7) was designed to resolve this issue for the S-MD Pods, since they exhibit the smallest O-rings. Using the O-ring dispenser, 1 in 40 membranes was torn during O-ring placement, compared to >12 in 40 membranes without using the O-ring dispenser. Using the O-ring dispenser also shortened the assembly time to approximately 3 mins. Despite the great improvement and efficiency offered by the O-ring dispenser, care must be taken when flipping the S-MD Pod for sample loading, since micro-splashes could result from the action of O-ring snapping on the membrane when the O-ring dispenser is wet from the washing sterile DI water bath. This issue could be solved by washing the S-MD Pod (with the bottom membrane already assembled) in another unused bath of sterile DI water before loading the S-MD Pod with the sample and assembling the top membrane.

2.3.3 Encapsulation rate

According to the Poisson distribution, the number of cells used in the encapsulation of *E. coli* and marine sediment bacteria, approximately 8.35×10^6 cells, should result in approximately 36% single-cell encapsulation in 100 μm diameter microbeads. To verify this result, *E. coli* cells were counted using bright field imaging (Figure 2.18) from approximately 1000 microbeads. The cell count frequency resulted in a bell-shaped curve (Figure 2.19) peaking at approximately 23% for microbeads containing a single cell. This result was similar to the single-cell encapsulation rate estimated by the Poisson distribution when $\lambda = 1$ [312] and also correlated with similar studies of encapsulated *E. coli* using cross-flow channels [96,106,206,207]. The difference between the Poisson estimation (36%) and the actual cell encapsulation rate (23%) could be attributed to the relatively large size of the microfluidic channels used, which resulted in the generation of microbeads of various sizes, most of which were larger than 100 μm. Larger microbeads were removed using cell strainers and excluded from any tests performed in this thesis to have consistent results, unless otherwise stated. Also, it should be noted that some of the *E. coli* were observed in the solution surrounding the microbeads, most likely due to their migration out of the microbeads during growth. Finally, MSB cell density was low after dislodging, given the low number of cells living in the natural environment. Therefore, $OD_{600\ nm}$ was measured and the MSB cell density was concentrated by pelleting cells from a volume that corresponded to approximately 6.68×10^6 cells/mL to obtain approximately 23% single-cell encapsulation.

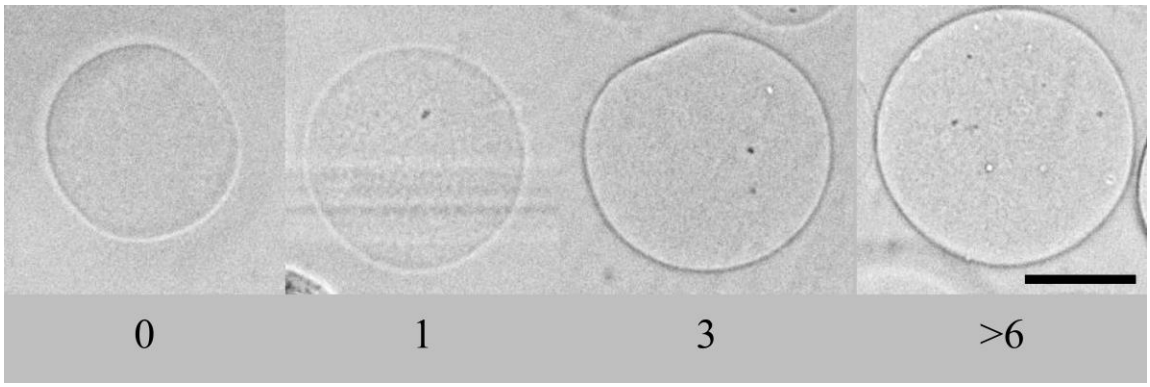

Figure 2.18: Representative images of *E. coli* in microbeads captured using bright field imaging (Cytation™ 5). Encapsulation rate was evaluated based on the cell count frequency inside the microbeads, with the cell count shown below each microbead. Scale bar is 50 μm.

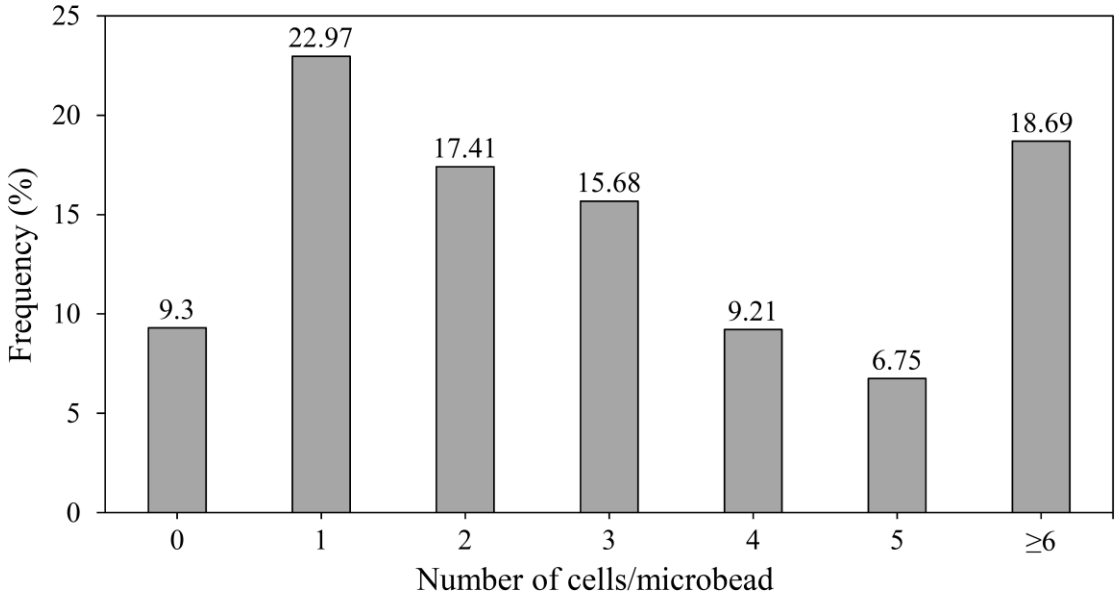

Figure 2.19: Encapsulation rate obtained using 2×10^6 cells/mL agarose.

2.3.4 Cell survival and viability

2.3.4.1 PrestoBlue®

2.3.4.1.1 *Escherichia coli*

The ability for cells to survive the encapsulation process was demonstrated using PrestoBlue® cell viability reagent. Cell concentration in working solutions of encapsulated cells was in the order of 10^6 cells/mL, which is equivalent to a 10^{-3} dilution of the re-suspended samples. Therefore, encapsulated *E. coli* was compared to a 10^{-3} dilution of *E. coli* inoculum, and over 3 days, these samples showed similar fluorescence (Figure 2.20). This could be attributed to cell growth in the microbeads over time, through which agarose was used as a nutrient source. This also demonstrated the ability of encapsulated *E. coli* to withstand the vortex force used to suspend them in agarose, the shear stress imposed on them in the microfluidic cross-flow channel, the relatively high temperature of encapsulation (45ºC), the shear stress imposed on the microbeads during the washing process, and the low amount of mineral oil remaining in the EWS after washing. It was also observed that encapsulated *E. coli* samples showed a sudden increase of fluorescence readings from day 1 to day 2, which was attributed to the acclamation of individual *E. coli* cells in their microbeads (showing a low fluorescence on day 1) and reaching the exponential growth phase in the microbeads between day 1 and day 2. Hence, fast conversion of resazurin into resorufin occurred and higher fluorescence values were observed on day 2. Samples of blank microbeads and LB broth showed similar fluorescence lower than samples containing bacteria, indicating that the plain microbeads did not contain cells [142] and that the encapsulation process did not result in contamination. Four independent runs were performed to ensure the repeatability

of these results. Error bars reflect standard error of results obtained from four samples. This is true for all error bars in this thesis, unless otherwise stated.

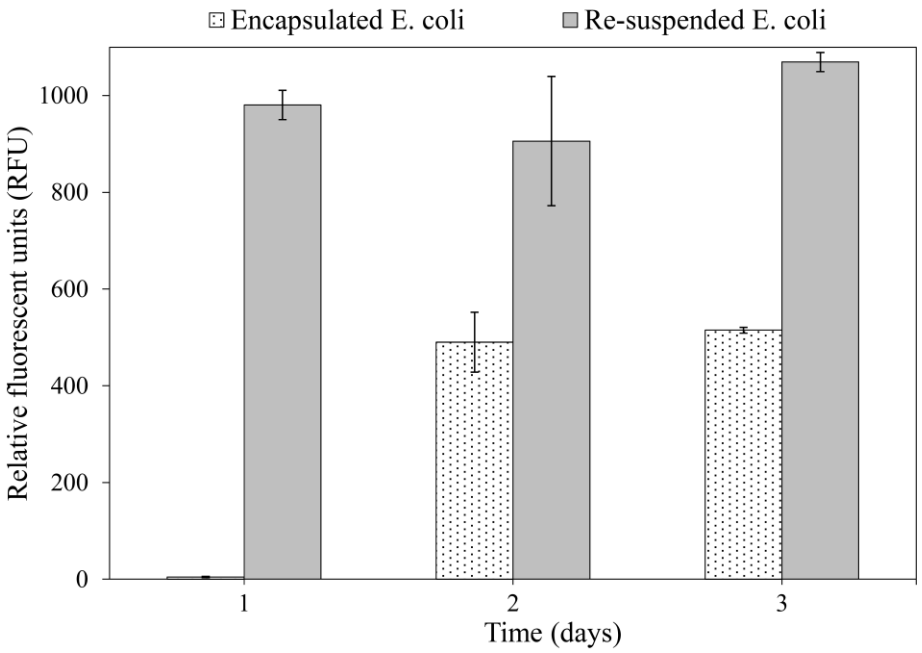

Figure 2.20: *E. coli* survival in microbeads using PrestoBlue® over 3 days. Re-suspended *E. coli* is of the 10^{-3} dilution.

Another test was performed to examine the ability of encapsulated *E. coli* to match the cell survival of non-diluted *E. coli* inoculum over time. Samples and PrestoBlue® were loaded into a well plate on the day of encapsulation, and the well plate was incubated at 37ºC for 30 mins after addition, then at 30ºC throughout the analysis duration. All fluorescence values plateaued during the first week (Figure 2.21) due to the high reduction of resazurin present in each micro-well [314]. The values started decreasing over the second week likely due to the decrease in viable cells in each well, with a sharp decrease for re-suspended *E. coli* from day 6 to day 7 and a smoother overall decrease and error bars for encapsulated *E. coli*. Overall, the viability over time was similar to that reported by Kontturi *et al.* [142], and the values obtained for encapsulated *E. coli* over time were close to those of *E. coli* inoculum, suggesting the ability of cells to

retain their survival rate after encapsulation. Four independent runs were carried out to confirm the repeatability of the encapsulation process. Error bars reflect measurements from eight samples and are based on standard error. Although this test was not performed according to normal sampling procedure (i.e. taking a sample and adding PrestoBlue® on every reading day), the data provided an insight of what happens to encapsulated cells over time when they were left undisturbed and without nutrients added. This showed the probable reliance of cells on agarose to multiply in cell number as opposed to cell growth in the LB broth inoculum.

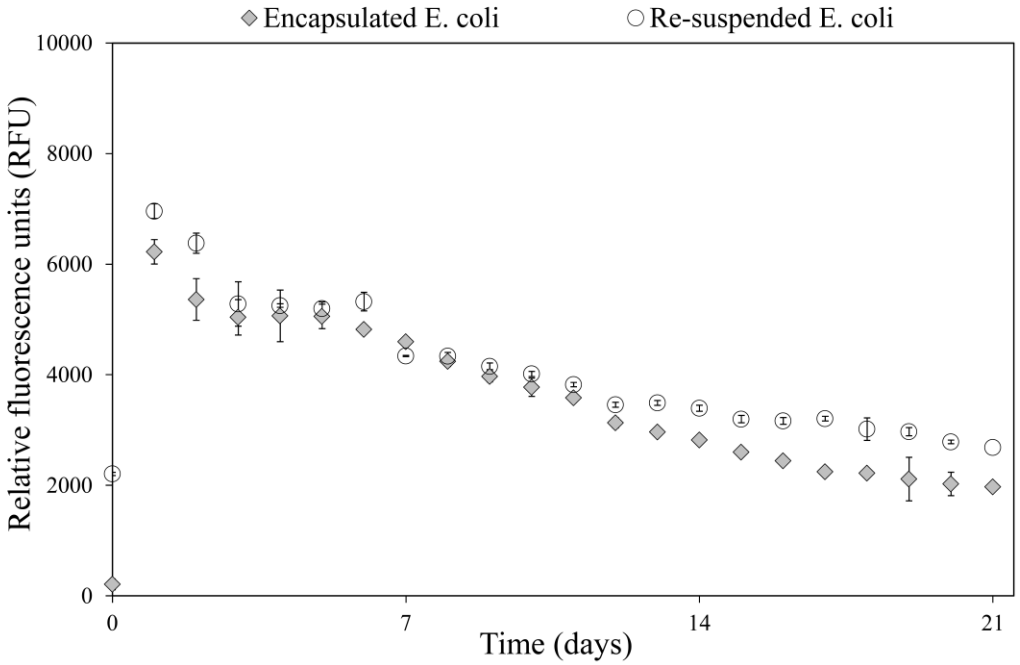

Figure 2.21: *E. coli* survival in microbeads using PrestoBlue® over 21 days, with single sampling and PrestoBlue® addition. Re-suspended *E. coli* was non-diluted.

2.3.4.1.2 Environmental marine sediment bacteria

MSB cell survival was also monitored using PrestoBlue®. Over a period of 5 days (Figure 2.22), PrestoBlue® was added daily to MWS and 10^{-3}-diluted MRS samples. Although encapsulated and re-suspended MSB samples show very close

fluorescence values on day 1, fluorescence became more variable and inconsistent with time, with negative values recorded for almost all samples at various points in time. The negative values were a result of subtracting blank sample values from the values of cell-containing samples. Through repeated sampling and observation, FSS and blank microbead solutions showed fluorescence that is equal, higher, or lower than MWS and MRS samples. It should be noted that positive and higher RFU values correlate to more viable cells. Moreover, a dilution series of MRS, from 10^0 to 10^{-4}, also showed approximately the same fluorescence for all dilutions (data not shown). Therefore, it can be concluded that FSS most probably contained a material and/or an organism that caused disturbance to the fluorescence or inhibition of the conversion of resazurin into resorufin, occasionally resulting in higher values of blank samples compared to cell-containing samples.

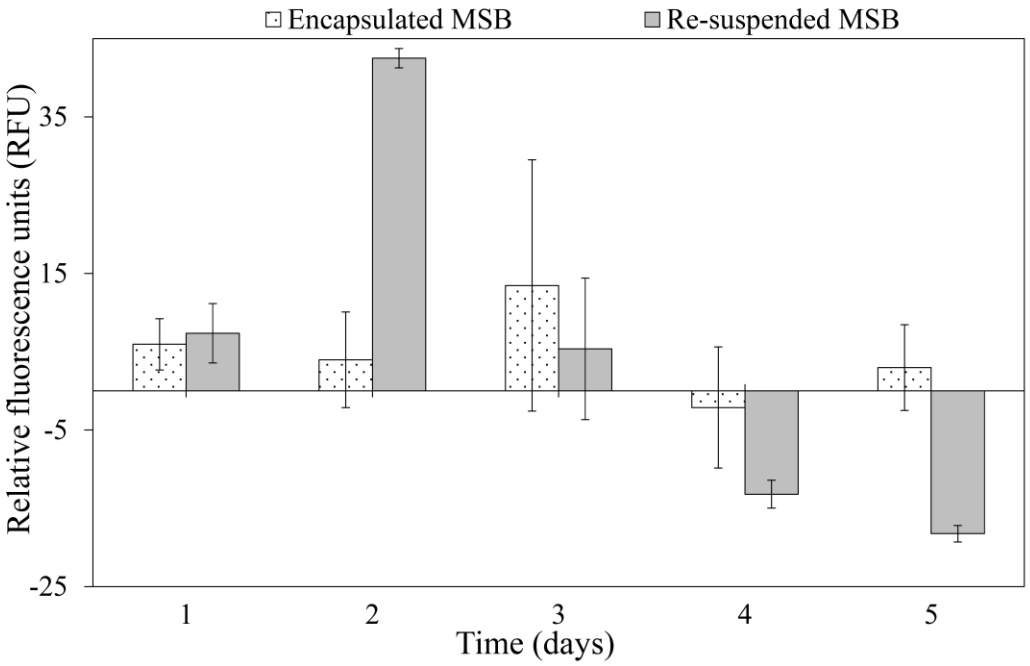

Figure 2.22: MSB survival in microbeads using PrestoBlue® over 5 days. Re-suspended MSB was of the 10^{-3} dilution.

In fact, some organisms show autofluorescence [343] caused by chlorophyll and phycoerythrin pigments [344], with red fluorescence (>650 nm) and orange fluorescence (564 – 606 nm) [345,346], respectively. Autofluorescence is commonly observed from algae, such a *Phaeophyceae*, *Synurophyceae*, *Chrysophyceae*, *Prymnesiophyceae*, *Euglenophyceae*, heterotrophic and autotrophic dinoflagellates [347], and from phytoplankton [345–349]. Picoplankton cells (0.2 – 2 μm [350]) are abundant enough in seawater to the point that studies involving their analysis do not require concentrating them [349], and they exist in surface waters [345] and in the euphotic zone (upper 75 m) [343]. Additionally, filtration of seawater can be prone to artifacts [349] and some researchers showed that few organisms still manage to pass through filters [351]. As a result, it is likely that the FSS used in this thesis (collected from <1 m deep water and filtered through a 0.2 μm filter) contained picoplankton and algae, which could likely disturb fluorescence readings by emitting background fluorescence. Hence, using PrestoBlue® (at ex/em 560/590 nm) to determine the viability of MSB over time is not feasible in FSS.

2.3.4.1.3 Known PE marine sediment species

Before applying PrestoBlue® to the known PE marine bacteria, *M. polaris* was used to identify the solution(s) in which resazurin conversion into resorufin was not disturbed and the time at which the PrestoBlue® readings should be taken. *M. polaris* was inoculated in 1 mL of each of DI water, 0.85% NaCl, FSS, autoclaved seawater, and 100% Instant Ocean® and biomass (growth) was monitored by fluorescence. Readings were taken at 30-minute intervals for 3.5 hrs (Figure 2.23). It was clear that the inoculums prepared using FSS (Figure 2.23(c)) and autoclaved seawater (Figure 2.23(d))

did not have high enough and stable, increasing trends with time, respectively, when PrestoBlue® was added, as was the case with the other solutions and as is the common behavior of growing populations of bacteria [352]. The autoclaved seawater also showed a negative value at 30 mins after subtracting the control value from the reading, which disqualified this liquid. Therefore, it could be inferred that there was definitely a substance in the seawater that caused inhibition of the conversion of resazurin into resorufin (possibly the high salt concentration), regardless of filter-sterilizing or autoclaving the seawater. Additionally, it could be concluded that any of the other solutions could be used for cell survival observation using PrestoBlue®, especially those that gave high maximum RFU values (i.e. DI water and 0.85% NaCl), since a higher magnitude of fluorescence correlates to more reliable data. However, since the observed species were marine, DI water was not a good candidate. On the other hand, Instant Ocean® is saline and could be easily replicated by other researchers. As for the reading time, 1 hr after the addition of PrestoBlue® was observed to allow for a clear distinction between the readings, and was, therefore, used to take the readings for *M. polaris*, *P. aquimaris*, and *B. licheniformis*. The difference in the maximum RFU values recorded using each media (Figure 2.23(a, b, and e) could be attributed to the difference in interaction between each media type and the reduction of resazurin into resorufin, most probably due to the salt content difference among these media.

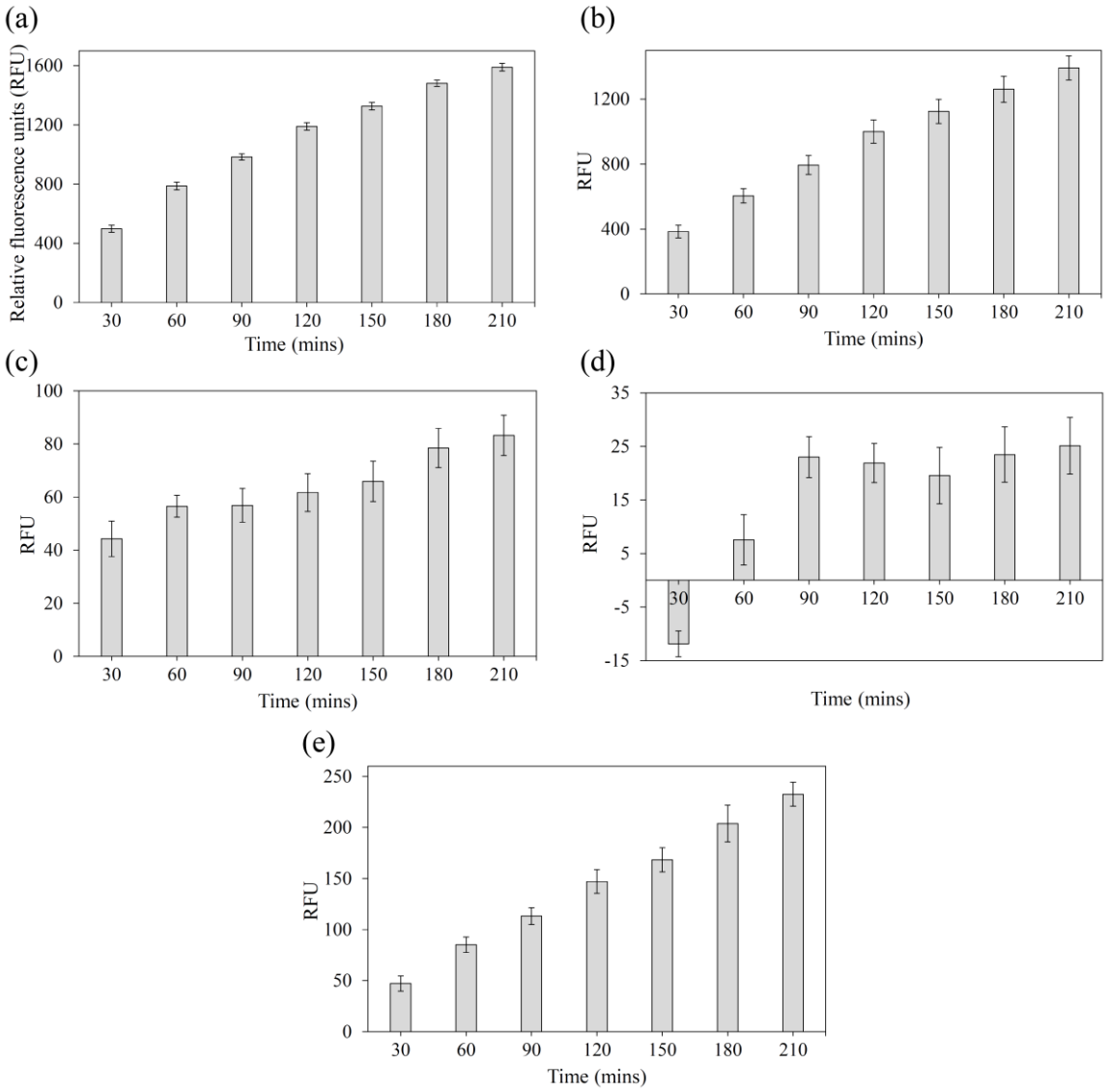

Figure 2.23: PrestoBlue® assessment data over time using *M. Polaris* suspended in five solutions: (a) DI water, (b) 0.85% NaCl, (c) filter-sterilized seawater, (d) autoclaved seawater, and (e) 100% Instant Ocean®.

The three marine bacteria (*M. polaris*, *P. aquimaris*, and *B. licheniformis*) were encapsulated and re-suspended according to the same procedure outlined in section 2.2.4.1, except that they were suspended in 50% Instant Ocean®. Both sets of samples (i.e. encapsulated and re-suspended) were transferred to sterile test tubes and left on the bench. Samples were taken daily from the tubes and PrestoBlue® was added. The

RFU data obtained was very low (data not shown), indicating the potential interference of 50% Instant Ocean® with viability measurements using PrestoBlue®.

Therefore, 10% Marine Broth was used to suspend encapsulated and re-suspended bacterial samples (the encapsulation and re-suspension were repeated according to the same procedures outlined previously, with the exception of the microbead washing solution being 10% Marine Broth, and the microbeads are washed between 100 μm and 200 μm cell strainers). This medium was chosen because it was suspected to sustain the cell viability of the three bacterial strains over time by providing a dilute saline solution (final NaCl concentration is 1.945 g/L) while containing nutrients. The compatibility of this liquid with PrestoBlue® was confirmed using *M. Polaris* (data not shown). The cell survival of encapsulated and re-suspended *M. polaris*, *P. aquimaris*, and *B. licheniformis* was monitored over 10 days (Figure 2.24), with all samples incubated in Falcon tubes on a rocker at room temperature. All samples showed minimal fluorescence on day 1 due to the low cell concentration present. As the cells grew overnight, their fluorescence increased significantly from day 1 to day 2. It could be observed that *M. Polaris* did not survive well in the encapsulated samples as it did after re-suspension. On the other hand, encapsulated *P. aquimaris* and *B. licheniformis* survived very well over time. It could be seen that the survival of encapsulated samples of these species was more stable than their respective re-suspensions, indicating the success of the microbeads in providing sufficient nutrients to the cells and sustaining their viability.

Overall, it could be concluded that cell encapsulation is better than cell re-suspending in terms of sustaining long term viability of most environmental marine sediment bacteria through the observed behavior of encapsulated *P. aquimaris*

(Gram-negative) and *B. licheniformis* (Gram-positive). The observed behavior of *M. polaris* suggested that some of the environmental marine sediment bacteria will not survive the encapsulation process and/or sustain their viability in the microbeads. It could also be concluded that 10% Marine Broth is a better suspension candidate (than 50% Instant Ocean® and FSS) for the survival of cells over time.

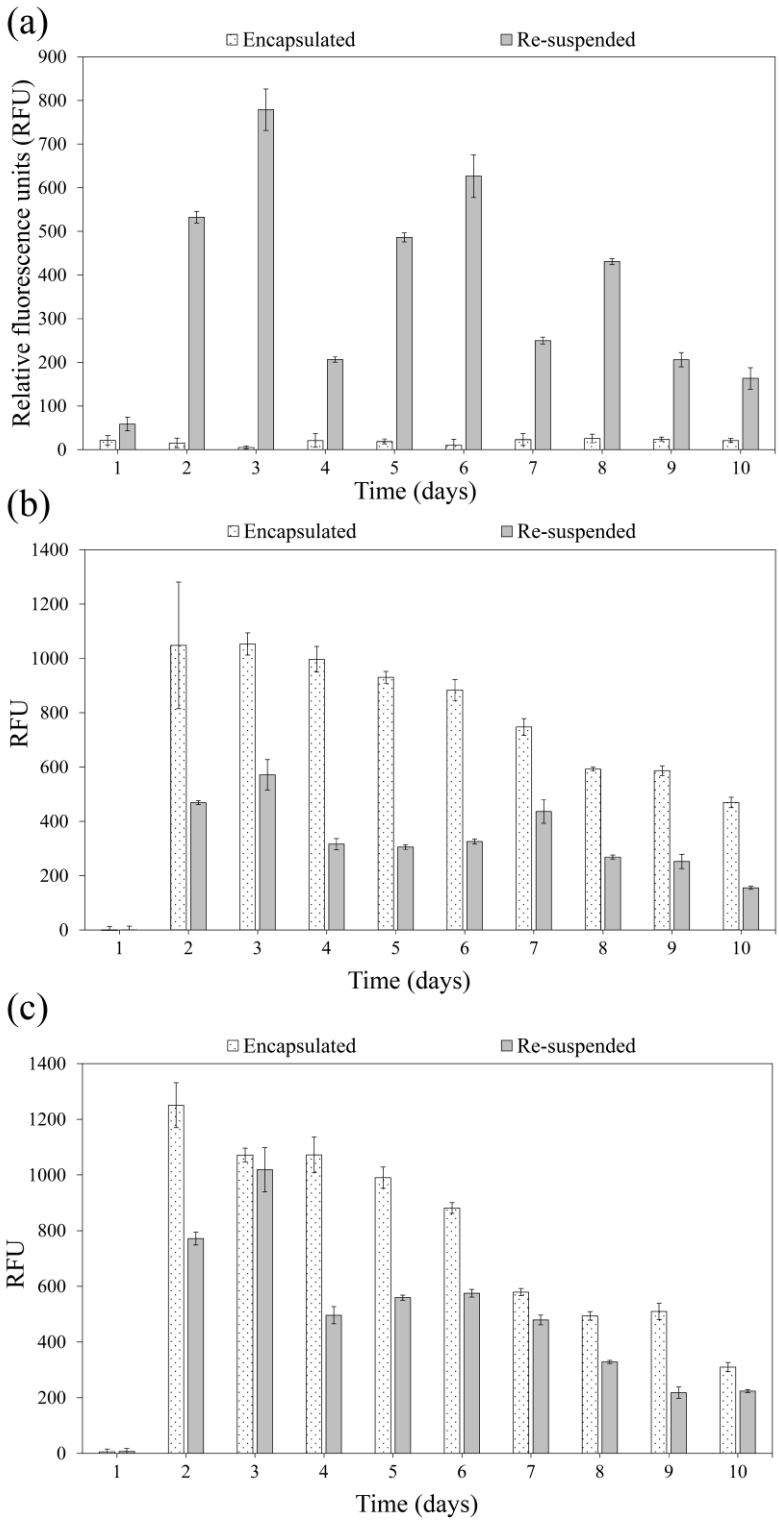

Figure 2.24: Cell survival over 10 days of three representative marine bacteria after encapsulation and re-suspension using PrestoBlue®. (a) *M. polaris*. (b) *P. aquimaris.* (c) *B. licheniformis*. The microbeads and the re-suspended species were suspended in 10% Marine Broth. Day 1 is the day of encapsulation.

Another interesting study performed in this thesis was an investigation of the effect of encapsulation temperature on the representative marine bacteria. *M. polaris*, *P. aquimaris*, and *B. licheniformis*, suspended in 10% Marine Broth, were placed on a hotplate set at 40ºC for 1 hr, with the vials shaken every 15 mins to prevent killing the cells that settle at the bottom of the vial. A second set was placed at 45ºC (the encapsulation temperature) for 1 hr, and a third set was left at room temperature. All sets were then incubated on a rocker at room temperature, with samples taken daily to observe cell survival and growth using PrestoBlue® (Figure 2.25). All solutions use 10^{-3} dilutions of re-suspended samples to match the cell concentration in the agarose + cells syringe during encapsulation. A 1 hr placement over the hotplate was chosen to match the maximum time the cells could spend in the agarose + cells syringe during encapsulation. It could be observed that higher temperatures clearly decreased the cell survival of the three species. No clear trend was observed between the specific effect of 40ºC and 45ºC on cell survival. When the temperature effect data at 45ºC was compared to the data of encapsulated *P. aquimaris* and *B. licheniformis* in Figure 2.24, the encapsulation stands out to be further enhancing to cell survival. Ultimately, these observations reflect on the possibility of sustaining long term cell viability of most environmental marine sediment bacteria, which could be beneficial when incubating them *in-situ*.

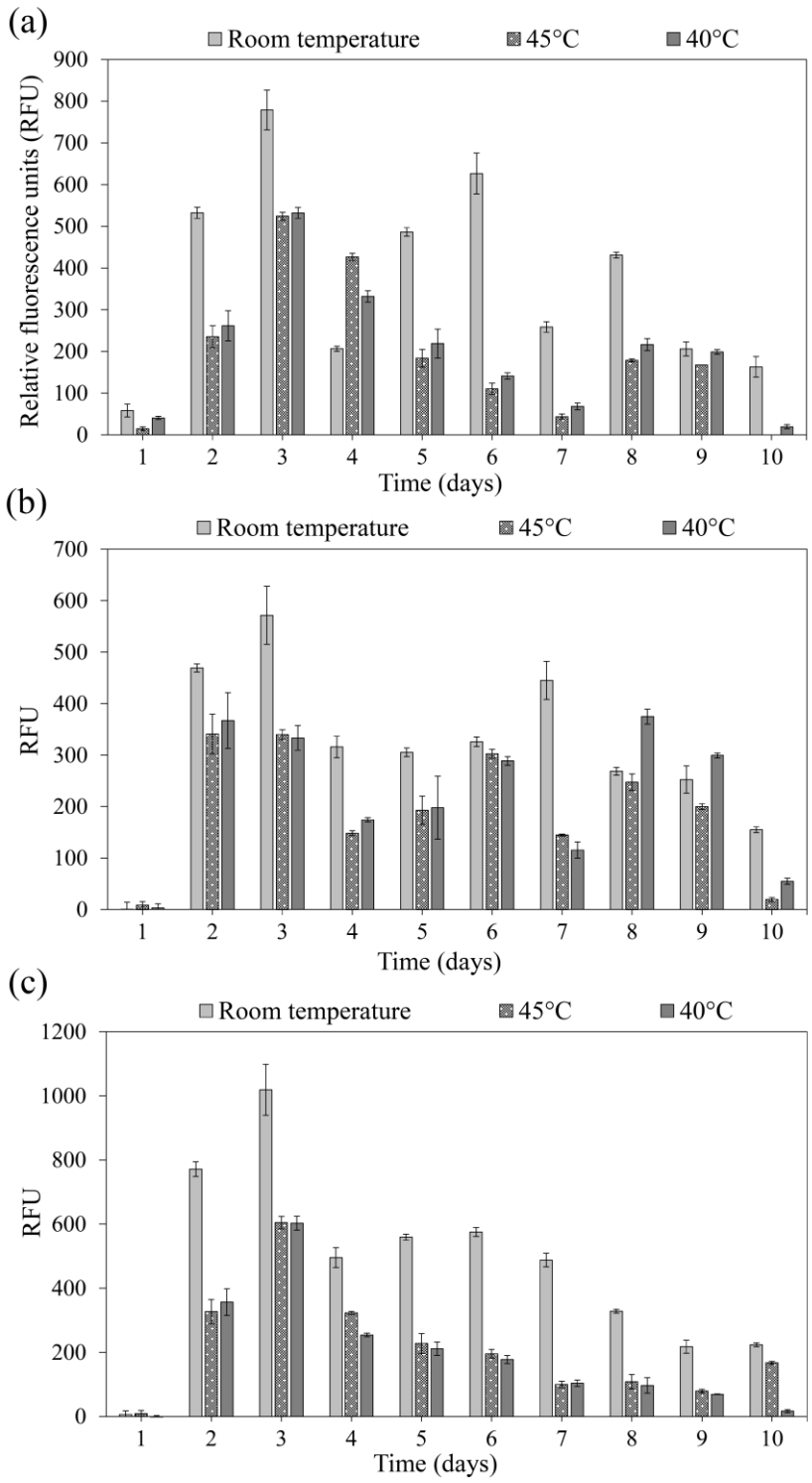

Figure 2.25: Cell survival using PrestoBlue® over 10 days of three representative marine bacteria after placement of each sample at room temperature, 40ºC, and 45ºC for 1 hr. (a) *M. polaris*. (b) *P. aquimaris*. (c) *B. licheniformis*. The marine bacteria were inoculated in 10% Marine Broth. Day 1 is the day of temperature application. All solutions used 10^{-3} dilutions of re-suspended samples.

2.3.4.2 Live/Dead bacterial staining

2.3.4.2.1 *Escherichia coli*

The results from the PrestoBlue® cell viability reagent were further confirmed using the Live/Dead assay. The percentage of live *E. coli* cells in encapsulated and re-suspended samples was monitored (Figure 2.26) over 5 days (Figure 2.27). The viability of *E. coli* cells encapsulated in microbeads on the first day of encapsulation was slightly higher (87% ± 8) than that of the inoculum (77% ± 12). This indicated the ability of *E. coli* to survive the encapsulation process. A decreasing trend over time was observed for both samples likely due to the consumption of available nutrients in the surrounding media. The encapsulated *E. coli* showed slightly higher cell viability over time compared to re-suspended *E. coli*, which could be attributed to the nutrients in the agarose microbeads. Error bars reflect readings taken from six samples and are based on standard error.

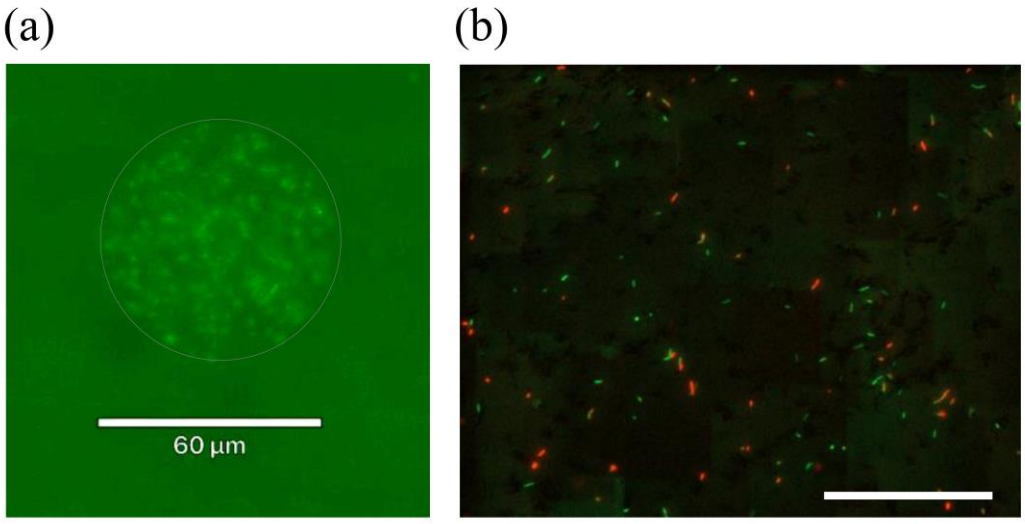

Figure 2.26: Representative (a) encapsulated and (b) re-suspended *E. coli* stained with the Live/Dead dye after one day of encapsulation and re-suspension. The images are an overlay of GFP and Texas Red images using Revolve 4 and Cytation™ 5, respectively. The microbead in (a) is encircled with a gray perimeter for ease of microbead identification. Scale bar in (b) is 100 µm.

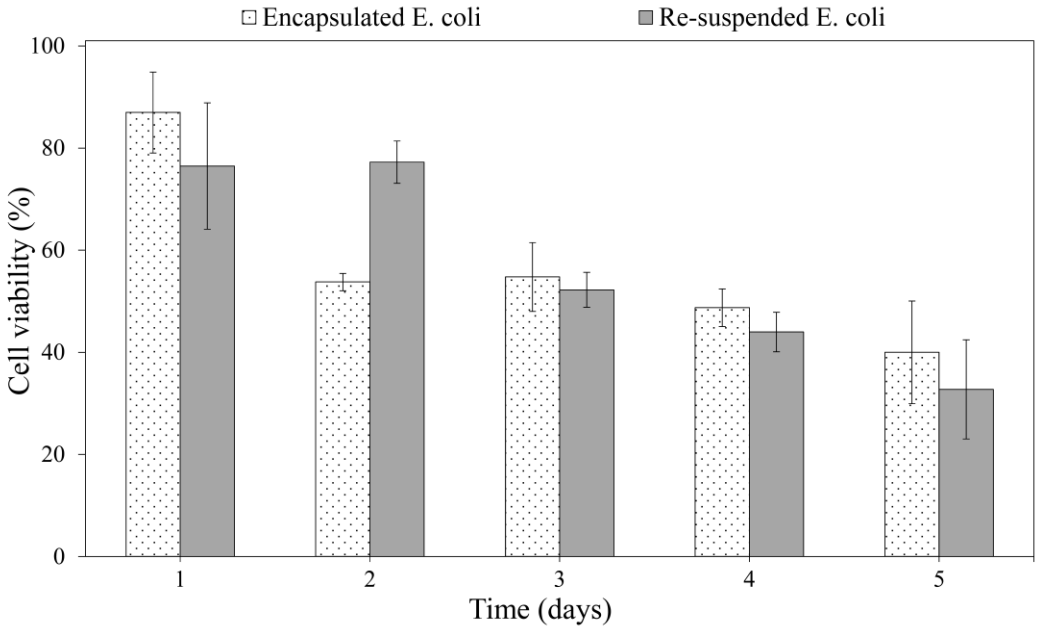

Figure 2.27: *E. coli* cell viability using Live/Dead bacterial staining over 5 days, with single sampling and Live/Dead dye addition. Re-suspended *E. coli* was non-diluted.

2.3.4.2.2 Environmental marine sediment bacteria

Live/Dead staining was also implemented on MSB samples. However, the green dye did not show up in fluorescence imaging (Figure 2.28). Multiple attempts were implemented to identify the source of the problem, such as trying to change the concentration of the dye mixture and the ratio of dye:cell culture. Details about the different concentrations used and the obtained results are shown in Table 2.7.

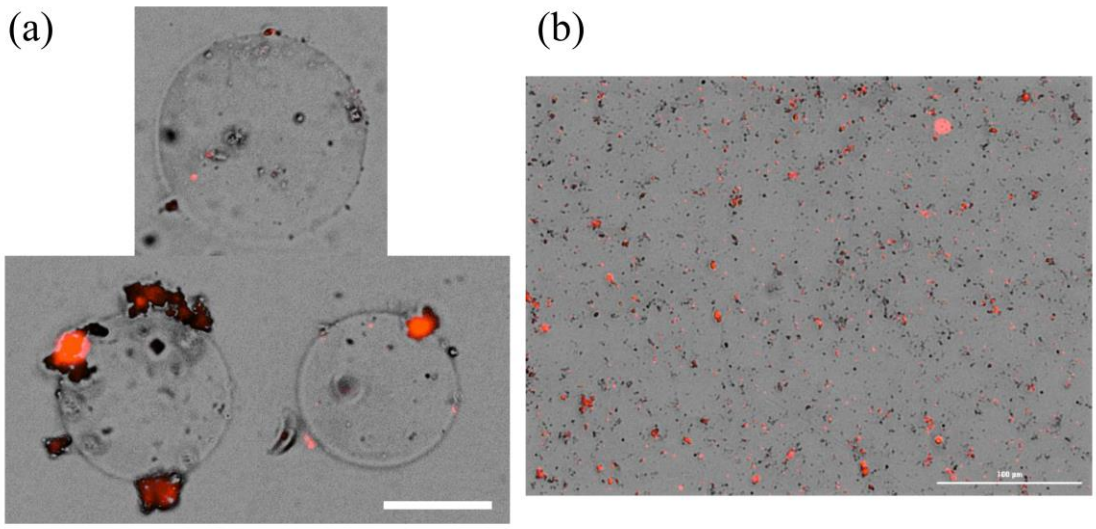

Figure 2.28: Representative images of (a) encapsulated and (b) re-suspended MSB samples stained with the Live/Dead dye, with only red fluorescence observed. The images are an overlay of bright field and Texas Red images using Cytation™ 5. The shown encapsulated MSB images were after *in-situ* incubation Run #2, while the image of re-suspended MSB was taken before *in-situ* incubation. Scale bar in (a) is 50 µm and 100 µm in (b).

Table 2.7: Live/Dead dye concentrations used to stain MRS samples.

Volume of 100x dye mixture (µL)	**Volume of additional DMAO dye (µL)**	**Volume of MSB cell culture (µL)**	**Result Observed**
1.0	0.0	100	Only red fluorescence
1.2	0.0	100	Only red fluorescence
1.4	0.0	100	Only red fluorescence
2.0	0.0	100	Only red fluorescence
2.5	0.0	100	Only red fluorescence
1.0	0.2	100	Only red fluorescence
1.0	0.5	100	Only red fluorescence
1.0	1.0	100	Only red fluorescence

Further investigation was performed by culturing *E. coli* in LB broth and in FSS overnight, then 10 µL of each inoculum was mixed with 90 µL of FSS, to which 1 µL of 100x Live/Dead dye was added. Both samples were imaged. *E. coli* that was cultured in LB broth showed both green and red fluorescence, while *E. coli* that was cultured in FSS showed only red fluorescence. This could be largely attributed to the fact that the used *E. coli* strain did not prefer to grow in a saline environment, hence the dead cells in the

second solution. However, *E. coli* that was cultured in LB broth still managed to show green fluorescence when suspended in FSS. Additionally, an MSB pellet was re-suspended in 0.85% NaCl, and 1 μL of the Live/Dead dye was added to 100 μL of this culture. Imaging showed only red fluorescence. Therefore, fluorescence imaging was more likely to be disturbed by some of the organisms existing in the MSB samples rather than from the FSS contents.

In fact, some researchers reported the interference of green-fluorescing microalgae or chlorophyll with green-fluorescing stains [346,347]. Green autofluorescence is exhibited in both live and dead algae and picoplankton cells [347]. Background autofluorescence is often observed [343] when natural aquatic samples are viewed under a fluorescence microscope, and imaging such samples can also be disturbed by light-scattering and fluorescing compounds, such as flavins (yellow) and luciferins (green) [344]. Additionally, diatoms were observed in the MRS samples used in this thesis (Figure 2.29; observed to be approximately 10 μm to >100 μm in length) and are known to contain chlorophyll [353]. Hence, diatoms could be one of the contributors to hindering green fluorescence imaging in this thesis. Moreover, sediment particles were often observed during imaging (Figure 2.29), and they often show red fluorescence, further complicating the viability analyses using the Live/Dead assay.

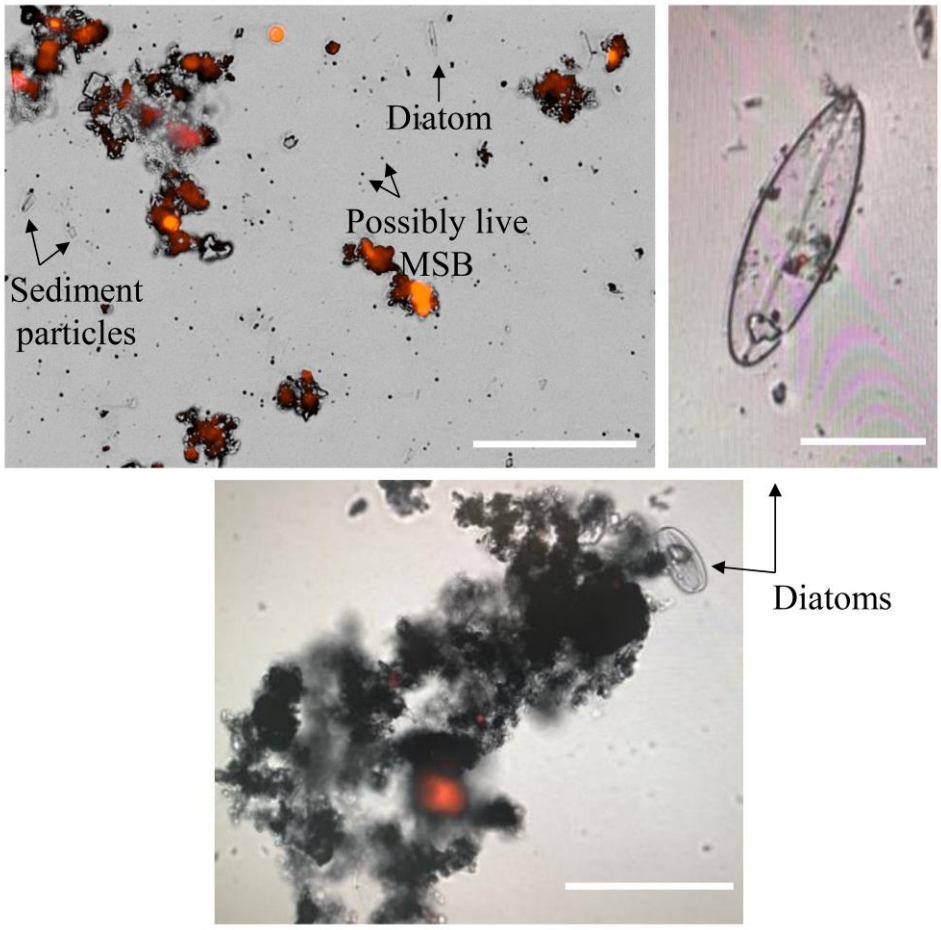

Figure 2.29: Diatoms observed in MRS samples after MD Pod *in-situ* incubation. Some sediment particles are indicated. The images are an overlay of bright field and Texas Red images using Cytation™ 5. Scale bars are 100 µm.

One could argue that the MSB samples could be completely dead at the time of imaging, hence no green fluorescence was observed. However, 100 µL aliquots of the same samples used for imaging were plated on dMA plates and growth was always observed. This could explain the non-stained black dots seen in Figures 2.28 and 2.29. Overall, imaging MRS samples using Live/Dead staining was not easily applicable in this context due to the existing complex and mostly-unknown species in these samples that disturb fluorescence. Consequently, obtaining the percent cell viability of MSB samples before and after encapsulation could not be performed.

Other parameters could affect cell viability. For example, the microbeads containing cells were formed at 45ºC (instead of the commonly-used 50ºC) to decrease the effect of temperature on bacterial viability. Additionally, the microbeads were in contact with mineral oil for a total duration of 1 hr during encapsulation and washing. We expect the effect of mineral oil on the cells to be minimal, but prolonged suspension in oil might have unexpectedly reduced viability of encapsulated bacterial cells. Moreover, the dislodging process required shaking and vortexing the marine sediment multiple times, and pelleted MSB cells were vortexed. Both of these steps might affect cell viability. The effect of pelleting MSB cells was briefly examined through spreading 100 µL samples, obtained before and after MSB pelleting, over dMA plates, and less growth was observed with the pelleted samples. Therefore, the examined samples in this thesis were encapsulated species and 're-suspended' species, which were pelleted then re-suspended to the same concentration as that of the microbeads working solution. Cell viability could be improved by reducing the centrifugation speed and/or by avoiding vortexing through gentle aspiration to re-suspend the cells.

2.3.4.2.3 Known PE marine sediment species

Finally, the representative PE marine bacteria (*M. polaris*, *P. aquimaris*, and *B. licheniformis*) were used to examine their viability over time in an effort to assess the effect of encapsulation on known Gram-positive and Gram-negative marine bacteria. Aliquots of these bacteria were prepared by inoculating each of them in a set of five 1 mL solutions: DI water, 0.85% NaCl, FSS, autoclaved seawater, and 100% Instant Ocean®. This was done to identify any re-suspension media that inhibit the Live/Dead assay stains. The results are shown in Table 2.8. From the data, it could be observed that the

green dye stained these marine bacteria, and that it was not inhibited by the seawater components (whether filter-sterilized or autoclaved). However, the red dye behaved differently with the used saline solutions, resulting in 'faint' signals obtained from the stained cells. Therefore, 50% Instant Ocean® was used as the washing solution in the encapsulation of these species as well as for their re-suspension since it provided a saline environment for their growth while providing fair signals obtained from Live/Dead staining. It was also the only saline solution (other than 0.85% NaCl) out of the five tested solutions that showed a plausible trend over a short period of time when tested with PrestoBlue® (refer to Figure 2.23).

Table 2.8: Results of compatibility of Live/Dead stains with *M. polaris*, *P. aquimaris*, and *B. licheniformis* using five different suspending solutions.

	M. polaris					*P. aquimaris*					*B. licheniformis*				
Solution	A[a]	B[b]	C[c]	D[d]	E[e]	A	B	C	D	E	A	B	C	D	E
L/D[f] Green	✓	✓	✓	✓	✓	✓	✓	✓	✓	✓	✓	✓	✓	✓	✓
L/D Red	✓	✓	✓	Faint	Faint	✓	Faint	Very faint	Very faint	Very faint	✓	✓	✓	✓	✓

[a]DI water
[b]0.85% NaCl
[c]FSS
[d]Autoclaved seawater
[e]100% Instant Ocean®
[f]Live/Dead stain

Next, aliquots of the encapsulated and re-suspended marine bacteria solutions (*M. polaris*, *P. aquimaris*, and *B. licheniformis*) in 50% Instant Ocean® were taken the day after preparation and imaged for cell viability. All samples were prepared by adding 1.5 µL of a 1x Live/Dead dye mixture to 15 µL of cell culture on a glass slide. Samples were imaged using Revolve 4. The obtained cell viability for the three species when in 50% Instant Ocean® was acceptable (data not shown), but since their cell survival did not

perform greatly with the PrestoBlue® assay in this suspending solution (refer to section 2.3.4.1.3), the three species were encapsulated and re-suspended in 10% Marine Broth. The compatibility of this liquid with the Live/Dead dyes was confirmed using inoculated *M. polaris*. The same sampling and imaging procedure outlined above was applied for the encapsulated and re-suspended samples. Cell viability was calculated as the percentage of living cells (Figure 2.30). It was observed that the cell viability of encapsulated *M. polaris* (55.3% ± 8.8) was lower than the re-suspended *M. polaris* (96.6% ± 0.8) on the day after encapsulation and re-suspension, matching the results previously obtained using PrestoBlue® (refer to Figure 2.24). As for the other two species, *P. aquimaris* and *B. licheniformis*, the cell viability of the encapsulated (99.0% ± 0.7 and 90.8% ± 2.0, respectively) and re-suspended samples (91.3% ± 2.6 and 85.7% ± 4.9, respectively) was very close. Their cell viability trend also matched the PrestoBlue® results previously shown in Figure 2.24. Therefore, it could be concluded that the encapsulation is indeed beneficial to most types of marine sediment bacteria.

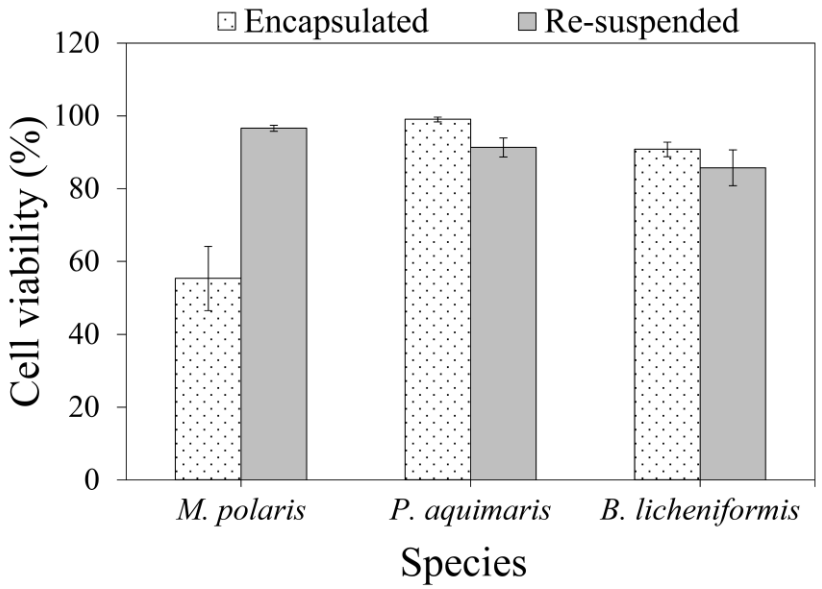

Figure 2.30: Cell viability of *M. polaris*, *P. aquimaris*, and *B. licheniformis* on the day following encapsulation using Live/Dead imaging and Revolve 4. The microbeads and the re-suspended samples were suspended in 10% Marine Broth. 15 microbeads were surveyed for each species.

2.3.4.3 DAPI

To further investigate the possibility of analyzing the viability of MSB samples given the inhibition of the green dye, DAPI was used to provide the total cell count of the samples. To do that, 1:1 v/v of MRS:methanol were vortexed for 1 min to fix the cells. The best fluorescence was observed when 7 µL of the 0.1 µg/mL DAPI stain solution was added to 2 µL of the fixed cells on a glass slide (Figure 2.31). Cell viability was calculated based on the total cell count obtained by DAPI staining and the dead cell count obtained by EthD-III staining from the Live/Dead dye (Figure 2.32). Three samples were taken and imaged for each stain, resulting in six samples per MSB sample. A minimum of five images were captured for each sample. Although the viability obtained by this staining process (76% ± 4 for encapsulated MSB and 65% ± 17 for re-suspended MSB) matched the trend observed with *E. coli* on the first day of encapsulation (refer to Figure 2.27), the sampling procedure was not reliable since two different sample pairs

were compared for viable cell count, assuming that their cell concentration and cell viability were almost identical. Moreover, many of the DAPI-stained cells showed faint fluorescent signals (Figure 2.31), making counting them harder and more subjective. Finally, encapsulated MSB samples were imaged for dead count in 100 µL aliquots, while the total count was obtained by vortexing the microbeads with methanol. Vortexing resulted in emulsifying the microbeads and, hence, counting all observed cells, some of which did not exist in the microbeads but in the surrounding solution before vortexing. Therefore, due to the great uncertainty entailed with this sampling procedure, MSB cell viability determination was not further investigated.

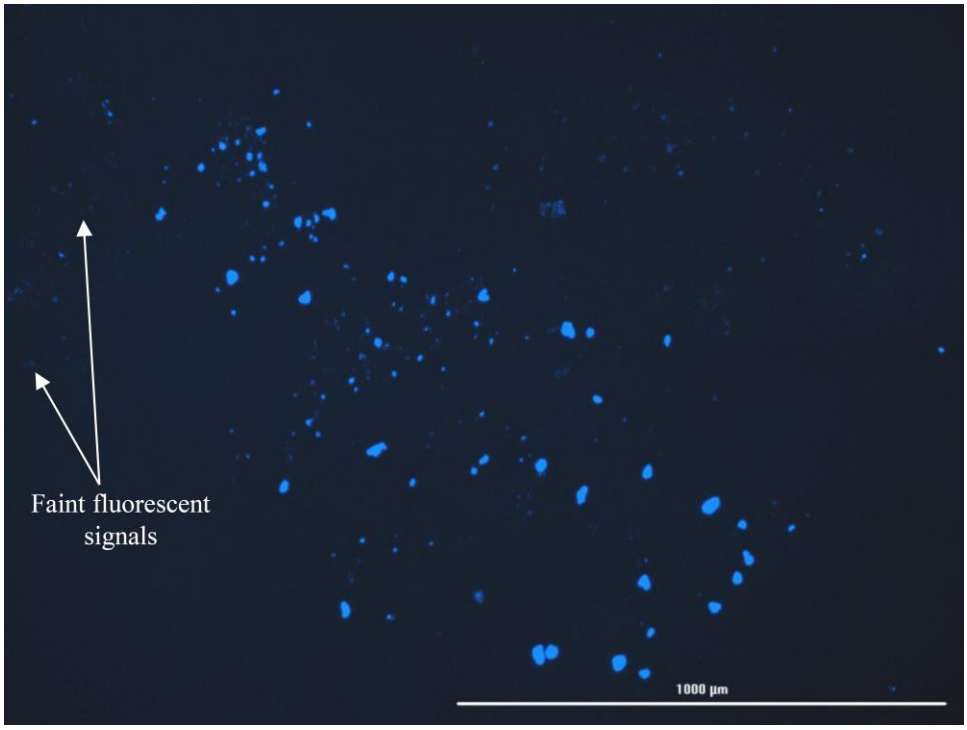

Figure 2.31: DAPI-stained MSB cells imaged using Cytation™ 5.

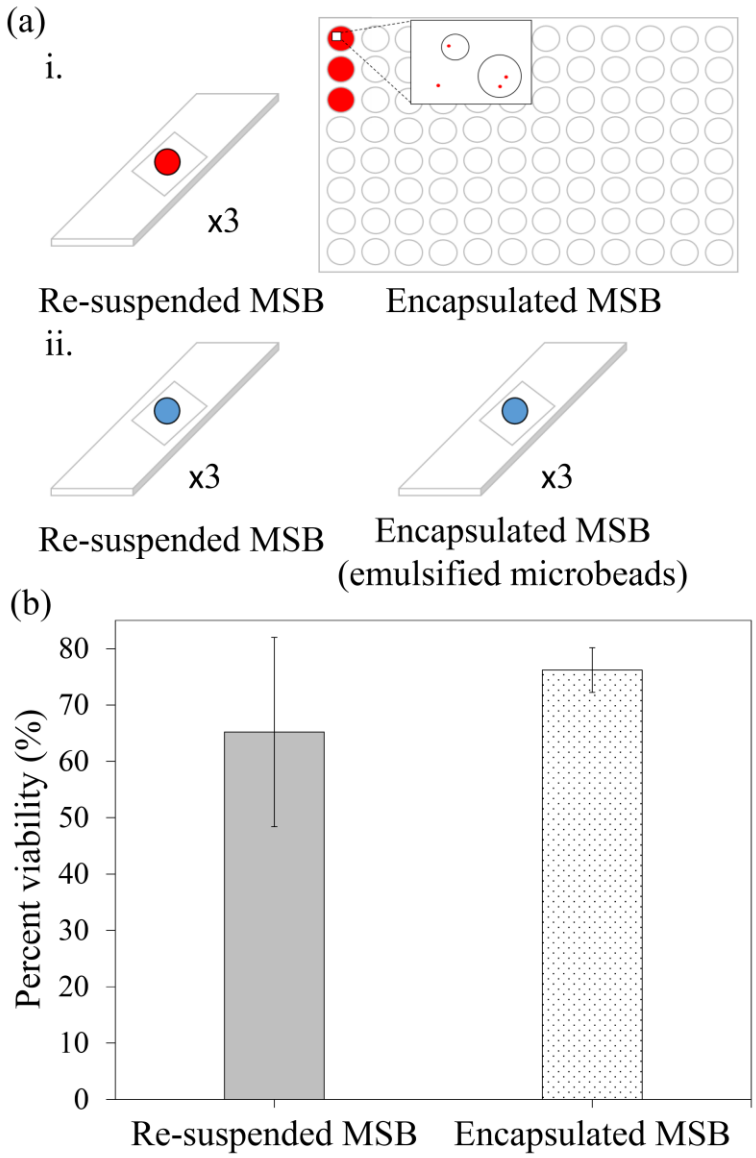

Figure 2.32: MSB cell viability assessment using DAPI. (a) The sampling and imaging procedure followed to obtain the i. dead (red) and ii. total (blue) cell counts. For dead cell count, three samples of re-suspended MSB were viewed over microscope slides, and three 100 µL aliquots of encapsulated MSB were viewed in a 96-well plate (only cells in microbeads were counted). For total cell count, MSB samples were mixed with methanol (1:1 (v/v)), thereby emulsifying the microbeads. Three samples of each MSB sample were viewed over microscope slides for each of re-suspended and encapsulated samples. Imaging was performed using Cytation™ 5. (b) Obtained cell viability of encapsulated and re-suspended MSB before *in-situ* incubation using DAPI cell viability assessment.

2.3.5 Material biocompatibility

The biocompatibility of the used 3D printing and machining materials with *E. coli* (Figure 2.33(a)) and MSB (Figure 2.33(b)) was tested using PrestoBlue® cell viability reagent. The fluorescence readings of sterile LB broth and FSS were used as controls. Fluorescence of *E. coli* samples was observed over 3 days due to the short life cycle of *E. coli*. Fluorescence was read in the presence and absence of these materials with *E. coli* and MSB samples that were suspended in LB broth and FSS, respectively. Additionally, the fluorescence was confirmed to be unaffected by the presence of each material by placing pieces of each material in sterile LB broth solutions and measuring fluorescence. For these, the values obtained were very close, if not identical, to plain LB broth solutions.

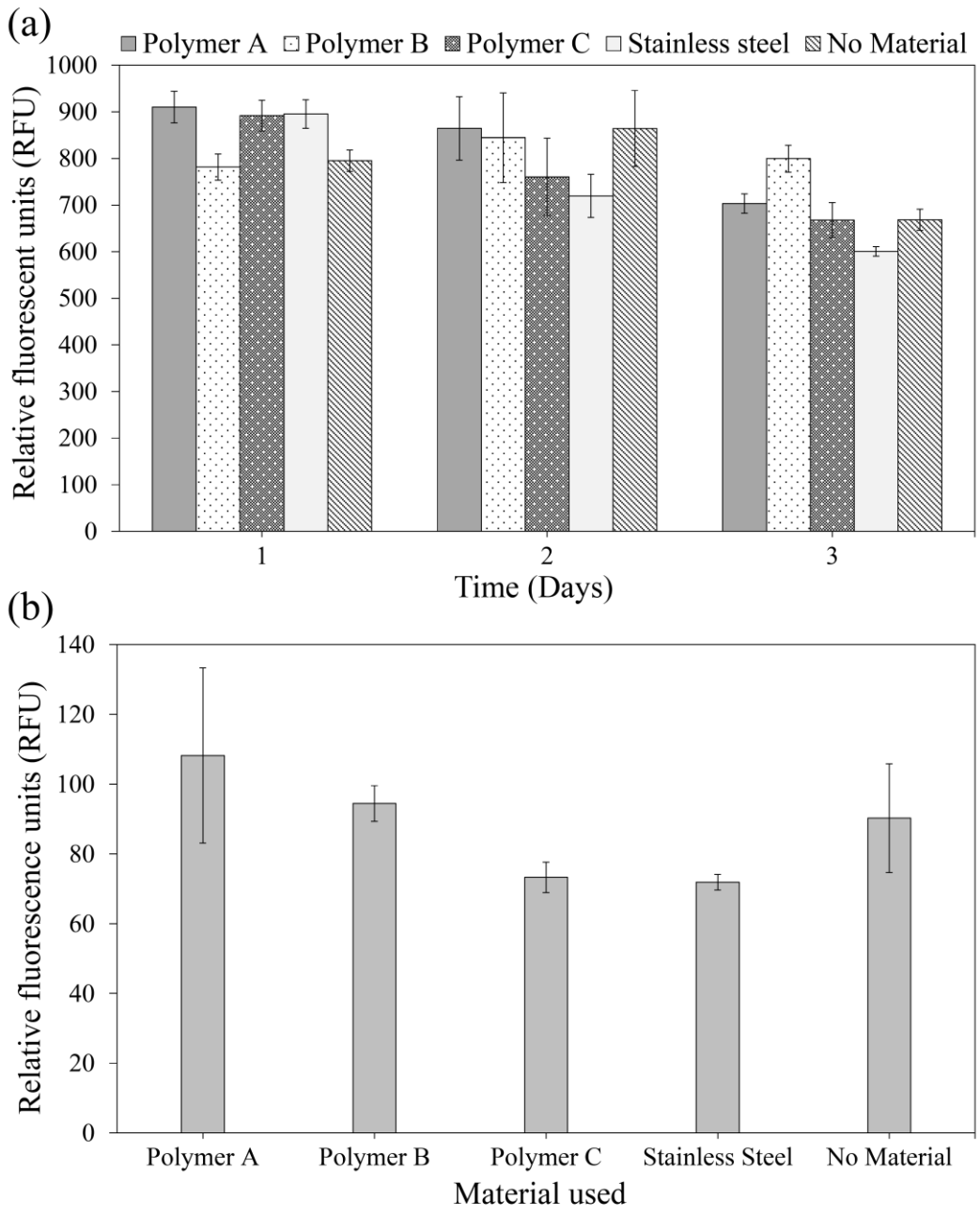

Figure 2.33: Biocompatibility of four 3D printing and a machining material (stainless steel) with (a) *E. coli* (over 3 days) and (b) MSB (on day 2 after re-suspension and incubation with the materials) using PrestoBlue®. Polymer A is Clear resin, Polymer B is Dental LT, and Polymer C is ABS filament.

It could be seen from the graphs above that the observed fluorescence for both samples in the presence of each of these materials was not significantly different from samples that were incubated with no added material. Although it was previously

discussed that PrestoBlue® readings with MSB samples were affected with background autofluorescence (see section 2.3.4.1), it could be seen that the data for MSB on the second incubation day closely match that of *E. coli* on the second incubation day, which is inexplicable in the context of this thesis. However, all in all, it could be concluded that the used materials do not significantly alter the growth of the monitored bacteria, and, hence, could be used to fabricate the microfluidic ship and the MD Pods.

The biocompatibility of four 3D printing materials was also confirmed using the Live/Dead assay. The viability of *E.coli* cells in the presence and absence of these materials was compared over five days, for encapsulated (Figure 2.34(a)) and re-suspended *E. coli* (Figure 2.34(b)). Data for Polymer C with re-suspended *E. coli* on day 1 is missing due to lack of sufficient time to take the reading during access hours to the Cytation™ 5 reader. While a decreasing trend in cell viability was observed for both encapsulated and re-suspended *E. coli* (similar to that observed in Figure 2.27), the polymers did not have a tremendous effect on the viability of cells over this time period, confirming the results previously obtained through PrestoBlue®. Therefore, Clear resin and ABS filament were used to fabricate the microfluidic chip and the F- and S-MD Pods, respectively, due to their non-detrimental effect on cell viability. No absolute inference could be made about the effect of encapsulation on cell viability when the microbeads were placed with the different materials due to the non-uniform trends of each of the four materials when placed with encapsulated and non-encapsulated cells over time.

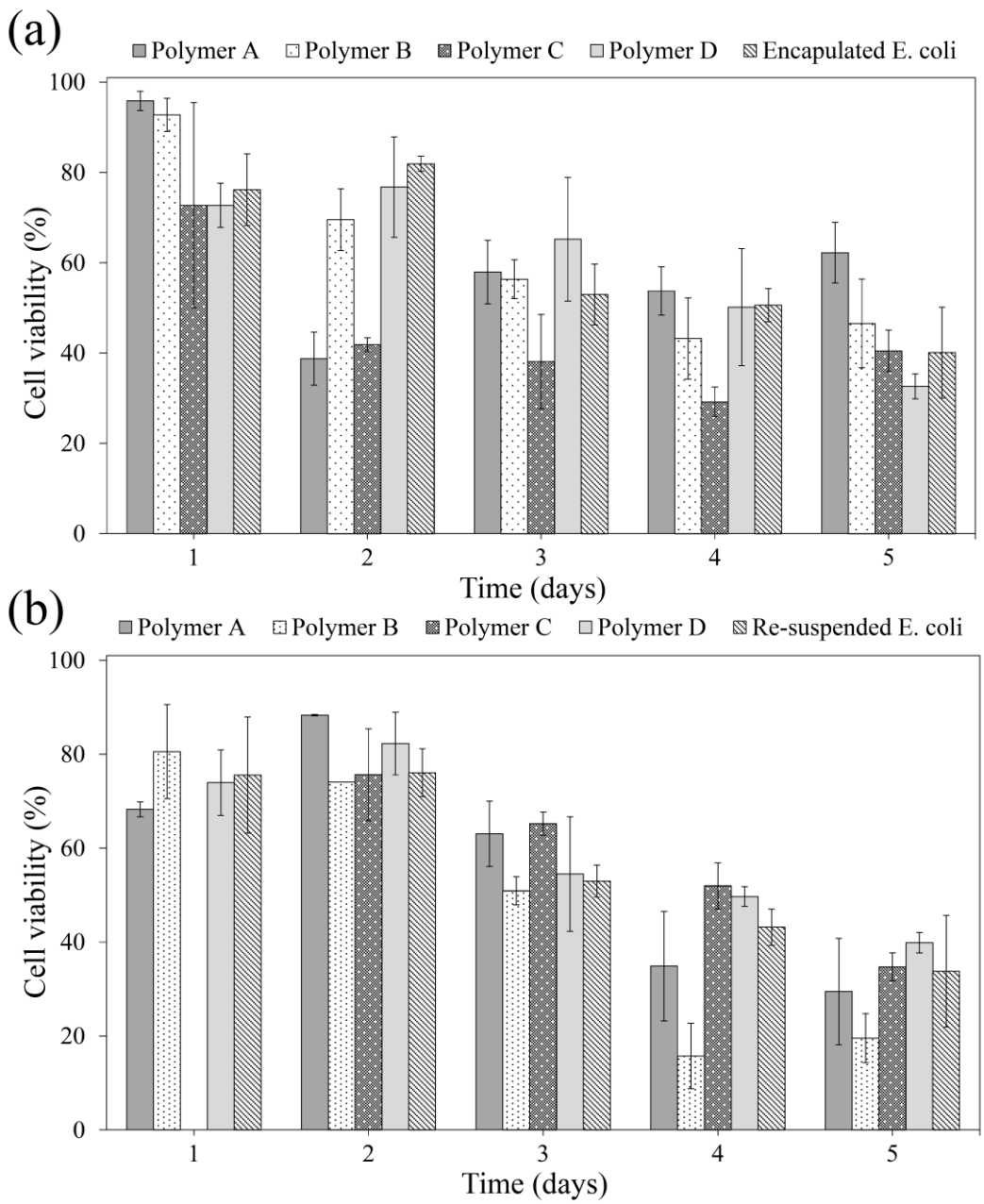

Figure 2.34: Photopolymer biocompatibility with (a) encapsulated and (b) re-suspended *E. coli* over 5 days with a single sampling step. Cells were stained using the Live/Dead dye and were observed using Cytation™ 5. Polymer A is Clear resin, Polymer B is Dental LT, Polymer C is Tough resin, and Polymer D is ABS filament.

2.3.6 Cell migration across the MD Pod

Cell migration into the MD Pod was examined through a series of contamination tests. Contamination was determined through observation of growth on the plates containing 100 μL of the MD Pods internal solutions and comparison of this growth to growth observed on plates containing 100 μL of FSS (or in some tests, DI water).

In general, all FSS plates serving as the control showed growth of several species, most of which were clear/transparent in color and grew abundantly on the entire plate (Figure 2.35(a)). Therefore, if species other than these were observed after three days of plating the MD Pod contents, the MD Pod was considered contaminated. For example, a commonly-observed 'contaminant' was a species that formed individual white colonies (Figure 2.35(b)), while other 'contaminants' were observed to have different colony sizes and colors (Figure 2.35(c and d); different colors are not identifiable in the shown images). The results observed from the cell migration tests are presented in Table 2.9. Success rate is the percentage of successful MD Pods in each test.

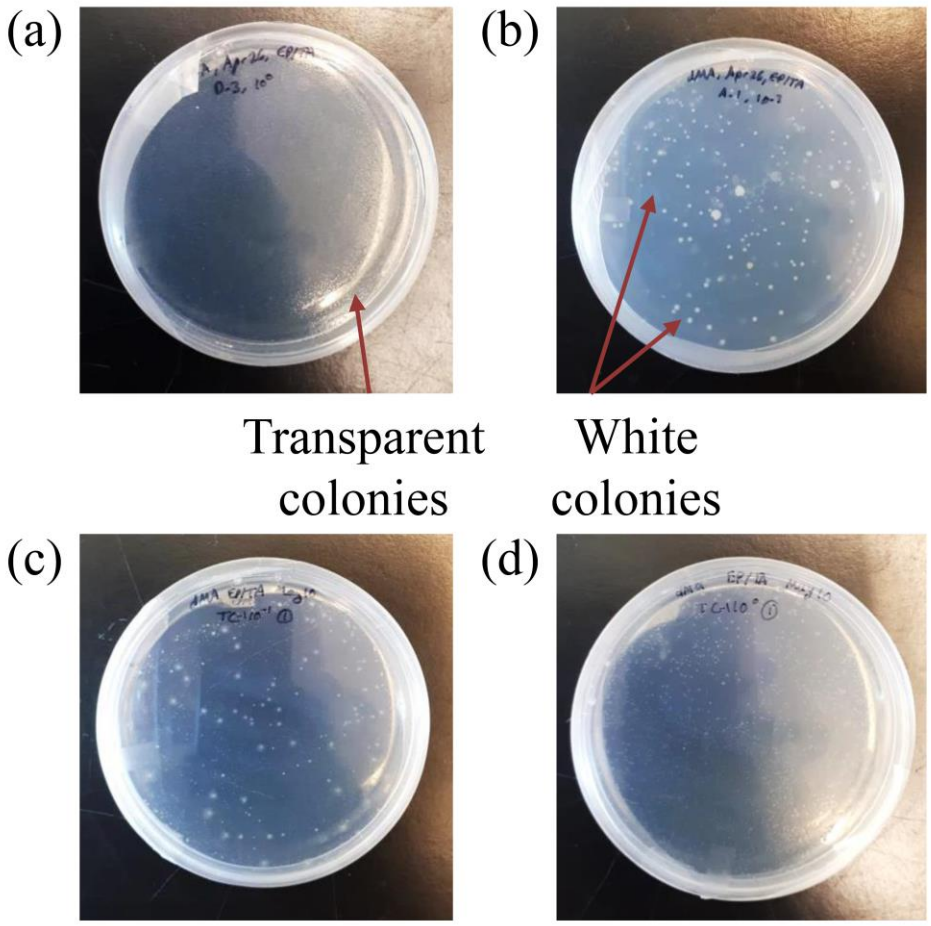

Figure 2.35: Species observed to grow abundantly on plates containing (a) FSS aliquots and (b – d) post *in-situ* incubation MD Pod contents.

Table 2.9: Results of cell migration tests across the MD Pod.

Test #	MD Pods Used	Successful MD Pods	Contaminated MD Pods	Success Rate (%)
1	1 × F-MD Pod 2 × S-MD Pod	-	1 × F-MD Pod 2 × S-MD Pod	0
2	2 × F-MD Pod 2 × S-MD Pod	2 × F-MD Pod 1 × S-MD Pod	1 × S-MD Pod	75
3	5 × S-MD Pod	-	5 × S-MD Pod	0
4	4 × S-MD Pod 1 × M-MD Pod	-	4 × S-MD Pod 1 × M-MD Pod	0
5	3 × S-MD Pod 1 × M-MD Pod	-	3 × S-MD Pod 1 × M-MD Pod	0
6	5 × M-MD Pod	-	5 × M-MD Pod	0
7	5 × S-MD Pod	1 × S-MD Pod	4 × S-MD Pod	20
8	6 × S-MD Pod	2 × S-MD Pod (1 with autoclaved PCTE and 1 with 70% IPA-sterilized PCTE)	4 × S-MD Pod	33.3
9	1 × S-MD Pod 1 × F-MD Pod	1 × S-MD Pod 1 × F-MD Pod	-	100
10	1 × S-MD Pod 1 × F-MD Pod	50%	50%	50

Through Table 2.9, it could be observed that the MD Pods did not offer repeatable success rates. However, *in-situ* incubations were carried out after confirming that at least one MD Pod passed the cell migration test, except for Runs #1 and 3, which were carried out directly after fabrication of their respective MD Pods. Cell migration testing across the MD Pod shown in Figure B.1(e) is discussed in Appendix B.

Test #1 likely failed due to the closure of the MD Pods using needle tips, which might have allowed for external cells to enter the MD Pods through the outer surface of the tips. Test #2 had a higher success rate than that of Test #3 likely due to the condition of the sediment box at the time of testing. Also, these tests showed that autoclaving the PCTE membranes did not lead the MD Pods to have a higher success rate. Nonetheless, to increase the chances of success, all PCTE membranes were autoclaved thereafter in this thesis, unless otherwise stated.

Tests #4 and 5 investigated the effect of using different membrane materials, i.e. PES and nylon, respectively, on the success of the MD Pods. Although these materials have higher mechanical strength than PCTE, they have noticeably higher thicknesses than PCTE (110 – 150 μm for PES and 65 – 125 μm for nylon, compared to 3 – 24 μm for PCTE; lower thicknesses of these two materials were not available from the providing company). As a result, when the O-rings were placed over MD Pods equipped with PES or nylon, folds were observed. Although the O-rings exert sufficient pressure over the membranes, they did not seem to enclose these folds, based on the obtained success rates. Therefore, PCTE membranes were continued to be used in subsequent tests and *in-situ* incubations, despite their fragility and ease of tearing.

Through Tests #4 – 6 (and *in-situ* incubation Run #3), the M-MD Pods never showed success. They repeatedly showed rust around the internal rim, which might have been a result of dilute bleach drops and/or splashes that came in contact with the M-MD Pod stainless steel body. Therefore, they were not further investigated but could still be optimized in the future, especially that sterilizing them was considerably easier than S- and F-MD Pods (autoclaving vs. soaking in bleach and IPA baths).

Test #7 was to assess if the S-MD Pods could be used to conduct the *in-situ* incubation Run #4; since one S-MD Pod passed the test, the *in-situ* incubation commenced.

Test #8 was used to assess the effect of autoclaving the PCTE membranes as opposed to soaking them in 70% IPA for 10 mins. Since 33.3% of the MD Pods worked with either type of sterilization, PCTE membranes were autoclaved for the remainder of this thesis due to the ease of autoclaving the membranes vs. soaking them in 70% IPA. It

should be noted that soaking the membranes in 70% IPA caused them to fold over themselves, making the assembly process more difficult and causing the membranes to tear upon unfolding.

Tests #9 and 10 were conducted to examine if the source of contamination occured before or after placing the MD Pods in the incubation environment. These tests used MD Pods filled with sterile DI water instead of FSS because, as discussed earlier, the FSS control plates always showed growth of certain species. Test #9 showed no growth on the plates (Figure 2.36(a)), suggesting that the MD Pod assembly, loading, and disassembly did not cause contamination to the MD Pod's contents, regardless if the F-MD Pod or the S-MD Pod was used. Moreover, Test #10 showed 8 ± 3 cfu/mL on the plates after 1 week (Figure 2.36(b)), suggesting that contamination possibly happens when the MD Pods are in the incubation environment. Nonetheless, since this abundance was very low, it could be subtracted from the abundance obtained after *in-situ* incubation.

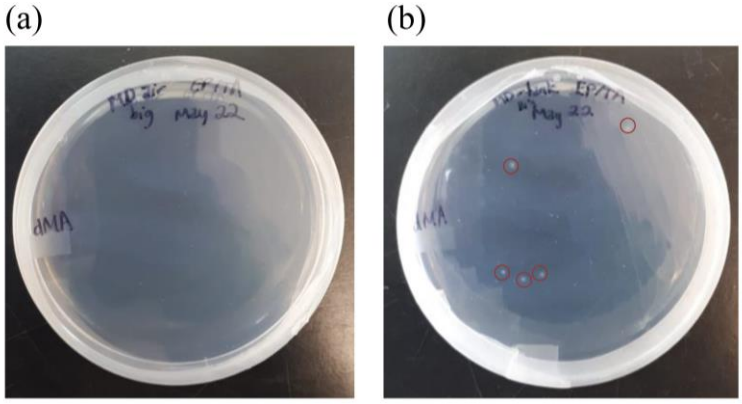

Figure 2.36: Representative plates containing MD Pod contents from (a) Test #9 and (b) Test #10 after 1 week of plating, 10^0 dilution. The MD Pods were loaded with DI water. Five colonies were spotted on the plate of Test #10.

2.3.7 MD Pod in-situ incubation

The MD Pods were *in-situ* incubated to meet the main objective of this thesis. Table 2.4 (in section 2.2.8) provides a detailed outline of the parameters used with the *in-situ* incubation runs performed. Runs #1 – 3 were performed for >15 days due to the cold nature of the incubation environments, which was suspected to cause slow growth of MSB. On the other hand, the incubation time for Runs #4 and 5 was decreased to 10 days because the aquarium was maintained at 23ºC, which was also suspected to cause fast growth of MSB. Different MD Pod types were used in each test depending on the success rate obtained through cell migration tests performed before each run and/or the results of each previous run.

A media study was conducted by Emily Pope in which MSB was grown over plates of Marine Agar, dMA, Reasoner's 2A agar (R2A), dilute R2A, SMS agar (containing seawater, casein, potato starch, and casamino acid), seawater agar, and seawater agar containing each of vitamins, iron, fatty acid, and siderophore, individually and in different combinations. It was observed that more diverse species grew on dMA during a shorter period of time compared to the other media tested for MSB growth. Therefore, MSB were grown on dMA in this thesis to allow for greater microbial diversity.

2.3.7.1 Run #1

Run #1 was performed in the natural environment at Location 1. The MD Pods were checked every two days to confirm that they did not become unburied due to natural tides. Moreover, the MD Pods were tied together using a long rope that was tied to a dive weight to ensure that the MD Pods do not drift away with currents. Unfortunately, at

day 17 of incubation, the river in which the MD Pods were incubated froze. The MD Pods were collected on day 19, with some MD Pods intact and others having destroyed membranes (Figure 2.37). The contents of the intact MD Pods were plated on dMA plates and observed for growth. All the plates showed contamination similar to that explained previously in section 2.3.6. Therefore, no microbial isolation was performed for any of the obtained MD Pod contents. The source of contamination in this run might be from the outer rim of the needle tips used to close the MD Pod loading port (see Figure B.1(l) and Figure 2.37) or from closing the MD Pods using sets of 4 O-rings, both of which might not have provided enough seal. Additionally, the 10^{-4} dilution plates of MRS showed minimum-to-no growth. Therefore, all subsequent runs used 10^{0} – 10^{-3} dilution plates or less. Plates containing blank microbeads and FSS were of the 10^{0} dilution since no microbes should grow on those.

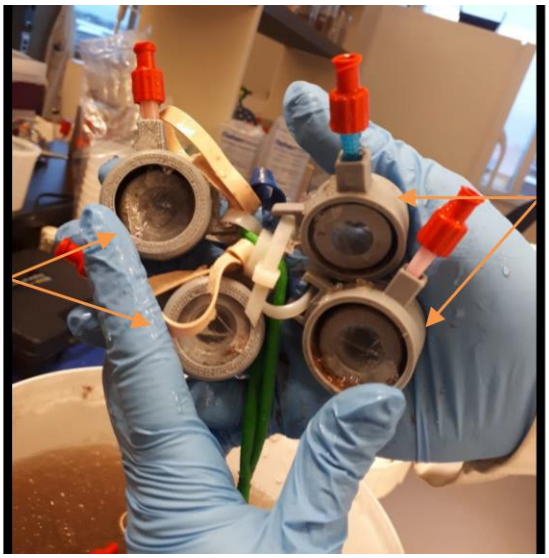

Figure 2.37: MD Pods collected after 19 days of *in-situ* incubation in Location 1. Intact and damaged membranes are observed. Needle tips with red caps were used to close the loading ports of these MD Pods.

Aliquots of the MD Pod contents were imaged for Live/Dead assessment. However, due to noticing autofluorescence of the samples, the green stain did not work

properly at this time and, hence, the assessment was discontinued for this run. Alternatively, cell survival determination through PrestoBlue® was commenced after this result for the following runs.

2.3.7.2 Run #2

Run #2 was performed in the sediment box using samples from Location 2. In this run, enhanced seal was attempted through the use of a set of 6 O-rings for each MD Pod. Additionally, all loading ports were plugged using an acetone/ABS mixture, thereby decreasing sources of contamination and resulting in the MD Pods shown previously in Figure 2.5. Plating the MD Pod contents after *in-situ* incubation revealed success rates of 66.6%, 83.3%, 50%, and 50% for MWS, MRS, blank beads, and FSS MD Pods, respectively. This meant that 1 – 2 MD Pods of each sample showed contamination similar to that seen in Figure 2.35. Therefore, all MD Pods in subsequent runs used 6 sealing O-rings and no loading ports.

Moreover, grown microbes on the plates obtained from the successful MD Pods contents showed interesting results. Microbes grown from MWS samples showed individual, separated colonies (Figure 2.38(a)) that were not covered by the transparent colonies repeatedly seen with almost all other plates (see Figure 2.35(a)). This is especially important for expediting downstream microbial isolation. As for microbes grown from MRS samples, less diversity was observed when compared to traditional plating of those samples (Figure 2.38(b and c), respectively). This could be due to the lack of sufficient nutrients and chemicals diffusing into the MD Pod during incubation, which could be due to the lack of sediment and seawater motion. It could also be due to

the abundant growth of fast-growing microbes, which could have led to decreased potential for the growth of slow-growing microbes.

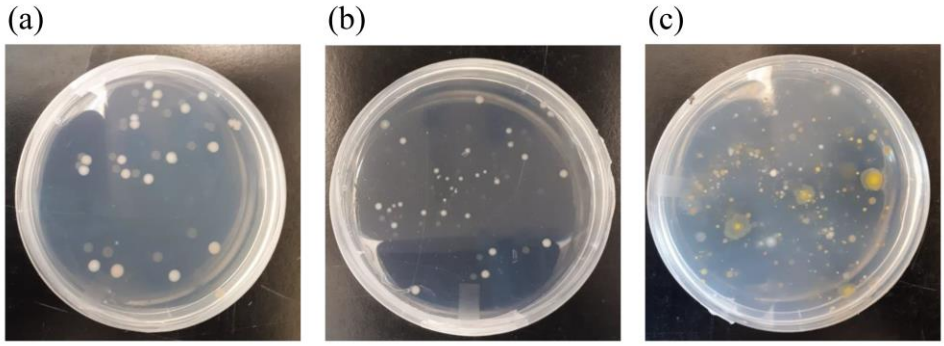

Figure 2.38: Representative plates of microbes grown from Run #2 after 2 weeks of plating. (a) Encapsulated MSB after *in-situ* incubation, 10^0 dilution. (b) Re-suspended MSB after *in-situ* incubation, 10^{-1} dilution. (c) Re-suspended MSB before *in-situ* incubation (traditional plating), 10^{-1} dilution.

Moreover, grown colonies were counted and compared in terms of abundance for all samples after two weeks of preparing triplicate plates of each sample (Figure 2.39). It could be seen that the colony-forming units (cfu) per milliliter of cell culture for the traditional plating of encapsulated MSB samples was significantly lower than that of re-suspended MSB samples, which could be due to the lack of sufficient cells in each microbead to form a colony. Furthermore, the cfu/mL of encapsulated MSB samples was lower than that of re-suspended MSB samples after *in-situ* incubation. This was likely due to the lower cell concentration of MWS compared to MRS used for MD Pod incubation, which could have led to fewer cell-to-cell communications, and, therefore, less growth. The large drop in abundance of re-suspended MSB samples before and after *in-situ* incubation could, again, be attributed to minimal chemical and nutrient diffusion into the MD Pod due to lack of sediment and seawater motion. On the other hand, abundance was observed to increase for encapsulated MSB samples after incubation, which could be due to successful growth of cells in the microbeads during the incubation

into colony-sustaining units. Overall, it should be noted that this method of counting colonies can be subjective due to the existence of 'contaminants' that commonly grew from FSS on the sample plates, making the distinguishability between grown microbes and 'contaminants' difficult. It should also be noted that the incubated MSB samples were taken from frozen sediment samples stored at -24ºC for over a month before conducting Runs #2 and 3. Up to Run #3, the author did not know that cell samples should typically be stored under glycerol to preserve their viability. Therefore, the relatively low abundance observed in Figure 2.39 could be due to cell lysis during the freezing period. This fact was taken into consideration in Runs #4 and 5.

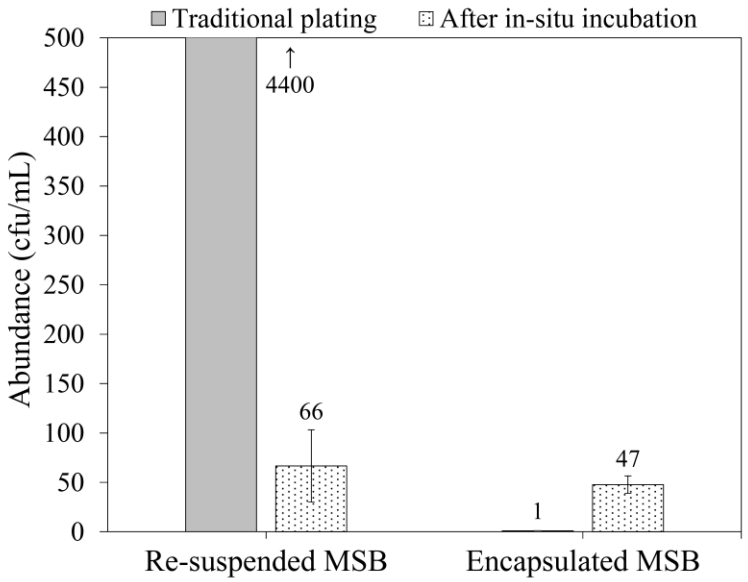

Figure 2.39: Colony abundance for samples obtained from Run #2 and traditional plating after two weeks of plating.

Live/Dead imaging was also unsuccessful with this run, but imaging the samples after *in-situ* incubation repeatedly showed black 'clumps' in re-suspended samples (see Figure 2.29) and an accumulation of similar, smaller 'clumps' on the outer surface of the microbeads (see Figure 2.28(a)). This was likely due to the growth of cells, originally existing outside of the microbeads, into colonies that, apparently, adhered to the

microbeads' outer surfaces for ease of access to the nutrients available in agarose. This could pose an issue for slow-growing bacteria that rely on the agarose microbeads to be a nutrient source and a growing medium, ultimately leading back to the 'Great Plate Count Anomaly' [19]. As for PrestoBlue®, the well plate in which the samples were placed was incubated at 30ºC for the reading duration according to published literature using this assay [314,352,354]. However, at this time, the readings looked minimal and nearly equal for all samples (data not shown). Therefore, it could be concluded that this incubation temperature of the well plate is not ideal, and subsequent runs took this observation into consideration (the relationship between these observations and autofluorescence was not made at the time).

2.3.7.3 Run #3

Run #3 implemented the use of metallic MD Pods only, using samples from Location 2. Upon retrieval of the incubated M-MD Pods and plating of their contents, it was noticed that the plates came out all contaminated. Therefore, no abundance (in terms of colony counts) was reported. It should be noted that the assembly of the M-MD Pods resulted in repeated tearing of the membranes due to the heavier weight of these MD Pods. Torn membranes were replaced with new membranes every time a membrane tore during assembly. However, one cannot tell using the naked eye if there were microscopic tears that also might have occurred during assembly. Hence, the source of contamination for this run was probably due to these microscopic tears. This mishap was been taken into consideration when implementing cell migration Test #6 by assembling the M-MD Pods over an O-ring that acted to decrease the friction between the bottom of the M-MD Pod and the assembly petri dish. Additionally, the membranes used in this run

were autoclaved for the first time, so the effect of autoclaving was not known. It was later validated in cell migration Test #8 as discussed previously. Last but not the least, retrieval of the M-MD Pods showed at least three of them to have rust around the internal rim, which could be due to drops and/or splashes of bleach that occurred during assembly (from the casings) or due to bacteria that caused 304 stainless steel to rust, such as *Pseudomonas aeruginosa* [355].

Run #3 also featured shaking the sediment box twice daily, with each shake including 10 times sideways and 10 times back and forth. This shaking was in aim for increasing the viability of the incubated cells by semi-mimicking the movement of natural tides. Moreover, more sediment was included with the MSB cells. This was achieved through letting the dislodged solution settle down after the 1 hr shake, without the centrifugation step. The $OD_{600\ nm}$ was then measured from the top part of the solution, being careful not to disturb the settled fine particles. After that, the volume needed to achieve a pellet that corresponds to approximately 8.35×10^6 cells was identified. The solution was then shaken and the volume was collected. The aim of this modified step was to include more sediment particles in the MD Pod solutions since more than 84% of soil bacteria adheres to particles [34], which could be beneficial to increasing bacterial growth in the MD Pods.

In addition, Run #3 examined the effect of plate temperature incubation temperature on microbial growth (using duplicate traditional method petri dishes and two identical well-plates having PrestoBlue®). It was observed that the petri dishes and the well-plate incubated at room temperature showed higher and faster microbial growth than the ones incubated at 4ºC. Therefore, all plates in subsequent runs were incubated at

room temperature. Finally, the Live/Dead assay was implemented using the modified approach outlined in Figure 2.32(a) and resulted in the data shown in Figure 2.32(b), and PrestoBlue® did not yield satisfactory results. At this point, it was suspected that autofluorescence was disturbing the fluorescence signals of the Live/Dead and PrestoBlue® assay reagents. Therefore, these assessments were not further investigated with MSB samples associated with *in-situ* incubation runs.

2.3.7.4 Run #4

Run #4 implemented the use of only S-MD Pods in the aquarium and using samples collected directly from the aquarium. The aquarium was prepared using sediment from Location 3 and left for 1 week in the aquarium before sample collection to give time for dormant cells to acclimate. On average, the aquarium exhibited a temperature of 23ºC, a pH of 8.57, and a salinity of 25.7 ppt. Additionally, more sediment was included in the MSB samples due to the same reasons outlined in section 2.3.7.3. The O-ring dispenser was used to assemble all S-MD Pods in this run. Plated contents showed a mixture of the 'contaminants' and grown microbes. Colony counts were, therefore, not implemented due to the difficulty in distinguishing between the 'contaminants' and truly grown microbes. Suspected contamination in this run could be due to the use of the O-ring dispenser, which might splash liquids onto the opposite, unassembled side of the MD Pod (see section 2.3.2).

2.3.7.5 Run #5

Run #5 was implemented in the same way as Run #4, except that it used F-MD Pods for the cell-containing MD Pods and the controls, and one S-MD Pod for each of the controls. The S-MD Pods here were assembled without using the O-ring dispenser.

After plating the MD Pods contents, it was observed that all F-MD Pods did not show growth of the 'contaminants,' while the S-MD Pods did. This indicated that the S-MD Pods did not quite prevent cell migration, and that using the O-ring dispenser could/could not be the source of contamination of the MD Pods used in Run #4.

The grown microbes from Run #5 were observed to have greater diversity and abundance after *in-situ* incubation than those obtained from Run #2 (Figure 2.40). The abundance obtained using traditional plating in Run #5 was 9633 ± 384 cfu/mL for re-suspended MSB, which was higher than that obtained in Run #2 (4400 ± 378 cfu/mL), and 1 ± 0 cfu/mL for encapsulated MSB in Run #5, which was the same as that obtained in Run #2. This could be due to using MSB samples taken directly from the aquarium, as opposed to incorrectly frozen and, likely, dormant MSB. Higher diversity and abundance were also observed before and after the *in-situ* incubation in Run #5 (Figure 2.40(a – d)), which could mean the true success of the MD Pods. This could be due to the inclusion of fine sediment particles with the MSB samples. It could also be due to having a water filter and a sediment aerator in the aquarium, which could have assisted in the diffusion of chemicals and nutrients into the MD Pods. Last but not the least, the higher diversity and abundance could also be attributed to the higher *in-situ* incubation temperature used in the aquarium (23ºC) than that of the sediment box (4ºC). Colonies were not counted after *in-situ* incubation due to their high counts (even at a 10^{-3} dilution). The low abundance of encapsulated MSB samples before *in-situ* incubation could, again, be due to the low number of cells in the microbeads, which made it difficult for the cells to grow into colonies without *in-situ* incubation. The abundance shown on the control plates (Figure 2.40(e and f)) was not diverse. Therefore, when subtracted from the total number

of species grown after *in-situ* incubation, the true ability of the MD Pod to support the growth of different types of microbes could be known.

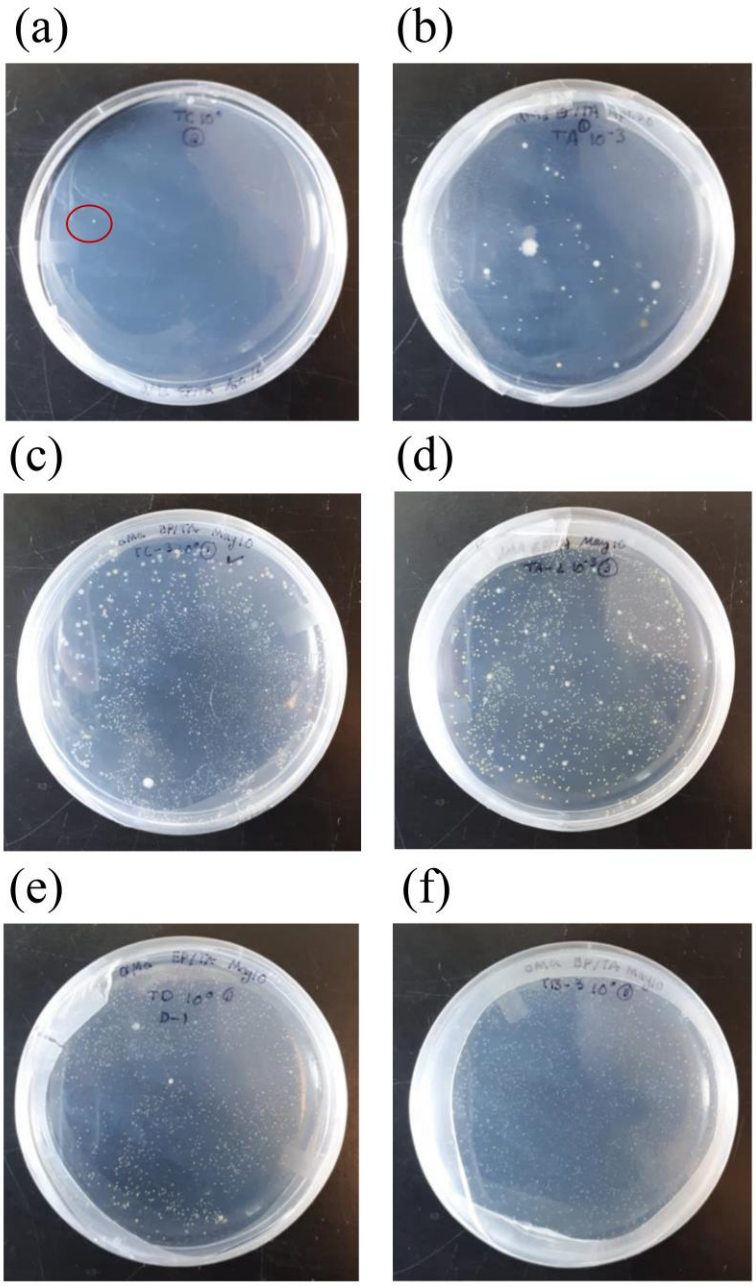

Figure 2.40: Representative plates of microbes grown from Run #5 after 2 weeks of plating. (a) Traditional plating of encapsulated MSB, 10^0 dilution. A single colony was observed and indicated. (b) Traditional plating of re-suspended MSB, 10^{-3} dilution. (c) Encapsulated MSB after *in-situ* incubation, 10^0 dilution. (d) Re-suspended MSB after *in-situ* incubation, 10^{-3} dilution. (e) Blank microbeads control plate after *in-situ* incubation, 10^0 dilution. (f) FSS control plate after *in-situ* incubation, 10^0 dilution.

2.3.8 Cell diversity

2.3.8.1 PCR process verification

The DNA of four re-suspended MSB samples obtained from Location 2 was extracted and amplified. Nested PCR was performed using Primer Sets A, B, and C according to the procedures outlined in section 2.2.9.2 and using a 25 μL reaction mixture. The PCR products were then run on a 1% agarose gel for amplification verification and DNA fragment size determination (Figure 2.41). This procedure was repeated three times for verification. Through the gel shown in Figure 2.41, it could be observed that Primer Set A resulted in easily-identifiable bands across lanes 1 – 4 (each lane contains the DNA of one MSB sample). In contrast, Primer Set B was observed to amplify the DNA of some of the samples (e.g. lane 9), moderately amplify others (e.g. lanes 8 and 10), or to provide no readable results (e.g. lane 7). No readable results were obtained using Primer Set C (lanes 13 – 16). Therefore, Primer Set A was used for the remainder of PCRs in this thesis. It was also observed that the size of the produced DNA fragments using Primer Set A was approximately 500 bps when compared to the DNA ladder, which matched the final amplicon length outlined in Table 2.5 (507 bps). Nonspecific amplification was also observed for Primer Set A, which could be attributed to having a high DNA template and/or a high primer concentration, using more than necessary annealing cycles, and/or the assembly of amplification reactions at the time of combining the reagents. Furthermore, it could be seen through the gel that Control 1 (lanes 5 and 6) and Control 2 (lanes 11 and 12) contained amplified DNA, which could be from cross-contamination. Even though Control 3 did not show bands (lanes 17 and

18), it cannot be considered not contaminated because its corresponding reaction did not yield bands.

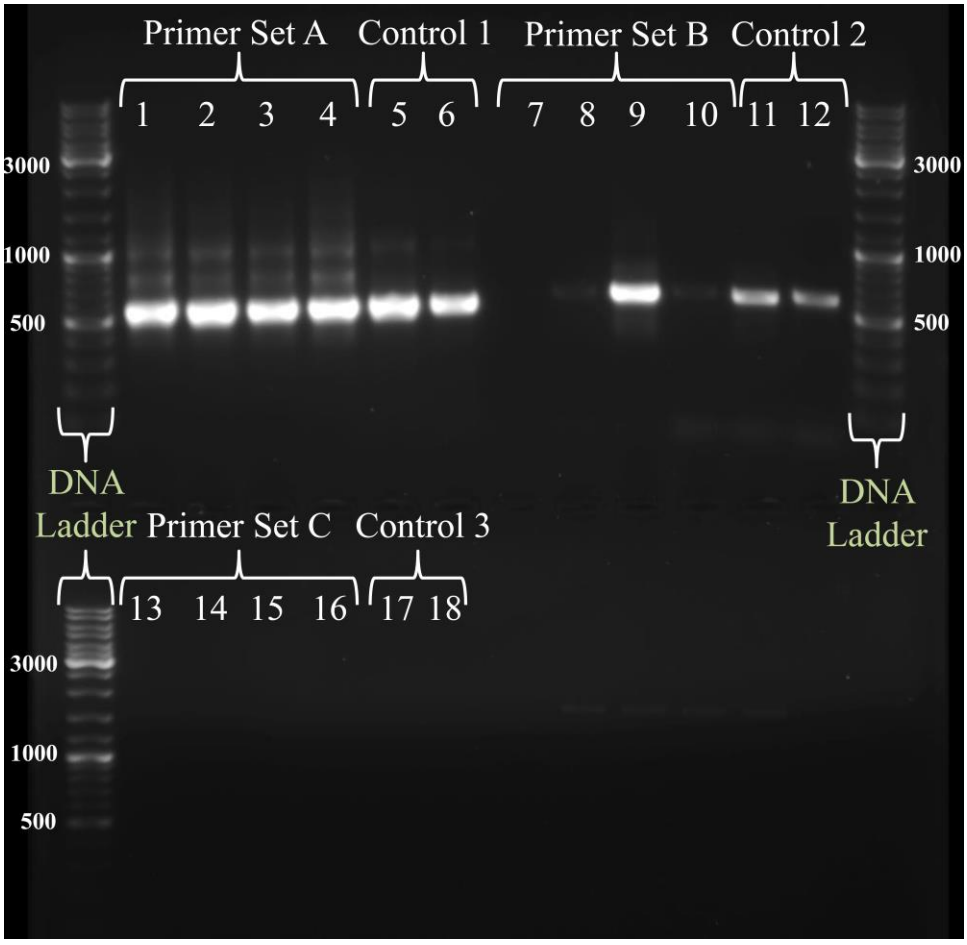

Figure 2.41: PCR products of single samples of four re-suspended MSB samples that were amplified using Primer Sets A, B, and C and viewed using BioSpectrum®. Controls were sterile DI water samples amplified according to the respective parameters of each primer set. A DNA ladder was used as a marker for DNA fragment size.

Next, the DNA of the known PE marine bacteria and *E. coli* was extracted and amplified using Primer Set A. The products of the initial PCR and the nested PCR were each run on a 1% agarose gel (Figure 2.42). A dilution of the initial PCR products (1:10) was also run on the gel. The lanes from left to right in each PCR product section on the gel correspond to *M. polaris* (lanes 1, 7, and 13), *P. aquimaris* (lanes 2, 8, and 14), *B. licheniformis* (lanes 3, 9, and 15), and *E. coli* (lanes 4, 10, and 16). It could be seen

through the gel that the initial PCR resulted in bands corresponding to approximately 1500 bps, which match the expected size (1498 bps). The same was observed after the nested PCR (approximately 500 bps for an expected 507 bps). The diluted initial PCR products show more distinct bands that were easier to read and correlate to a certain DNA size. In fact, dilution is observed to result in more bands on DGGE gels [339]. Therefore, all PCR products of the MSB samples were diluted before DGGE was performed. Additionally, it could be observed through the gel that Control 1 (lanes 5 and 6) did not result in any bands, meaning that the initial PCR was, in fact, free of contamination. However, Control 2 showed a band at lane 11, which contained the PCR product of a sterile DI water sample that went through both PCR steps, through which it might have picked up contamination. Nonetheless, lane 12 contained the PCR product of a sterile DI water sample that underwent the nested PCR only. Therefore, both reactions were free from contamination and/or error individually.

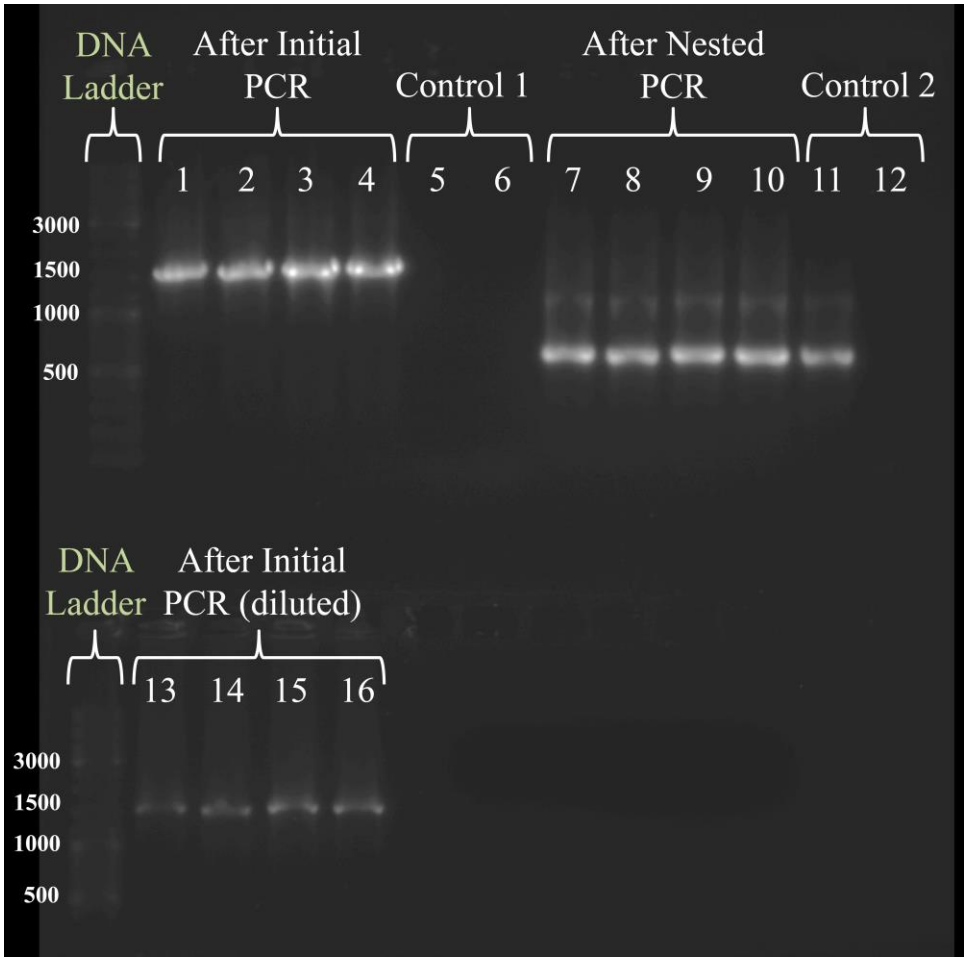

Figure 2.42: PCR products of *M. polaris*, *P. aquimaris*, *B. licheniformis*, and *E. coli* using the initial and nested PCR products using Primer Set A. Viewed using BioSpectrum®.

The final step in verifying the PCR process parameters was to determine the effect of purifying DNA after PCR. The initial PCR products of the three known marine bacteria were purified using EZ-10 Spin Column PCR Purification Kit (Bio Basic Inc., Canada) according to the manufacturer's protocols. The DNA concentration was then measured using NanoDrop® at 260 nm and normalized to approximately 50 ng/µL before nested PCR was performed. The nested PCR products were then run on a 1% agarose gel with triplicate samples for each species (Figure 2.43). It could be observed through the gel (lanes 1 – 9) that clearer and more distinct bands (at approximately 500 bps) resulted due to the DNA purification. This could be attributed to removing the nucleotides and the

primers existing in the initial PCR product, which could disturb the following nested PCR. The purification step also removes unincorporated nucleotides from the reaction mixture, which enables reading the DNA concentration using a spectrophotometer and, hence, the normalization of the concentrations before performing the nested PCR. In addition, the initial PCR products were diluted through the DNA elution step during purification. Therefore, the PCR products to be used for DGGE analysis of MSB samples were not diluted 1:10. The controls, which were run through both PCRs, did not show any contamination using this purification process (lanes 10 – 12).

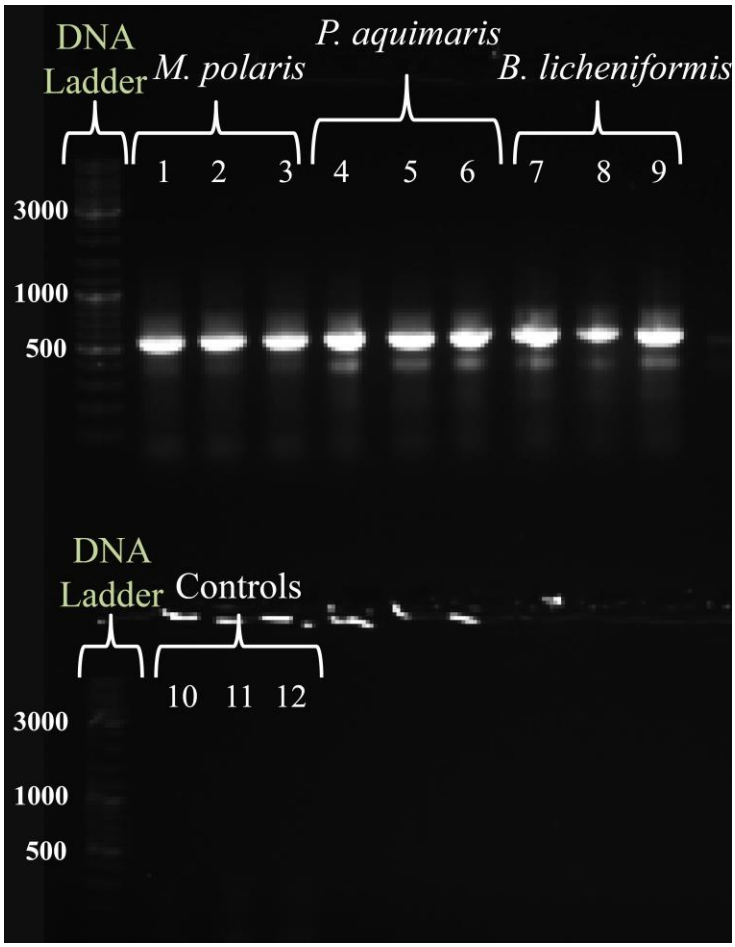

Figure 2.43: Nested PCR products of triplicates of *M. polaris*, *P. aquimaris*, and *B. licheniformis* (left to right) after purification of the initial PCR products. Viewed using BioSpectrum®.

2.3.8.2 DGGE of marine sediment bacteria before and after MD Pod *in-situ* incubation

The PCR products obtained for *M. polaris*, *P. aquimaris*, and *B. licheniformis* were run on an acrylamide gel as outlined in section 2.2.9.3. The obtained image (Figure 2.44) showed that the three species yielded different bands that could be distinguished from each other (lanes 1 – 9). However, a mixed sample of the PCR products of the three species yielded two bands (lane 10), which meant that inaccurate determination of the number of species present in a mixed environmental sample is possible since different species might show up as one band through DGGE. The third sample of *B. licheniformis* (lane 9) was not injected properly into the DGGE gel (human error) and, therefore, did not denature correctly.

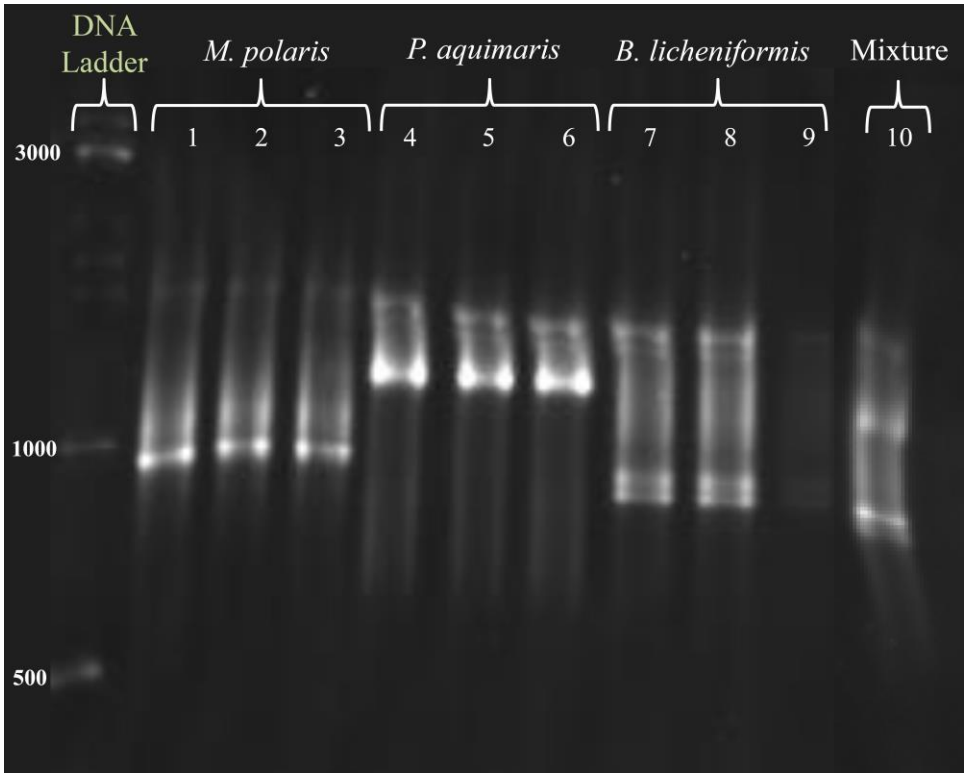

Figure 2.44: DGGE result of triplicates of *M. polaris*, *P. aquimaris*, and *B. licheniformis* (left to right) after purification of the initial PCR products. A mixed sample of the three species is indicated. The gel was viewed using BioSpectrum®.

After confirming the applicability of using DGGE with known MSB, the DNA of the samples obtained from *in-situ* incubation Run #5 and their respective MSB used before the *in-situ* incubation was extracted and amplified as explained in section 2.3.8.1. DGGE was then performed using the PCR products, with the initial PCR products purified and 1 μL of these was used as the DNA template in the nested PCR (with a 50 μL reaction volume). The obtained gel was then analyzed using BioNumerics 6.6 (Figure 2.45). Through the cluster tree, it could be observed that duplicates of certain samples returned very close results (e.g. A.1-1 and A.1-2, and C.1-1 and C.1-2). This confirmed that the DGGE was performed correctly on the used samples. Additionally, some samples showed close relations through the cluster tree, such as C.2 and C.3 with D.2, in which D was the control for C, and B.1 and B.2 with A.2, in which B was the control for A. Although these results seemed plausible, the fact that D.1 existed in the same branch as A.2, B.1, and B.2 made the results questionable, since B and D should not contain organisms in the first place. Furthermore, it could be observed that the duplicates of A.1 and C.1 closely matched with the MSB before *in-situ* incubation, which seemed plausible. However, the FSS showed a close similarity to the MSB before *in-situ* incubation (99.2% similarity through pairwise comparison in BioNumerics 6.6), which nullified the observations made, not to mention that the A.1 and C.1 duplicates were on a completely different branch than A.2, C.2, and C.3. Therefore, unfortunately, the contamination incurred in the MD Pods in Run #5 was significant and negatively altered the desired outcomes.

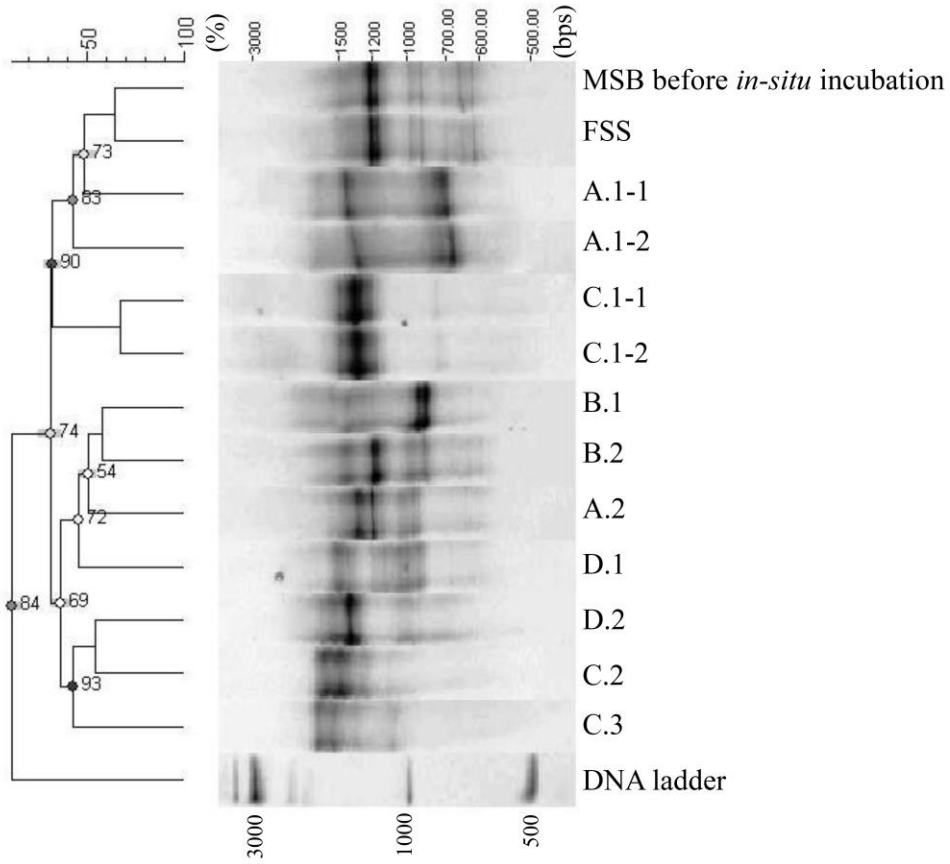

Figure 2.45: DGGE results obtained for samples collected from *in-situ* incubation Run #5, with a software-generated cluster tree based on band size similarity (BioNumerics 6.6). Numbers on the cluster tree represent percent similarity between the branches. A.1 and A.2 were samples taken from two different MD Pods containing encapsulated MSB. B.1 and B.2 were samples taken from two different MD Pods containing blank microbeads. C.1, C.2, and C.3 were samples taken from three different MD Pods containing re-suspended MSB. D.1 and D.2 were samples taken from two different MD Pods containing FSS. All of the A, B, C, and D samples were from MD Pods that were *in-situ* incubated. The MSB and FSS shown in the image did not go through the *in-situ* incubation and were used to serve as a comparison for the effect of *in-situ* incubation on the microbial community fingerprint.

CHAPTER 3 : MINERAL OIL REMOVAL FROM A MICROFLUIDIC DROPLET GENERATION SYSTEM USING A HYDROPHOBIC-OLEOPHILIC MATERIAL

3.1 Introduction

In general, droplet generation in microfluidic devices is often achieved through the use of the shear stress of an oil phase on an aqueous phase. As discussed earlier in Chapter 1, oil can cause lower cell viability after encapsulation when washed off-chip [48]. It was also observed to cause aggregation of the collected microbeads during the work performed in Chapter 2, not to mention the commonly-faced problem of imaging the microbeads after washing (Figure 3.1). Therefore, developing an efficient method for mineral oil removal was needed. In this thesis, oil was attempted to be removed after completion of droplet generation. Two systems were built and tested for their separation efficiency of oil/water mixtures.

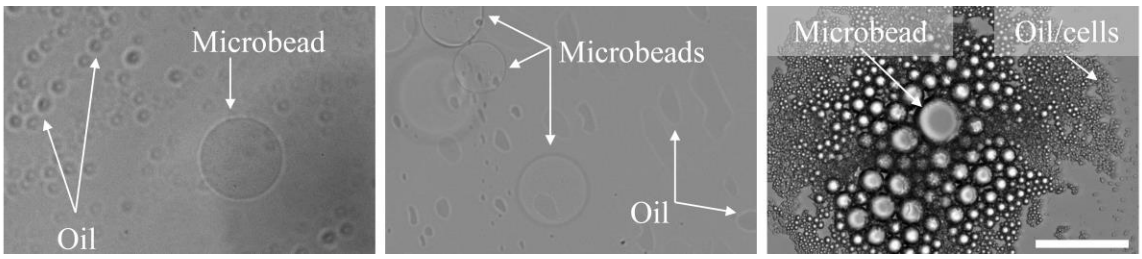

Figure 3.1: Representative images of mineral oil disturbing the imaging and identification of microbeads after they were washed with FSS. Imaged using bright field imaging, Cytation™ 5. Scale bar is 100 μm.

3.2 Materials and Methods

3.2.1 Vacuum-assisted oil removal system

3.2.1.1 Separation device fabrication

In the vacuum-assisted oil removal system, oil/water separation was achieved through precise control of pressure drop across a hydrophilic-oleophilic treated membrane. The membrane used was a 1.59 mm thick, porous, 316L stainless steel disc that is capable of removing particles ≥10 μm in size, according to the manufacturer (McMaster-Carr, USA). It was treated with 1 mL of WaterSlip NE (Cytonix, USA). After 5 mins, the WaterSlip NE was removed and the membrane coating was left to cure in a closed container for one week. After that, the membrane was tested for its oil permeability and water impermeability by placing a drop of each liquid on the membrane's surface.

After curation, the membrane was placed in a 3D printed separation device (Figure 3.2(a)), which was designed using CAD software (Figure 3.2(b)) and fabricated from Clear resin (Formlabs, USA) according to the steps outlined in section 2.2.1. The separation device was composed of an inlet (through which the oil/water mixture entered), a curved region (with the membrane placed at its tangent to achieve better contact of the oil on the membrane), an oil outlet (underneath the membrane to allow for the oil to exit), a multi-curved region (to add resistance for the flowing liquids), and a water outlet (to collect the water, ultimately with microbeads). All internal channels were 3 mm x 4 mm and were 3D printed without using internal supports.

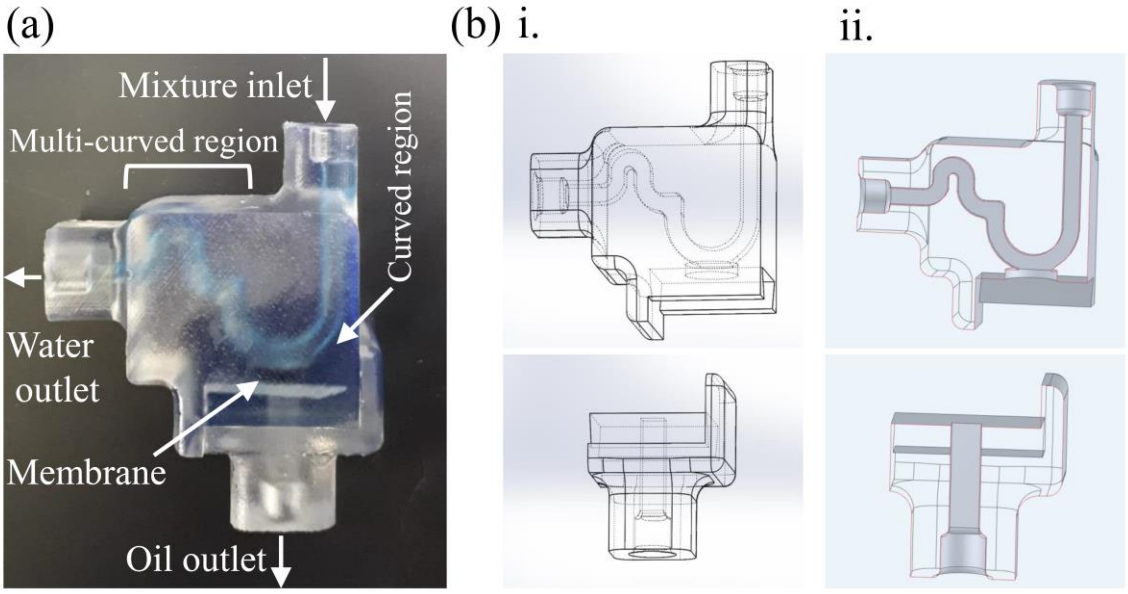

Figure 3.2: (a) 3D printed oil/water separation device equipped with internal channels and a hydrophobic-oleophilic treated membrane. (b) i. CAD design and ii. longitudinal cross-section of the oil/water separation device.

The membrane was fitted inside the separator using an x-profile O-ring (McMaster-Carr, USA) to provide sealing (Figure 3.3(a)). Moreover, the membrane was placed inside the separator through a modular feature (Figure 3.3(b)), which allowed for coupling the oil outlet while providing seal. The shape and dimensions used for the modular feature were inspired by previous literature [57], in which seal was achieved by using 60°/120° for all angles. It should be noted that no supports should be placed on the internal side of the modular feature during 3D printing. This will create rough surfaces which will not ensure seal. A similar separation device was also fabricated according to this procedure but equipped with internal channels that passed twice over the membrane (Figure 3.3(c)) in an aim to achieve greater separation using one device.

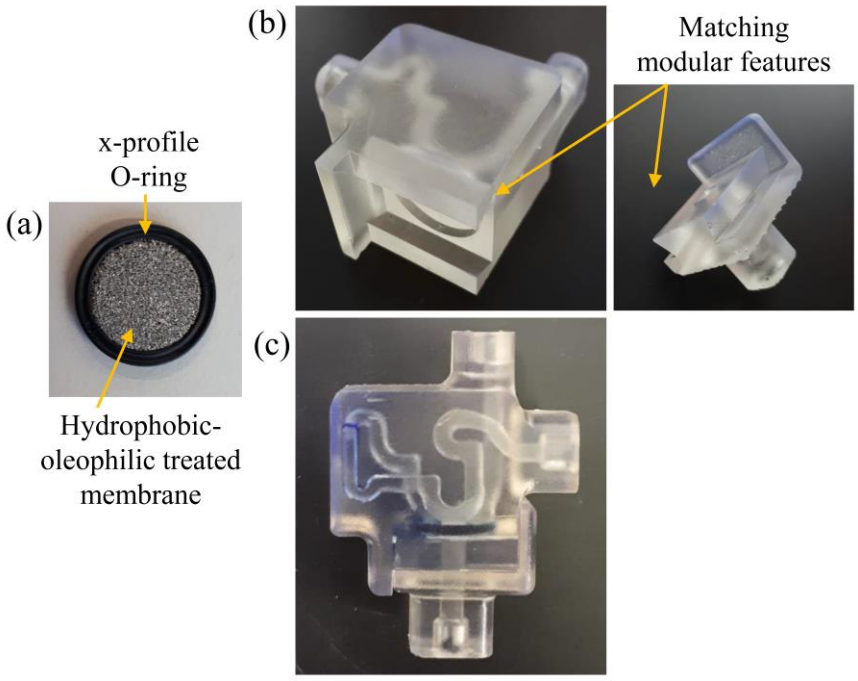

Figure 3.3: (a) An x-profile O-ring surrounding a porous 316L stainless steel membrane treated with a hydrophobic-oleophilic coating. (b) Modular features of the separation device. (c) A separation device containing double-twisted internal channels that pass twice over the membrane.

3.2.1.2 Vacuum pressure control system

Pressure drop across the membrane was controlled using a vacuum pressure control system (Figure 3.4). Vacuum pumps were used to provide vacuum (5 cfm, 15500 VacuMaster, Robinair, USA). Vacuum pressure at the oil and water outlets was controlled using vacuum regulators (SMC Corporation, Japan) and was monitored using vacuum gauges (McMaster-Carr, USA). Vacuum flow rate for these outlets was controlled using a precision needle valve (McMaster-Carr, USA). For proof of concept, the water and oil were injected into the system through a Y-junction to provide mixing and they were input using syringe pumps (Chemyx Fusion 100, USA). The oil phase flow rate was always set at 115 mL/hr, since this is the flow rate of the outlet of the microfluidic chip (see section 2.2.4.1). The variables to investigate were the water inlet

flow rate, the vacuum pressure at the oil outlet, and the vacuum pressure at the water outlet. Throughout this section and the following section, mineral oil was colored with a blue oil-soluble dye (FastColours, United Kingdom) for easy visualization and distinction between the two phases. Separation efficiency was calculated based on the water volume:total volume collected at the water outlet.

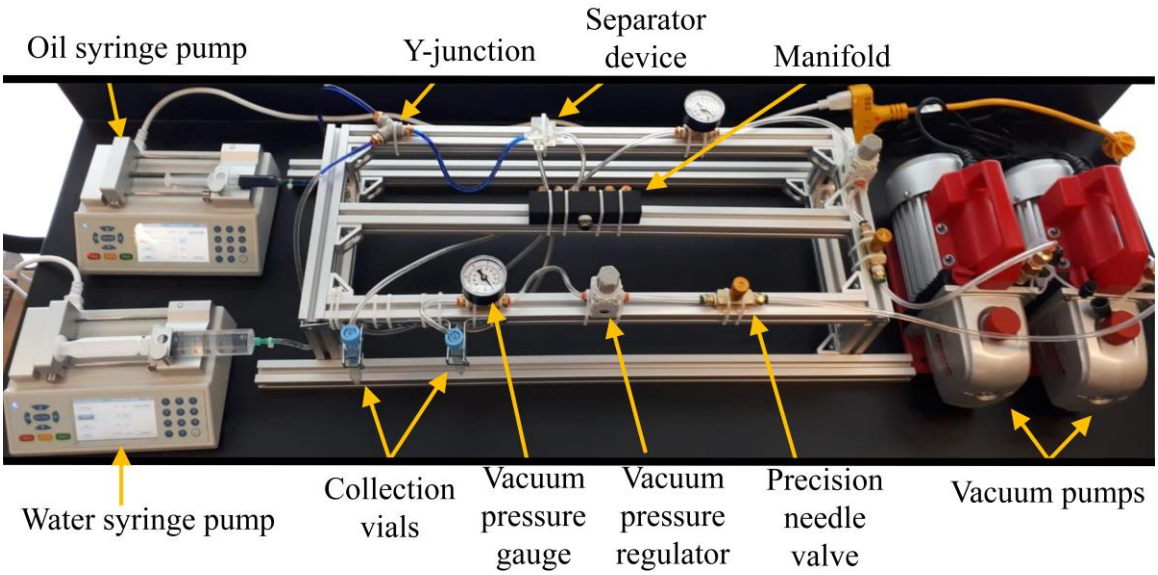

Figure 3.4: The vacuum pressure control system used to complement the oil/water separation device. A manifold was added for connecting multiple separator devices if needed.

3.2.2 Cartridge filter-inspired oil removal system

Cartridge filters are commonly used for water treatment applications [356]. Since cartridge filters enable the incorporation of a sorbent material, their working principle inspired the design of an oil/water separation column containing a sorbent (Figure 3.5(a)). The sorbent material used is an 'oil-only' absorbent pad that is pre-treated to absorb oil and retain water (Sorbent Pad, Oil Only, CAN-ROS, Acklands Grainer, Canada). The column was designed (Figure 3.5(b)) and 3D printed according to the same procedure outlined in section 2.2.1.

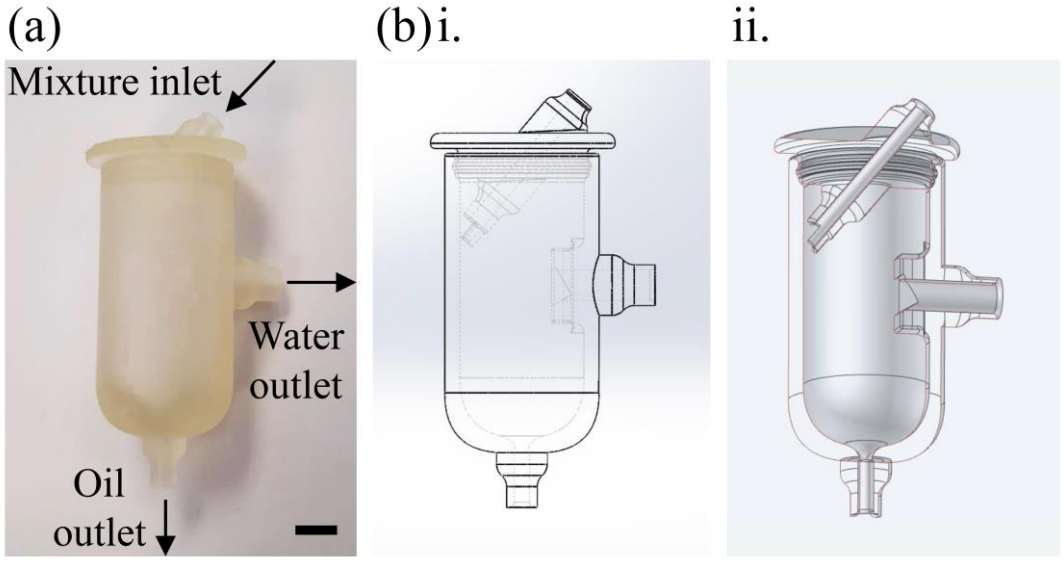

Figure 3.5: (a) 3D printed oil/water separation column. Scale bar is 10 mm (b) i. CAD design and ii. longitudinal cross-section of the oil/water separation column.

The designed column was composed of an oil/water mixture inlet that is tilted towards the absorbent pad to prevent the mixture from dripping into the cavity of the column. Through this way, the oil gets directly absorbed into the pad and exits through the bottom oil outlet (the pad should be fully saturated with mineral oil before beginning the separation for effective absorption to take place). Additionally, water entering the column travels down the outer surface of the absorbent pad and collects in the cavity of

the column. When the water level reaches the water outlet, it starts flowing out. To make this flow more efficient, the column is to be tilted at 45° towards the water outlet side during separation. It should be noted that that the column should be placed at an elevation higher than that of the water and oil collection vials to enable free flow into these vials (Figure 3.6). Separation efficiency was also calculated based on the water volume:total volume collected at the water outlet.

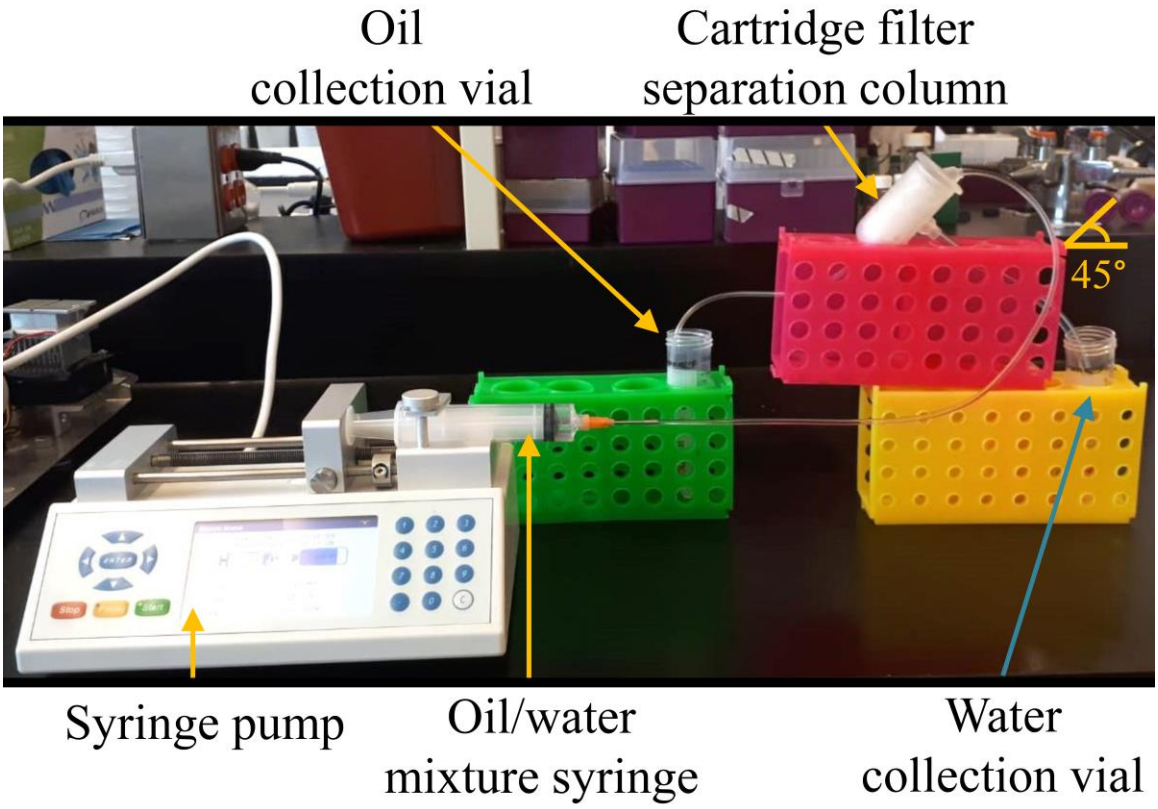

Figure 3.6: Setup of the oil/water separation column, with the column placed at a higher elevation than that of the water and oil collection vials. The column was tilted at 45° towards the water outlet side during separation.

3.3 Results and Discussion

3.3.1 Vacuum-assisted oil removal system

Through manipulation of the of the water inlet flow rate, the vacuum pressure at the oil outlet, and the vacuum pressure at the water outlet, the separation efficiency was calculated (Table 3.1). It could be observed that at equal inlet water flow rates (115 mL/hr) and decreasing vacuum pressure at the oil outlet, the separation efficiency somewhat increased (Tests #1 – 5). When the inlet water flow rate (230 mL/hr) was double that of the inlet oil flow rate (115 mL/hr), separation efficiency decreased with decreasing vacuum pressure at the oil outlet (Tests #7 – 9). When the inlet water flow rate (60 mL/hr) was approximately half that of the inlet oil flow rate (115 mL/hr), separation efficiency increased when the vacuum pressure at the oil outlet was decreased (Tests #10 and 12). Although Test# 5 resulted in the highest separation efficiency (71%), it was not repeatable (using the same parameters, repeating this test resulted in 50% separation efficiency). Moreover, it should not be neglected that oil still existed at the water outlet. Therefore, the setup should be modified to take into account these issues. Last but not the least, the separation device equipped with internal channels that passed twice over the membrane did not yield the results anticipated (data not shown). Therefore, it was not further investigated.

Table 3.1: Separation efficiency results obtained through changing several parameters using the vacuum-assisted oil removal system.

Test #	Phase	Inlet Flow Rate (mL/hr)	Outlet Vacuum Pressure (-in. Hg)	Volume Collected at Water Outlet (mL)	Separation Efficiency (%)
1	Oil	115	9	4	43
	Water	115	0.5	3	
2	Oil	115	8	1.5	25
	Water	115	1.5	0.5	
3	Oil	115	5	3	50
	Water	115	1.25	3	
4	Oil	115	4.5	3	50
	Water	115	1.25	3	
5	Oil	115	4	2	71
	Water	115	2	5	
6	Oil	115	9	2.5	38
	Water	175	0.5	1.5	
7	Oil	115	5	3	65
	Water	230	1.25	5.5	
8	Oil	115	4	7.5	63
	Water	230	2	12.5	
9	Oil	115	3	5	17
	Water	230	1	1	
10	Oil	115	5.5	4	20
	Water	60	0.75	1	
11	Oil	115	4	3	50
	Water	60	2	3	
12	Oil	115	3	6	48
	Water	60	1	5.5	

The setup was adjusted by adding more separators in series in an aim to remove more oil from the system (Table 3.2). Additionally, the inlet oil flow rate was decreased to give more time for the membrane to absorb oil, since it was noticed that at 115 mL/hr, the phases passed quickly over the membrane. No vacuum was applied to the water outlet side since it caused the mixture to flow out of the system without enough separation. It could be observed that using more separators, in fact, increased the separation efficiency compared to using only one separation device. Therefore, to further increase the separation efficiency using the least complex system, two separators in series were

chosen to compose a system of two parallel separation lines, with each line containing two separators in series (Figure 3.7). Using -5 in. Hg for the first set of separators and -10 in. Hg for the second set of separators (same as the vacuum pressures used with only two separators in series), the obtained separation efficiency was 60%. Hence, using only two separators in series at -5 in. Hg and -10 in. Hg, respectively, was observed to result in the highest, repeatable separation efficiency. Bearing in mind that this system still contained oil in the collected product, it was not ideal for the intended application. Additionally, when considering the inclusion of microbeads in the inlet oil phase, it was suspected that the pressure drop across the membrane will cause the microbeads to clog the pores of the membrane and/or not have sufficient time to transfer into the water phase. Therefore, given the high complexity and uncertainty incurred with this system, the cartridge filter-inspired oil removal system was built and tested.

Table 3.2: Separation efficiency results obtained through using multiple separation devices in series.

Number of separators in series	**Phase**	**Inlet Flow Rate (mL/hr)**	**Outlet Vacuum Pressure (-in. Hg)**	**Volume Collected at Water Outlet (mL)**	**Separation Efficiency (%)**
2	Oil	25	Separator 1: 5 Separator 2: 10	2.5	76
	Water	50	Open to atmosphere	8	
3	Oil	25	All separators: 7	3.5	76
	Water	50	Open to atmosphere	11	
4	Oil	25	Separators 1 and 2: 9 Separators 3 and 4: 7	4	65
	Water	50	Open to atmosphere	7.5	

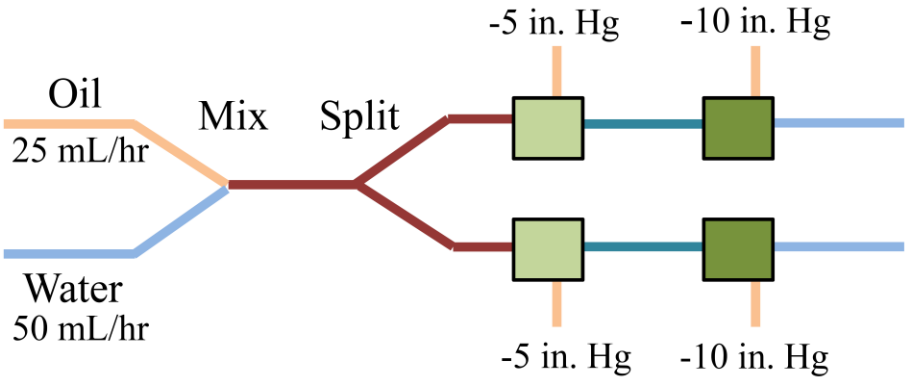

Figure 3.7: An oil/water separation vacuum-assisted system with two parallel lines, each containing two separation devices in series. Orange lines indicate oil, blue lines indicate water, and other line colors indicate a mixture of oil and water. The vacuum pressure at the oil outlet of the first set of separators (light green) was set at -5 in. Hg, while that at the second set of separators (dark green) was set at -10 in. Hg.

3.3.2 Cartridge filter-inspired oil removal system

For proof of concept, the sorbent pad was tested for its 'oil-only' property by using a 5 cm x 5 cm piece to separate 50 mL of blue-colored mineral oil from 100 mL of water (Figure 3.8(a)). Through repeated dipping and squeezing of the sorbent pad into a different beaker, the solutions were 100% separated (Figure 3.8(b)), providing grounds for proceeding with designing and using the cartridge filter separation column. The sorbent pad was also tested after being autoclaved; a 100% oil:water separation was achieved, indicating that the sorbent pad could be sterilized for potential use with cells.

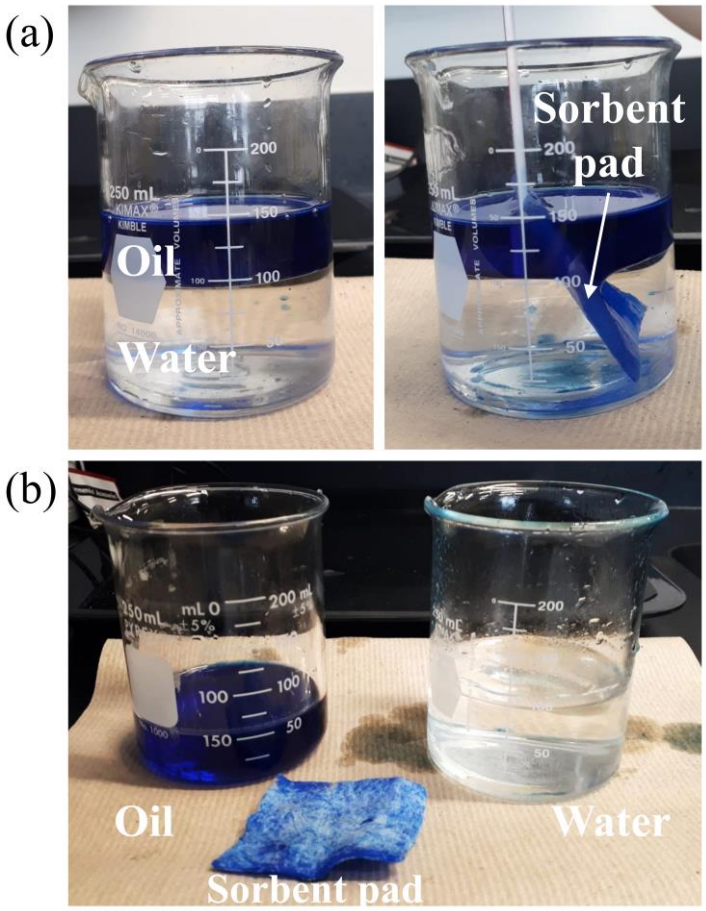

Figure 3.8: Confirming the 'oil-only' property of the absorbent pad to be used in the cartridge filter separation column. (a) A 1:2 oil (blue):water (transparent) emulsion to be separated through repeated dipping and squeezing of a 5 cm x 5 cm sorbent pad. (b) Final solutions obtained after separation using the sorbent pad.

In this system, separation of oil and water was implemented with and without having microbeads in the oil phase. With no microbeads in the oil phase and at 20 mL/hr flow rate of an equal oil and water volumes mixture, the separation efficiency was approximately 96% ±2. Therefore, proceeding to testing with the microbeads in the oil phase was legitimate.

Microbeads were formed according to the outlined procedure in section 2.2.4.1. However, the agarose was dyed with 1 mg/mL of Alcian blue (Sigma Aldrich, USA) for ease of visualization and were left in the mineral oil after formation (no washing implemented; refer to Appendix C for details about agarose-coloring dyes). The mineral oil was not dyed blue at this point onwards. After microbead formation, two 1 mL samples were taken to quantify the microbead concentration before separation (Figure 3.9(a)). Afterwards, exact volumes of oil and water were mixed and loaded into a syringe. The syringe mixture flow rate into the separation column was 20 mL/hr, and the sorbent pad was pre-saturated with mineral oil. The obtained liquid through the water outlet contained foam, which inhibited the visualization of microbeads (Figure 3.9(b)) and the volume ratio of oil:water, if any. The foam was suspected to be a result of using Span® 80 in the mineral oil during droplet formation. To confirm that the separation column actually provides oil/water separation while transferring the microbeads from the oil phase to the water phase, the obtained foamy solution was poured over a cell strainer and washed with 5 mL of water and mixed with a 1 µL loop to remove the foam. The top of the strainer was then carefully washed with 1 mL of water and samples were taken for observation (Figure 3.9(c) i. and ii.); 60 microbeads were observed in 100 µL of the solution. Therefore, using this separation column could provide an easier, single step

route to removing mineral oil after microbead formation. It should be noted that care must be taken if a loop (or a sterile stick) is to be used to move the microbeads over a cell strainer to fasten the straining process, since the microbeads could 'burst' due to their fragility (Figure 3.9(c) iii.).

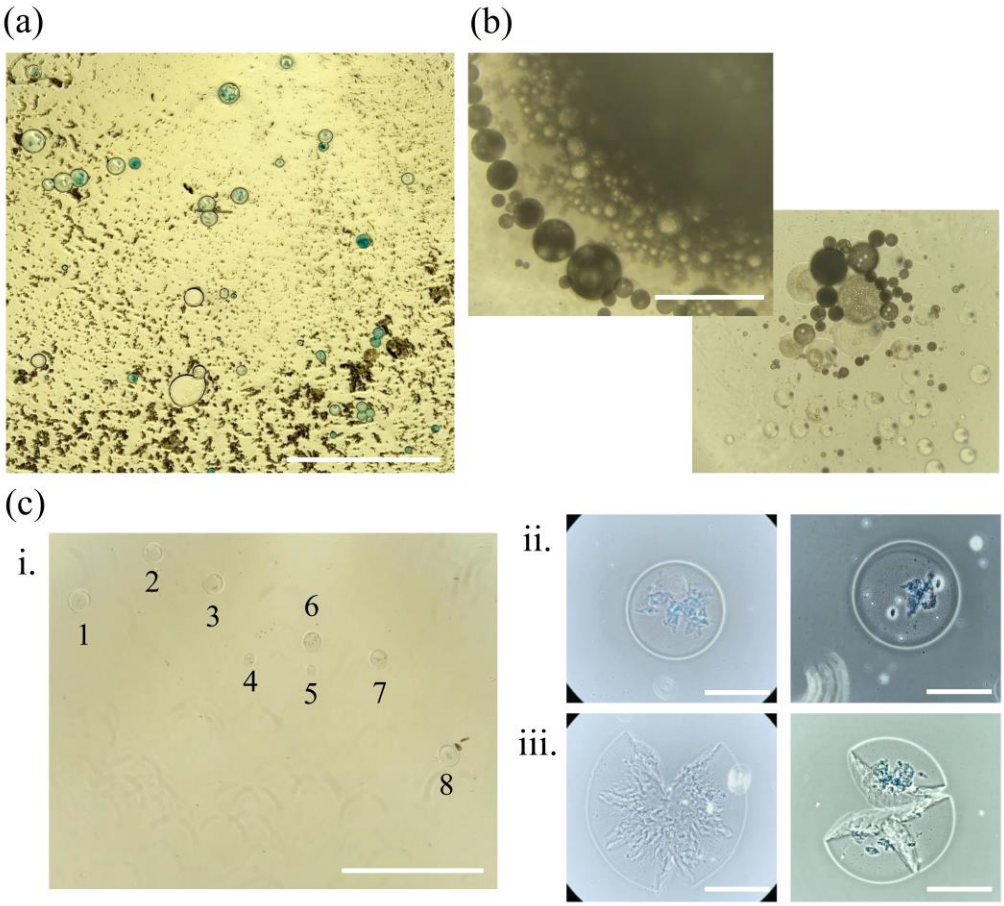

Figure 3.9: Images of the microbeads before and after oil removal using the cartridge filter-inspired oil removal system. (a) Images of the microbeads in oil before separation. Circular objects with blue hue represent the microbeads to be separated. Dirt particles were observed due to microbead generation under nonsterile conditions. Scale bar is 1110 μm. (b) Images of samples taken after separation using the cartridge filter-inspired oil removal system, with oil and foam inhibiting the distinguishability of microbeads, oil droplets, and/or surfactant droplets. Scale bar is 370 μm. (c) i. Eight microbeads observed after washing the solution obtained through the water outlet of the separation column. ii. Zoomed in microbeads obtained after the separation. iii. Zoomed in 'burst' microbeads obtained after the separation due to using a loop to move the microbeads over the cell strainer. Scale bar in i. is 1870 μm and 190 μm in ii. and iii. All images are taken using Revolve 4.

CHAPTER 4 : FABRICATION OF MICROFLUIDIC CHIPS USING CONTROLLED DISSOLUTION OF 3D PRINTED SCAFFOLDS

4.1 Introduction

To the best of the author's knowledge, there is no literature involving the study of ABS dissolution in acetone to obtain smaller channels for use with ISR. Hence, in this thesis, the addition of a controlled ABS scaffold dissolution step in acetone before placement in PDMS to fabricate microfluidic chips was proposed, resulting in a method called enhanced ISR, or eISR (Figure 4.1). It is known that ABS is soluble in acetone. Multiple studies have investigated the effect of acetone vapor smoothing [308,309] and acetone bath soaking [310] on the surface properties of ABS parts. Here, ABS channels of a known initial width, 1000 μm ± 55 μm, were printed using a commercial FDM 3D printer with a 400 μm nozzle head. The channels were placed in a bath of acetone for a certain amount of time until desired channel sizes were obtained. The channels were then dried, washed in DI water, and placed in a 3D printed mold chamber containing liquid PDMS for further processing. PDMS was used in this study due to its extensive use in microfluidic chip fabrication and because it is relatively unharmed by acetone [307]. This chapter examined the effect of agitation forces, time, and multiple washing steps on the final dimensions and surface topography of ABS scaffolds. Droplet generation was obtained and evaluated using a T-junction microfluidic device. Finally, the optimal conditions were used to fabricate microfluidic chips with different channel geometries.

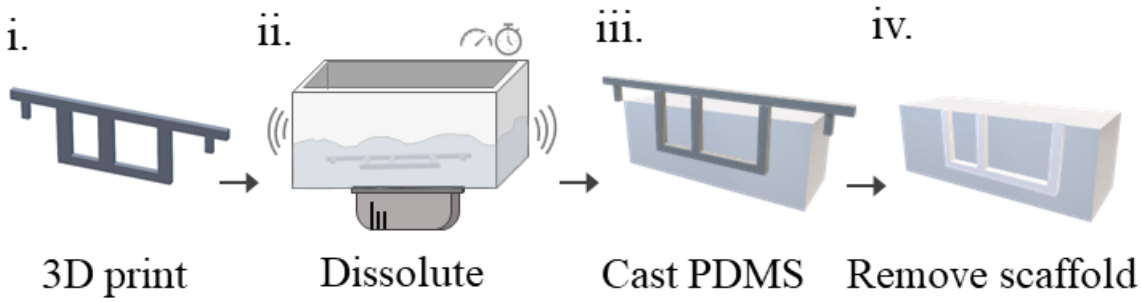

Figure 4.1: Workflow of the enhanced internal scaffold removal (eISR) method for microfluidic chip fabrication. (i) The scaffold was 3D printed using ABS, with a holder on top to place the channels inside the PDMS mold. It is recommended to have 'thick holders' (2.4 mm × 2.4 mm) to eliminate the need for punching inlets and outlets. (ii) The scaffold was dissoluted in 100% acetone for a certain duration and at a set frequency. The scaffold was carefully removed from the dissolution bath and left to dry at room temperature, after which it was washed in a bath of DI water. (iii) The scaffold was placed in a casting chamber. Then, PDMS was poured, cured, and carefully removed from the casting chamber. (iv) The ABS scaffold was completely dissolved in a bath of 100% acetone, resulting in sealed, hollow channels in the PDMS structure.

4.2 Materials and methods

4.2.1 3D printing

Channels used to quantify the extent of dissolution were of T-junction geometry (Figure 4.2(a)). T-junctions have the simplest shape of a microfluidic chip used for droplet generation using the pressure exerted on a dispersed phase by a continuous phase [357]. Other geometries were also developed in this chapter after identification of optimal dissolution parameters. The scaffolds used in this chapter were designed using CAD software with square channels of 800 µm width. The scaffolds were 3D printed using a Zortax M200 3D printer (Zortax, USA), with a 400 µm nozzle head and using a 1.75 mm ABS filament (Zortax, USA). The following settings were used: 0.19 mm layer thickness, 6 mm/3 mm top/bottom surface layers, 100% infill density, and no supports. All scaffolds were attached to 'thick holders' (Figure 4.2(b)) with 2.4 mm x 2.4 mm to suspend the scaffolds in PDMS and 'thick inlets' to eliminate the need for punching inlets and outlets after PDMS cures. These dimensions allow for a snug fit of 3/32" OD Tygon tubing in the fabricated microfluidic device. It is recommended to use grayscale colors of ABS filament since colored ABS tended to partially dye the PDMS structure. 2D structures (such as T-junction geometries) were printed flat on the printing bed, while structures involving printing in 3D space (such as the bifurcation and drug testing channels) were cut from the location where channels were connected to the 'thick inlets' and were later attached together using ABS glue (prepared as 16% (w/v) ABS: acetone). Bifurcation and drug testing channels were designed using CAD software based on figures illustrated elsewhere [271,358].

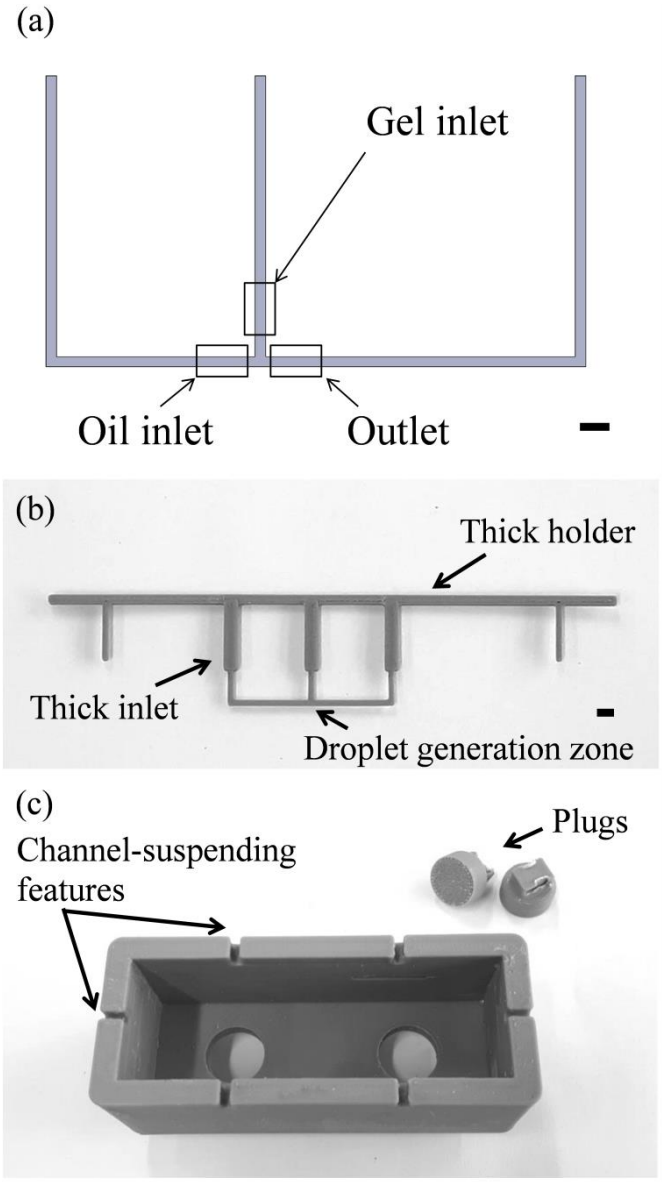

Figure 4.2: Scaffolds used to assess ABS dissolution properties and the chamber used to cast PDMS. (a) A T-junction scaffold was used to quantify the extent of dissolution under different parameters outlined in this chapter. Three locations of the scaffold were used for channel dimension measurement: the dispersed phase inlet to the T-junction (gel inlet), the continuous phase inlet to the T-junction (oil inlet), and the outlet of the T-junction (outlet). These annotations were used in subsequent graphs in this chapter. Scale bar is 2.3 mm. (b) A 3D printed T-junction scaffold with 'thick holders' and 'thick inlets' used for fabricating a T-junction microfluidic device using eISR. Scale bar is 2.4 mm. (c) The chamber used to cast PDMS, with features at the top to aid in suspending the channels in PDMS during curing. Internal chamber dimensions are the same as a standard glass slide, 75 x 25 mm, to allow for lining the PDMS device with glass slides to obtain the best optical properties. The bottom of the chamber has two holes to allow for ejecting the microfluidic device out of the chamber after PDMS is cured. The holes were closed using circular plugs.

4.2.2 Imaging

Initial and final channel dimensions were observed using a bright field microscope (CHT, Olympus, USA) and measured using ImageJ software. Three locations of the channels were used to quantify the extent of dissolution (Figure 4.2(a)), with three measurements recorded at each location. The three locations were chosen to provide three data points of channels that, theoretically, should end up with the same dimensions after dissolution. Although the designed channel width in CAD software was 800 μm, the average initial width of the tested channels at the three locations after 3D printing was approximately 1000 μm ± 55 μm. Additionally, other parameters were tested in this study, such as using different initial widths of ABS channels (875 μm ± 50 μm and 1260 μm ± 20 μm). However, satisfactory results were not obtained since bigger pieces of ABS tended to swell in acetone [359] and smaller channels exhibited no structural rigidity in acetone (data not shown). SEM images were taken using TM3000 Tabletop Microscope (Hitachi, Japan) at 15 kV in analytical mode and COMPO image mode. High speed imaging of droplet generation was performed using Fastcam SA-X2 (Photron Limited, Japan) at 4,000 fps. Generated droplets were imaged using Cytation™ 5 and analyzed using ImageJ software.

4.2.3 PDMS device fabrication

Scaffolds used to produce microfluidic chips were casted with Sylgard™ 184 Elastomer Kit (Dow, USA) with 10:1 weight ratio of elastomer:curing agent. The channels and PDMS were placed in a 3D printed casting chamber (Figure 4.2(c)) lined with glass slides from the bottom and both sides to obtain good optical properties. The PDMS was degassed using a desiccator set at -10 in. Hg for 30 mins. The PDMS was then cured at 70°C for 2.5 h in an INCU-Line® IL 10 Digital Incubator (VWR, USA). The cured chip was carefully ejected from the casting chamber, and the outside ABS channels were cut using clippers. The internal ABS scaffold was completely dissolved by immersion in 100% acetone for 16 h at 1500 RPM using Isotemp™ stirring hotplate (Fisher Scientific, USA) and a 1/2" x 5/16" spin bar. The channels were later flushed repeatedly with acetone to completely remove any remaining ABS.

4.2.4 Scaffold dissolution

ABS scaffolds were dissoluted using four different setups (Figure 4.3). Setup A was simply composed of a 1000 mL beaker filled with 600 mL of 100% acetone (Sigma Aldrich, USA) (Figure 4.3(a)). The scaffolds were dropped into acetone for a certain duration, taken out using tweezers, held in air to dry for 60 s, shaken gently in DI water for 10 s, held in air to dry for 10 s, and gently placed on a glass slide for observation. The same washing procedure was applied to all scaffolds in this chapter unless otherwise noted. For better results, the scaffolds should be taken out from the acetone bath by holding them from a location far away from the desired microfluidic zones. Acetone continues to dissolute ABS for a short period of time after being taken out from the dissolution bath, which might cause deformation in channel shape. Such deformations could be eliminated by careful channel straightening using tweezers over a hotplate set at 90°C. Higher temperatures cause bubble formation from inside of the ABS scaffolds, causing further channel deformation.

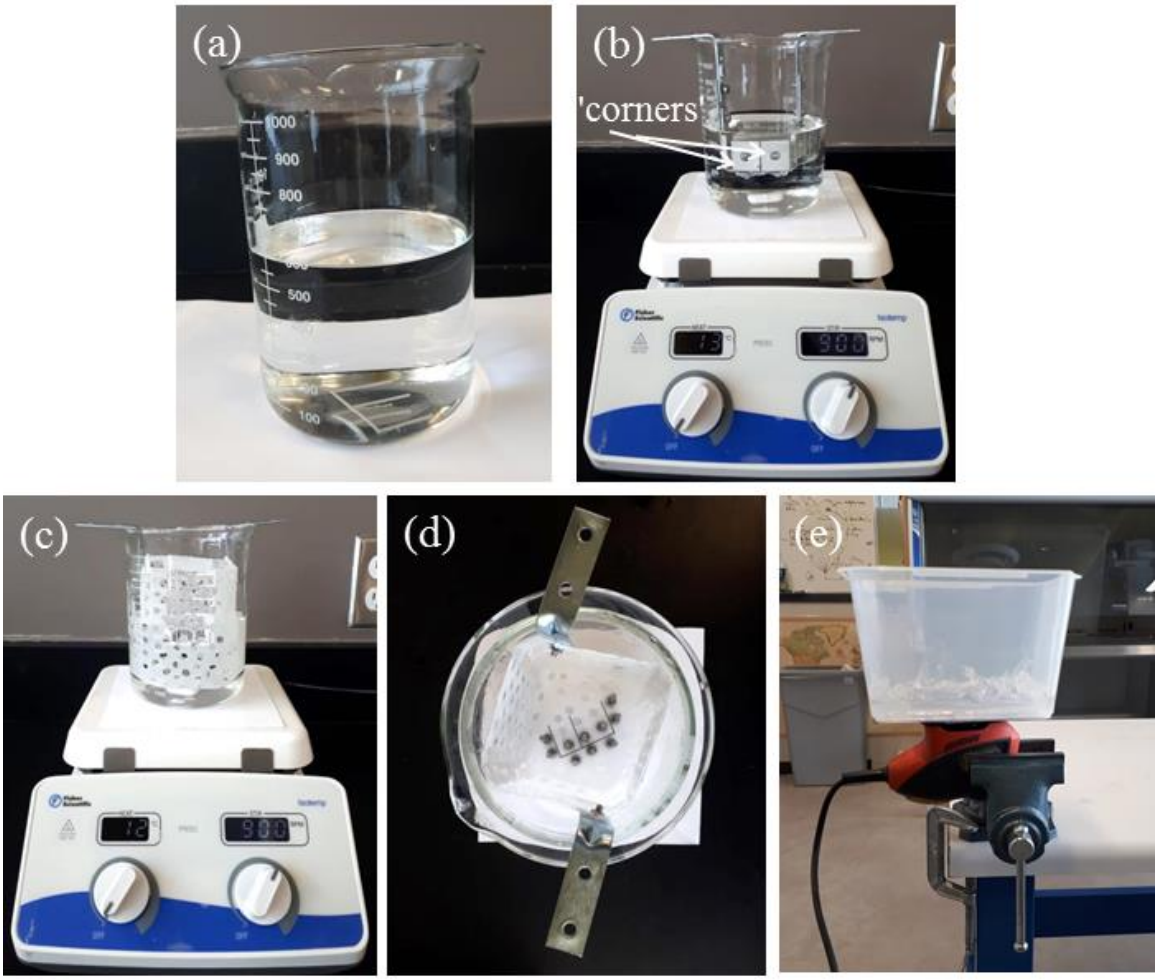

Figure 4.3: Setups used to examine the effect of agitation forces on ABS dissolution. (a) Setup A: scaffold dropped into a beaker of acetone with no movement. (b) Setup B: metallic structure setup containing a square vicinity made from ‘corners’ to allow for scaffold placement. The structure was suspended in a beaker, leaving enough space for magnetic stirring bar rotation. (c) Setup C: bottle-with-holes setup. The structure was suspended to leave room underneath for the rotation of a magnetic stirring bar. (d) Top view of Setup C, showing screws and nuts forming a shape matching the T-junction scaffold dimensions to keep the scaffold in place during rotation. (e) Setup D: shaker setup equipped with a variable frequency generator to set the shaking frequency.

Setup B was a metallic structure built from aluminum brackets, corners, screws, and nuts and suspended in a 1000 mL beaker (Figure 4.3(b)). The corners were placed in a way that allows for placement of the channels. A space of 4 cm was left between the bottom of the metallic structure and the beaker to place a magnetic stirring bar. The metallic structure was meant to allow for rotational forces to aid in the dissolution of

ABS while preventing the magnetic stirring bar from hitting and/or damaging the channels.

The third setup, Setup C, was prepared in the same beaker using an off-the-shelf plastic bottle (equate™ IPA USP 70%, 946 mL), cut to 10 cm height and drilled with 220 evenly-spaced ¼" holes (Figure 4.3(c)). The bottom of the bottle was elevated at 1 cm from the bottom of the beaker and was equipped with 10 pairs of screws and nuts, which were used to prevent the channels from movement during stirring (Figure 4.3(d)). The rotation of the magnetic stirring bar in Setups B and C was controlled using the Isotemp™ stirring hotplate.

Finally, Setup D employed a horizontal shaking motion as opposed to rotational. An open, flat-bottom container, made of polypropylene, was attached to a sander/polisher (Mouse®, Black & Decker, USA) using hook-and-loop fasteners (Figure 4.3(e)). The shaking frequency was controlled using a variable autotransformer (Staco Energy Products, USA). This setup was mounted on a vice, leveled, and filled with 400 mL of 100% acetone. All setups were placed in a chemical fume hood or in a well-ventilated space, depending on the nature of the setup.

4.2.5 Droplet generation

Using a T-junction device fabricated according to the optimized conditions identified in this chapter (final channel width approximately 435 µm ± 25 µm), droplets were formed by the pressure force exerted on the dispersed phase by the continuous phase. The dispersed phase was 1% w/v agarose which was kept at 45°C during droplet generation using a heated aluminum block to prevent agarose from gelling in tubing and/or in the microfluidic device (see Figure 4.4). A Peltier cooler was installed after the microfluidic chip to cool down the microbeads before collection. The continuous phase was mineral oil and 4% v/v Span® 80 non-ionic surfactant. The flow of the phases was controlled using two Fusion 100 syringe pumps (Chemyx, USA), with 1 mL/hr and 30 mL/hr flow rates used for both phases, respectively. Tygon tubing of 1/32" ID and 3/32" OD was used to drive the reagents to and from the PDMS device. A snug fit was obtained by insertion into holes in the PDMS surface that resulted from having 'thick holders' that were initially 3D printed with the desired ABS scaffolds. Approximately 1000 microbeads were used for size characterization.

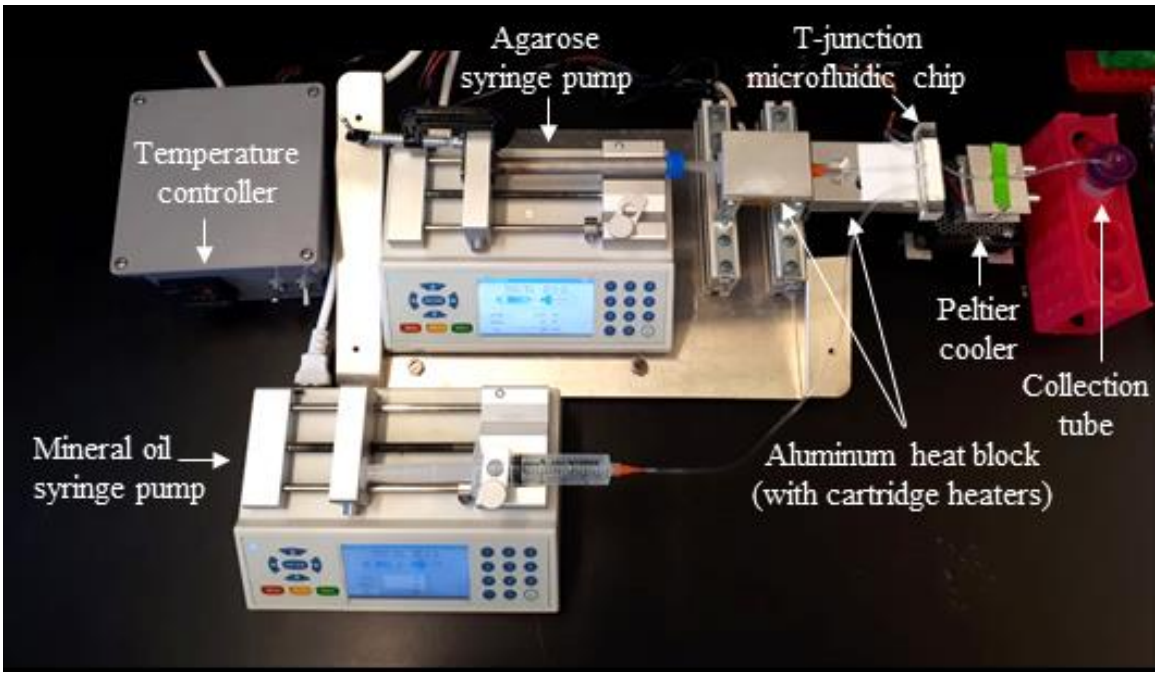

Figure 4.4: Microbead formation setup. Flow rates of agarose and mineral oil were controlled using syringe pumps. Agarose was maintained at 45°C to prevent gelation prior to microbead formation. Agarose heating was achieved through an aluminum heat block equipped with two cartridge heaters and a thermocouple. Temperature was set and regulated through a PID temperature controller. After microbead formation, microbeads were cooled down using a Peltier cooler and collected in a tube.

4.3 Results and discussion

4.3.1 Effect of dissolution setup

The final channel dimensions obtained using the dissolution setups are plotted in Figure 4.5. Each bar represents the average dimensions of three channels that underwent independent dissolution, with error bars reflecting standard error. The smallest obtained channel dimension was 270 μm. However, at this width, the channels exhibited poor structural integrity and collapsed. Dropping the scaffolds in acetone and providing no motion to the acetone bath (Setup A) resulted in almost no ABS dissolution, most likely due to the redeposition of dissoluted ABS on surface gaps of the ABS scaffold [359]. For setups having bath motion, Setup D resulted in the smallest repeatable channel sizes. This was due to the horizontal shaking motion, which caused layers of dissoluted ABS to uniformly wash away into the acetone bath. This trend was not observed in Setups B and C due to the non-uniform agitation force on the channels caused by the vortex created by the stirring bar. Also, the holes created in the bottle in Setup C likely disturbed the vortex created by the stirring bar, leading to reduced acetone movement around the channels, greatly weakening the dissolution process. Therefore, other parameters in this chapter were studied using Setup D. It should be noted that 90% and 95% acetone were also used, with no noticeable change in channel dimensions (data not shown). Therefore, 100% acetone was selected to be the most effective in rapid ABS dissolution and is, hence, used for the remainder of this work.

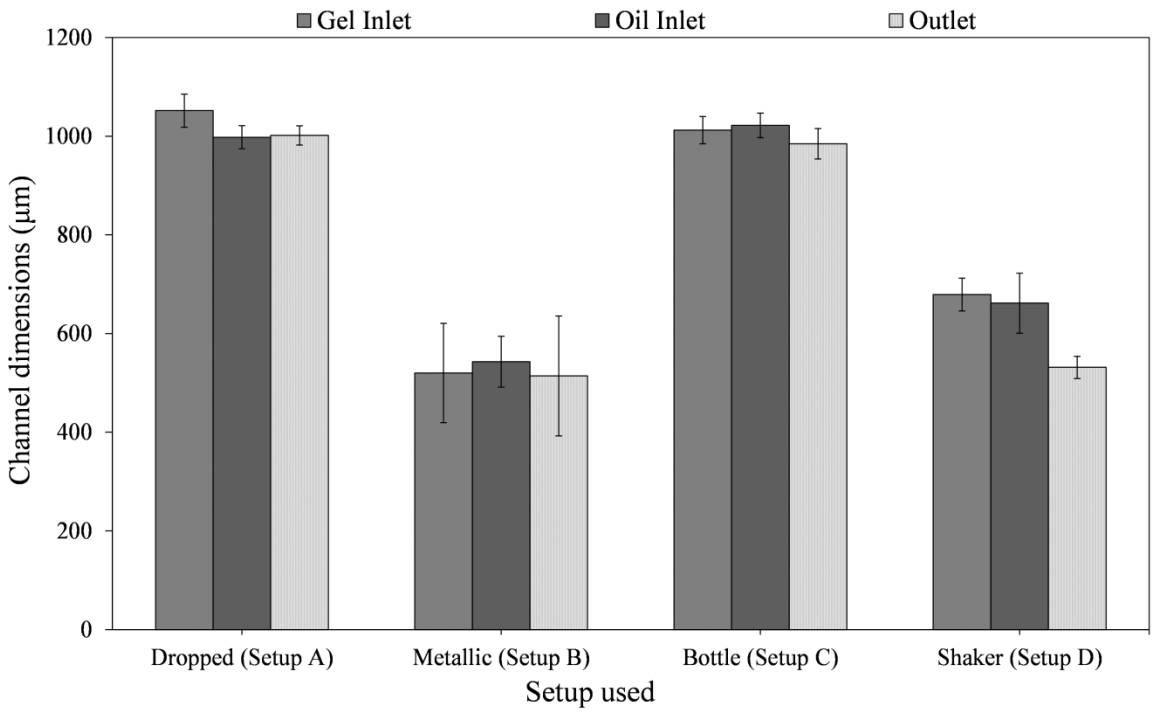

Figure 4.5: Effect of setup and bath motion on final channel dimensions at 200 s and 1200 RPM for Setups B and C, and 20 Hz for Setup D. Initial channel width was 1000 µm ± 55 µm.

4.3.2 Effect of shaking frequency and dissolution time

The effect of the shaking frequency on channel dimensions and uniformity were investigated (see Figure 4.6). Uniformity is defined as the ratio of the minimum measured channel dimension to the average measured dimension. Interestingly, channel dimensions did not decrease with increasing shaking frequency (Figure 4.6(a)). In fact, higher frequencies resulted in non-repeatable channel dimensions and non-uniform channels (Figure 4.6(b)). This was likely due to the lack of sufficient time for dissoluted ABS to wash away into the acetone bath at higher frequencies. Instead, ABS was dissoluted and rapidly redeposited on the channels. Hence, a frequency of 10 Hz was used for the remainder of this study. The effect of dissolution time on channel dimensions had a similar trend (see Figure 4.7). With more dissolution time, more disruption to channel shape and necking were observed. For example, the smallest channel dimension observed was 160 μm at 240 s of dissolution, but the channels were extremely fragile and could not retain their shape. Therefore, increasing the dissolution time was not proportional to decreasing channel dimensions [359], and smaller dimensions were observed to exhibit poor structural integrity. Since 200 s was observed to result in repeatable channel dimensions with no effect on channel integrity (final dimensions obtained were 540 μm ± 20 μm), 200 s dissolution time was used for further analysis of ABS dissolution properties.

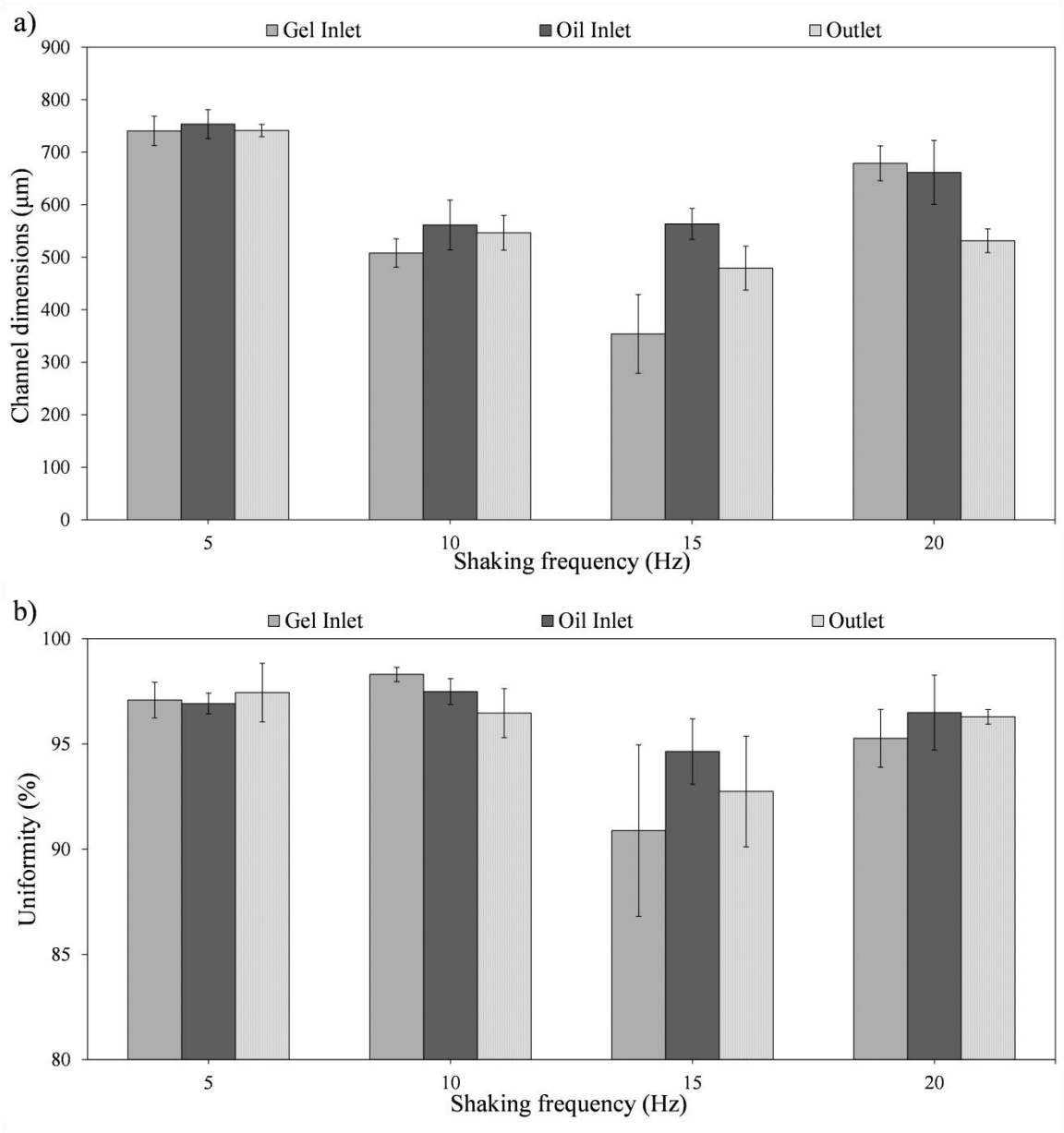

Figure 4.6: Effect of shaking frequency on final channel dimensions (a) and channel uniformity (b) at 200 s using Setup D.

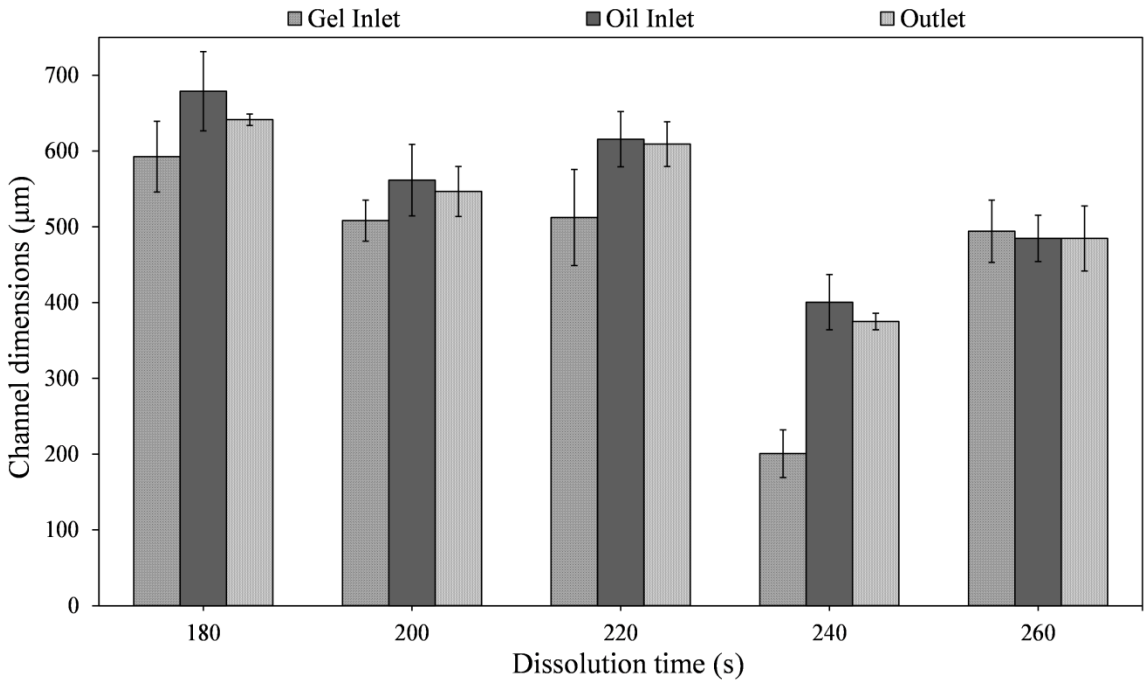

Figure 4.7: Effect of dissolution time on channel dimensions at 10 Hz using Setup D.

4.3.3 Effect of the number of washing steps and the washing solvent

Other parameters affecting ABS dissolution in acetone were also investigated, such as the number of washing steps after each dissolution and the solvent in which the scaffolds were washed (Figure 4.8). For a total duration of 200 s and 10 Hz shaking frequency, ABS scaffolds were washed in DI water once (after 200 s of dissolution), 3 times (at 67 s dissolution intervals), and 5 times (at 40 s dissolution intervals). Each washing step involved gently taking out the scaffolds from the shaker bath using tweezers, holding them in air to dry for 60 s, gently shaking them in DI water for 10 s, holding them in air to dry for 10 s, and gently placing them on a glass slide for observation or back in the shaker bath for further dissolution (for the 3 and 5 washing steps). The same procedure was followed for washing ABS channels in 70% IPA. It was observed that no significant change to channel width resulted from varying the number of washing steps. Also, the choice of washing solvent (DI water or IPA) did not significantly affect final channel dimensions. However, SEM images of ABS channels undergoing 3 washing steps in DI water and IPA showed that washing in DI water resulted in noticeably smoother surfaces (Figure 4.9(a) and (b)). Moreover, comparison of the effect of a single DI water washing step (Figure 4.9(c)) and 3 washing steps (Figure 4.9(a)) on surface topography showed that 3 washing steps resulted in smoother surfaces. A single dissolution step in acetone is likely to cause pitting on the ABS surface [310], while repeated dissolution (i.e. through multiple washing steps) is likely to cause ABS existing in a ‘semi-molten’ state [308] on the channels surfaces to re-enter and close the pores [360] caused by acetone pitting. The SEM images also showed that washing using IPA might have had a more pronounced effect on surface pitting than washing in

water. Therefore, from the obtained data, having 3 washing steps resulted in the most reproducible channel dimensions (480 μm ± 30 μm), and washing in DI water is recommended to reduce potential effects of IPA on final channel topography.

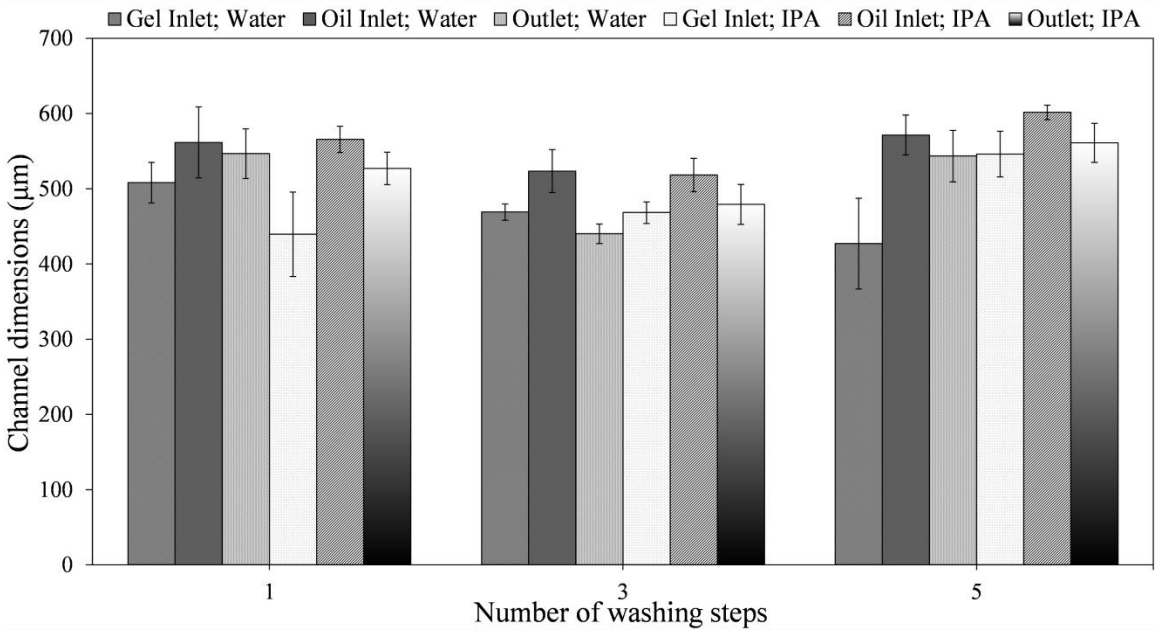

Figure 4.8: Effect of multiple washing steps on channel dimensions at 200 s and 10 Hz, using DI water and 70% IPA as washing solvents.

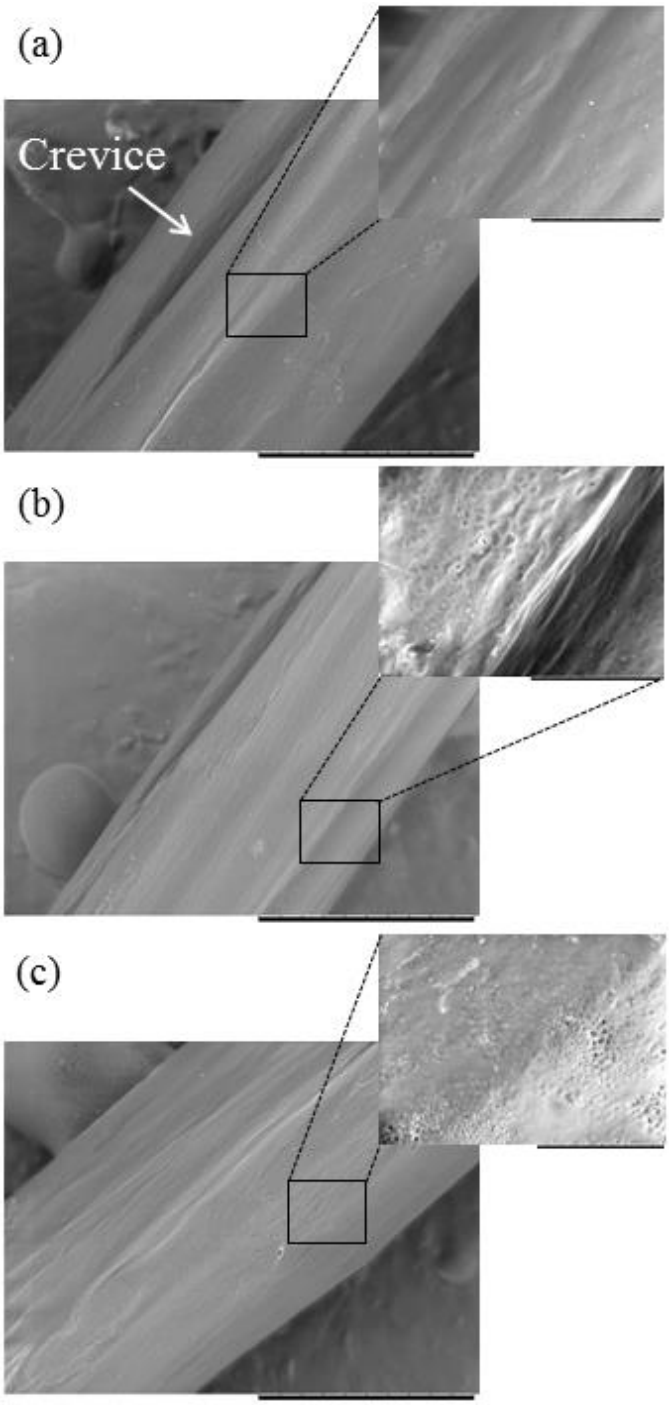

Figure 4.9: SEM images of ABS channel surfaces obtained after different dissolution conditions in 100% acetone using Setup D. (a) Channel surface after 3 washing steps in DI water at 67 s dissolution intervals and 10 Hz. A crevice is identified on the channel surface. Crevices also exist in all presented SEM images but not identified. (b) Channel surface after 3 washing steps in 70% IPA at 67 s dissolution intervals and 10 Hz. (c) Channel surface after undergoing a single washing step in DI water after dissolution for 200 s at 10 Hz. Scale bars are 500 μm. Inset scale bars are 50 μm.

4.3.4 Effect of adding a secondary dissolution step

Dissolution process was further enhanced by adding a secondary dissolution step in 90% acetone (prepared as 90:10 v/v acetone:70% IPA) to channels dissoluted for 200 s at 10 Hz with 3 washing steps in DI water. In this secondary step, acetone was diluted with IPA since IPA did not show fibrous ABS formation from dissoluted ABS as that observed with DI water (data not shown). Increasing the duration of this secondary dissolution step resulted in relatively smaller channel dimensions (see Figure 4.10), but higher channel deformity and necking were noticed. Also, the obtained channels exhibited a white, rough surface. SEM images showed that the secondary step resulted in highly rough ABS surfaces (Figure 4.11(a)), which could result in low quality PDMS microfluidic devices after eISR. Therefore, a single dip in 100% acetone for 1 s after the secondary dissolution step (followed by the traditional washing procedure) was added. This dip resulted in greatly improved surface smoothness (Figure 4.11(b)) and no observed change in channel width (data not shown). Therefore, adding a secondary dissolution step in 90% acetone for 120 s resulted in the most reproducible channels with good integrity and surface topography and further reduced channel dimensions (435 μm ± 25 μm) previously obtained by primary dissolution (480 μm ± 30 μm). Moreover, the SEM images shown in Figures 4.9 and 4.11 showed a crevice in the obtained channels, which could be due to the layered deposition of fused filaments used in FDM 3D printing. Using a bigger nozzle head diameter could eliminate this issue, but could result in bigger initial channel dimensions. It should also be noted that the total amount of time required to fabricate a microfluidic device using the eISR method

described in this chapter was approximately 21 hrs (1 hr printing, 15 mins dissolution, 30 mins PDMS degassing, 2.5 hrs PDMS curing, and 16 hrs ISR).

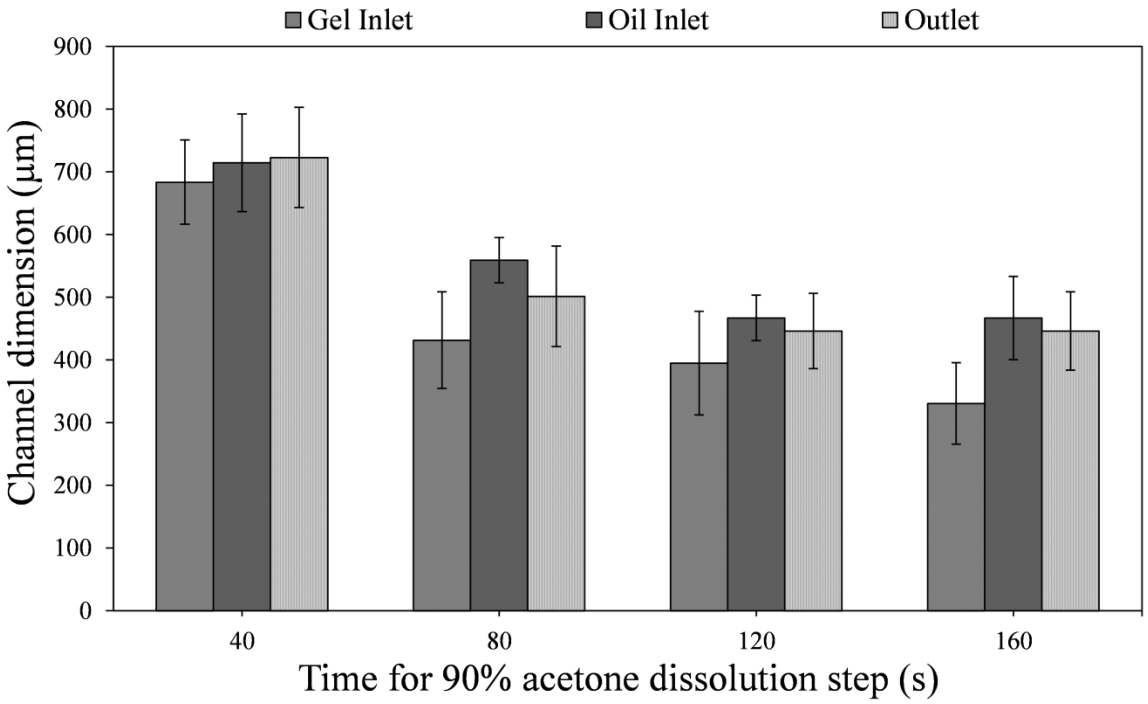

Figure 4.10: Effect of the duration of a secondary dissolution step in 90% acetone (diluted with 70% IPA) after dissolution in 100% acetone for 200 s at 10 Hz with 3 washing steps in DI water using Setup D.

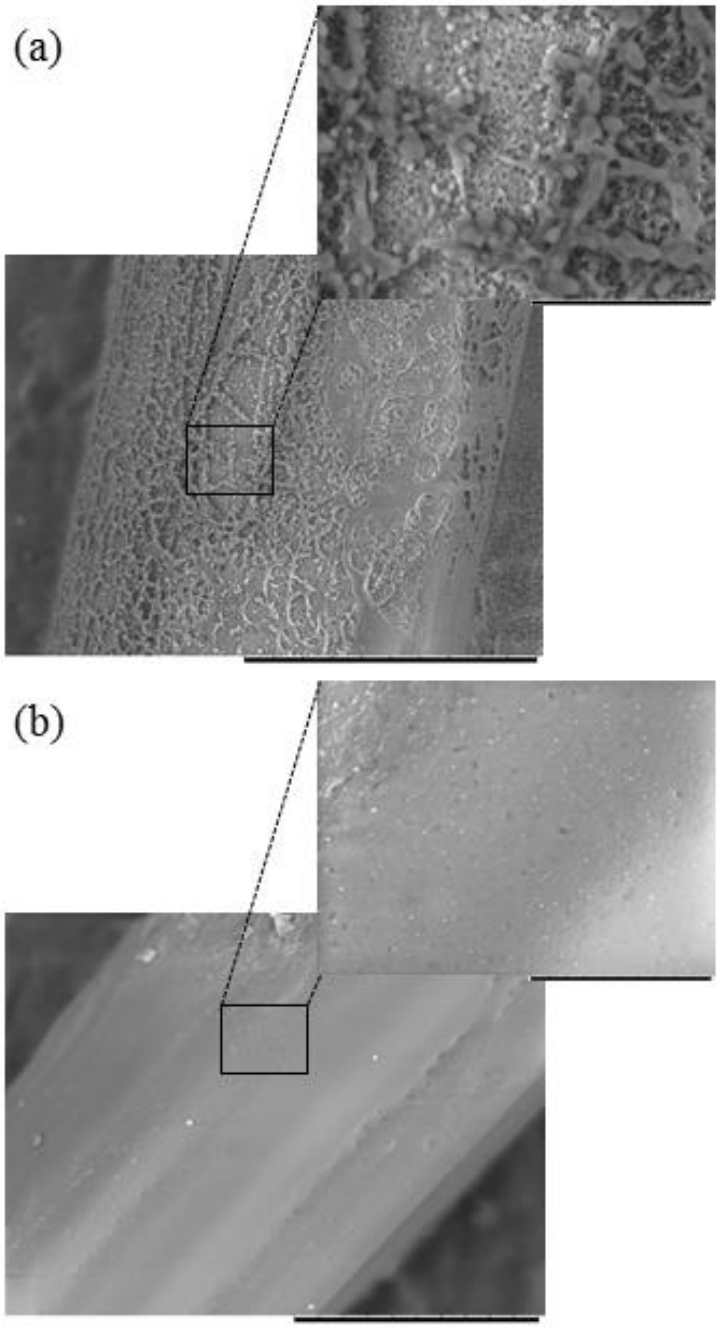

Figure 4.11: SEM images of ABS channel surfaces obtained after application of a secondary dissolution step in 90% acetone (diluted with 70% IPA) using Setup D. (a) Channel surface after 3 washing steps in DI water at 67 s dissolution intervals and 10 Hz and followed by a secondary dissolution step in 90% acetone (diluted with 70% IPA) for 120 s, then washed in DI water. (b) Channels undergoing same conditions as (a) and followed by a 1 s dip in 100% acetone and traditional washing in DI water. Scale bars are 300 μm. Inset scale bars are 50 μm.

4.3.5 Droplet generation

A T-junction microfluidic device, fabricated using the recommended conditions, was used to produce droplets. Tygon tubing was snugly placed in the inlets and outlet (Figure 4.12(a)), leading to no leaks observed during droplet generation. Using high speed imaging (Figure 4.12(b)), droplet formation was observed to be stable and at high-throughput. The size distribution of the produced microbeads showed that approximately 93% of the microbeads had a diameter between 1 μm and 20 μm (Figure 4.12(c)). The average microbead diameter obtained was 9 μm, with a standard deviation of 8.7%. Increasing the aqueous phase flow rate could result in larger microbeads [40]. Size uniformity could be enhanced through further decreasing the ABS channel dimensions by adding chemicals and/or solvents to acetone and/or ABS to increase the structural stability of ABS during dissolution.

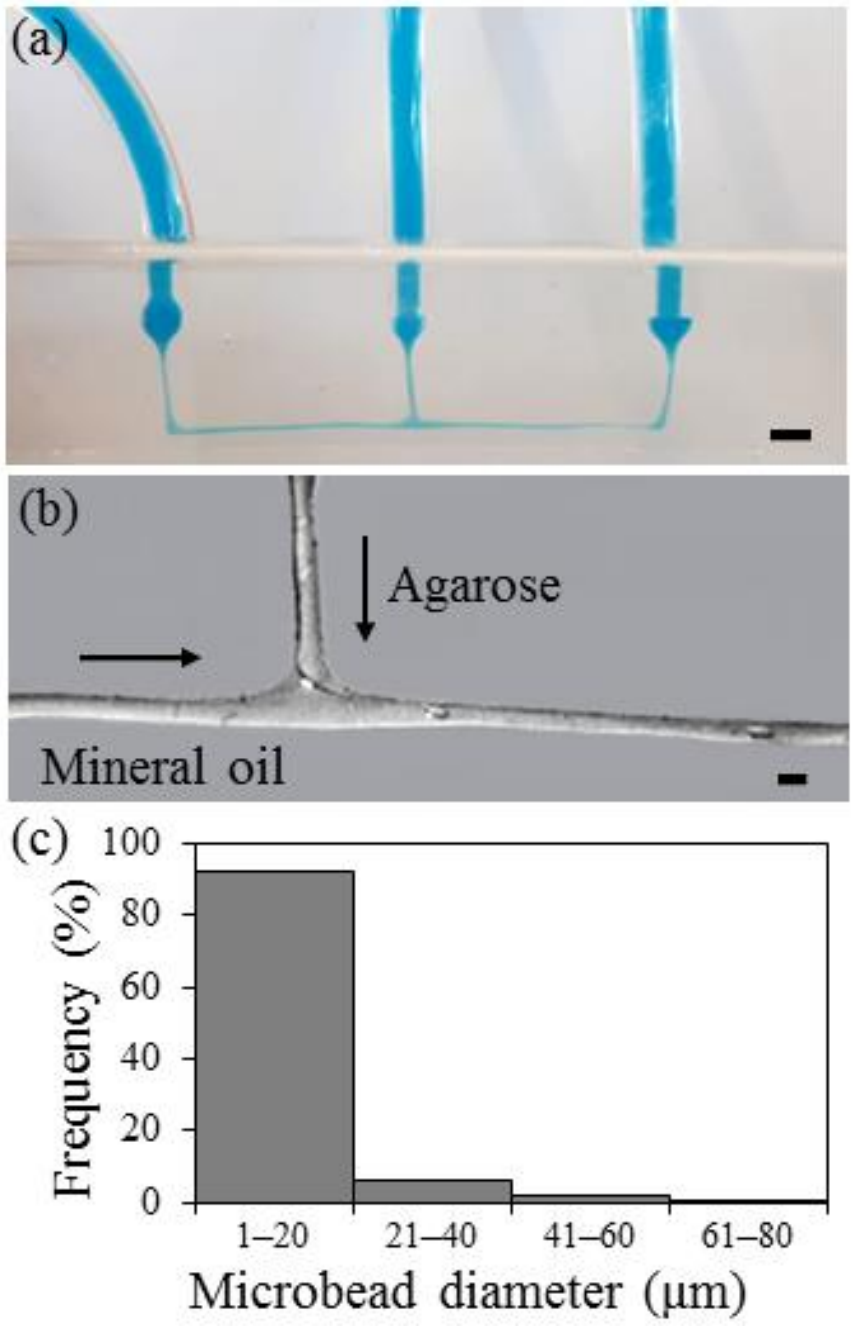

Figure 4.12: Droplet formation obtained through a T-junction microfluidic chip fabricated using eISR. (a) Reagents were introduced through snugly-fit Tygon tubing and were blue colored for clarity. Scale bar is 2.4 mm. (b) Droplets formed and observed using a high-speed camera. Agarose was used as the dispersed phase and mineral oil was used as the continuous phase. Scale bar is 400 μm. (c) Size distribution of approximately 1000 microbeads produced using a T-junction device.

4.3.6 Fabrication of other geometries of microfluidic channels

eISR was also used to fabricate channels with different geometries, such as bifurcation channels (Figure 4.13(a)), which could be used for particle transfer from/to an oil phase to/from an aqueous phase [271]. eISR was also used to fabricate channels exhibiting curved features and wells (Figure 4.13(b)), which could be used for drug testing on cell cultures [358]. This demonstrated the ability of eISR to produce microfluidic channels of any desired shape, given that the channels can be 3D printed using a commercial 3D printer with no supports. Parts that have more complex geometries that must be printed in 3D space are recommended to be printed with dissolvable or sacrificial supports [307,361,362]. This is because supports printed using commercial 3D printers are likely to break the channels upon detachment. Additionally, both geometries shown in Figure 4.13 had four inlets/outlets, increasing the port numbers shown in a previously published study implementing ISR [303]. Finally, the ability of eISR to smooth the surface of 3D printed curved ABS channels greatly enhanced the drawback of having void spaces typically existing at the edges of 3D printed layers of ABS using FDM [309].

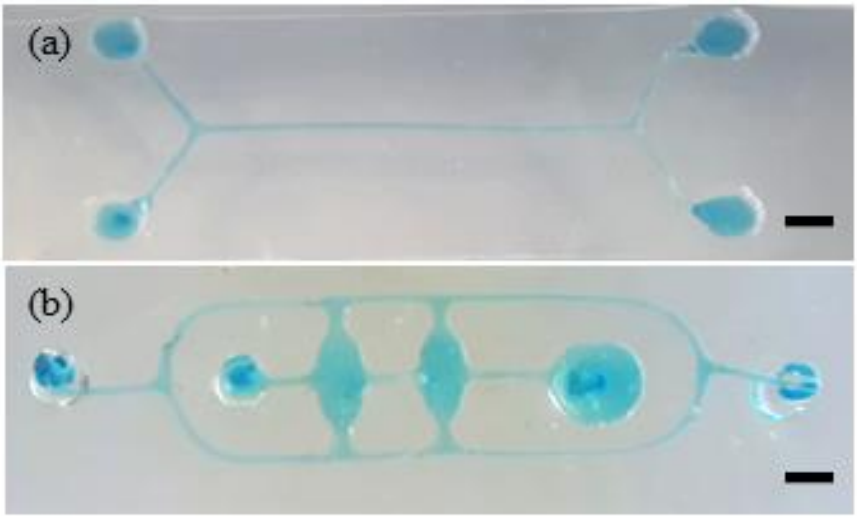

Figure 4.13: Microfluidic chips fabricated using eISR and exhibiting different channel geometries. Channels were filled with blue-colored water for ease of visualization. (a) Top view of bifurcation channels that could be used for particle transfer across a laminar interface. (b) Bottom view of channels with curved features and wells that could be used for drug testing by application to cell cultures. Scale bars are 2.4 mm.

CHAPTER 5 : CONCLUSIONS AND FUTURE RECOMMENDATIONS

5.1 Overview

The road to discovering new natural products derived from marine sources is difficult, but it is not impossible. The projects undertaken in this thesis served to provide the initial setting stones to pave that road. Briefly, several growth chambers, defined as MD Pods in this thesis, were developed and tested for their effectiveness in culturing and domesticating marine sediment bacteria. An encapsulation system was developed to encapsulate these bacteria in agarose microbeads, which were placed in the MD Pods during *in-situ* incubation. The system used a 3D printed microfluidic device to provide microbead formation. Additionally, two systems were developed to provide a mechanism of separating oil from water, giving a way of collecting the microbeads from the microfluidic device without going through traditional washing steps. Finally, a new, quick method was developed for fabricating cheap microfluidic chips from 3D printed scaffolds. These chips could easily be used to encapsulate marine sediment bacteria in more uniformly-sized microbeads because of their smaller channels than the 3D printed microfluidic device used.

All in all, the overall objectives of this thesis were achieved. More research can definitely be implemented to examine the exact effects of using the MD Pod on microbial culture domestication, and more development can be applied to improve the multiple systems presented in this thesis, which will, ultimately, yield better results in the future. The following sections shed more light on the details of the results achieved from each chapter in this thesis, with highlighted recommendations of improvements that could be implemented in the future.

5.2 Microfluidic Chip Fabrication

As discussed in Chapter 1 (section 1.3.5.2), 3D printing microfluidic chips is a one-step, inexpensive, and customizable process. However, smallest printable channels, optical transparency, and residue resins removal still remain common issues with this process. The developed microfluidic chip in this thesis was 3D printed using a material that was tested for its biocompatibility with the species that will be passing through it (refer to section 2.5.3). The smallest channel size printable using the used 3D printer (Form 2) was confirmed by designing a comb-like structure containing channels of 100 μm increments from 100 μm to 1400 μm. Flushing all channels resulted in opening all channels ≥600 μm in size, resulting in conservatively designing the used cross-flow microfluidic chip to have 1000 μm square channels. The optical transparency of the used chip was not needed to be of perfect transparency since on-chip imaging of microbead formation was not critical to the intended application. The residue resin in the internal channels after 3D printing was repeatedly flushed using 99% IPA until completely removed (refer to section 2.2.1).

The used cross-flow microfluidic chip was designed with inline inlets and outlets because they resulted in easy removal of residue resin after 3D printing. Multiple microfluidic chips with different designs of inlets and outlets and internal channel sizes were investigated before coming up with the used chip design (refer to Appendix A). Further improvement to the current chip design using Form 2 could be made through decreasing the channel size while investigating efficient and compatible residue resin removal methods, such as using a customized high pressure air source or a high flow rate vacuum system.

Chapter 4 offered a different, alternative method of fabricating microfluidic chips relatively quickly (herein called eISR). These chips have excellent optical transparency since they were fabricated from PDMS. Moreover, these chips exhibited significantly smaller internal channel dimensions (435 μm ± 25 μm) than their 3D printed microfluidic chip counterpart (1000 μm for the chip used in this thesis). The smaller channels will help in producing more uniform microbeads than the used 1000 μm microfluidic chip, which would aid in single-cell encapsulation and increase the microbead concentration in the collected solution after washing. Therefore, more microbial growth could be achieved since a higher cell concentration, and therefore, more microbial diversity and quorum sensing, would exist in the collected microbead solution. Nevertheless, the biocompatibility of chips produced through eISR should be investigated before using them for cell encapsulation, since the acetone used to dissolve the scaffolds and to remove the scaffolds after PDMS curing could compromise cell viability.

Combining 3D printing and eISR could prove to be a significant enhancement to the traditional method of microfluidic chip fabrication using soft lithography, especially if more control is achieved over scaffold stability in acetone. This method eliminated two of the most problematic fabrication steps typically faced through soft lithography: channel sealing and hole punching. It also proved to produce channels with smooth surfaces and micro-scale features, such as channels with final dimensions of 435 μm ± 25 μm, and in a comparatively short total fabrication time (21 hrs). Adding 'thick features' to the 3D printed part resulted in the ease of connecting tubing and eliminated the need for punching holes for inlets and outlets (refer to Figure 4.12).

Additionally, eISR showed to be successful for use for droplet generation. The average diameter of the produced microbeads was 9 μm with a standard deviation of 8.7%. Higher monodispersity could be achieved by further dissoluting ABS scaffolds to smaller dimensions without compromising structural integrity. Increasing the aqueous phase flow rate could result in producing larger microbeads. Moreover, bifurcation channels and curved channels were successfully fabricated using eISR (refer to section 4.3.6), with multiple inlets and outlets, opening the potential for using this method for other applications, such as mixing, droplet sorting, and drug testing. eISR can definitely be improved by 3D printing the desired channels using a smaller nozzle head diameter. It can also be improved by achieving more channel shape and structural stability after acetone dissolution through the addition of chemicals and/or solvents to acetone and/or ABS without decreasing PDMS quality.

5.3 MD Pod Development and Testing

As discussed in Chapter 2 and shown in Appendix B, several MD Pod ideas were designed, 3D printed, and tested for water leaks for initial confirmation of MD Pod sealing. The shape of the F-MD Pod (capable of holding 2.68 mL of liquid) was chosen because it decreased the assembly time required while decreasing the chance of cross-contamination that was commonly faced with the design shown in Figure B.1(e). This shape also holds the potential for being miniaturized, which is a subject of interest in performing *in-situ* incubations in sea sponges and Octocorals in the future. In fact, a miniaturized concept design was 3D printed and presented in Appendix B (Figure B.1(n)), capable of holding 100 μL of liquid. Although *in-situ* incubations using miniaturized MD Pods might provide more access to natural product-rich organisms, these MD Pods will be holding minute amounts of volume, which could be difficult in terms of downstream analysis. This could be overcome by incubating numerous MD Pods at once and pooling their incubated solutions.

Furthermore, the developed casing helped protect the PCTE membrane from tearing during insertion and retrieval of the MD Pod from marine sediment. This casing could further be developed to include a closable cap with a mesh to provide additional protection to the fragile membrane. Moreover, the M-MD Pod offered a window into exploring the potential for using metals to manufacture the MD Pods, in an aim to use an easily autoclavable material. Although the used 304 stainless steel showed corrosion after the *in-situ* incubations, other types of metals, such as 316L stainless steel and aluminum, could be tested as the building materials of the MD Pods to increase efficiency through easier sterilization. It should be noted that although the sterilization method for

non-metallic MD Pods was multi-step (40 mins in 20% bleach, a water bath dip, 10 mins in 70% IPA, then another water bath dip), it proved to decontaminate these MD Pods (refer to cell migration Test #9).

The MD Pod design and assembly process was adjusted according to the experimental work performed over the course of the thesis. For example, the loading port (closed with a needle tip and a cap) was eliminated because it resulted in increased contamination of the MD Pods upon *in-situ* incubation (refer to cell migration Test #1 and *in-situ* incubation Run #1). Therefore, the loading process was adjusted to assembling one side of the MD Pod, inverting it, loading the sample directly in the MD Pod's internal cavity, then assembling the top membrane. Similarly, the unloading process after *in-situ* incubation was adjusted from punching the top membrane using a sterilized screwdriver tip (which might increase chances of cross-contamination) to carefully unrolling the top membrane and its supporting O-rings. These loading and unloading methods proved to be easy to implement using the current MD Pod size. However, in the future, if this shape of the MD Pod was to be miniaturized, the unloading process will need revision since it would be difficult to unroll a tiny O-ring and a small membrane without knocking the MD Pod over or contaminating it due to the small space available to perform these tasks. Nonetheless, the concept design shown in Figure B.1(n) included a part which provides a method for closing the top membrane after loading. This part is similar to the O-ring dispenser developed and used in this thesis, which greatly decreased assembly time (to approximately 3 mins) and effort. These O-ring dispensers could be further developed to be made from an autoclavable material that will not cause

micro splashes when the device ‘snaps’ the O-ring over the MD Pod (refer to section 2.3.2).

Through the performed cell migration tests and *in-situ* incubation runs (sections 2.3.6 and 2.3.7), it could be seen that the MD Pods still suffer from contamination during incubation in a non-sterile environment. The DGGE analysis performed on the MD Pod products of Run #5 confirmed that contamination existed in that run (refer to Figure 2.45), which, unfortunately, suggested that the MD Pod design and PCTE membrane enclosure mechanism should be revised. Additionally, incubated MSB samples could be suspended in 10% Marine Broth instead of FSS in the future, to decrease chances of contamination from organisms existing in the FSS.

As is the case with any research and development project, the shape of the tested product is not absolute. Therefore, the shape of the MD Pod used in this thesis could be changed to incorporate the PCTE membrane differently in a way that could decrease burdensome assembly and offer better control over possible MD Pod contamination during *in-situ* incubation. Other designs could also get rid of the PCTE membrane altogether and use a different membrane material and/or meshed materials to provide the required diffusion of nutrients, chemicals, and wastes while preventing cell migration. Since the fragility of the PCTE membranes was the probable main cause of contamination of most of the tests implemented in this thesis, finding a suitable, alternative material could be key to the success of the intended microbial domestication.

5.4 Cell Encapsulation

Three different groups of samples have been prepared and encapsulated in this thesis: an *E. coli* strain, MSB, and representative marine sediment bacteria (*M. polaris*, *P. aquimaris*, and *B. licheniformis*). The cell concentration of each of these groups (except the representative species grown in 10% Marine Broth) was normalized before the encapsulation in order to follow the Poisson distribution and result in approximately 23% single-cell encapsulation in 100 μm microbeads. This percentage could go up if a lower cell concentration was used. It should be noted that a lower cell concentration will not result in the formation of a pellet if a volume of approximately 0.5 – 3 mL was used. Therefore, more cell culture volume should be used to successfully form a pellet that could later be suspended in an agarose volume calculated to result in 6.68×10^6 cells/mL or higher, depending on the desired single-cell encapsulation rate in the desired microbead diameter. For proof-of-concept purposes, the cell concentration of the three representative marine sediment species grown in 10% Marine Broth was not normalized according to the Poisson distribution because the intended outcome was to examine the effect of changing the media type of the growth solution and the size of the used microbeads.

The designed cell encapsulation setup gave reproducible results in terms of microbead generation. The used heater block kept the agarose + cell mixture in the syringe in a liquid state throughout the encapsulation, resulting in stable flow. Although the second part of the heat block (refer to Figure 2.10; the right part of the indicated heat block) provided heat to the tubing and microfluidic chip, it was not possible to completely enclose them inside the heat block (their top parts were exposed to allow for

user-friendly assembly). This has caused the microbead formation to be unstable at regular periods of time when parts of the agarose + cell mixture gel in the microfluidic chip due to exposure to room temperature from the top. The unstable microbead formation resulted in large agarose + cell mixture 'chunks' that were manually removed by alternating the outlet tubing between the wanted microbeads collection vial and a waste collection vial. This drawback could be improved by completely enclosing the tubing and the microfluidic chip inside the heat block, and/or to install an imaging system which recognizes 'chunks' from microbeads and automatically alternates the outlet tubing accordingly. Ultimately, the imaging system could be used to separate microbeads based on their sizes.

Moreover, marine samples were cultured in saline liquids, such as FSS, 50% Instant Ocean, and 10% Marine Broth. As a result, the agarose + cell mixture tended to gel faster due to the presence of ions in these liquids, resulting in the requirement of quickly vortexing the cells with agarose, loading a syringe with the mixture, then quickly inserting the syringe into the heat block to keep the mixture in a liquid state. Although this was possible to be performed, it could be difficult to keep the mixture in a liquid state before reaching the heat block. This could be resolved by repeated washing of the collected pellet with DI water to remove any salts remaining in the cell pellet. An agarose-gelling study could also be performed using an increasing gradient of NaCl concentrations.

Furthermore, the size of the microbeads is an important factor in the reproducibility and culturing of the intended 'unculturable' bacteria. In this thesis, the used 1000 μm microfluidic chip produced polydisperse microbeads, which were later

strained and washed using a pair of different-sized cell strainers to collect microbeads in one desired range of diameters (either 60 – 100 μm or 100 – 200 μm). Although the final collected microbeads in the working solutions were in the desired size range, conducting this size-separation step caused the loss of many of the produced microbeads which do not fall in the desired size range. Therefore, the final cell concentration in the working solution was low (in the order of 10^3 cells/mL). Despite the fact that the cell concentration could be increased by decreasing the volume of the microbead washing solution, doing so does not greatly affect the final cell concentration. It also results in a lower working solution volume which is likely not enough to be loaded into multiple MD Pods, to conduct a long term PrestoBlue® study, and/or to be used for other applications. In addition, this cell concentration was considerably lower than that of the dislodged MSB (approximately in the order of 10^6 cells/mL), which could be not ideal during *in-situ* incubations that are intended to mimic natural habitat conditions. Hence, it is recommended to use a microfluidic chip with smaller channel dimensions to result in more monodisperse microbeads. As a result, when these microbeads are washed using two cell strainers, most of the microbeads will fall in the intended size range, resulting in a higher microbead (and cell) concentration in the final working solution.

Another study performed in this thesis investigated the effect of the encapsulation temperature on the cell survival of *M. polaris*, *P. aquimaris*, and *B. licheniformis.* Clearly, a higher temperature resulted in lower cell survival of the three marine bacteria (refer to Figure 2.25). This is important because MSB samples were collected from cold environments, and encapsulating them using 45ºC could be decreasing their cell viability well before they are incubated, which limits their cultivability. An interesting study to

further investigate this effect is to perform a DGGE analysis on MSB samples incubated at different temperatures and, accordingly, examine shifts in their microbial communities.

Additionally, the cell survival and viability of *M. polaris*, *P. aquimaris*, and *B. licheniformis* was examined for encapsulated and re-suspended samples in 50% Instant Ocean® and 10% Marine Broth. It was observed that the cells did not perform well in 50% Instant Ocean®, likely due to the lack of nutrients in this solution. On the other hand, samples in 10% Marine Broth showed improved growth and survival over time. Specifically, the encapsulated samples of *P. aquimaris* and *B. licheniformis* showed more stable cell survival trends over time than their re-suspended counterparts (refer to Figure 2.24). This indicated the advantage of using cell encapsulation in sustaining the cell viability of most environmental marine sediment bacteria over time. The fact that encapsulated *M. polaris* did not perform well over time suggests that some of the environmental marine sediment bacteria would not be able to survive the encapsulation process and/or to sustain their viability in the microbeads. The cell viability of the three species (refer to Figure 2.30) matched the cell survival trends observed after one day of encapsulation.

Last but not the least, encapsulated samples of MSB and the three representative marine sediment species were spread on dMA plates to compare their colony growth to a 10^{-3} dilution of their respective re-suspended samples. For MSB, the incubated dMA plates of encapsulated samples before *in-situ* incubation repeatedly showed minimal growth (1 ± 0 cfu/mL; see section 2.3.7.5) after 2 weeks of plate incubation. This trend was also similar to that of the three representative marine sediment species when they were grown in 50% Instant Ocean. However, when these species were grown in 10%

Marine Broth, *B. licheniformis* was the only species that showed growth from encapsulated samples ($5.7 \times 10^4 \pm 7.5 \times 10^3$ cfu/mL after 1 week of plate incubation), which implied that not all species are able to grow into colonies when spread on agar plates from encapsulated samples. Moreover, this implied that it might be best to grow the encapsulated 'uncultivable' bacteria while in suspension. In the future, isolation of the grown microbes (in microbeads) from the suspension could be performed by using a liquid handling system, which dispenses known amounts of volume containing an optimized number of microbeads (ideally 1 microbead/droplet).

5.5 Material Biocompatibility

The biocompatibility of the materials used to fabricate the microfluidic chip (Clear resin), F- and S-MD Pods (ABS), and M-MD Pods (stainless steel), as well as other materials (Dental LT and Tough resins) was tested in this thesis. Bacterial cultures of *E. coli* and MSB were incubated with pieces of each of these materials (refer to section 2.2.6). The cell survival and viability did not seem to be majorly affected by the presence of these materials in the bacterial cultures during incubation (refer to Figures 2.33 and 2.34, respectively). Therefore, the microfluidic chip and the MD Pods were fabricated from their respective building materials.

More in-depth biocompatibility testing could be performed using bacterial cultures of *M. polaris*, *P. aquimaris*, and *B. licheniformis* to investigate the effect of these materials on representative known marine bacteria, since the MD Pods will be used to incubate marine species, and the MSB samples did not yield great fluorescence results in this thesis overall. Moreover, testing could be expanded to observe the bacterial cultures incubated with the materials over a longer time period, to sub-culture and/or inoculate the bacterial cultures in the presence of these materials, and/or to incubate the bacterial cultures in MD Pods and microfluidic chips made from these materials for the period of time for which the bacteria will spend inside these devices during use. Finally, a biocompatibility test similar to the one performed in this thesis could also be performed using pieces of the 'oil-only' sorbent pad used in Chapter 3 and the microfluidic chip developed in Chapter 4 to examine the effect of the sorbent pad and acetone-treated PDMS, respectively, on the cell survival and viability of *E. coli* and/or known marine bacteria.

5.6 Mineral Oil Removal

This thesis investigated the possibility of removing oil from a continuous flow of an oil/water mixture in an aim to collect the microbeads in an aqueous phase after they exit the microfluidic chip. Two systems were built and tested for this separation: the vacuum-assisted oil removal system and the cartridge filter-inspired oil removal system.

The first system resulted in fair separation of the two phases, with a maximum separation efficiency of 76%. This system could be further tested by changing the porosity of the used stainless steel disc, varying the oil:water flow rates, and varying the vacuum pressure at the water and oil outlets. Although 76% is fairly acceptable (with a possible higher separation when multiple separations of the separated product are applied), the used system lacked in terms of supporting microbead transfer to the aqueous phase, since the used pressure drop across the membrane will likely cause the microbeads to move towards the membrane and stick to it. This gave the grounds for developing the second system: the cartridge filter-inspired oil removal system.

The second system enabled the separation of the oil and water phases. The use of the sorbent pad enabled 100% separation of oil and water when the feed flow rate into the separation column equaled the rate at which the oil exits through its outlet. The foam observed in the solution collected at the water outlet was suspected to be caused by the Span® 80 surfactant. Therefore, the use of an oil-based defoamer could be considered.

Additionally, the sorbent pad used could be readily purchased and is autoclavable, making its integration with microbiology use easy and possible. Through using this system, microbeads were observed in the collected solution from the water outlet. This

meant that the system enabled microbead transfer from the oil phase to the aqueous phase, accomplishing one of the objectives of this thesis.

To improve this system further, the ability of aseptically inserting an autoclaved sorbent pad into a sterilized separation column could be investigated. After that, the separation column could be tested for oil/water separation efficiency when the oil phase contains microbeads with encapsulated cells. The microbead concentration in a known volume as well as cell survival and/or viability before and after the separation can be calculated, giving a solid ground for comparison against other oil/water separation systems which use more difficult-to-fabricate microfluidic systems [48]. If the microbead concentration was found to be lower at the water outlet, it is likely that the microbeads are retained in the separation column due to the fibrous nature of the sorbent pad. This issue could be resolved by investigating filter papers and/or membranes that are oil-permeable and water-impermeable (preliminary testing was performed; refer to Appendix F). Such filter papers and/or membranes would enable the oil to pass through into the sorbent pad while creating a barrier through which water and microbeads cannot pass. Ultimately, this would provide a way for preventing the microbeads from sticking to/in the fibers of the sorbent pad. Finally, the system could be integrated with the droplet-forming microfluidic chip used in this thesis to provide a complete microbead formation and washing process with a single handling step.

APPENDIX

A. Microfluidic Chip Prototypes

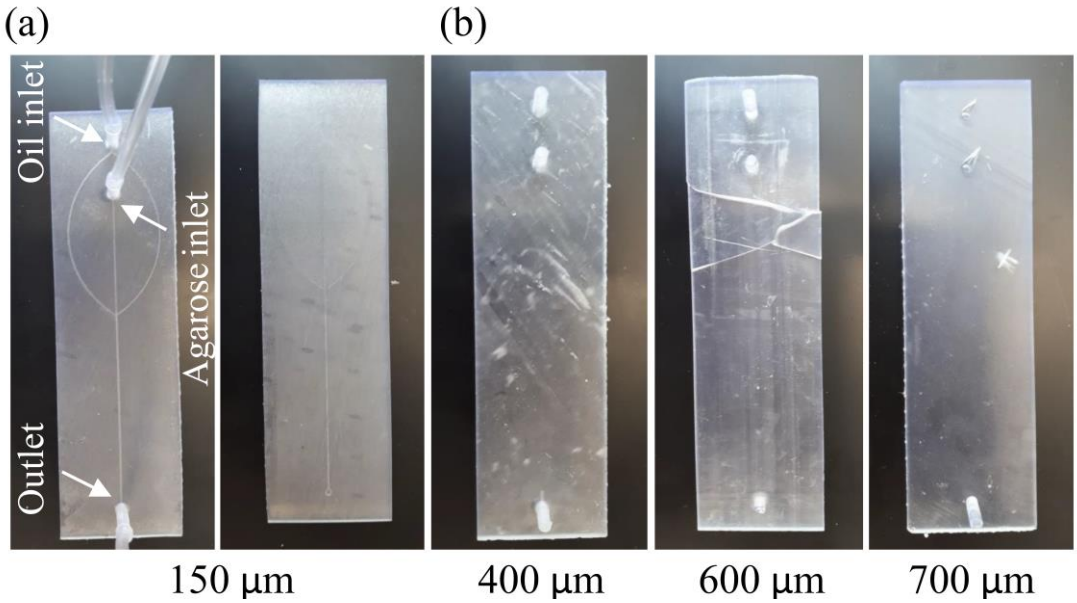

Figure A.1: First microfluidic chip prototypes using Clear resin, Form 2. (a) Microfluidic chips fabricated from two halves that are to be attached and sealed using a water-resistant sealant. The channels were printed with high quality and distinct features. However, both halves 'warped' after printing, making sealing difficult. (b) Microfluidic chips fabricated using the same shape of the channels shown in (a) but using a single body (the channels were designed to be inside the body). However, due to the length of the channels and their small dimensions, the residue resin inside them was difficult to flush. Therefore, it cured inside the body and clogged the channels. It can also be seen that the inlets and outlets were designed perpendicular to the channels, which made the flushing harder and they were easily breakable.

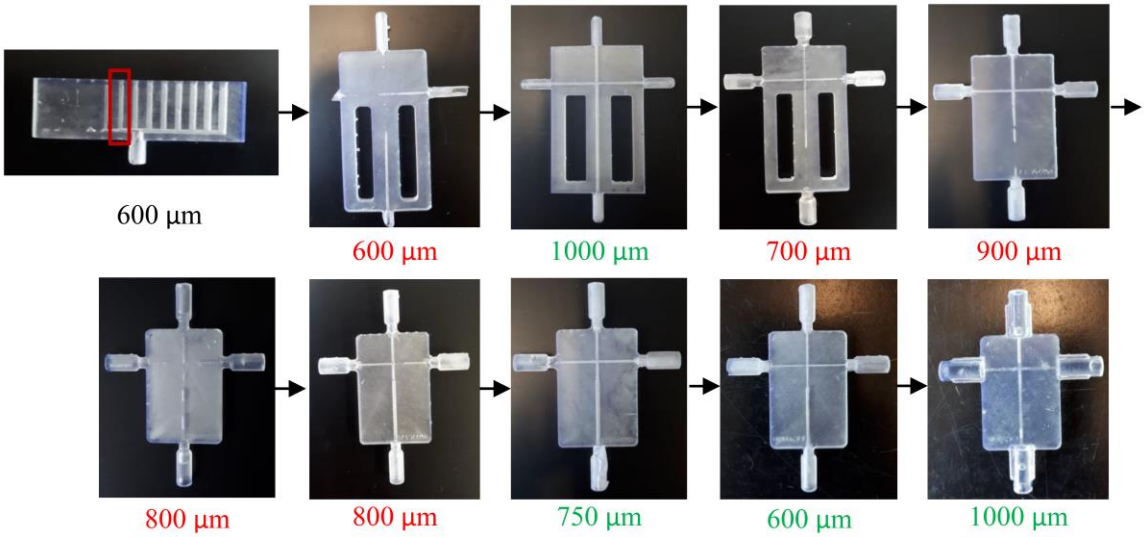

Figure A.2: Microfluidic chip design evolution using internal channels in 3D printed structures using Clear resin, Form 2. Inline inlets and outlets were used to enable easy flushing of residue resin after 3D printing. Red text resembles clogged channels, while green text represents successful, open channels. Channels were designed to be 600 µm after confirming that this channel is printable using the comb-like structure. The channel size was increased to 1000 µm to examine if cross-flow channels could be flushed open. After the success of printing the 1000 µm chip, channel sizes were alternated in an aim to fabricate chips with the smallest possible channel sizes, resulting in 600 µm open channels. The inlets and outlets were reinforced to prevent their breakage, and a chip with 1000 µm channels was finally used for the remainder of this thesis.

B. MD Pod Prototypes

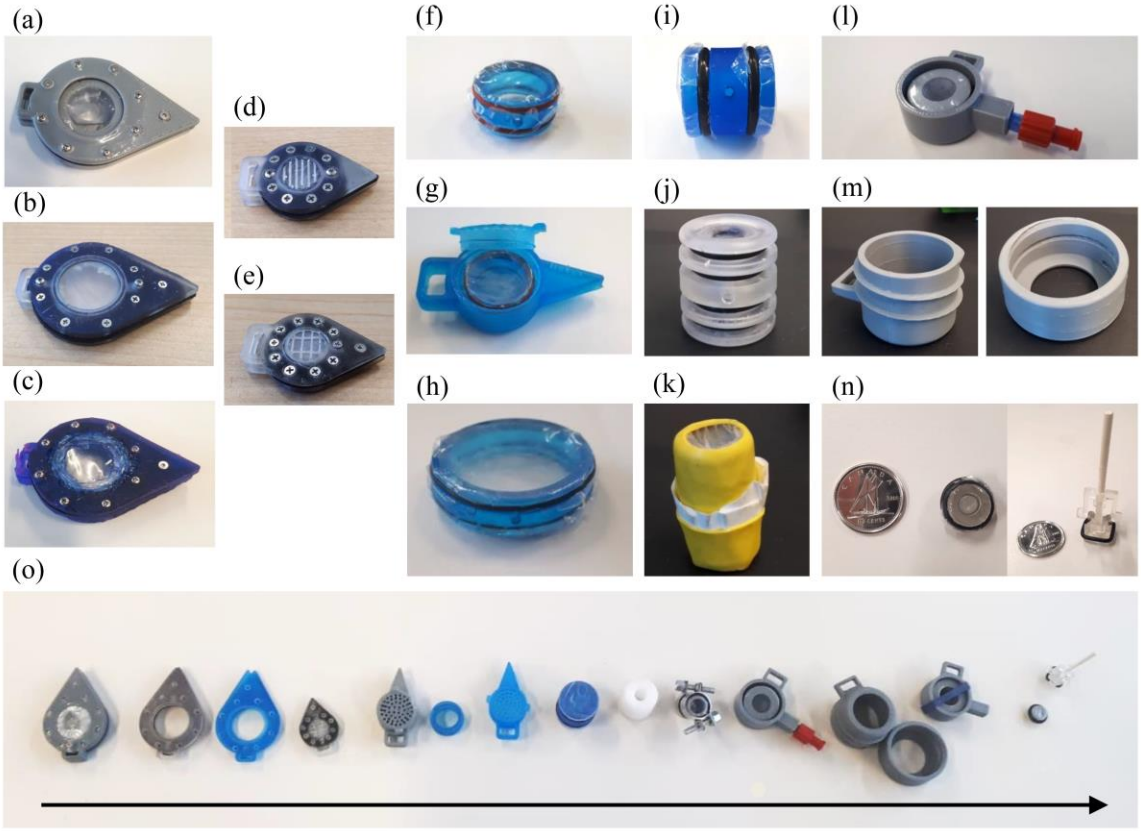

Figure B.1: MD Pod prototypes using different materials, shapes, and sizes. (a – c) The 'first-developed' MD Pod shape with nine pairs of screws and nuts used to provide seal and two pairs of screws and nuts for a loading port and a purge port. The MD Pod in (a) was made from ABS, in (b) was made from Clear resin, and in (c) was made from Tough resin. (d and e) Miniaturized versions of the first developed MD Pod (approximately $1/4^{th}$ the size). The MD Pod in (d) was made from Clear resin and in (e) was made from Dental LT. (f – i) The first prototypes of cylindrical MD Pods, made from Tough resin. (g) A casing developed for the MD Pod shown in (f) in an aim to produce the same shape of the MD Pods presented in (a – e) through having a triangular feature for easy insertion in sea sponges and a tag feature. (j) A cylindrical MD Pod made from Clear resin with two pairs of grooves to allow for folding the PCTE membrane twice to mimic dry bags commonly used in diving to provide seal. (k) A cylindrical MD Pod made from ABS and is enclosed using two heat shrinks (yellow). Applying heat resulted in sealing the MD Pod, but the relatively high temperature required to contract the heat shrink (measured to be approximately 110ºC) is detrimental to the microbes to be placed inside the MD Pod. (l) An S-MD Pod with the loading port closed using a needle tip and a cap, which also provided a way of coupling the MD Pod inside the casing. (m) A casing and a cap including threads to place the F-MD Pod inside it without using a needle tip and a cap nor a rubber band. (n) A concept design of a miniature cylindrical MD Pod (left) enclosed by two O-rings placed using a miniature O-ring dispenser (right). (o) The design evolution of the MD Pod.

B.1 The 'first-developed' MD Pod

B.1.1 Assembly and sterilization

The body of the 'first-developed' MD Pod, shown in Figure B.1(e), was 3D printed using Dental LT photopolymer. After printing, the body was immediately agitated in 99% IPA for 1 min, then immersed in 99% IPA for 5 mins, then agitated again for 1 min. The MD Pod body was then cured for 20 mins under UV light using four F8T5 black light bulbs (Hitachi Appliances Inc., Japan), 8 W each, placed in a UV cross-linker (Select™ Series, Spectroline, USA) and the observed UV wavelength during cross-linking was between 1320 $\mu W/cm^2$ and 1435 $\mu W/cm^2$. The body was then immersed in 70% IPA for sterilization. PCTE membranes were cut to approximately 15 mm diameter and placed on the top and bottom covers of the body. Two nuts were placed inside the top cover to help close the inlet and outlet ports. Two rubber oil-resistant soft Buna-N O-rings (13 mm OD) were placed on the PCTE membranes for sealing. Two smaller O-rings were used for the inlet and outlet ports to ensure seal. A middle body ring and a rubber sheet were aligned with the body and sandwiched between the top and bottom covers. All body parts were enclosed together using 9 pairs of screws and nuts, which were tightened according to the order shown in Figure B.2 to prevent leaks and/or misalignment. The outlet port was used for purging the air that was inside the MD Pods during loading (Figure B.2). Each MD Pod from this design could hold a maximum volume of 325 μL.

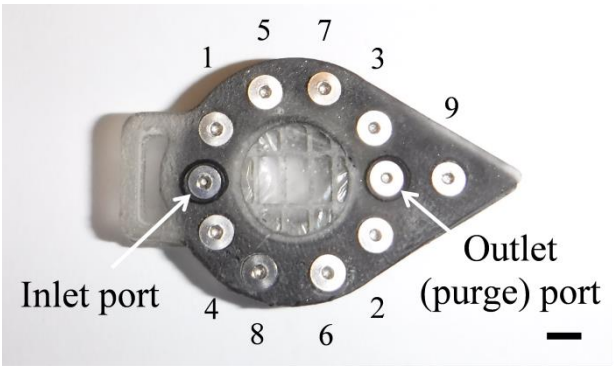

Figure B.2: Recommended order (1 to 9) for assembling screws to prevent leaks and/or misalignment of the top and bottom MD Pod covers. The inlet and outlet ports were closed using a pair of screws and O-rings after MD Pod loading. Scale bar is 3.5 mm.

Before MD Pod loading, the MD Pod body and the inlet and purge screws were soaked in 20% bleach for 25 mins. The loading procedure was performed under a laminar flow hood to prevent contamination. Each MD Pod and its port screws were gently washed with 70% IPA and placed on a petri dish using sterile tweezers. A pipette was used to gently drive the sample through the inlet port, then the inlet and purge screws were carefully aligned and tightened to close the MD Pod. It is important to load the MD Pods slowly and gently. It is also recommended to press evenly on the outer surface of the top membrane during loading to prevent inflation and splashing of the loaded contents from the MD Pod.

B.1.2 Cell migration testing

The ‘first-developed’ MD Pod was tested for outward cell migration. Three MD Pods were loaded with 200 µL of *E. coli* inoculum, while three other MD Pods were loaded with 200 µL of LB broth to serve as the control. All MD Pods were placed in 50 mL of LB broth and incubated at 30ºC for 5 days (Figure B.3). Visual inspection of turbidity was performed every day to ensure no cell migration out of the MD Pods has occurred.

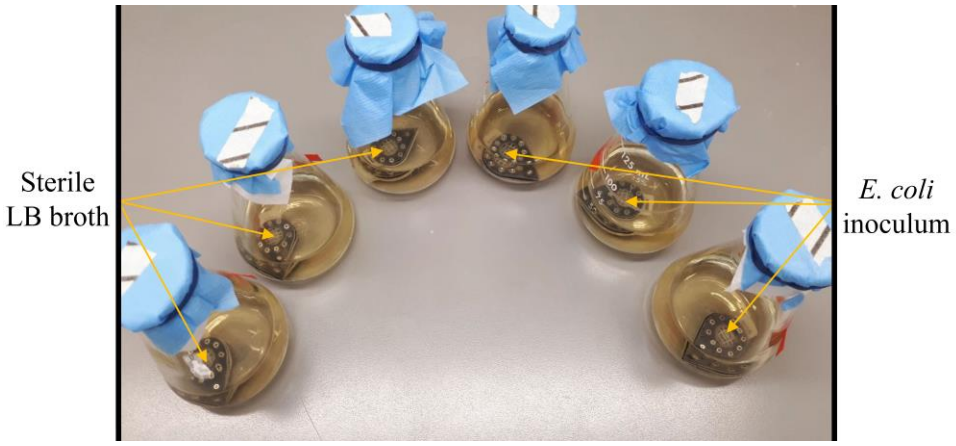

Figure B.3: Outward cell migration test using the ‘first-developed’ MD Pods, with three MD Pods containing *E. coli* inoculum and three containing sterile LB broth. All MD Pods were incubated in sterile LB broth surrounding media.

One of the three MD Pods containing *E. coli* inoculum and one of the three MD Pods loaded with LB broth showed no turbidity in their surrounding solutions, resulting in 33.3% success rate. This was not repeatable since a 16.6% success rate was obtained after carrying out another cell migration test in which one out of six MD Pods loaded with *E. coli* inoculum did not show turbidity. The MD Pods that showed turbidity in their surrounding solutions could have had contamination at the crevices underneath their screws and nuts. Cell migration could also be tested by placing a sterile liquid inside the MD Pod and inspecting the sterility of the liquid after a certain incubation duration.

C. Agarose-Coloring Dyes

Table C.1: Four dyes tested for solubility in agarose beads placed in water and mineral oil.

Type of Dye	Water	Agarose Beads in Water	Mineral Oil	Agarose Beads in Mineral Oil
Alcian blue (Sigma Aldrich, USA)	Soluble	Soluble (does not diffuse out of agarose)	Insoluble	Soluble (does not diffuse out of agarose)
Basic fuschin (Sigma Aldrich, USA)	Soluble	Soluble (diffuses out of agarose)	Soluble	Soluble (diffuses out of agarose)
Food coloring (Club House, Canada)	Soluble	Soluble (diffuses out of agarose)	Insoluble	Insoluble
Fast blue RR (Sigma Aldrich, USA)	Insoluble	Insoluble	Insoluble	Insoluble

D. Encapsulation Protocol

For the encapsulation of marine sediment bacteria (MSB):

A. Sample collection and preparation (approximately 1 hr); (Perform the day before)

1. Aseptically obtain sample and seawater from location. Record as much metadata about the collection location as possible (i.e. GPS coordinates, water and sediment collection depth, temperature, salinity, pH, etc.)
2. Return to the laboratory
3. Filter sterilize seawater (sequentially through 0.45 µm filter then 0.2 µm filter)
4. Autoclave: membranes (place each membrane between filter papers), O-rings, metallic pods (if used: assemble one side with a membrane and O-rings), wide-mouth pipette tips (i.e. cut regular pipette tips), tweezers, 20 mL syringes, and 5 mL syringes
5. Ensure there is enough autoclaved 1% agarose (w/v)
6. Ensure there is enough stock solution of 4% mineral oil (v/v with Span® 80)

B. Bacterial preparation (approximately 1.5 hrs)

1. Remove seawater bacteria from sediment sample:
   a. Let sediment settle
   b. Pour off excess seawater
   c. Add sterile seawater to sediment and invert approximately 10 times then decant to gently remove seawater bacteria – repeat 2 times
   d. Measure a specific amount of sediment into new tubes
   e. Add equal volume of sterile seawater to washed sediment and agitate vigorously to dislodge bacteria adhered to sediment (i.e. 10 mL sediment + 10 mL sterile seawater)
   f. Vortex for 3 mins then place on a shaker in the horizontal position at 400 RPM for 1 hour
   g. Vortex for an additional 30 s then centrifuge at 500 × *g* for 5 mins (May alter time based on sediment composition)
   h. Transfer supernatant to a 15 mL Falcon tube
   i. Measure optical density ($OD_{600\ nm}$) of the supernatant and record (Must be above 0.025 to be able to pellet the cells)
   j. Centrifuge volume equivalent to 2 x10^6 cells/mL at 4,500 × *g* for 10 mins to form a pellet

C. Bacteria encapsulation (approximately 2 hrs for one type of bacteria and blank microbeads)

1. If there is no enough stock solution of 4% mineral oil, weigh Span® 80 and add respective mineral oil to prepare a 4% (v/v) solution then shake well (for a Falcon tube, weigh 1.8 g of Span® 80 and add 45 mL of mineral oil)

2. Soak the needed tubing, needle tips, microfluidic chip, split junction, and ON/OFF valve in 70% IPA for at least 10 mins before assembling the system
3. Fill 20 – 30 mL of the mineral oil solution into a sterile syringe using a 20-gauge needle tip (orange)
4. Turn on the heater and set it at 45ºC (takes approximately 15 mins to reach to this temperature)
5. Open the flame on the tip of a scissor and pinch 1 hole on top of 3 Falcon tubes. One is used to collect blank microbeads, one is used to collect microbeads with encapsulated bacteria, and one is used to flush the system after encapsulation and to collect wastes during encapsulation
6. Assemble the system aseptically (refer to Figure 2.8). Leave the agarose inlet in the microfluidic chip unconnected
7. Add 4 mL of agarose to the obtained pellet in step 1.j. (to achieve 2×10^6 cells/mL cell concentration based on the $OD_{600\ nm}$ value obtained), and vortex the tube for 5 s and collect the suspension in a 5 mL syringe using a 2 inch long 20-gauge needle tip (orange). Replace the needle tip with a 0.5 inch long 20-gauge needle tip (orange). Place into the syringe pump-mounted heat block. *Note: This step must be performed very fast to prevent the gelation of agarose. Moreover, the agarose volume can be adjusted according to the number of cells present in the pellet*
8. Complete the assembly of all tubing by connecting the agarose needle tip to the agarose inlet in the microfluidic chip
9. Turn on the cooler
10. Set the mineral oil syringe pump to 110 mL/hr and press Start
11. When no air bubbles are observed in tubing, set the agarose syringe pump to 10 mL/hr and press Start. When the flow is stable, decrease the agarose flowrate to 5 mL/hr
12. Always observe the outlet tubing to ensure that microbeads of the desired size are formed – collect inadequately sized microbeads in the waste tube. *Note: Refill the mineral oil syringe when it is empty; the agarose pump should be on Pause and the oil pump should be on Stop; aseptically disconnect the tubing from the oil needle tip and connect the ON/OFF valve to the tubing in the OFF position to prevent the oil from leaking onto the working space*
13. Run the encapsulation for about 10 – 20 mins or until desired amount of microbeads is collected. Do not leave the system unattended. From time to time, check the temperature of the heat block and the cooler to ensure that neither is overheating
14. When enough microbeads are collected (approximately 30 mL in the collection tube), stop both syringe pumps. Rearrange the tubing to have 2 outlets going to the flush tube. Adjust the flowrate to 200 mL/hr. Start the mineral oil syringe pump until the mineral oil finishes. Stop the pump. Pour the flushed solution into an Erlenmeyer flask labelled as waste. Pour all collected wasted tubes into this flask. Place the flask in the autoclave for sterile disposal

15. Repeat the flushing step using a syringe loaded with 20 mL 70% IPA to sterilize the system. Ensure that the flushed liquid is collected in a different Falcon tube since IPA is flammable and should not be placed in the autoclave
16. Dispose of all syringes, needles, and tubing in an appropriate manner. *Note: These could be used for multiple cell encapsulation following empty microbead formation performed on the same day.*
17. Wash the microfluidic chip and split junction with adequate 70% IPA and DI water. Be careful not to splash the contents (use tubing to flush)
18. Pour the collected microbeads (present in mineral oil) over a 30 μm cell strainer placed on a Falcon tube. Pour 10 mL of filter-sterilized seawater over the microbeads on the strainer. Use more seawater if needed or if oil is still observed with the microbeads. *Note: the washing solution can be replaced based on the nature of the encapsulated cells. Moreover, a different cell strainer pore size can be used based on the desired size of microbeads*
19. Carefully flip the 30 μm cell strainer with its contents over a 100 μm cell strainer set on a new Falcon tube. Carefully wash down the contents using 5 mL filter-sterilized seawater. Pour an additional 5 mL of filter-sterilized seawater over the microbeads on the strainer. The solution in the Falcon tube is now "the working solution," containing 30 μm to 100 μm microbeads.
20. *Note: every 100 μL contains approximately 150 – 250 microbeads if stable microbead formation was observed for most of the encapsulation process. The washing solution can be replaced based on the nature of the encapsulated cells. Moreover, a different cell strainer pore size can be used based on the desired size of microbeads to be collected in the working solution*

E. MD Pod Protocols

A. MD Pod loading (approximately 1.5 hrs for 15 – 20 MD Pods)

1. If plastic MD Pods are to be used, sterilize them by soaking in a 20% bleach solution for 20 – 40 mins, rinsing in a sterile DI water bath, soaking in 70% IPA for 10 mins, followed by rinsing in another sterile DI water bath. Metallic MD Pods are used after autoclaving
2. MD Pods are loaded with the following solutions (the MD Pods are loaded with 60% of their total inner volume):

Table E.1: Samples typically loaded into the MD Pods.

MD Pod	Loaded Solution
Encapsulated Bacteria (A)	Encapsulated bacteria solution formed by re-suspending a pellet of bacteria in 4 mL 1% agarose (a.k.a. working solution)
Blank Microbeads (B)	Blank microbead working solution formed from 1% agarose
Re-suspended Bacteria (C)	Bacteria pellet re-suspended in 4 mL of filter-sterilized seawater (or other media appropriate with the nature of the used cells)
Sterile Media (D)	Filter-sterilized seawater (or other media appropriate with the nature of the used cells)

Note: the OD_{600nm} of the pellet used should be adjusted to give a cell concentration of 2×10^6 cells/mL

3. Each solution is pipetted into the MD Pod using a micropipette then the MD Pod is sealed. (Use wide-mouth tips for samples containing microbeads). A PCTE membrane is then placed over the MD Pod and two O-rings are used to seal the MD Pod. The MD Pod is then placed in a casing and secured with a rubber band. The casing could be tagged according to the sample it contains

B. MD Pod incubation (approximately 10 mins for an in-laboratory aquarium)

1. Gently bury MD Pods beneath approximately 5 cm of sediment, being careful not to disrupt the membranes
2. Incubate for 2 – 4 weeks at 4ºC or for 1 – 2 weeks at 20ºC

C. MD Pod unloading (approximately 1.5 hrs for 15 – 20 MD Pods)

1. Gently remove the MD Pods from the incubation location and place them on a sterile surface
2. Return to the laboratory
3. Rinse the outer surface of the MD Pods in a bath of sterile DI water
4. Gently remove the MD Pod top membrane. Carefully collect the solution within the MD Pod using a micropipette and transfer it to a sterile Falcon tube (this serves as the 10^0 dilution). Use wide-mouth tips for samples

containing microbeads. Remove the inside contents while holding the MD Pod tilted. Do not pipette all of the solution from the MD Pod, as outside contents might get into the MD Pod through the membrane due to the suction force of the micropipette, possibly leading to contamination

5. Place all emptied MD Pods in a proper container for sterilization. Add 20% bleach and soak for 20 – 40 mins
6. Serially dilute the MD Pod 10^0 solutions from 10^{-1} to 10^{-3}.
7. Plate 100 µL of each dilution onto 3 dilute Marine Agar plates using a micropipette, then use cell spreaders to spread the samples over the plate. Incubate at room temperature (or at a temperature suitable for the cells used)
8. Count observed colonies on each plate once a week over a period of 2 weeks to obtain cell abundance value. Convert to cfu/mL

D. Comparison to the traditional plating method (approximately 0.5 hrs)

1. Obtain an aliquot of all solutions to be loaded into the MD Pods (refer to Table E.1) to plate on dilute Marine Agar plates prior to *in-situ* incubation to serve as the traditional plating method control.
2. Serially dilute solutions from 10^{-1} to 10^{-3}.
3. Plate 100 µL of each dilution onto 3 dilute Marine Agar plates using a micropipette, then use cell spreaders to spread the samples over the plate. Incubate at room temperature (or at a temperature suitable for the cells used)
4. Count observed colonies on each plate once a week over a period of 2 weeks to obtain cell abundance value. Convert to cfu/mL

E. Comparison of taxonomic diversity (via denaturing gradient gel electrophoresis (DGGE); see section 2.2.9.3 for more details)

1. Plan to run DGGE for cell suspensions obtained before and after the *in-situ* incubation (encapsulated and re-suspended bacteria samples) to visualize differences in abundance and diversity before and after encapsulation and the *in-situ* incubation
2. Extraction of DNA from the cell suspension samples
    i. If to be performed at a later time, freeze all samples obtained before and after the *in-situ* incubation
    ii. Extract genomic DNA from the samples using an appropriate kit
    iii. Perform DNA extraction for filter-sterilized seawater and blank microbeads collected before and after the *in-situ* incubation to serve as the negative controls
3. Run PCR
    i. Obtain the PCR products for all the samples used in step E. 2 (refer to section 2.2.9.2 for the PCR parameters to be used)
    ii. Include a negative control with no DNA extract (sterile DI water and mastermix). If possible, include a positive control with a DNA template known to amplify (e.g. *E. coli*)
4. Run all samples on the prepared acrylamide gel (see section 2.2.9.3 for more details)
5. Stain and visualize the gel (see section 2.2.9.3 for more details)

6. Analyze the obtained gels using BioNumerics 6.6 (Applied Maths, USA).

F. Percent Viability (via PrestoBlue®)

1. Add 10 µL of 40 µg/mL PrestoBlue® cell viability reagent to 90 µL of each sample in a 96-well plate. Incubate the plate at room temperature for 1 – 2 hrs then read fluorescence using a spectrophotometer (use excitation/emission: 560/590 and define the type of well plate used). *Note: perform this sampling and PrestoBlue® addition process on every day a reading is intended to be taken*
2. Obtain fluorescence readings of all samples (A – D) before and after the *in-situ* incubation every other day for 2 weeks using a spectrophotometer (or at any time interval desired).
3. Obtain fluorescence readings of empty wells to make sure that background fluorescence is approximately 20 – 30 RFU. Subtract this background fluorescence from all readings

G. Percent Viability (via Live/Dead assay)

1. Add 1 µL of Live/dead dye to 100 µL of each sample in a 96-well plate
2. Use a GFP filter for the green dye and a Texas Red filter for the red dye. Image each sample. For encapsulated samples, count the cells existing only in the microbeads
3. Calculate percent viability based on the living cell count compared to the total cell count

F. Filter Papers Tested for Water Impermeability and Oil Permeability

Table F.1: Permeability of water and mineral oil through different materials of filter paper.

Type of Filter	Water	Mineral Oil
GTTP (0.2 µm)	Impermeable	Impermeable
GSWP (0.22 µm)	Permeable (very slow)	Permeable (very slow)
SCWP (8.0 µm)	Permeable (very slow)	Permeable
SMWP (5.0 µm)	Permeable	Impermeable
Cellulose nitrate (0.45 µm)	Permeable	Permeable (very slow)
Cyclopore track etched (0.2 µm)	Impermeable	Impermeable
Cellulosic (1.2 µm)	Permeable	Permeable (very slow)
PCTE (0.03 µm)	Permeable	Impermeable
Whatman filter paper	Permeable (very slow)	Impermeable
Milk filter paper	Permeable	Permeable
Weighing paper	Impermeable	Impermeable
Blue filter paper	Impermeable	Impermeable
Coffee filter paper	Permeable	Permeable (very slow)

REFERENCES

[1] D.L. Mayers, J.D. Sobel, M. Ouellette, K.S. Kaye, D. Marchaim, Antimicrobial Drug Resistance: Mechanisms of Drug Resistance, 2nd ed., Springer, 2017.

[2] R.E. Condon, Bacterial Resistance to Antibiotics, 2002. doi:10.1001/archsurg.137.12.1417.

[3] K. Bush, P. Courvalin, G. Dantas, J. Davies, B. Eisenstein, P. Huovinen, G.A. Jacoby, R. Kishony, B.N. Kreiswirth, E. Kutter, S.A. Lerner, S. Levy, K. Lewis, O. Lomovskaya, J.H. Miller, S. Mobashery, L.J. Piddock, S. Projan, C.M. Thomas, A. Tomasz, P.M. Tulkens, T.R. Walsh, J.D. Watson, J. Witkowski, W. Witte, G. Wright, P. Yeh, H.I. Zgurskaya, Tackling Antibiotic Resistance, Nat Rev Microbiol. 9 (2011) 894–896. doi:10.1038/nrmicro2693.

[4] K.E. Thorpe, P. Joski, K.J. Johnston, Antibiotic-resistant infection treatment costs have doubled since 2002, now exceeding $2 billion annually, Health Aff. 37 (2018) 662–669. doi:10.1377/hlthaff.2017.1153.

[5] Antibiotic / Antimicrobial Resistance, Centers Dis. Control Prev. (2018). https://www.cdc.gov/drugresistance/index.html.

[6] W. Wencewicz, C. Wencewicz, T. Wencewicz, Challenges for Antibiotics, in: Antibiot. Challenges, Mech. Oppor., ASM Press, 2016: pp. 5–31.

[7] K. Lewis, New approaches to antimicrobial discovery, Biochem. Pharmacol. 134 (2017) 87–98. doi:10.1016/j.bcp.2016.11.002.

[8] L. Katz, R.H. Baltz, Natural product discovery: past, present, and future, J. Ind. Microbiol. Biotechnol. 43 (2016) 155–176. doi:10.1007/s10295-015-1723-5.

[9] W.H. Gerwick, B.S. Moore, Lessons from the past and charting the future of marine natural products drug discovery and chemical biology, Chem. Biol. 19 (2012) 85–98. doi:10.1016/j.chembiol.2011.12.014.

[10] J.W. Blunt, A.R. Carroll, B.R. Copp, R.A. Davis, R.A. Keyzers, M.R. Prinsep, Marine natural products, Nat. Prod. Rep. 35 (2018) 8–53. doi:10.1039/c7np00052a.

[11] A.T. Bull, J.E.M. Stach, Marine actinobacteria: new opportunities for natural product search and discovery, Trends Microbiol. 15 (2007) 491–499. doi:10.1016/j.tim.2007.10.004.

[12] P. Manivasagan, K.H. Kang, K. Sivakumar, E.C.Y. Li-Chan, H.M. Oh, S.K. Kim, Marine actinobacteria: An important source of bioactive natural products, Environ. Toxicol. Pharmacol. 38 (2014) 172–188. doi:10.1016/j.etap.2014.05.014.

[13] J. Blunt, J. Buckingham, M. Munro, Handbook of Marine Natural products, 2013. doi:10.1007/978-90-481-3834-0.

[14] T.A. Gulder, B.S. Moore, Chasing the treasures of the sea - bacterial marine natural products, Curr. Opin. Microbiol. 12 (2009) 252–260. doi:10.1016/j.mib.2009.05.002.

[15] V.L. Challinor, H.B. Bode, Bioactive natural products from novel microbial sources, Ann. N. Y. Acad. Sci. 1354 (2015) 82–97. doi:10.1111/nyas.12954.

[16] J.T. Staley, Microorganisms in Aquatic and Terrestrial Habitats, (1985).

[17] V.H.T. Pham, J. Kim, Cultivation of unculturable soil bacteria, Trends Biotechnol. 30 (2012) 475–484. doi:10.1016/j.tibtech.2012.05.007.

[18] S.R. Vartoukian, Cultivation strategies for growth of uncultivated bacteria, J. Oral Biosci. 58 (2016) 143–149. doi:10.1016/j.job.2016.08.001.
[19] Z. Zhang, Y. Wu, X.H. Zhang, Cultivation of microbes from the deep-sea environments, Deep. Res. Part II. (2017) 1–10. doi:10.1016/j.dsr2.2017.07.008.
[20] D. Harwani, Recent advances in culturing the unculturable bacteria, Int. J. Recent Sci. Res. 4 (2013) 1488–1491. doi:10.15373/22778179/SEP2013/122.
[21] E.J. Stewart, Growing unculturable bacteria, J. Bacteriol. 194 (2012) 4151–4160. doi:10.1128/JB.00345-12.
[22] K. Alain, J. Querellou, Cultivating the uncultured: Limits, advances and future challenges, Extremophiles. 13 (2009) 583–594. doi:10.1007/s00792-009-0261-3.
[23] I. Joint, M. Mühling, J. Querellou, Culturing marine bacteria - An essential prerequisite for biodiscovery: Minireview, Microb. Biotechnol. 3 (2010) 564–575. doi:10.1111/j.1751-7915.2010.00188.x.
[24] R. Noorani, 3D Printing: Technology, Applications, and Selection, Taylor & Francis Group, Boca Raton, 2018.
[25] B. Berdy, A.L. Spoering, L.L. Ling, S.S. Epstein, In situ cultivation of previously uncultivable microorganisms using the ichip, Nat. Protoc. 12 (2017) 2232–2242. doi:10.1038/nprot.2017.074.
[26] B.C. Ferrari, T. Winsley, M. Gillings, S. Binnerup, Cultivating previously uncultured soil bacteria using a soil substrate membrane system, Nat. Protoc. 3 (2008) 1261–1269. doi:10.1038/nprot.2008.102.
[27] C.B. Doty, W.J. Rivers, M.A. Furlong, A novel method for cultivating soil bacteria, Beta Beta Beta Biol. Soc. 84 (2013) 65–73.
[28] D. Jung, E.Y. Seo, S.S. Epstein, Y. Joung, J. Han, V. V. Parfenova, O.I. Belykh, A.S. Gladkikh, T.S. Ahn, Application of a new cultivation technology, I-tip, for studying microbial diversity in freshwater sponges of Lake Baikal, Russia, FEMS Microbiol. Ecol. 90 (2014) 417–423. doi:10.1111/1574-6941.12399.
[29] X. Zhao, X. Liu, X. Xu, Y. V. Fu, Microbe social skill: the cell-to-cell communication between microorganisms, Sci. Bull. 62 (2017) 516–524. doi:10.1016/j.scib.2017.02.010.
[30] B. Perbal, Cell Communication and Signaling Communication is the key, Cell Commun. Signal. 4 (2003) 1–4. http://www.biosignaling.com/content/1/1/3.
[31] A.F. Lodhi, Y. Zhang, M. Adil, Y. Deng, Antibiotic discovery : combining isolation chip (iChip) technology and co-culture technique, Appl. Microbiol. Biotechnol. 102 (2018) 1–9. doi:10.1007/s00253-018-9193-0.
[32] B.C. Ferrari, S.J. Binnerup, M. Gillings, Microcolony cultivation on a soil substrate membrane system selects for previously uncultured soil bacteria, Appl. Environ. Microbiol. 71 (2005) 8714–8720. doi:10.1128/AEM.71.12.8714-8720.2005.
[33] Y. Akselband, C. Cabral, T.P. Castor, H.M. Chikarmane, P. McGrath, Enrichment of slow-growing marine microorganisms from mixed cultures using gel microdrop (GMD) growth assay and fluorescence-activated cell sorting, J. Exp. Mar. Bio. Ecol. 329 (2006) 196–205. doi:10.1016/j.jembe.2005.08.018.
[34] J. Overmann, B. Abt, J. Sikorski, Present and Future of Culturing Bacteria, Annu. Rev. Microbiol. 71 (2017) 711–730. doi:10.1146/annurev-micro-090816-093449.
[35] B. Lin, ed., Microfluidics: Technologies and Applications, Springer, 2011.

doi:10.1007/128_2011_147.
[36] Y. Xia, G.M. Whitesides, Soft Lithography, Annu. Rev. Mater. Sci. 28 (1998) 153–184. doi:10.1146/annurev.matsci.28.1.153.
[37] A.K. Au, W. Huynh, L.F. Horowitz, A. Folch, 3D-Printed Microfluidics, Angew. Chemie. 55 (2016) 3862–3881. doi:10.1002/anie.201504382.
[38] S. Waheed, J.M. Cabot, N.P. Macdonald, T. Lewis, R.M. Guijt, B. Paull, M.C. Breadmore, 3D printed microfluidic devices: Enablers and barriers, Lab Chip. 16 (2016) 1993–2013. doi:10.1039/c6lc00284f.
[39] H. Liu, Y. Zhang, Droplet formation in microfluidic cross-junctions, Phys. Fluids. 23 (2011) 082101. doi:10.1063/1.3615643.
[40] T. Alkayyali, T. Cameron, B. Haltli, R. Kerr, A. Ahmadi, Microfluidic and Cross-Linking Methods for Encapsulation of Living Cells and Bacteria - A Review, Anal. Chim. Acta. 1053C (2019) 1–21. doi:S0003267019300236.
[41] M. Chabert, J. Viovy, Microfluidic high-throughput encapsulation and hydrodynamic self-sorting of single cells, 105 (2007) 3191–3196. doi:10.1073/pnas.0708321105.
[42] T.P. Brackbill, Polymer microfluidic device for high-throughput single-cell encapsulation, lysis, and biological assay, University of California, Berkeley, 2012.
[43] E. Um, D.S. Lee, H.B. Pyo, J.K. Park, Continuous generation of hydrogel beads and encapsulation of biological materials using a microfluidic droplet-merging channel, Microfluid. Nanofluidics. 5 (2008) 541–549. doi:10.1007/s10404-008-0268-6.
[44] R. Seemann, M. Brinkmann, T. Pfohl, S. Herminghaus, Droplet based microfluidics, Reports Prog. Phys. 75 (2012) 016601. doi:10.1088/0034-4885/75/1/016601.
[45] S. Sugaya, M. Yamada, A. Hori, M. Seki, Microfluidic production of single micrometer-sized hydrogel beads utilizing droplet dissolution in a polar solvent, Biomicrofluidics. 7 (2013) 054120. doi:10.1063/1.4826936.
[46] S. Akbari, T. Pirbodaghi, Microfluidic encapsulation of cells in alginate particles via an improved internal gelation approach, Microfluid. Nanofluidics. 16 (2014) 773–777. doi:10.1007/s10404-013-1264-z.
[47] H. Huang, Y. Yu, Y. Hu, X. He, O. Berk Usta, M.L. Yarmush, Generation and manipulation of hydrogel microcapsules by droplet-based microfluidics for mammalian cell culture, Lab Chip. 17 (2017) 1913–1932. doi:10.1039/C7LC00262A.
[48] Y. Deng, N. Zhang, L. Zhao, X. Yu, X. Ji, W. Liu, S. Guo, K. Liu, X.Z. Zhao, Rapid purification of cell encapsulated hydrogel beads from oil phase to aqueous phase in a microfluidic device, Lab Chip. 11 (2011) 4117–4121. doi:10.1039/c1lc20494g.
[49] Y. Zhou, The recent development and applications of fluidic channels by 3D printing, J. Biomed. Sci. 24 (2017) 1–22. doi:10.1186/s12929-017-0384-2.
[50] M.J. Beauchamp, G.P. Nordin, A.T. Woolley, Moving from millifluidic to truly microfluidic sub-100-μm cross-section 3D printed devices, Anal. Bioanal. Chem. 409 (2017) 4311–4319. doi:10.1007/s00216-017-0398-3.
[51] J.M. Lee, M. Zhang, W.Y. Yeong, Characterization and evaluation of 3D printed

microfluidic chip for cell processing, Microfluid. Nanofluidics. 20 (2016) 1–15. doi:10.1007/s10404-015-1688-8.
[52] A.A. Yazdi, A. Popma, W. Wong, T. Nguyen, Y. Pan, J. Xu, 3D printing: an emerging tool for novel microfluidics and lab-on-a-chip applications, Microfluid. Nanofluidics. 20 (2016) 1–18. doi:10.1007/s10404-016-1715-4.
[53] H.N. Chan, Y. Chen, Y. Shu, Y. Chen, Q. Tian, H. Wu, Direct, one-step molding of 3D-printed structures for convenient fabrication of truly 3D PDMS microfluidic chips, Microfluid. Nanofluidics. 19 (2015) 9–18. doi:10.1007/s10404-014-1542-4.
[54] S. Wang, A. Bruning, O. Jeon, F. Long, E. Alsberg, C.K. Choi, An in-situ photocrosslinking microfluidic technique to generate non-spherical, cytocompatible, degradable, monodisperse alginate microgels for chondrocyte encapsulation, Biomicrofluidics. 12 (2018) 014106. doi:10.1063/1.5017644.
[55] M.T. Guler, P. Beyazkilic, C. Elbuken, A versatile plug microvalve for microfluidic applications, Sensors Actuators, A Phys. 265 (2017) 224–230. doi:10.1016/j.sna.2017.09.001.
[56] X. Zhang, L. Li, C. Luo, Gel integration for microfluidic applications, Lab Chip. 16 (2016) 1757–1776. doi:10.1039/C6LC00247A.
[57] Q. Ji, J.M. Zhang, Y. Liu, X. Li, P. Lv, D. Jin, H. Duan, A Modular Microfluidic Device via Multimaterial 3D Printing for Emulsion Generation, Sci. Rep. 8 (2018) 1–11. doi:10.1038/s41598-018-22756-1.
[58] R. Subramani, W. Aalbersberg, Culturable rare Actinomycetes: Diversity, isolation and marine natural product discovery, Appl. Microbiol. Biotechnol. 97 (2013) 9291–9321. doi:10.1007/s00253-013-5229-7.
[59] L. Ma, J. Kim, R. Hatzenpichler, M.A. Karymov, N. Hubert, I.M. Hanan, E.B. Chang, R.F. Ismagilov, Gene-targeted microfluidic cultivation validated by isolation of a gut bacterium listed in Human Microbiome Project's Most Wanted taxa, Proc. Natl. Acad. Sci. 111 (2014) 9768–9773. doi:10.1073/pnas.1404753111.
[60] J.Z. Wang, Z.Q. Ding, F. Zhang, W. Bin Ye, Recent development in cell encapsulations and their therapeutic applications, Mater. Sci. Eng. C. 77 (2017) 1247–1260. doi:10.1016/j.msec.2017.04.103.
[61] M.K. Alam, E. Koomson, H. Zou, C. Yi, C.W. Li, T. Xu, M. Yang, Recent advances in microfluidic technology for manipulation and analysis of biological cells (2007–2017), Anal. Chim. Acta. 1044 (2018) 29–65. doi:10.1016/j.aca.2018.06.054.
[62] E. Gencturk, S. Mutlu, K.O. Ulgen, Advances in microfluidic devices made from thermoplastics used in cell biology and analyses, Biomicrofluidics. 11 (2017) 051502. doi:10.1063/1.4998604.
[63] Q. Zhang, T. Wang, Q. Zhou, P. Zhang, Y. Gong, H. Gou, J. Xu, B. Ma, Development of a facile droplet-based single-cell isolation platform for cultivation and genomic analysis in microorganisms, Sci. Rep. 7 (2017) 1–11. doi:10.1038/srep41192.
[64] C.J. Ingham, A. Sprenkels, J. Bomer, D. Molenaar, A. van den Berg, J.E.T. van Hylckama Vlieg, W.M. de Vos, The micro-Petri dish, a million-well growth chip for the culture and high-throughput screening of microorganisms, Proc. Natl. Acad. Sci. 104 (2007) 18217–18222. doi:10.1073/pnas.0701693104.
[65] T. Geng, C.R. Smallwood, E.L. Bredeweg, K.R. Pomraning, A.E. Plymale, S.E.

Baker, J.E. Evans, R.T. Kelly, Multimodal microfluidic platform for controlled culture and analysis of unicellular organisms, Biomicrofluidics. 11 (2017). doi:10.1063/1.4986533.
[66] L. Lin, M. Jie, F. Chen, J. Zhang, Z. He, J.-M. Lin, Efficient cell capture in an agarose–PDMS hybrid chip for shaped 2D culture under temozolomide stimulation, RSC Adv. 6 (2016) 75215–75222. doi:10.1039/C6RA15734C.
[67] A. Grünberger, C. Probst, S. Helfrich, A. Nanda, B. Stute, W. Wiechert, E. von Lieres, K. Nöh, J. Frunzke, D. Kohlheyer, Spatiotemporal microbial single-cell analysis using a high-throughput microfluidics cultivation platform, Cytom. Part A. 87 (2015) 1101–1115. doi:10.1002/cyto.a.22779.
[68] S. Sarkar, P. Sabhachandani, D. Stroopinsky, K. Palmer, N. Cohen, J. Rosenblatt, D. Avigan, T. Konry, Dynamic analysis of immune and cancer cell interactions at single cell level in microfluidic droplets, Biomicrofluidics. 10 (2016) 054115. doi:10.1063/1.4964716.
[69] I. Meyvantsson, D.J. Beebe, Cell Culture Models in Microfluidic Systems, Annu. Rev. Anal. Chem. 1 (2008) 423–449. doi:10.1146/annurev.anchem.1.031207.113042.
[70] K. Lewis, S. Epstein, A. D'Onofrio, L.L. Ling, Uncultured microorganisms as a source of secondary metabolites, J. Antibiot. (Tokyo). 63 (2010) 468–476. doi:10.1038/ja.2010.87.
[71] E. Rosenberg, E.F. DeLong, S. Lory, E. Stackebrandt, F. Thompson, eds., The Prokaryotes: Prokaryotic Biology and Symbiotic Associations, 4th ed., Springer Heidelberg, London, 2013. doi:10.1007/978-3-642-30141-4.
[72] S. Hoshino, T. Wakimoto, H. Onaka, I. Abe, Chojalactones A-C, cytotoxic butanolides isolated from streptomyces sp. cultivated with mycolic acid containing bacterium, Org. Lett. 17 (2015) 1501–1504. doi:10.1021/acs.orglett.5b00385.
[73] H.B. Park, H.C. Kwon, C.H. Lee, H.O. Yang, Glionitrin A , an Antibiotic-Antitumor Metabolite Derived from Competitive Interaction, J. Nat. Prod. 72 (2009) 248–252. doi:10.1021/np800606e.
[74] D.C. Oh, C.A. Kauffman, P.R. Jensen, W. Fenical, Induced production of emericellamides A and B from the marine-derived fungus Emericella sp. in competing co-culture, J. Nat. Prod. 70 (2007) 515–520. doi:10.1021/np060381f.
[75] A. Marmann, A.H. Aly, W. Lin, B. Wang, P. Proksch, Co-cultivation - A powerful emerging tool for enhancing the chemical diversity of microorganisms, Mar. Drugs. 12 (2014) 1043–1065. doi:10.3390/md12021043.
[76] B.H. Chueh, Y. Zheng, Y.S. Torisawa, A.Y. Hsiao, C. Ge, S. Hsiong, N. Huebsch, R. Franceschi, D.J. Mooney, S. Takayama, Patterning alginate hydrogels using light-directed release of caged calcium in a microfluidic device, Biomed. Microdevices. 12 (2010) 145–151. doi:10.1007/s10544-009-9369-6.
[77] C. Siltanen, M. Diakataou, J. Lowen, A. Haque, A. Rahimian, G. Stybayeva, A. Revzin, One step fabrication of hydrogel microcapsules with hollow core for assembly and cultivation of hepatocyte spheroids, Acta Biomater. 50 (2017) 428–436. doi:10.1016/j.actbio.2017.01.010.
[78] J. Park, A. Kerner, M.A. Burns, X.N. Lin, Microdroplet-enabled highly parallel co-cultivation of microbial communities, PLoS One. 6 (2011) e17019. doi:10.1371/journal.pone.0017019.

[79] C. Nai, V. Meyer, From Axenic to Mixed Cultures: Technological Advances Accelerating a Paradigm Shift in Microbiology, Trends Microbiol. 26 (2018) 538–554. doi:10.1016/j.tim.2017.11.004.
[80] I. Dewi Puspita, Y. Kamagata, M. Tanaka, K. Asano, C.H. Nakatsu, Are Uncultivated Bacteria Really Uncultivable?, Microbes Environ. 27 (2012) 356–366. doi:10.1264/jsme2.ME12092.
[81] S.S. Epstein, The phenomenon of microbial uncultivability, Curr. Opin. Microbiol. 16 (2013) 636–642. doi:10.1016/j.mib.2013.08.003.
[82] T. Kaeberlein, K. Lewis, S.S. Epstein, Isolating “Uncultivable” Microorganisms in Pure Culture in a Simulated Natural Environment, Science (80-.). 296 (2002) 1127–1129.
[83] A. Bollmann, K. Lewis, S.S. Epstein, Incubation of environmental samples in a diffusion chamber increases the diversity of recovered isolates, Appl. Environ. Microbiol. 73 (2007) 6386–6390. doi:10.1128/AEM.01309-07.
[84] D. Nichols, N. Cahoon, E.M. Trakhtenberg, L. Pham, A. Mehta, A. Belanger, T. Kanigan, K. Lewis, S.S. Epstein, Use of ichip for high-throughput in situ cultivation of "uncultivable microbial species, Appl. Environ. Microbiol. 76 (2010) 2445–2450. doi:10.1128/AEM.01754-09.
[85] D. Jung, Y. Aoi, S.S. Epstein, In Situ Cultivation Allows for Recovery of Bacterial Types Competitive in Their Natural Environment, Microbes Environ. 31 (2016) 456–459. doi:10.1264/jsme2.ME16079.
[86] L.L. Ling, T. Schneider, A.J. Peoples, A.L. Spoering, I. Engels, B.P. Conlon, A. Mueller, T.F. Schäberle, D.E. Hughes, S. Epstein, M. Jones, L. Lazarides, V.A. Steadman, D.R. Cohen, C.R. Felix, K.A. Fetterman, W.P. Millett, A.G. Nitti, A.M. Zullo, C. Chen, K. Lewis, A new antibiotic kills pathogens without detectable resistance, Nature. 517 (2015) 455–459. doi:10.1038/nature14098.
[87] K. Zengler, G. Toledo, M. Rappe, J. Elkins, E.J. Mathur, J.M. Short, M. Keller, Cultivating the uncultured., Proc. Natl. Acad. Sci. U. S. A. 99 (2002) 15681–15686. doi:10.1073/pnas.252630999.
[88] K. Zengler, M. Walcher, G. Clark, I. Haller, G. Toledo, T. Holland, E.J. Mathur, G. Woodnutt, J.M. Short, M. Keller, High-throughput cultivation of microorganisms using microcapsules, Methods Enzymol. 397 (2005) 124–130. doi:10.1016/S0076-6879(05)97007-9.
[89] S. Ji, R. Zhao, Q. Yin, Y. Zhao, C. Liu, T. Xiao, X. Zhang, Gel microbead cultivation with a subenrichment procedure can yield better bacterial cultivability from a seawater sample than standard plating method, J. Ocean Univ. China. 11 (2012) 45–51. doi:10.1007/s11802-012-1869-y.
[90] M. Keller, K. Zengler, Tapping into microbial diversity, Nat. Rev. Microbiol. 2 (2004) 141–150. doi:10.1038/nrmicro819.
[91] L. Boitard, D. Cottinet, N. Bremond, J. Baudry, J. Bibette, Growing microbes in millifluidic droplets, Eng. Life Sci. 15 (2015) 318–326. doi:10.1002/elsc.201400089.
[92] S.E. Nybo, M.K. Kharel, Recent Developments in the Quest for Novel Microbial Natural Products, in: Stud. Nat. Prod. Chem., 1st ed., Elsevier B.V., 2019: pp. 109–152. doi:10.1016/B978-0-444-64179-3.00004-9.
[93] M. Hamon, J. Dai, S. Jambovane, J.W. Hong, Microfluidic Systems for Marine

Biotechnology, in: S.-K. Kim (Ed.), Springer Handb. Mar. Biotechnol., Springer Heidelberg, Berlin, 2015: pp. 509–530.
[94] S. Kou, D. Cheng, F. Sun, I.M. Hsing, Microfluidics and microbial engineering, Lab Chip. 16 (2016) 432–446. doi:10.1039/c5lc01039j.
[95] K. Aleklett, E.T. Kiers, P. Ohlsson, T.S. Shimizu, V.E. Caldas, E.C. Hammer, Build your own soil: Exploring microfluidics to create microbial habitat structures, ISME J. 12 (2018) 312–319. doi:10.1038/ismej.2017.184.
[96] Y.J. Eun, A.S. Utada, M.F. Copeland, S. Takeuchi, D.B. Weibel, Encapsulating bacteria in agarose microparticles using microfluidics for high-throughput cell analysis and isolation, ACS Chem. Biol. 6 (2011) 260–266. doi:10.1021/cb100336p.
[97] J.M. Rabanel, X. Banquy, H. Zouaoui, M. Mokhtar, P. Hildgen, Progress technology in microencapsulation methods for Cell therapy, Biotechnol. Prog. 25 (2009) 946–963. doi:10.1002/btpr.226.
[98] S.-Y. Teh, R. Lin, L.-H. Hung, A.P. Lee, Droplet microfluidics, Lab Chip. 8 (2008) 198–220. doi:10.1039/b715524g.
[99] Š. Selimović, J. Oh, H. Bae, M. Dokmeci, A. Khademhosseini, Microscale strategies for generating cell-encapsulating hydrogels, Polymers (Basel). 4 (2012) 1554–1579. doi:10.3390/polym4031554.
[100] L. Gasperini, J.F. Mano, R.L. Reis, Natural polymers for the microencapsulation of cells, J. R. Soc. Interface. 11 (2014) 1–19. doi:10.1098/rsif.2014.0817.
[101] D. Velasco, E. Tumarkin, E. Kumacheva, Microfluidic encapsulation of cells in polymer microgels, Small. 8 (2012) 1633–1642. doi:10.1002/smll.201102464.
[102] J. Lin, Cell Analysis on Microfluidics, Springer Nature, Beijing, 2018. doi:10.1007/978-981-10-5394-8.
[103] J.L. Drury, D.J. Mooney, Hydrogels for tissue engineering: Scaffold design variables and applications, Biomaterials. 24 (2003) 4337–4351. doi:10.1016/S0142-9612(03)00340-5.
[104] N. Buffi, D. Merulla, J. Beutier, F. Barbaud, S. Beggah, H. van Lintel, P. Renaud, J. Roelof van der Meer, Development of a microfluidics biosensor for agarose-bead immobilized Escherichia coli bioreporter cells for arsenite detection in aqueous samples, Lab Chip. 11 (2011) 2369. doi:10.1039/c1lc20274j.
[105] S. Yoshida, M. Takinoue, H. Onoe, Compartmentalized Spherical Collagen Microparticles for Anisotropic Cell Culture Microenvironments, Adv. Healthc. Mater. 6 (2017) 1601463. doi:10.1002/adhm.201601463.
[106] J.M. Duarte, I. Barbier, Y. Schaerli, Bacterial Microcolonies in Gel Beads for High-Throughput Screening of Libraries in Synthetic Biology, ACS Synth. Biol. 6 (2017) 1988–1995. doi:10.1021/acssynbio.7b00111.
[107] H.H. Tuson, G.K. Auer, L.D. Renner, M. Hasebe, C. Tropini, M. Salick, W.C. Crone, A. Gopinathan, K.C. Huang, D.B. Weibel, Measuring the stiffness of bacterial cells from growth rates in hydrogels of tunable elasticity, Mol. Microbiol. 84 (2012) 874–891. doi:10.1111/j.1365-2958.2012.08063.x.
[108] K. Jain, H. Yang, B.-R. Cai, B. Haque, A.I. Hurvitz, C. Diehl, T. Miyata, B.H. Smith, K. Stenzel, M. Suthanthiran, A.L. Rubin, Retrievable, Replaceable, Macroencapsulated Pancreatic Islet Xenografts, Transplantation. 59 (1995) 319–324.

[109] S. Sakai, I. Hashimoto, K. Kawakami, Agarose-gelatin conjugate for adherent cell-enclosing capsules, Biotechnol. Lett. 29 (2007) 731–735. doi:10.1007/s10529-007-9312-y.
[110] N. Wang, X.S. Wu, A novel approach to stabilization of protein drugs in poly(lactic-co-glycolic acid) microspheres using agarose hydrogel, Int. J. Pharm. 166 (1998) 1–14. doi:10.1016/S0378-5173(97)00339-6.
[111] E. Murano, Use of natural polysaccharides in the microencapsulation techniques, J. Appl. Ichthyol. 14 (1998) 245–249. doi:10.1111/j.1439-0426.1998.tb00650.x.
[112] A. Kumachev, J. Greener, E. Tumarkin, E. Eiser, P.W. Zandstra, E. Kumacheva, High-throughput generation of hydrogel microbeads with varying elasticity for cell encapsulation, Biomaterials. 32 (2011) 1477–1483. doi:10.1016/j.biomaterials.2010.10.033.
[113] H.-F. Lu, E.D. Targonsky, M.B. Wheeler, Y.-L. Cheng, Thermally Induced Gelable Polymer Networks for Living Cell Encapsulation, Biotechnol. Bioeng. 96 (2006) 146–155. doi:10.1002/bit.21121.
[114] S. Ma, M. Natoli, X. Liu, M.P. Neubauer, F.M. Watt, A. Fery, W.T.S. Huck, Monodisperse collagen-gelatin beads as potential platforms for 3D cell culturing, J. Mater. Chem. B. 1 (2013) 5128–5136. doi:10.1039/c3tb20851f.
[115] S.H. Huang, Y.S. Lin, C.W. Wu, C.J. Wu, Assessment of the inhibition of dengue virus infection by carrageenan via real-time monitoring of cellular oxygen consumption rates within a microfluidic device, Biomicrofluidics. 8 (2014) 024110. doi:10.1063/1.4870772.
[116] S. Rochín-Wong, A. Rosas-Durazo, P. Zavala-Rivera, A. Maldonado, M.E. Martínez-Barbosa, I. Vélaz, J. Tánori, Drug release properties of diflunisal from layer-by- layer self-assembled k-carrageenan/chitosan nanocapsules: Effect of deposited layers, Polymers (Basel). 10 (2018) 1–16. doi:10.3390/polym10070760.
[117] S. Sakai, S. Ito, H. Inagaki, K. Hirose, T. Matsuyama, M. Taya, K. Kawakami, Cell-enclosing gelatin-based microcapsule production for tissue engineering using a microfluidic flow-focusing system, Biomicrofluidics. 5 (2011) 013402. doi:10.1063/1.3516657.
[118] J. Barlow, K. Gozzi, C.P. Kelley, B.M. Geilich, T.J. Webster, Y. Chai, S. Sridhar, A.L. van de Ven, High throughput microencapsulation of Bacillus subtilis in semi-permeable biodegradable polymersomes for selenium remediation, Appl. Microbiol. Biotechnol. 101 (2017) 455–464. doi:10.1007/s00253-016-7896-7.
[119] V. Zamora-Mora, D. Velasco, R. Hernández, C. Mijangos, E. Kumacheva, Chitosan/agarose hydrogels: Cooperative properties and microfluidic preparation, Carbohydr. Polym. 111 (2014) 348–355. doi:10.1016/j.carbpol.2014.04.087.
[120] R. Yegappan, V. Selvaprithiviraj, S. Amirthalingam, R. Jayakumar, Carrageenan based hydrogels for drug delivery, tissue engineering and wound healing, Carbohydr. Polym. 198 (2018) 385–400. doi:10.1016/j.carbpol.2018.06.086.
[121] Y.S. Lin, C.H. Yang, C.T. Wu, A.M. Grumezescu, C.Y. Wang, W.C. Hsieh, S.Y. Chen, K.S. Huang, A microfluidic chip using phenol formaldehyde resin for uniform-sized polycaprolactone and chitosan microparticle generation, Molecules. 18 (2013) 6521–6531. doi:10.3390/molecules18066521.
[122] E. Poggi, J.-F. Gohy, Janus particles: from synthesis to application, Colloid Polym. Sci. 295 (2017) 2083–2108. doi:10.1007/s00396-017-4192-8.

[123] W.H. Tan, S. Takeuchi, Monodisperse alginate hydrogel microbeads for cell encapsulation, Adv. Mater. 19 (2007) 2696–2701. doi:10.1002/adma.200700433.
[124] L. Capretto, S. Mazzitelli, G. Luca, C. Nastruzzi, Preparation and characterization of polysaccharidic microbeads by a microfluidic technique: Application to the encapsulation of Sertoli cells, Acta Biomater. 6 (2010) 429–435. doi:10.1016/j.actbio.2009.08.023.
[125] A.G. Håti, N.B. Arnfinnsdottir, C. Østevold, M. Sletmoen, G. Etienne, E. Amstad, B.T. Stokke, Microarrays for the study of compartmentalized microorganisms in alginate microbeads and (W/O/W) double emulsions, RSC Adv. 6 (2016) 114830–114842. doi:10.1039/c6ra23945e.
[126] D.M.G. Boggione, L.S. Batalha, M.T.P. Gontijo, M.E.S. Lopez, A.V.N.C. Teixeira, I.J.B. Santos, R.C.S. Mendonça, Evaluation of microencapsulation of the UFV-AREG1 bacteriophage in alginate-Ca microcapsules using microfluidic devices, Colloids Surfaces B Biointerfaces. 158 (2017) 182–189. doi:10.1016/j.colsurfb.2017.06.045.
[127] T. Jankowski, M. Zielinska, A. Wysakowska, Encapsulation of lactic acid bacteria with alginate/starch capsules, Biotechnol. Tech. 11 (1997) 31–34. doi:10.1007/bf02764447.
[128] K.Y. Lee, D.J. Mooney, Alginate: Properties and biomedical applications, Prog. Polym. Sci. 37 (2012) 106–126. doi:10.1016/j.progpolymsci.2011.06.003.
[129] M.A. LeRoux, F. Guilak, L.A. Setton, Compressive and shear properties of alginate gel: Effects of sodium ions and alginate concentration, J. Biomed. Mater. Res. 47 (1999) 46–53. doi:10.1002/(SICI)1097-4636(199910)47:1<46::AID-JBM6>3.0.CO;2-N.
[130] S. Morelli, R.G. Holdich, M.M. Dragosavac, Microparticles for cell encapsulation and colonic delivery produced by membrane emulsification, J. Memb. Sci. 524 (2017) 377–388. doi:10.1016/j.memsci.2016.11.058.
[131] S. Ryu, H. Kim, S. Kang, K. Shin, S.Y. Jung, J. Heo, J. Han, J.K. Yoon, J.R. Lee, J. Hong, K.H. Ahn, T. Hyeon, N.S.Y. Hwang, B.S. Kim, Reversible Cell Layering for Heterogeneous Cell Assembly Mediated by Ionic Cross-Linking of Chitosan and a Functionalized Cell Surface Membrane, Chem. Mater. 29 (2017) 5294–5305. doi:10.1021/acs.chemmater.7b01484.
[132] X.Z. Shu, K.J. Zhu, Controlled Drug Release Properties of Ionically Crosslinked-Chitosan Beads : The Influence of Anion Structure, Int. J. Pharm. 233 (2002) 217–225.
[133] K.C. Gupta, F.H. Jabrail, Preparation and characterization of sodium hexameta phosphate cross-linked chitosan microspheres for controlled and sustained delivery of centchroman, Int. J. Biol. Macromol. 38 (2006) 272–283. doi:10.1016/j.ijbiomac.2006.03.013.
[134] G.K. Vinner, D.J. Malik, High precision microfluidic microencapsulation of bacteriophages for enteric delivery, Res. Microbiol. 169 (2018) 522–530. doi:10.1016/j.resmic.2018.05.011.
[135] A.K. Anal, W.F. Stevens, Chitosan-alginate multilayer beads for controlled release of ampicillin, Int. J. Pharm. 290 (2005) 45–54. doi:10.1016/j.ijpharm.2004.11.015.
[136] M. Chávarri, I. Marañón, R. Ares, F.C. Ibáñez, F. Marzo, M. del C. Villarán, Microencapsulation of a probiotic and prebiotic in alginate-chitosan capsules

improves survival in simulated gastro-intestinal conditions, Int. J. Food Microbiol. 142 (2010) 185–189. doi:10.1016/j.ijfoodmicro.2010.06.022.
[137] L. Baruch, M. Machluf, Alginate–Chitosan Complex Coacervation for Cell Encapsulation: Effect on Mechanical Properties and on Long-Term Viability, Biopolymers. 82 (2006) 570–579. doi:10.1002/bip.
[138] Y. Liu, L.J. Duan, M.J. Kim, J.H. Kim, D.J. Chung, In situ sodium alginate-hyaluronic acid hydrogel coating method for clinical applications, Macromol. Res. 22 (2014) 240–247. doi:10.1007/s13233-014-2001-5.
[139] A. Srinatha, J. Pandit, S. Singh, Ionic cross-linked chitosan beads for extended release of ciprofloxacin: In vitro characterization, Indian J. Pharm. Sci. 70 (2008) 16. doi:10.4103/0250-474X.40326.
[140] P.M. Rocha, V.E. Santo, M.E. Gomes, R.L. Reis, J.F. Mano, Encapsulation of adipose-derived stem cells and transforming growth factor-β1 in carrageenan-based hydrogels for cartilage tissue engineering, J. Bioact. Compat. Polym. 26 (2011) 493–507. doi:10.1177/0883911511420700.
[141] A.S. Michel, M.M. Mestdagh, M.A.V. Axelos, Physico-chemical properties of carrageenan gels in presence of various cations, Int. J. Biol. Macromol. 21 (1997) 195–200. doi:10.1016/S0141-8130(97)00061-5.
[142] L.S. Kontturi, M. Yliperttula, P. Toivanen, A. Määttä, A.M. Määttä, A. Urtti, A laboratory-scale device for the straightforward production of uniform, small sized cell microcapsules with long-term cell viability, J. Control. Release. 152 (2011) 376–381. doi:10.1016/j.jconrel.2011.03.005.
[143] N.P. Desal, a Sojomihardjo, Z. Yao, P. Soon-Shiong, N.P. Desai, N. Ron, Interpenetrating polymer networks of alginate and polyethylene glycol for encapsulation of islets of Langerhans, J. Microencapsul. 17 (2000) 667–690. doi:10.1080/02652040050161675.
[144] Y. Oh, J. Cha, S.G. Kang, P. Kim, A polyethylene glycol-based hydrogel as macroporous scaffold for tumorsphere formation of glioblastoma multiforme, J. Ind. Eng. Chem. 39 (2016) 10–15. doi:10.1016/j.jiec.2016.05.012.
[145] H.J. Kong, D.J. Mooney, The Effects of Poly(Ethyleneimine) (PEI) Molecular Weight on Reinforcement of Alginate Hydrogels, Cell Transplant. 12 (2003) 779–785. doi:10.3727/000000003108747253.
[146] C. Lee, I. Chu, Characterization of Modified Alginated-Poly-L-Lysine Microcapsules, Artif. Organs. 21 (1997) 1002–1006.
[147] S.M. Luna, M.E. Gomes, J.F. Mano, R.L. Reis, Development of a novel cell encapsulation system based on natural origin polymers for tissue engineering applications, J. Bioact. Compat. Polym. 25 (2010) 341–359. doi:10.1177/0883911510372173.
[148] P. Xue, Y. Wu, N. V. Menon, Y. Kang, Microfluidic synthesis of monodisperse PEGDA microbeads for sustained release of 5-fluorouracil, Microfluid. Nanofluidics. 18 (2015) 333–342. doi:10.1007/s10404-014-1436-5.
[149] Z. Jiang, B. Xia, R. McBride, J. Oakey, A microfluidic-based cell encapsulation platform to achieve high long-term cell viability in photopolymerized PEGNB hydrogel microspheres, J. Mater. Chem. B. 5 (2017) 173–180. doi:10.1039/C6TB02551J.
[150] J.A. Burdick, K.S. Anseth, Photoencapsulation of osteoblasts in injectable RGD-

modified PEG hydrogels for bone tissue engineering, Biomaterials. 23 (2002) 4315–4323. doi:10.1016/S0142-9612(02)00176-X.
[151] P. Panda, S. Ali, E. Lo, B.G. Chungb, T.A. Hatton, A. Khademhosseinib, P.S. Doyle, Stop-Flow Lithography to Generate Cell-Laden Microgel Particles, Lab Chip. 8 (2008) 1056–1061. doi:doi:10.1039/b804234a.
[152] P. Li, M. Müller, M.W. Chang, M. Frettlöh, H. Schönherr, Encapsulation of Autoinducer Sensing Reporter Bacteria in Reinforced Alginate-Based Microbeads, ACS Appl. Mater. Interfaces. 9 (2017) 22321–22331. doi:10.1021/acsami.7b07166.
[153] E.Y. Liu, S. Jung, D.A. Weitz, H. Yi, C.H. Choi, High-throughput double emulsion-based microfluidic production of hydrogel microspheres with tunable chemical functionalities toward biomolecular conjugation, Lab Chip. 18 (2018) 323–334. doi:10.1039/c7lc01088e.
[154] C.R. Lee, A.J. Grodzinsky, M. Spector, The effects of cross-linking of collagen-glycosaminoglycan scaffolds on compressive stiffness, chondrocyte-mediated contraction, proliferation and biosynthesis, Biomaterials. 22 (2001) 3145–3154. doi:10.1016/S0142-9612(01)00067-9.
[155] R. Holmes, X. Bin Yang, A. Dunne, L. Florea, D. Wood, G. Tronci, Thiol-ene photo-click collagen-PEG hydrogels: Impact of water-soluble photoinitiators on cell viability, gelation kinetics and rheological properties, Polymers (Basel). 9 (2017) 226. doi:10.3390/polym9060226.
[156] K.G. Lee, T.J. Park, S.Y. Soo, K.W. Wang, B.I.I. Kim, J.H. Park, C.S. Lee, D.H. Kim, S.J. Lee, Synthesis and utilization of E. coli-encapsulated PEG-based microdroplet using a microfluidic chip for biological application, Biotechnol. Bioeng. 107 (2010) 747–751. doi:10.1002/bit.22861.
[157] K. Ono, Y. Saito, H. Yura, K. Ishikawa, A. Kurita, T. Akaike, M. Ishihara, Photocrosslinkable chitosan as a biological adhesive, J. Biomed. Mater. Res. 49 (2000) 289–295. doi:10.1002/(SICI)1097-4636(200002)49:2<289::AID-JBM18>3.0.CO;2-M.
[158] B. Xia, Z. Jiang, D. Debroy, D. Li, J. Oakey, Cytocompatible cell encapsulation via hydrogel photopolymerization in microfluidic emulsion droplets, Biomicrofluidics. 11 (2017) 044102. doi:10.1063/1.4993122.
[159] K.W. Bong, J. Lee, P.S. Doyle, Stop flow lithography in perfluoropolyether (PFPE) microfluidic channels, Lab Chip. 14 (2014) 4680–4687. doi:10.1039/C4LC00877D.
[160] V.A. Liu, S.N. Bhatia, Three-dimensional photopatterning of hydrogels containing living cells, Biomed. Microdevices. 4 (2002) 257–266. doi:10.1023/A:1020932105236.
[161] C.L. Lewis, Y. Lin, C. Yang, A.K. Manocchi, K.P. Yuet, P.S. Doyle, H. Yi, Microfluidic fabrication of hydrogel microparticles containing functionalized viral nanotemplates, Langmuir. 26 (2010) 13436–13441. doi:10.1021/la102446n.
[162] S.R. Shin, B. Aghaei-Ghareh-Bolagh, T.T. Dang, S.N. Topkaya, X. Gao, S.Y. Yang, S.M. Jung, J.H. Oh, M.R. Dokmeci, X. Tang, A. Khademhosseini, Cell-laden microengineered and mechanically tunable hybrid hydrogels of gelatin and graphene oxide, Adv. Mater. 25 (2013) 6385–6391. doi:10.1002/adma.201301082.
[163] A.I. Van Den Bulcke, B. Bogdanov, N. De Rooze, E.H. Schacht, M. Cornelissen,

H. Berghmans, Structural and rheological properties of methacrylamide modified gelatin hydrogels, Biomacromolecules. 1 (2000) 31–38. doi:10.1021/bm990017d.
[164] R. Samanipour, Z. Wang, A. Ahmadi, K. Kim, Experimental and computational study of microfluidic flow-focusing generation of gelatin methacrylate hydrogel droplets, J. Appl. Polym. Sci. 133 (2016) 43701. doi:10.1002/app.43701.
[165] X. Zhou, Y. Du, X. Wang, Azo Polymer Janus Particles and Their Photoinduced, Symmetry-Breaking Deformation, ACS Macro Lett. 5 (2016) 234–237. doi:10.1021/acsmacrolett.5b00932.
[166] A. Zhu, M. Guo, Single emulsion microfluidic production of Janus and core-shell particles via off-chip polymerization, Chinese J. Polym. Sci. 34 (2016) 367–377. doi:10.1007/s10118-016-1748-x.
[167] A. Khademhosseini, G. Eng, J. Yeh, J. Fukuda, J.B. III, R. Langer, J.A. Burdick, Micromolding of photocrosslinkable hyaluronic acid for cell encapsulation and entrapment, J. Biomed. Mater. Res. Part A. (2016) 522–532. doi:10.1002/jbm.a.30821.
[168] D. Dendukuri, P.S. Doyle, The synthesis and assembly of polymeric microparticles using microfluidics, Adv. Mater. 21 (2009) 4071–4086. doi:10.1002/adma.200803386.
[169] G.F. Christopher, S.L. Anna, Microfluidic methods for generating continuous droplet streams, J. Phys. D. Appl. Phys. 40 (2007) R319–R336. doi:10.1088/0022-3727/40/19/R01.
[170] M. Jang, S. Yang, P. Kim, Microdroplet-based cell culture models and their application, Biochip J. 10 (2016) 310–317. doi:10.1007/s13206-016-0407-1.
[171] J. Burgain, C. Gaiani, M. Linder, J. Scher, Encapsulation of probiotic living cells: From laboratory scale to industrial applications, J. Food Eng. 104 (2011) 467–483. doi:10.1016/j.jfoodeng.2010.12.031.
[172] S. Chopde, N. Pawar, V. Kele, S. Changade, Microencapsulation of probiotic bacteria of available techniques, focusing on biomaterials - A review, Agric. Rev. 35 (2014) 287–294. doi:10.5958/0976-0741.2014.00916.7.
[173] K.J. De France, F. Xu, T. Hoare, Structured Macroporous Hydrogels: Progress, Challenges, and Opportunities, Adv. Healthc. Mater. 7 (2018) 1700927. doi:10.1002/adhm.201700927.
[174] A. Jaworek, Electrostatic micro- and nanoencapsulation and electroemulsification: A brief review, J. Microencapsul. 25 (2008) 443–468. doi:10.1080/02652040802049109.
[175] H.B. Eral, V. López-Mejías, M. O'Mahony, B.L. Trout, A.S. Myerson, P.S. Doyle, Biocompatible alginate microgel particles as heteronucleants and encapsulating vehicles for hydrophilic and hydrophobic drugs, Cryst. Growth Des. 14 (2014) 2073–2082. doi:10.1021/cg500250e.
[176] T. Visted, R. Bjerkvig, P.O. Enger, Cell encapsulation technology as a therapeutic strategy for CNS malignancies., Neuro. Oncol. 3 (2001) 201–210. doi:10.1215/S1522851700000648.
[177] O. Khanna, J.C. Larson, M.L. Moya, E.C. Opara, E.M. Brey, Generation of Alginate Microspheres for Biomedical Applications, J. Vis. Exp. 66 (2012) e3388. doi:10.3791/3388.
[178] D.K. Nguyen, Y.M. Son, N.E. Lee, Hydrogel Encapsulation of Cells in Core-Shell

Microcapsules for Cell Delivery, Adv. Healthc. Mater. 4 (2015) 1537–1544. doi:10.1002/adhm.201500133.
[179] C.H. Goh, P.W.S. Heng, L.W. Chan, Alginates as a useful natural polymer for microencapsulation and therapeutic applications, Carbohydr. Polym. 88 (2012) 1–12. doi:10.1016/j.carbpol.2011.11.012.
[180] K. Lee, J. Hong, H.J. Roh, S.H. Kim, H. Lee, S.K. Lee, C. Cha, Dual ionic crosslinked interpenetrating network of alginate-cellulose beads with enhanced mechanical properties for biocompatible encapsulation, Cellulose. 24 (2017) 4963–4979. doi:10.1007/s10570-017-1458-8.
[181] L. Capretto, S. Mazzitelli, A. Tosi, C. Nastruzzi, Preparation of microspheres based on alginate/agarose blends by microfluidic technique, J. Control. Release. 132 (2008) e55–e56. doi:10.1016/j.jconrel.2008.09.053.
[182] R.L. Srinivas, S.D. Johnson, P.S. Doyle, Oil-isolated hydrogel microstructures for sensitive bioassays on-chip, Anal. Chem. 85 (2013) 12099–12107. doi:10.1021/ac403201p.
[183] Y. Hu, G. Azadi, A.M. Ardekani, Microfluidic fabrication of shape-tunable alginate microgels: Effect of size and impact velocity, Carbohydr. Polym. 120 (2015) 38–45. doi:10.1016/j.carbpol.2014.11.053.
[184] G. Zhao, X. Liu, K. Zhu, X. He, Hydrogel Encapsulation Facilitates Rapid-Cooling Cryopreservation of Stem Cell-Laden Core-Shell Microcapsules as Cell-Biomaterial Constructs, Adv. Healthc. Mater. 6 (2017) 1700988. doi:10.1002/adhm.201700988.
[185] D. Dendukuri, S.S. Gu, D.C. Pregibon, T.A. Hatton, P.S. Doyle, Stop-flow lithography in a microfluidic device, Lab Chip. 7 (2007) 818–828. doi:10.1039/b703457a.
[186] S.H. Huang, C.K. Lin, Stop-flow lithography to continuously fabricate microlens structures utilizing an adjustable three-dimensional mask, Micromachines. 5 (2014) 667–680. doi:10.3390/mi5030667.
[187] Y.S. Lin, C.H. Yang, K. Lu, K.S. Huang, Y.Z. Zheng, Synthesis of agar microparticles using temperature-controlled microfluidic devices for Cordyceps militaris cultivation, Electrophoresis. 32 (2011) 3157–3163. doi:10.1002/elps.201100343.
[188] C.H. Choi, J.H. Jung, Y.W. Rhee, D.P. Kim, S.E. Shim, C.S. Lee, Generation of monodisperse alginate microbeads and in situ encapsulation of cell in microfluidic device, Biomed. Microdevices. 9 (2007) 855–862. doi:10.1007/s10544-007-9098-7.
[189] T. Thorsen, R.W. Roberts, F.H. Arnold, S.R. Quake, Dynamic pattern formation in a vesicle-generating microfluidic device, Phys. Rev. Lett. 86 (2001) 4163–4166. doi:10.1103/PhysRevLett.86.4163.
[190] H.A. Stone, A.D. Stroock, A. Ajdari, Engineering Flows in Small Devices, Annu. Rev. Fluid Mech. 36 (2004) 381–411. doi:10.1146/annurev.fluid.36.050802.122124.
[191] H. Liu, M. Nakajima, T. Kimura, Production of monodispersed water-in-oil emulsions using polymer microchannels, J. Am. Oil Chem. Soc. 81 (2004) 705–711. doi:10.1007/s11746-004-965-9.
[192] E.E. Ekanem, S.A. Nabavi, G.T. Vladisavljevic, S. Gu, Structured Biodegradable

Polymeric Microparticles for Drug Delivery Produced Using Flow Focusing Glass Microfluidic Devices, ACS Appl. Mater. Interfaces. 7 (2015) 23132–23143. doi:10.1021/acsami.5b06943.
[193] G.K. Vinner, G.T. Vladisavljević, M.R.J. Clokie, D.J. Malik, Microencapsulation of Clostridium difficile specific bacteriophages using microfluidic glass capillary devices for colon delivery using pH triggered release, PLoS One. 12 (2017) e0186239. doi:10.1371/journal.pone.0186239.
[194] J.H. Xu, S.W. Li, J. Tan, Y.J. Wang, G.S. Luo, Controllable preparation of monodisperse O/W and W/O emulsions in the same microfluidic device, Langmuir. 22 (2006) 7943–7946. doi:10.1021/la0605743.
[195] A.R. Abate, A. Poitzsch, Y. Hwang, J. Lee, J. Czerwinska, D.A. Weitz, Impact of inlet channel geometry on microfluidic drop formation, Phys. Rev. E - Stat. Nonlinear, Soft Matter Phys. 80 (2009) 026310. doi:10.1103/PhysRevE.80.026310.
[196] S. Yang, W. Long, Y. Chen, Analysis of Poiseuille Flow Property in Two-Dimensional Micro Channels of Microfluidic Pneumatic Micro-Valve, in: J. Phys. Conf. Ser., 2018: p. 012014. doi:10.1088/1742-6596/986/1/012014.
[197] M. Darekar, K.K. Singh, J.M. Joshi, S. Mukhopadhyay, K.T. Shenoy, Single-stage microscale solvent extraction in parallel microbore tubes using a monoblock distributor with integrated microfluidic junctions, Sep. Sci. Technol. 52 (2017) 2213–2223. doi:10.1080/01496395.2017.1279181.
[198] T. Femmer, A. Jans, R. Eswein, N. Anwar, M. Moeller, M. Wessling, A.J.C. Kuehne, High-Throughput Generation of Emulsions and Microgels in Parallelized Microfluidic Drop-Makers Prepared by Rapid Prototyping, ACS Appl. Mater. Interfaces. 7 (2015) 12635–12638. doi:10.1021/acsami.5b03969.
[199] T. Han, L. Zhang, H. Xu, J. Xuan, Factory-on-chip: Modularised microfluidic reactors for continuous mass production of functional materials, Chem. Eng. J. 326 (2017) 765–773. doi:10.1016/j.cej.2017.06.028.
[200] M.S.G. Nandagopal, E. Abraham, N. Selvaraju, Advanced neural network prediction and system identification of liquid-liquid flow patterns in circular microchannels with varying angle of confluence, Chem. Eng. J. 309 (2017) 850–865. doi:10.1016/j.cej.2016.10.106.
[201] Y. Ding, X. Casadevall I Solvas, A. Demello, “V-junction”: A novel structure for high-speed generation of bespoke droplet flows, Analyst. 140 (2015) 414–421. doi:10.1039/c4an01730g.
[202] R. Lin, J.S. Fisher, M.G. Simon, A.P. Lee, Novel on-demand droplet generation for selective fluid sample extraction, Biomicrofluidics. 6 (2012) 024103. doi:10.1063/1.3699972.
[203] C.-H. Lee, S.-K. Hsiung, G.-B. Lee, A tunable microflow focusing device utilizing controllable moving walls and its applications for formation of micro-droplets in liquids, J. Micromechanics Microengineering. 17 (2007) 1121–1129. doi:10.1088/0960-1317/17/6/004.
[204] M.T. Chung, D. Núñez, D. Cai, K. Kurabayashi, Deterministic droplet-based co-encapsulation and pairing of microparticles: Via active sorting and downstream merging, Lab Chip. 17 (2017) 3664–3671. doi:10.1039/c7lc00745k.
[205] P. Sundararajan, J. Wang, L.A. Rosen, A. Procopio, K. Rosenberg, Engineering

polymeric Janus particles for drug delivery using microfluidic solvent dissolution approach, Chem. Eng. Sci. 178 (2018) 199–210. doi:10.1016/j.ces.2017.12.013.
[206] P. Kumaresan, C.J. Yang, S.A. Cronier, R.G. Blazej, R.A. Mathies, High-Throughput Single Copy DNA Amplification and Cell Analysis in Engineered Nanoliter Droplets, ACS Publ. 80 (2008) 3522–3529. doi:10.1021/ac800327d.
[207] Y. Zeng, R. Novak, J. Shuga, M.T. Smith, R.A. Mathies, High-Performance Single Cell Genetic Analysis Using Micro uidic Emulsion Generator Arrays, Anal. Chem. 82 (2008) 3183–3190.
[208] N. Tottori, T. Nisisako, High-throughput production of satellite-free droplets through a parallelized microfluidic deterministic lateral displacement device, Sensors Actuators, B Chem. 260 (2018) 918–926. doi:10.1016/j.snb.2018.01.112.
[209] H.H. Jeong, S. Yadavali, D. Issadore, D. Lee, Liter-scale production of uniform gas bubbles: Via parallelization of flow-focusing generators, Lab Chip. 17 (2017) 2667–2673. doi:10.1039/c7lc00295e.
[210] T. Nisisako, T. Torii, Microfluidic large-scale integration on a chip for mass production of monodisperse droplets and particles, Lab Chip. 8 (2008) 287–293. doi:10.1039/b713141k.
[211] S. Xu, Z. Nie, M. Seo, P. Lewis, E. Kumacheva, H.A. Stone, P. Garstecki, D.B. Weibel, I. Gitlin, G.M. Whitesides, Generation of monodisperse particles by using microfluidics: Control over size, shape, and composition, Angew. Chemie - Int. Ed. 44 (2005) 724–728. doi:10.1002/anie.200462226.
[212] E. Hondroulis, A. Movila, P. Sabhachandani, S. Sarkar, N. Cohen, T. Kawai, T. Konry, A droplet-merging platform for comparative functional analysis of m1 and m2 macrophages in response to e. coli-induced stimuli, Biotechnol. Bioeng. 114 (2017) 705–709. doi:10.1002/bit.26196.
[213] Z. Nie, M.S. Seo, S. Xu, P.C. Lewis, M. Mok, E. Kumacheva, G.M. Whitesides, P. Garstecki, H.A. Stone, Emulsification in a microfluidic flow-focusing device: Effect of the viscosities of the liquids, Microfluid. Nanofluidics. 5 (2008) 585–594. doi:10.1007/s10404-008-0271-y.
[214] B.R. Benson, H.A. Stone, R.K. Prud'homme, An "Off-the-shelf" Capillary Microfluidic Device that Enables Tuning of the Droplet Breakup Regime at Constant Flow Rates, Lab Chip. 13 (2013) 4507–4511. doi:10.1039/c3lc50804h.
[215] A.J.L. Morgan, L.H. San Jose, W.D. Jamieson, J.M. Wymant, B. Song, P. Stephens, D.A. Barrow, O.K. Castell, Simple and versatile 3D printed microfluidics using fused filament fabrication, PLoS One. 11 (2016) e0152023. doi:10.1371/journal.pone.0152023.
[216] Z. Wang, N. Martin, D. Hini, B. Mills, K. Kim, Rapid Fabrication of Multilayer Microfluidic Devices Using the Liquid Crystal Display-Based Stereolithography 3D Printing System, 3D Print. Addit. Manuf. 4 (2017) 156–164. doi:10.1089/3dp.2017.0028.
[217] H. Yamashita, M. Morita, H. Sugiura, K. Fujiwara, H. Onoe, M. Takinoue, Generation of monodisperse cell-sized microdroplets using a centrifuge-based axisymmetric co-flowing microfluidic device, J. Biosci. Bioeng. 119 (2015) 492–495. doi:10.1016/j.jbiosc.2014.09.018.
[218] C. Deng, H. Wang, W. Huang, S. Cheng, Numerical and experimental study of oil-in-water (O/W) droplet formation in a co-flowing capillary device, Colloids

Surfaces A Physicochem. Eng. Asp. 533 (2017) 1–8. doi:10.1016/j.colsurfa.2017.05.041.
[219] A.S. Utada, E. Lorenceau, D.R. Link, P.D. Kaplan, H.A. Stone, D.A. Weitz, Monodisperse Double Emulsions Generated from a Microcapillary Device, Science (80-.). 308 (2005) 537–541. doi:10.1126/science.1109164.
[220] Z. Zhou, T. Kong, H. Mkaouar, K.N. Salama, J.M. Zhang, A hybrid modular microfluidic device for emulsion generation, Sensors Actuators, A Phys. 280 (2018) 422–428. doi:10.1016/j.sna.2018.08.005.
[221] F.N. Sang, Z. Chen, Y.D. Wang, J.H. Xu, Dynamic formation and scaling law of hollow droplet with gas/oil/water system in dual-coaxial microfluidic devices, AIChE J. 64 (2018) 730–739. doi:10.1002/aic.15930.
[222] S.H. Kim, J.W. Kim, D.H. Kim, S.H. Han, D.A. Weitz, Enhanced-throughput production of polymersomes using a parallelized capillary microfluidic device, Microfluid. Nanofluidics. 14 (2013) 509–514. doi:10.1007/s10404-012-1069-5.
[223] S. Tendulkar, S.H. Mirmalek-Sani, C. Childers, J. Saul, E.C. Opara, M.K. Ramasubramanian, A three-dimensional microfluidic approach to scaling up microencapsulation of cells, Biomed. Microdevices. 14 (2012) 461–469. doi:10.1007/s10544-011-9623-6.
[224] C. Cramer, P. Fischer, E.J. Windhab, Drop formation in a co-flowing ambient fluid, Chem. Eng. Sci. 59 (2004) 3045–3058. doi:10.1016/j.ces.2004.04.006.
[225] I. Chakraborty, J. Ricouvier, P. Yazhgur, P. Tabeling, A.M. Leshansky, Microfluidic step-emulsification in axisymmetric geometry, Lab Chip. 17 (2017) 3609–3620. doi:10.1039/c7lc00755h.
[226] K. Xu, J.H. Xu, Y.C. Lu, G.S. Luo, A novel method of fabricating, adjusting, and optimizing polystyrene colloidal crystal nonspherical microparticles from gas-water janus droplets in a double Coaxial Microfluidic Device, Cryst. Growth Des. 14 (2014) 401–405. doi:10.1021/cg401653b.
[227] Y. Chen, J.H. Xu, G.S. Luo, The dynamic adsorption of different surfactants on droplet formation in coaxial microfluidic devices, Chem. Eng. Sci. 138 (2015) 655–662. doi:10.1016/j.ces.2015.08.048.
[228] Y. Chen, G.T. Liu, J.H. Xu, G.S. Luo, The dynamic mass transfer of surfactants upon droplet formation in coaxial microfluidic devices, Chem. Eng. Sci. 132 (2015) 1–8. doi:10.1016/j.ces.2015.04.006.
[229] W.J. Jeong, J.Y. Kim, J. Choo, E.K. Lee, C.S. Han, D.J. Beebe, G.H. Seong, S.H. Lee, Continuous fabrication of biocatalyst immobilized microparticles using photopolymerization and immiscible liquids in microfluidic systems, Langmuir. 21 (2005) 3738–3741. doi:10.1021/la050105l.
[230] E. Kang, S.J. Shin, K.H. Lee, S.H. Lee, Novel PDMS cylindrical channels that generate coaxial flow, and application to fabrication of microfibers and particles, Lab Chip. 10 (2010) 1856–1861. doi:10.1039/c002695f.
[231] A. Shams Khorrami, P. Rezai, Oscillating dispersed-phase co-flow microfluidic droplet generation: Multi-droplet size effect, Biomicrofluidics. 12 (2018) 034113. doi:10.1063/1.5034473.
[232] S.L. Anna, N. Bontoux, H.A. Stone, Formation of dispersions using “flow focusing” in microchannels, Appl. Phys. Lett. 82 (2003) 364–366. doi:10.1063/1.1537519.

[233] C. Bayly, K. Cheung, Alginate Encapsulation of Cell-Laden Beads for Microfluidic Tumor Spheroid Culture, 17th Int. Conf. Miniaturized Syst. Chem. Life Sci. (2013) 1710–1712. http://www.rsc.org/images/loc/2013/PDFs/Papers/572_1179.pdf.
[234] V. Trivedi, E.S. Ereifej, A. Doshi, P. Sehgal, P.J. Vandevord, A.S. Basu, Microfluidic encapsulation of cells in alginate capsules for high throughput screening, Proc. 31st Annu. Int. Conf. IEEE Eng. Med. Biol. Soc. Eng. Futur. Biomed. EMBC 2009. (2009) 7037–7040. doi:10.1109/IEMBS.2009.5333308.
[235] R. Suryo, O.A. Basaran, Tip streaming from a liquid drop forming from a tube in a co-flowing outer fluid, Phys. Fluids. 18 (2006) 082102. doi:10.1063/1.2335621.
[236] P.B. Umbanhowar, V. Prasad, D.A. Weitz, Monodisperse emulsuion generation via drop break-off in a co-flowing stream, Langmuir. 16 (1999) 347–351.
[237] P. Moslemy, S.R. Guiot, R.J. Neufeld, Production of size-controlled gellan gum microbeads encapsulating gasoline-degrading bacteria, Enzyme Microb. Technol. 30 (2002) 10–18. doi:10.1016/S0141-0229(01)00440-9.
[238] G. Della Porta, F. Castaldo, M. Scognamiglio, L. Paciello, P. Parascandola, E. Reverchon, Bacteria microencapsulation in PLGA microdevices by supercritical emulsion extraction, J. Supercrit. Fluids. 63 (2012) 1–7. doi:10.1016/j.supflu.2011.12.020.
[239] I. El-Gibaly, Development and in vitro evaluation of novel floating chitosan microcapsules for oral use: Comparison with non-floating chitosan microspheres, Int. J. Pharm. 249 (2002) 7–21. doi:10.1016/S0378-5173(02)00396-4.
[240] L. Lu, R.M. Irwin, M.A. Coloma, J.W. Schertzer, P.R. Chiarot, Removal of excess interfacial material from surface-modified emulsions using a microfluidic device with triangular post geometry, Microfluid. Nanofluidics. 18 (2015) 1233–1246. doi:10.1007/s10404-014-1521-9.
[241] T.C. Scanlon, S.M. Dostal, K.E. Griswold, A high-throughput screen for antibiotic drug discovery, Biotechnol. Bioeng. 111 (2014) 232–243. doi:10.1002/bit.25019.
[242] X. Cui, L. Ren, Y. Shan, X. Wang, Z. Yang, C. Li, J. Xu, B. Ma, Smartphone-based rapid quantification of viable bacteria by single-cell microdroplet turbidity imaging, Analyst. 143 (2018) 3309–3316. doi:10.1039/C8AN00456K.
[243] M. Chau, M. Abolhasani, H. Thérien-Aubin, Y. Li, Y. Wang, D. Velasco, E. Tumarkin, A. Ramachandran, E. Kumacheva, Microfluidic generation of composite biopolymer microgels with tunable compositions and mechanical properties, Biomacromolecules. 15 (2014) 2419–2425. doi:10.1021/bm5002813.
[244] H. Lu, O. Caen, J. Vrignon, E. Zonta, Z. El Harrak, P. Nizard, J.C. Baret, V. Taly, High throughput single cell counting in droplet-based microfluidics, Sci. Rep. 7 (2017) 1–9. doi:10.1038/s41598-017-01454-4.
[245] S. Holler, C. Porcelli, I.A. Ieropoulos, M.M. Hanczyc, Transport of Live Cells Under Sterile Conditions Using a Chemotactic Droplet, Sci. Rep. 8 (2018) 1–9. doi:10.1038/s41598-018-26703-y.
[246] N. Ahmed, D. Sukovich, A.R. Abate, Operation of droplet-microfluidic devices with a lab centrifuge, Micromachines. 7 (2016) 161. doi:10.3390/mi7090161.
[247] J.H. Xu, P.F. Dong, H. Zhao, C.P. Tostado, G.S. Luo, The dynamic effects of surfactants on droplet formation in coaxial microfluidic devices, Langmuir. 28 (2012) 9250–9258. doi:10.1021/la301363d.

[248] K. Kailasapathy, Microencapsulation of Probiotic Bacteria: Technology and Potential Applications, Curr. Issues Intest. Microbiol. 3 (2002) 39–48.
[249] M. Karle, S.K. Vashist, R. Zengerle, F. von Stetten, Microfluidic solutions enabling continuous processing and monitoring of biological samples: A review, Anal. Chim. Acta. 929 (2016) 1–22. doi:10.1016/j.aca.2016.04.055.
[250] C. Holtze, A.C. Rowat, J.J. Agresti, J.B. Hutchison, F.E. Angilè, C.H.J. Schmitz, S. Köster, H. Duan, K.J. Humphry, R.A. Scanga, J.S. Johnson, D. Pisignano, D.A. Weitz, Biocompatible surfactants for water-in-fluorocarbon emulsions, Lab Chip. 8 (2008) 1632–1639. doi:10.1039/b806706f.
[251] G. Luka, A. Ahmadi, H. Najjaran, E. Alocilja, M. Derosa, K. Wolthers, A. Malki, H. Aziz, A. Althani, M. Hoorfar, Microfluidics integrated biosensors: A leading technology towards lab-on-A-chip and sensing applications, Sensors. 15 (2015) 30011–30031. doi:10.3390/s151229783.
[252] G. Muschiolik, Multiple emulsions for food use, Curr. Opin. Colloid Interface Sci. 12 (2007) 213–220. doi:10.1016/j.cocis.2007.07.006.
[253] Droplet Pack - Easy Generation, Elveflow. (2018). https://www.elveflow.com/microfluidic-flow-control-products/microfluidic-application-packs/droplet-pack/ (accessed October 16, 2018).
[254] Droplet Generation, Dolomite Microfluid. (2018). https://www.dolomite-microfluidics.com/applications/droplet-generation/ (accessed October 16, 2018).
[255] Organ-on-Chip Platform, Fluigent. (2018). https://www.fluigent.com/product/microfluidic-components/organ-on-chip-platform/ (accessed October 16, 2018).
[256] Microfluidic Organ-On-Chip Pack, Elveflow. (2018). https://www.elveflow.com/microfluidic-flow-control-products/microfluidic-application-packs/organ-on-chip-pack/ (accessed October 16, 2018).
[257] C.W. Shields, K.A. Ohiri, L.M. Szott, G.P. López, Translating microfluidics: Cell separation technologies and their barriers to commercialization, Cytom. Part B (Clinical Cytom. 92B (2017) 115–125. doi:10.1002/cyto.b.21388.
[258] J. Wang, M. Zou, L. Sun, Y. Cheng, L. Shang, F. Fu, Y. Zhao, Microfluidic generation of Buddha beads-like microcarriers for cell culture, Sci. China Mater. 60 (2017) 857–865. doi:10.1007/s40843-017-9081-5.
[259] M.G. Guerra, C. Volpone, L.M. Galantucci, G. Percoco, Photogrammetric measurements of 3D printed microfluidic devices, Addit. Manuf. 21 (2018) 53–62. doi:10.1016/j.addma.2018.02.013.
[260] A.I. Shallan, P. Smejkal, M. Corban, R.M. Guijt, M.C. Breadmore, Cost-effective three-dimensional printing of visibly transparent microchips within minutes, Anal. Chem. 86 (2014) 3124–3130. doi:10.1021/ac4041857.
[261] B. Parker, R. Samanipour, A. Ahmadi, K. Kim, Rapid fabrication of circular channel microfluidic flow-focusing devices for hydrogel droplet generation, Micro Nano Lett. 11 (2016) 41–45. doi:10.1049/mnl.2015.0329.
[262] P.G. Shankles, L.J. Millet, J.A. Aufrecht, S.T. Retterer, Accessing microfluidics through feature-based design software for 3D printing, PLoS One. 13 (2018) e0192752. doi:10.1371/journal.pone.0192752.
[263] S.M. Hampson, W. Rowe, S.D.R. Christie, M. Platt, 3D printed microfluidic device with integrated optical sensing for particle analysis, Sensors Actuators, B

Chem. 256 (2018) 1030–1037. doi:10.1016/j.snb.2017.10.041.
[264] W. Wang, R. Xie, X.J. Ju, T. Luo, L. Liu, D.A. Weitz, L.Y. Chu, Controllable microfluidic production of multicomponent multiple emulsions, Lab Chip. 11 (2011) 1587–1592. doi:10.1039/c1lc20065h.
[265] A.S. Utada, A. Fernandez-Nieves, H.A. Stone, D.A. Weitz, Dripping to jetting transitions in coflowing liquid streams, Phys. Rev. Lett. 99 (2007) 094502. doi:10.1103/PhysRevLett.99.094502.
[266] M. V. Bandulasena, G.T. Vladisavljević, O.G. Odunmbaku, B. Benyahia, Continuous synthesis of PVP stabilized biocompatible gold nanoparticles with a controlled size using a 3D glass capillary microfluidic device, Chem. Eng. Sci. 171 (2017) 233–243. doi:10.1016/j.ces.2017.05.035.
[267] R. Othman, G.T. Vladisavljević, H.C. Hemaka Bandulasena, Z.K. Nagy, Production of polymeric nanoparticles by micromixing in a co-flow microfluidic glass capillary device, Chem. Eng. J. 280 (2015) 316–329. doi:10.1016/j.cej.2015.05.083.
[268] X. Cheng, R. Liu, Y. He, A simple method for the preparation of monodisperse protein-loaded microspheres with high encapsulation efficiencies, Eur. J. Pharm. Biopharm. 76 (2010) 336–341. doi:10.1016/j.ejpb.2010.07.013.
[269] T.P. Lagus, J.F. Edd, A review of the theory, methods and recent applications of high-throughput single-cell droplet microfluidics, J. Phys. D. Appl. Phys. 46 (2013). doi:10.1088/0022-3727/46/11/114005.
[270] N.N. Deng, W. Wang, X.J. Ju, R. Xie, L.Y. Chu, Spontaneous transfer of droplets across microfluidic laminar interfaces, Lab Chip. 16 (2016) 4326–4332. doi:10.1039/c6lc01022a.
[271] E.H.M. Wong, E. Rondeau, P. Schuetz, J. Cooper-White, A microfluidic-based method for the transfer of biopolymer particles from an oil phase to an aqueous phase, Lab Chip. 9 (2009) 2582–2590. doi:10.1039/b903774h.
[272] E. Gogolides, K. Ellinas, A. Tserepi, Hierarchical micro and nano structured, hydrophilic, superhydrophobic and superoleophobic surfaces incorporated in microfluidics, microarrays and lab on chip microsystems, Microelectron. Eng. 132 (2015) 135–155. doi:10.1016/j.mee.2014.10.002.
[273] N.M. Catafard, HIGH-THROUGHPUT CELL ENCAPSULATION IN MONODISPERSE AGAROSE MICROCAPSULES USING A MICROFLUIDIC DEVICE In the Faculty of Graduate Studies (Physics), University of Ottawa, 2014.
[274] S. Hong, H.J. Hsu, R. Kaunas, J. Kameoka, Collagen microsphere production on a chip, Lab Chip. 12 (2012) 3277–3280. doi:10.1039/c2lc40558j.
[275] D.E. Angelescu, D. Siess, Microfluidic phase separation, Proc. IEEE Sensors. 2005 (2005) 175–178. doi:10.1109/ICSENS.2005.1597664.
[276] Y.Y. Chiu, C.K. Huang, Y.W. Lu, Enhancement of microfluidic particle separation using cross-flow filters with hydrodynamic focusing, Biomicrofluidics. 10 (2016). doi:10.1063/1.4939944.
[277] Y. Jiang, Z. Yu, X. Huang, R. Chen, W. Chen, Y. Zeng, C. Xu, H. Min, N. Zheng, X. Cheng, A multilayer lateral-flow microfluidic device for particle separation, Microfluid. Nanofluidics. 22 (2018) 1–7. doi:10.1007/s10404-018-2053-5.
[278] X. Fan, C. Jia, J. Yang, G. Li, H. Mao, Q. Jin, J. Zhao, A microfluidic chip

integrated with a high-density PDMS-based microfiltration membrane for rapid isolation and detection of circulating tumor cells, Biosens. Bioelectron. 71 (2015) 380–386. doi:10.1016/j.bios.2015.04.080.
[279] J.R. Haliburton, S.C. Kim, I.C. Clark, R.A. Sperling, D.A. Weitz, A.R. Abate, Efficient extraction of oil from droplet microfluidic emulsions, Biomicrofluidics. 11 (2017) 1–7. doi:10.1063/1.4984035.
[280] A. Huebner, D. Bratton, G. Whyte, M. Yang, A.J. Demello, C. Abell, F. Hollfelder, Static microdroplet arrays: A microfluidic device for droplet trapping, incubation and release for enzymatic and cell-based assays, Lab Chip. 9 (2009) 692–698. doi:10.1039/b813709a.
[281] A. Viana, J. Marchalot, Y. Fouillet, L. Digianantonio, P. Claustre, M. Cubizolles, J.L. Achard, A passive microfluidic fragmentation system for continuous fluid-particles separation, Prog. Biomed. Opt. Imaging - Proc. SPIE. 8765 (2013) 87650M. doi:10.1117/12.2017211.
[282] A. Viana, J. Marchalot, Y. Fouillet, L. Digianantonio, P. Claustre, M. Cubizolles, J.L. Achard, A passive microfluidic fragmentation system for continuous fluid-particles separation, Prog. Biomed. Opt. Imaging - Proc. SPIE. 8765 (2013) 87650M. doi:10.1117/12.2017211.
[283] A.M. Pit, M.H.G. Duits, F. Mugele, Droplet manipulations in two phase flow microfluidics, Micromachines. 6 (2015) 1768–1793. doi:10.3390/mi6111455.
[284] M. Fingas, A.H. Walker, Oil Spills and Risk Perceptions, in: Oil Spill Sci. Technol., 2nd ed., Elsevier, 2017: pp. 1–70. doi:10.1016/B978-0-12-809413-6.00001-1.
[285] J. Li, L. Yan, Y. Zhao, F. Zha, Q. Wang, Z. Lei, One-step fabrication of robust fabrics with both-faced superhydrophobicity for the separation and capture of oil from water, Phys. Chem. Chem. Phys. 17 (2015) 6451–6457. doi:10.1039/c5cp00154d.
[286] J. Wang, J.X.H. Wong, H. Kwok, X. Li, H.Z. Yu, Facile preparation of nanostructured, superhydrophobic filter paper for efficient water/oil separation, PLoS One. 11 (2016) 1–13. doi:10.1371/journal.pone.0151439.
[287] Z.R. Jiang, J. Ge, Y.X. Zhou, Z.U. Wang, D. Chen, S.H. Yu, H.L. Jiang, Coating sponge with a hydrophobic porous coordination polymer containing a low-energy CF3-decorated surface for continuous pumping recovery of an oil spill from water, NPG Asia Mater. 8 (2016) e253-8. doi:10.1038/am.2016.22.
[288] D.D. Nguyen, N.H. Tai, S.B. Lee, W.S. Kuo, Superhydrophobic and superoleophilic properties of graphene-based sponges fabricated using a facile dip coating method, Energy Environ. Sci. 5 (2012) 7908–7912. doi:10.1039/c2ee21848h.
[289] R.F. Shiu, C.L. Lee, P.Y. Hsieh, C.S. Chen, Y.Y. Kang, W.C. Chin, N.H. Tai, Superhydrophobic graphene-based sponge as a novel sorbent for crude oil removal under various environmental conditions, Chemosphere. 207 (2018) 110–117. doi:10.1016/j.chemosphere.2018.05.071.
[290] L. Zhang, H. Li, X. Lai, X. Su, T. Liang, X. Zeng, Thiolated graphene-based superhydrophobic sponges for oil-water separation, Chem. Eng. J. 316 (2017) 736–743. doi:10.1016/j.cej.2017.02.030.
[291] J.N. Wang, Y.L. Zhang, Y. Liu, W. Zheng, L.P. Lee, H.B. Sun, Recent

developments in superhydrophobic graphene and graphene-related materials: From preparation to potential applications, Nanoscale. 7 (2015) 7101–7114. doi:10.1039/c5nr00719d.
[292] J. Li, D. Li, W. Hu, J. Li, Y. Yang, Y. Wu, Stable superhydrophobic and superoleophilic silica coated polyurethane sponges for the continuous capture and removal of oils from the water surface, New J. Chem. 39 (2015) 9958–9962. doi:10.1039/c5nj01565k.
[293] C. Wang, T. Yao, J. Wu, C. Ma, Z. Fan, Z. Wang, Y. Cheng, Q. Lin, B. Yang, Facile approach in fabricating superhydrophobic and superoleophilic surface for water and oil mixture separation, ACS Appl. Mater. Interfaces. 1 (2009) 2613–2617. doi:10.1021/am900520z.
[294] S. Roy, L. Zhai, L. Van Hai, J.W. Kim, J.H. Park, H.C. Kim, J. Kim, One-step nanocellulose coating converts tissue paper into an efficient separation membrane, Cellulose. 25 (2018) 4871–4886. doi:10.1007/s10570-018-1945-6.
[295] S.W. Ahn, S.S. Lee, S.J. Lee, J.M. Kim, Microfluidic particle separator utilizing sheathless elasto-inertial focusing, Chem. Eng. Sci. 126 (2015) 237–243. doi:10.1016/j.ces.2014.12.019.
[296] H. Liu, S.W. Gao, J.S. Cai, C.L. He, J.J. Mao, T.X. Zhu, Z. Chen, J.Y. Huang, K. Meng, K.Q. Zhang, S.S. Al-Deyab, Y.K. Lai, Recent progress in fabrication and applications of superhydrophobic coating on cellulose-based substrates, Materials (Basel). 9 (2016) 1–37. doi:10.3390/ma9030124.
[297] Y.Q. Liu, Y.L. Zhang, X.Y. Fu, H.B. Sun, Bioinspired Underwater Superoleophobic Membrane Based on a Graphene Oxide Coated Wire Mesh for Efficient Oil/Water Separation, ACS Appl. Mater. Interfaces. 7 (2015) 20930–20936. doi:10.1021/acsami.5b06326.
[298] Q. Ke, Y. Jin, P. Jiang, J. Yu, Oil/Water separation performances of superhydrophobic and superoleophilic sponges, Langmuir. 30 (2014) 13137–13142. doi:10.1021/la502521c.
[299] F. Wang, S. Lei, M. Xue, J. Ou, W. Li, In situ separation and collection of oil from water surface via a novel superoleophilic and superhydrophobic oil containment boom, Langmuir. 30 (2014) 1281–1289. doi:10.1021/la403778e.
[300] S.K. Anciaux, M. Geiger, M.T. Bowser, 3D Printed Micro Free-Flow Electrophoresis Device, Anal. Chem. 88 (2016) 7675–7682. doi:10.1021/acs.analchem.6b01573.
[301] N.P. Macdonald, J.M. Cabot, P. Smejkal, R.M. Guijt, B. Paull, M.C. Breadmore, Comparing Microfluidic Performance of Three-Dimensional (3D) Printing Platforms, Anal. Chem. 89 (2017) 3858–3866. doi:10.1021/acs.analchem.7b00136.
[302] S.T. Beyer, A. Bsoul, A. Ahmadi, K. Walus, 3D alginate constructs for tissue engineering printed using a coaxial flow focusing microfluidic device, 2013 Transducers Eurosensors XXVII 17th Int. Conf. Solid-State Sensors, Actuators Microsystems, TRANSDUCERS EUROSENSORS 2013. (2013) 1206–1209. doi:10.1109/Transducers.2013.6626990.
[303] V. Saggiomo, A.H. Velders, Simple 3D Printed Scaffold-Removal Method for the Fabrication of Intricate Microfluidic Devices, Adv. Sci. 2 (2015) 1–5. doi:10.1002/advs.201500125.
[304] T. Dahlberg, T. Stangner, H. Zhang, K. Wiklund, P. Lundberg, L. Edman, M.

Andersson, 3D printed water-soluble scaffolds for rapid production of PDMS micro-fluidic flow chambers, Sci. Rep. 8 (2018) 1–10. doi:10.1038/s41598-018-21638-w.
[305] Y. He, J. Qiu, J. Fu, J. Zhang, Y. Ren, A. Liu, Printing 3D microfluidic chips with a 3D sugar printer, Microfluid. Nanofluidics. 19 (2015) 447–456. doi:10.1007/s10404-015-1571-7.
[306] P.C. Chen, C.C. Chou, Fabrication of a Nonplanar Microfluidics by Using Sonication-Assisted Dissolution Technique, Proc. 13th Annu. IEEE Int. Conf. Nano/Micro Eng. Mol. Syst. (2018) 421–424. doi:10.1109/NEMS.2018.8557023.
[307] K. Kang, S. Oh, H. Yi, S. Han, Y. Hwang, Fabrication of truly 3D microfluidic channel using 3D-printed soluble mold, Biomicrofluidics. 12 (2018) 014105. doi:10.1063/1.5012548.
[308] C.C. Kuo, C.W. Wang, Y.F. Lee, Y.L. Liu, Q.Y. Qiu, A surface quality improvement apparatus for ABS parts fabricated by additive manufacturing, Int. J. Adv. Manuf. Technol. 89 (2017) 635–642. doi:10.1007/s00170-016-9129-8.
[309] C.C. Kuo, C.M. Chen, S.X. Chang, Polishing mechanism for ABS parts fabricated by additive manufacturing, Int. J. Adv. Manuf. Technol. 91 (2017) 1473–1479. doi:10.1007/s00170-016-9845-0.
[310] E.J. McCullough, V.K. Yadavalli, Surface modification of fused deposition modeling ABS to enable rapid prototyping of biomedical microdevices, J. Mater. Process. Technol. 213 (2013) 947–954. doi:10.1016/j.jmatprotec.2012.12.015.
[311] R.A. Börner, M.T.A. Aliaga, B. Mattiasson, Microcultivation of anaerobic bacteria single cells entrapped in alginate microbeads, Biotechnol. Lett. 35 (2013) 397–405. doi:10.1007/s10529-012-1094-1.
[312] D.J. Collins, A. Neild, A. deMello, A.Q. Liu, Y. Ai, The Poisson distribution and beyond: Methods for microfluidic droplet production and single cell encapsulation, Lab Chip. 15 (2015) 3439–3459. doi:10.1039/c5lc00614g.
[313] T.J. Silhavy, D. Kahne, S. Walker, The Bacterial Cell Envelope, Cold Spring Harb. Perspect. Biol. 2 (2010) a000414. doi:10.1101/cshperspect.a000414.
[314] J. O'Brien, I. Wilson, T. Orton, F. Pognan, Investigation of the Alamar Blue (resazurin) fluorescent dye for the assessment of mammalian cell cytotoxicity, Eur. J. Biochem. 267 (2000) 5421–5426. doi:10.1046/j.1432-1327.2000.01606.x.
[315] K.G. Porter, Y.S. Feig, The use of DAPI for identifying and counting aquatic microflora, Limnol. Oceanogr. 25 (1980) 943–948. doi:Doi 10.4319/Lo.1980.25.5.0943.
[316] J. Kan, K. Wang, F. Chen, Temporal variation and detection limit of an estuarine bacterioplankton community analyzed by denaturing gradient gel electrophoresis (DGGE), Aquat. Microb. Ecol. 42 (2006) 7–18. doi:10.3354/ame042007.
[317] J. Liu, J. Wang, G. Gao, M.G. Bartlam, Y. Wang, Distribution and diversity of fungi in freshwater sediments on a river catchment scale, Front. Microbiol. 6 (2015). doi:10.3389/fmicb.2015.00329.
[318] C.J. Newberry, G. Webster, B.A. Cragg, R.J. Parkes, A.J. Weightman, J.C. Fry, Diversity of prokaryotes and methanogenesis in deep subsurface sediments from the Nankai Trough, Ocean Drilling Program Leg 190, Environ. Microbiol. 6 (2004) 274–287. doi:10.1111/j.1462-2920.2004.00568.x.
[319] P. Aguayo, P. González, V. Campos, T.L. Maugeri, M. Papale, C. Gugliandolo,

M.A. Martinez, Comparison of Prokaryotic Diversity in Cold, Oligotrophic Remote Lakes of Chilean Patagonia, Curr. Microbiol. 74 (2017) 598–613. doi:10.1007/s00284-017-1209-y.
[320] J. Wang, J. Kan, L. Borecki, X. Zhang, D. Wang, J. Sun, A snapshot on spatial and vertical distribution of bacterial communities in the eastern Indian Ocean, Acta Oceanol. Sin. 35 (2016) 85–93. doi:10.1007/s13131-016-0871-4.
[321] G. Muyzer, E.C. De Waal, A.G. Uitterlinden, Profiling of Complex Microbial Populations by Denaturing Gradient Gel Electrophoresis Analysis of Polymerase Chain Reaction-Amplified Genes Coding for 16S rRNA, Appl. Environ. Microbiol. 59 (1993) 695–700. doi:0099-2240/93/030695-06$02.00/0.
[322] L.A. Pray, Discovery of DNA Structure and Function: Watson and Crick, Nat. Educ. (2008). https://www.nature.com/scitable/topicpage/discovery-of-dna-structure-and-function-watson-397 (accessed May 9, 2019).
[323] M. Elstner, P. Hobza, T. Frauenheim, S. Suhai, E. Kaxiras, Hydrogen bonding and stacking interactions of nucleic acid base pairs: A density functional-theory based treatment, J. Chem. Phys. 114 (2001) 5149–5155. doi:10.1063/1.1329889.
[324] Nucleotide, Natl. Hum. Genome Res. Inst. (n.d.). https://www.genome.gov/genetics-glossary/Nucleotide (accessed May 9, 2019).
[325] F. Strathdee, A. Free, Denaturing Gradient Gel Electrophoresis (DGGE), in: S. Makovets (Ed.), DNA Electrophor. Methods Protoc. Methods Mol. Biol., Springer, New York, 2013: pp. 145–157. doi:10.1016/0958-1669(93)90029-V.
[326] M.D. Frank-Kamenetskii, Biophysics of the DNA molecule, Phys. Rep. 288 (1997) 13–60. doi:10.1016/S0370-1573(97)00020-3.
[327] S. Phadke, A.F. Salvador, J.I. Alves, O. Bretschger, M.M. Alves, M.A. Pereira, Harnessing the Power of PCR Molecular Fingerprinting Methods and Next Generation Sequencing for Understanding Structure and Function in Microbial Communities, in: L. Domingues (Ed.), PCR Methods Protoc., Springer, New York, NY, 2017: pp. 225–248. doi:10.1007/978-1-4939-7060-5.
[328] T.C. Lorenz, Polymerase Chain Reaction: Basic Protocol Plus Troubleshooting and Optimization Strategies, J. Vis. Exp. (2012) 1–14. doi:10.3791/3998.
[329] J. Welsh, M. McClelland, Fingerprinting using arbitrary primed PCR: application to genetic mapping, population biology, epidemiology, and detection of differentially expressed RNAs., in: K.B. Mullis, F. Ferré, R.A. Gibbs (Eds.), Polym. Chain React., Birkhäuser, Boston, MA, 1994: pp. 295–303.
[330] M. Tsukuda, K. Kitahara, K. Miyazaki, Comparative RNA function analysis reveals high functional similarity between distantly related bacterial 16 S rRNAs, Sci. Rep. 7 (2017) 1–8. doi:10.1038/s41598-017-10214-3.
[331] C.R. Woese, G.E. Fox, Phylogenetic structure of the prokaryotic domain: The primary kingdoms, Proc. Natl. Acad. Sci. U. S. A. 74 (1977) 5088–5090.
[332] K. Hayashi, Manipulation of DNA by PCR, in: K.B. Mullis, F. Ferré, R.A. Gibbs (Eds.), Polym. Chain React., Birkhäuser, Boston, MA, 1994: pp. 3–13. doi:10.1007/978-1-4612-0257-8_1.
[333] D. Caetano-Anollés, Polymerase Chain Reaction, Brenner's Encycl. Genet. Second Ed. 133 (2013) 392–395. doi:10.1016/B978-0-12-374984-0.01186-4.
[334] N. Boon, W. Windt, Evaluation of nested PCR–DGGE (denaturing gradient gel electrophoresis) with group-specific 16S rRNA primers for the analysis of

bacterial communities, FEMS Microbiol. …. 39 (2002) 101–112. http://onlinelibrary.wiley.com/doi/10.1111/j.1574-6941.2002.tb00911.x/full.
[335] DNeasy UltraClean Microbial Kit Handbook, QIAGEN. (n.d.). https://www.qiagen.com/ca/resources/resourcedetail?id=26d8d1f5-6aab-495e-931b-55a3b3c5ec36&lang=en (accessed May 14, 2019).
[336] R.E. Pike, A Comprehensive Analysis of the Microbial Diversity Associated with Eunicea Fusca and Related Plexauridae Octocorals, and the Isolation of New Natural Products from Selected, Associated Bactera, University of Prince Edward Island, 2013.
[337] B. Wawrik, L. Kerkhof, G.J. Zylstra, J.J. Kukor, Identification of unique type II polyketide synthase genes in soil, Appl. Environ. Microbiol. 71 (2005) 2232–2238. doi:10.1128/AEM.71.5.2232-2238.2005.
[338] C. Codling, L. O'Mahony, F. Shanahan, E.M.M. Quigley, J.R. Marchesi, A molecular analysis of fecal and mucosal bacterial communities in irritable bowel syndrome, Dig. Dis. Sci. 55 (2010) 392–397. doi:10.1007/s10620-009-0934-x.
[339] G. Webster, C.J. Newberry, J.C. Fry, A.J. Weightman, Assessment of bacterial community structure in the deep sub-seafloor biosphere by 16S rDNA-based techniques: A cautionary tale, J. Microbiol. Methods. 55 (2003) 155–164. doi:10.1016/S0167-7012(03)00140-4.
[340] C.W. Chong, G.Y. Annie Tan, R.C.S. Wong, M.J. Riddle, I.K.P. Tan, DGGE fingerprinting of bacteria in soils from eight ecologically different sites around casey station, Antarctica, Polar Biol. 32 (2009) 853–860. doi:10.1007/s00300-009-0585-6.
[341] C.P. Foong, C.M. Wong Vui Ling, M. González, Metagenomic analyses of the dominant bacterial community in the Fildes Peninsula, King George Island (South Shetland Islands), Polar Sci. 4 (2010) 263–273. doi:10.1016/j.polar.2010.05.010.
[342] DCode™ Universal Mutation Detection System, Bio-Rad. (n.d.). http://www.bio-rad.com/en-ca/product/dcode-universal-mutation-detection-system?ID=b06708b1-b4d2-4ac4-a32b-c696666a4f90 (accessed May 15, 2019).
[343] M. Veldhuis, G. Kraay, K. Timmermans, Cell death in phytoplankton: Correlation between changes in membrane permeability, photosynthetic activity, pigmentation and growth, Eur. J. Phycol. 36 (2001) 167–177. doi:10.1080/09670260110001735318.
[344] J. Dorsey, C.M. Yentsch, S. Mayo, C. McKenna, Rapid analytical technique for the assessment of cell metabolic activity in marine microalgae, Cytometry. 10 (1989) 622–628. doi:10.1002/cyto.990100518.
[345] B. Palenik, A.Z. Worden, J.K. Nolan, Assessing the Dynamics and Ecology of Marine Picophytoplankton: The Importance of the Eukaryotic Component, Limnol. Oceanogr. 49 (2004) 168–179. http://www.jstor.org/stable/3597622.
[346] F.J. Jochem, D. Meyerdierks, Cytometric measurement of the DNA cell cycle in the presence of chlorophyll autofluorescence in marine eukaryotic phytoplankton by the blue-light excited dye YOYO-1, Mar. Ecol. Prog. Ser. 185 (1999) 301–307. doi:10.3354/meps185301.
[347] Z.T. Ying, F.C. Dobbs, Green autofluorescence in dinoflagellates, diatoms, and other microalgae and its implications for vital staining and morphological studies, Appl. Environ. Microbiol. 73 (2007) 2306–2313. doi:10.1128/AEM.01741-06.

[348] T.J. Zananski, M.R. Twiss, T.B. Mihuc, Use of fluorimetry to evaluate atrazine toxicity to phytoplankton communities, Aquat. Ecosyst. Heal. Manag. 13 (2010) 56–65. doi:10.1080/14634980903565933.
[349] R.J. Olson, E.R. Zettler, O.K. Anderson, Discrimination of eukaryotic phytoplankton cell types from light scatter and autofluorescence properties measured by flow cytometry, Cytometry. 10 (1989) 636–643. doi:10.1002/cyto.990100520.
[350] G.E. Fogg, Some comments on picoplankton and its importance in the pelagic ecosystem, Aquat. Microb. Ecol. 9 (1995) 33–39. http://www.int-res.com/articles/ame/9/a009p033.pdf.
[351] B. Little, S. Gerchakov, L. Udey, A method for sterilization of natural seawater, J. Microbiol. Methods. 7 (1987) 193–200. doi:10.1016/0167-7012(87)90040-6.
[352] E. Lilly, G. Sitta Sittampalam, N.P. Coussens, K. Brimacombe Abigail Grossman, M. Arkin, D. Auld, C. Austin Jonathan Baell, B. Bejcek, J.M. Caaveiro Thomas DY Chung, J.L. Dahlin, V.L. Devanaryan Timothy Foley, M. Glicksman, M.D. Hall Joseph V Haas, J. Inglese, P.W. Iversen, S.D. Kahl Stephen C Kales, M. Lal-Nag, Z. Li, J. McGee Owen McManus, T. Riss, O. Joseph Trask, J.R. Weidner Mary Jo Wildey, M. Xia, X. Xu, Assay Guidance Manual, Eli Lilly & Company and the National Center for Advancing Translational Sciences Bethesda (MD), 2018. doi:PMID:22553881.
[353] P. Kuczynska, M. Jemiola-Rzeminska, K. Strzalka, Photosynthetic pigments in diatoms, Mar. Drugs. 13 (2015) 5847–5881. doi:10.3390/md13095847.
[354] A.M. Kaushik, K. Hsieh, L. Chen, D.J. Shin, J.C. Liao, T.H. Wang, Accelerating bacterial growth detection and antimicrobial susceptibility assessment in integrated picoliter droplet platform, Biosens. Bioelectron. 97 (2017) 260–266. doi:10.1016/j.bios.2017.06.006.
[355] R. Jia, D. Yang, D. Xu, T. Gu, Anaerobic corrosion of 304 stainless steel caused by the Pseudomonas aeruginosa biofilm, Front. Microbiol. 8 (2017) 1–9. doi:10.3389/fmicb.2017.02335.
[356] S. Evangelista, G. Viccione, O. Siani, A new cost effective, long life and low resistance filter cartridge for water treatment, J. Water Process Eng. 27 (2019) 1–14. doi:10.1016/j.jwpe.2018.11.004.
[357] P. Garstecki, M.J. Fuerstman, H.A. Stone, G.M. Whitesides, Formation of droplets and bubbles in a microfluidic T-junction - Scaling and mechanism of break-up, Lab Chip. 6 (2006) 437–446. doi:10.1039/b510841a.
[358] Y. Wang, Y. Hao, W. Wang, Z. Xu, Y. Gao, Z. Gao, Q. Wang, J. Zhang, E. Li, Application of a microfluidic chip-based 3D co-culture to test drug sensitivity for individualized treatment of lung cancer, Biomaterials. 34 (2013) 4109–4117. doi:10.1016/j.biomaterials.2013.02.045.
[359] M. Leite, A. Varanda, A.R. Ribeiro, A. Silva, M.F. Vaz, Mechanical properties and water absorption of surface modified ABS 3D printed by fused deposition modelling, Rapid Prototyp. J. 24 (2018) 195–203. doi:10.1108/RPJ-04-2016-0057.
[360] C. Neff, M. Trapuzzano, N.B. Crane, Impact of vapor polishing on surface quality and mechanical properties of extruded ABS, Rapid Prototyp. J. 24 (2018) 501–508. doi:10.1108/RPJ-03-2017-0039.
[361] Ultimaker PVA, (n.d.). https://ultimaker.com/en/products/materials/pva (accessed

March 28, 2019).
[362] A.A. de la Lastra, K.R. Hixon, L. Aryan, A.N. Banks, A.Y. Lin, A.F. Hall, S.A. Sell, Tissue engineering scaffolds fabricated in dissolvable 3D-Printed molds for patient-specific craniofacial bone regeneration, J. Funct. Biomater. 9 (2018) 46. doi:10.3390/jfb9030046.